



Universidad de Granada



Dinámica Ambiental

AN UNIFIED DESIGN METHOD OF MARITIME WORKS AGAINST WAVES

Doctoral Thesis

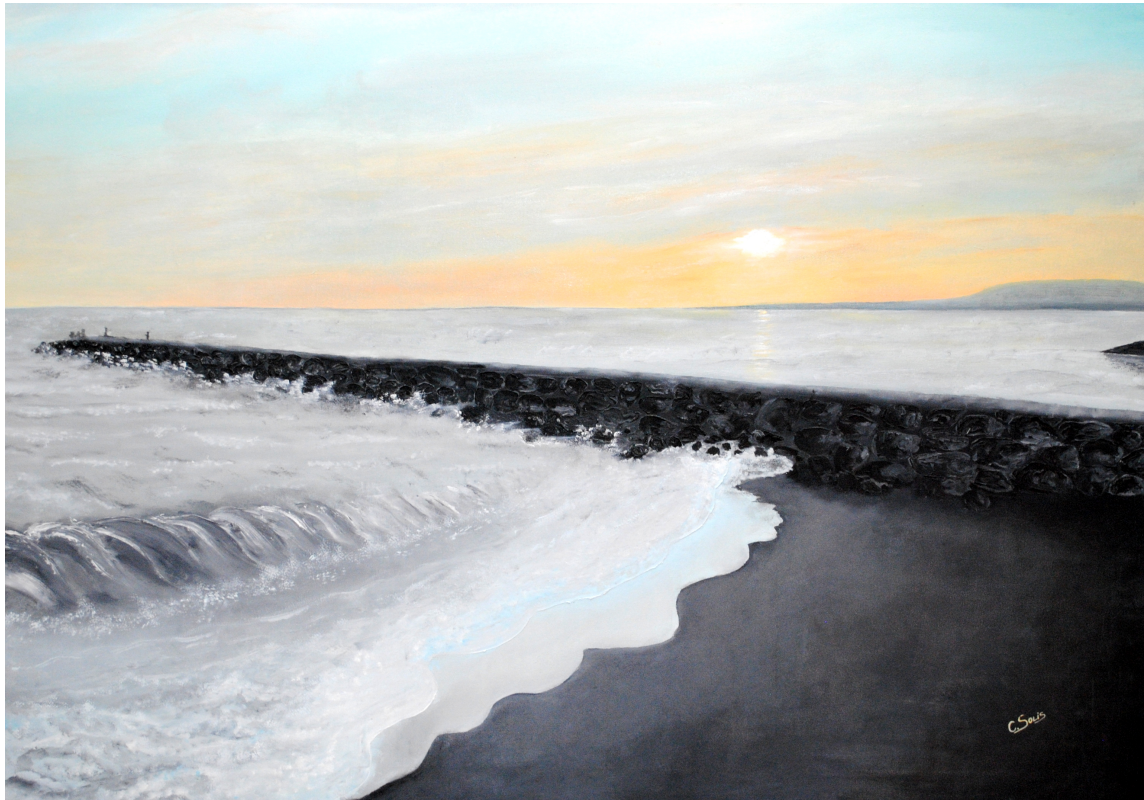
Montserrat Vílchez Solís

Advisor: Miguel Ángel Losada Rodríguez

Programa de Doctorado de Dinámica de Flujos
Biogeoquímicos y sus Aplicaciones
Instituto Interuniversitario de Investigación del
Sistema Tierra en Andalucía (IISTA)

January 2016

A Fran,
por hacerme más fácil y feliz el camino.



Playa de Caparica, Lisboa
Carmen Solís López

“Investigar es ver lo que todo el mundo ha visto
y pensar lo que nadie más ha pensado”

Albert Szent-Györgi

Agradecimientos

En un lugar de Granada de cuyo nombre no puedo olvidarme, tuvieron lugar mis primeros contactos con el mundo de la investigación. Ese lugar fue el CEAMA y el momento, hace ya unos cuantos años. Mentiría si dijera que preveía este trabajo como el trabajo de mi vida, pero tengo que reconocer que el desarrollo de esta tesis doctoral me ha enseñado a entusiasmarme y a disfrutar de él. El trabajo que tienes en tus manos es el fruto, por un lado, de largas horas de trabajo, pero por otro, de la ayuda de muchas personas que desinteresadamente me han prestado su ayuda. A todas ellas me gustaría mostrar mi agradecimiento.

En primer lugar a mi director de tesis, Miguel Losada. Bien sabemos los dos que este trabajo no es sólo mío. Muchas gracias por compartir conmigo todo el saber y la experiencia acumulada en tantos años de trabajo. Me ha encantado participar de tu emoción con cada nuevo resultado, como si siempre fuera el primero.

Gracias también a mis compañeros del laboratorio. A María por darme su apoyo y compañía durante todos estos años, y a todos los que cada día me han aportado su granito de arena, intelectual o personal, para endulzarme las jornadas de trabajo o los descansos del mismo, especialmente a Sergio, Somoano, Laura, Pedro, Jesús y Andrea, cuyas correcciones además, junto con las de María y Fran, han ayudado a mejorar este documento. A Iciar por colaborar en la realización de los ensayos. Sin ella esta tesis se hubiera hecho interminable. Y a todos los demás compañeros del Grupo de Dinámica de Flujos Ambientales por prestarse siempre a ayudar cuando les he necesitado. A los que siguen aquí y a los que se fueron.

A Graça, por acogerme, darme la oportunidad de conocer otra forma de trabajar, otros compañeros, otra ciudad, y hacerme sentir como en casa.

A mi familia, imprescindible en mi vida. A mis padres, Juan y Carmen, por apoyarme siempre incondicionalmente y enseñarme a valorar el trabajo bien hecho. A mis hermanos, Mari, Rocío y Juande, por brindarme siempre su cariño, su comprensión y consejo. De manera especial a mi sobrina, porque aunque ella ahora mismo no lo entienda ha colmado de alegría mis días en este año de intenso trabajo, sólo con dejarme verla crecer.

A ti Fran, te dedico esta tesis, justo hoy, el día en que se cumplen tres años caminando juntos. Sé que no te gusta que te dé las gracias, pero en esta ocasión vas a tener que perdonarme. Gracias, por estar ahí, por prestarme tu apoyo y ayuda, por tu dedicación, por ser mi fuente constante de motivación y por hacerme tan feliz.

Abstract

A breakwater is a maritime structure built to protect a harbor, sheltered area, or shoreline from the full impact of waves. Breakwaters differ in the way that they deal with impinging waves. The selection of a breakwater type and the dimensioning of its sections and elements depends on the project requirements, site characteristics and wave climate. Accordingly, such choices should be made after analyzing different alternatives in order to select the one that best guarantees the operability and safety of the breakwater at the lowest cost. The efficiency of each alternative can be evaluated from the verification of the failure modes that can affect the different parts and elements of the breakwater in its useful life. Currently, this verification is formulated independently for the different failure modes, even in the case in which the failure modes are affected by the same atmospheric and maritime agents. What is more, agents are considered without taken into account their transformation produced by the presence of the structure. This Thesis proposes a unified methodology to simultaneously verify the different failure modes resulting from wind waves-breakwater interaction in front of the breakwater. This is based on the hydraulic performance of the breakwater which is defined according to the wave transformation processes derived from this interaction. To achieve this objective, experimental and numerical works have been performed. The study is done for different breakwater typologies with irregular waves impinging perpendicularly onto the breakwater and with non-overtopping conditions.

Firstly, the hydraulic performance of the different breakwater typologies has been analysed as a function of the non-dimensional parameters representing the breakwater geometry, granular materials and incoming wave train. The hydraulic performance is defined by the complex reflection coefficient (modulus and phase), the transmission coefficient and the wave energy dissipation rate. The data confirm that the variation of those coefficients (as well as the energy dissipation rate) depends on the dimensions and properties of the parts and elements of the breakwater as well as on the wave characteristics. The logistic sigmoid function has been found to be able to describe the behavior of these coefficients. This curve depends primarily on a 2D scattering parameter, A_{eq}/L^2 (where A_{eq} is the area of a porous medium under the mean water level and L is the wavelength), and on the relative grain size of the porous medium and breakwater typology, Dk (where D is the diameter and k is the wave number). The logistic sigmoid curves help to include the phase of the reflection coefficient, which is essential to define the wave regime in front of, inside, and leeward of the breakwater. Furthermore, it provided smooth performance transitions between different breakwater typologies and discriminated the full spectrum of oscillatory regimes stemming from the wind wave-structure interaction. Parameters of the sigmoid function for the reflection coefficient, modulus and phase, and transmission coefficient (hydraulic performance curves) have been obtained for the different breakwater typologies.

An advantage of the sigmoid function is that the hydraulic performance can be define with a reduced number of experimental tests. Numerical models are increasingly being used in last years to assist the laboratory work in this type of problems because of its computing power and versatility. Since most breakwaters are either partially or totally composed of granular material, the quality of the numerical results depends on correctly defining the wave transformation inside the porous

medium. A characteristic friction diagram was obtained to evaluate this transformation. The friction diagram is based on a linear coefficient that is constant in the porous medium volume and stationary in the wave cycle. It was calibrated by minimizing the error in the hydraulic performance (reflection and transmission coefficients and wave phase) between the experimental measurements and the numerical calculations. The IH-2VOF numerical model was used in this work. Results show that the friction coefficient depends on the breakwater typology and geometry, mainly on the relative diameter of the granular material. This method is expected to reduce the costs and saves time in the breakwater design.

Next, the estimation of the statistical behavior of the wind waves interacting with different breakwater types has been done in terms of its hydraulic performance. Based on Rice's theory of envelope amplitude, an approximate solution of the total wave height distribution in front of the breakwater, caused by the linear superposition of the incident and reflected wave trains is presented. The experimental results in the wave flume confirmed that the incident, the reflected and the total wave trains in front of the breakwater could be treated as Gaussian processes. Moreover, the total wave height follows a Rayleigh distribution in which the parameter is the root-mean-square total wave height. Its value can be calculated from the modulus and phase of the reflection coefficient defined by the hydraulic performance curves. From the toe of the structure to the toe of the crown, the probability density function (pdf) of the total wave height evolves from a Rayleigh to a Weibull distribution. The scale and shape parameters of the Weibull distribution vary along the face of the structure, and depend on the breakwater typology, the relative grain diameter and the relative water depth. The largest deviation from the Rayleigh distribution occurs at the crown wall.

Finally, the verification equations to analyse the failure modes produced by wind waves in front or at the face of the breakwater are formulated as a function of the actions onto the breakwater. These actions are characterized by the kinematic and dynamic variables of the oscillation in the location in which they are acting. These variables have been analysed for the failure mode that considers sliding of the crown wall. Results show that the parameters of the pdf of the forces acting on this element can be obtained directly in terms of the total wave height at this location and therefore, the verification equation can be also formulated as a function of this variable. Then the failure probability for this failure mode can be calculated, as well as the safety margin. In the same way, the rest of the failure modes affected by this same agent (wind waves) in front or at the face of the breakwater could be analysed and verify simultaneously the breakwater design.

Resumen

Un dique de abrigo es una estructura marítima construida para proteger un puerto o una zona costera de la acción del oleaje. La diferencia entre unas tipologías y otras radica en la forma en la que hacen frente al oleaje incidente. Así, su selección y el dimensionamiento de sus partes y elementos depende de la localización de la obra, las características de los agentes y los demás requisitos de proyecto. Por tanto, debe estar condicionada al análisis de diferentes alternativas para poder elegir aquella que garantice la operatividad y seguridad de la obra al menor coste posible. Cada alternativa puede ser evaluada mediante la verificación de los modos de fallo que puedan afectar a las partes y elementos del dique durante su vida útil. Actualmente, la verificación suele ser formulada de manera independiente para cada modo de fallo, incluso en el caso en el que éstos estén afectados por los mismos agentes atmosféricos y marítimos. Además, los agentes actuantes son considerados sin tener en cuenta la transformación que sufren por la presencia de la obra. Esta Tesis propone una metodología unificada para verificar simultáneamente los diferentes modos de fallo producidos por la acción del oleaje en la sección del dique. Ésta se basa en el comportamiento hidráulico del dique frente a la acción del oleaje, el cual puede ser definido a partir de los procesos de transformación que se derivan de esta interacción. Para alcanzar este objetivo se han combinado técnicas experimentales y numéricas. Se han analizado diferentes tipologías sobre las que incide oleaje irregular normal a la estructura y sin condiciones de rebase.

En primer lugar, se ha analizado el comportamiento hidráulico de las diferentes tipologías en función de una serie de parámetros que representan la geometría del dique, las características del material granular y las condiciones del oleaje incidente. El comportamiento hidráulico se define por el coeficiente de reflexión complejo (módulo y fase), el coeficiente de transmisión y la tasa de disipación de energía. Los datos han confirmado que estos coeficientes dependen de las dimensiones de las partes y elementos del dique, así como de las características del oleaje incidente. La función logística sigmoide es capaz de describir adecuadamente esta dependencia en todas las tipologías de diques analizadas. La variable principal de esta curva es el parámetro de dispersión en 2D, A_{eq}/L^2 (donde A_{eq} es el área de material poroso bajo el nivel del mar de referencia y L es la longitud de onda). El resto de parámetros de la curva dependen del diámetro relativo del material poroso, Dk (donde D es el diámetro del material y k el número de onda) y la tipología de dique. La función sigmoide ayuda a incluir la fase de la reflexión, parámetro esencial para definir el régimen oscilatorio en frente, en el interior y detrás del dique. Además, proporciona modificaciones en el comportamiento del dique en función de la tipología y describe un abanico completo de regímenes oscilatorios derivados de la interacción. Los parámetros de la función sigmoide para el cálculo del coeficiente de reflexión, módulo y fase, y el coeficiente de transmisión (curvas de comportamiento hidráulico) han sido obtenidos para todas las tipologías de dique analizadas.

Una de las grandes ventajas de la función sigmoide es que permite caracterizar el comportamiento hidráulico de un dique con un número reducido de puntos que suelen ser obtenidos mediante métodos experimentales. Sin embargo, en los últimos años la aplicación de modelos numéricos para resolver este tipo de problemas se está incrementando considerablemente por el aumento de la capacidad computacional y la versatilidad que ofrecen. Como la mayoría de los diques están

compuestos total o parcialmente de material granular, la calidad de los resultados numéricos dependerá de la correcta definición de la transformación del flujo en el medio poroso. Para evaluar dicha transformación se ha obtenido un diagrama de fricción característico basado en un coeficiente de fricción lineal, que es contante en el volumen del medio poroso y estacionario en el ciclo de la onda. Este coeficiente ha sido calibrado minimizando el error entre las variables que definen el comportamiento hidráulico (modulo y fase del coeficiente de reflexión y coeficiente de transmisión) obtenidas numéricamente frente a los datos experimentales. El modelo numérico utilizado ha sido el IH-2VOF. Los resultados muestran que el coeficiente de fricción depende principalmente del diámetro relativo del material granular. Este método servirá como complemento al modelado físico y por tanto contribuirá a reducir costes y tiempo en el diseño de diques.

En el siguiente bloque de trabajo se ha llevado a cabo un análisis estadístico del oleaje en las inmediaciones del dique en términos del comportamiento hidráulico de la estructura. A partir de la teoría de Rice se ha obtenido una solución aproximada de la distribución de la altura de ola en frente del dique, causada por la superposición del tren incidente y del reflejado. Los resultados experimentales han confirmado que los trenes incidente, reflejado y total pueden ser tratados como procesos gaussianos. Además, la altura de ola del tren total sigue una distribución de Rayleigh cuyo parámetro de escala es su valor medio cuadrático, que puede ser calculado a partir del módulo y la fase del coeficiente de reflexión definido por las curvas de comportamiento hidráulico. Desde el pie de la estructura hasta la pared del espaldón, la función de densidad de la altura de ola evoluciona de una función Rayleigh a una tipo Weibull. Los parámetros de escala y forma de esta distribución de Weibull varían a lo largo del talud y dependen del tipo de dique, del diámetro relativo del material granular y de la profundidad relativa. La mayor desviación con respecto a la distribución de Rayleigh tiene lugar en la pared del espaldón.

Finalmente, se han formulado las ecuaciones de verificación de los modos de fallo producidos por el oleaje y que pueden afectar la cara frontal del dique, como una función de las acciones sobre la obra. Las acciones sobre la estructura son caracterizadas a partir de las variables cinemáticas y dinámicas de la oscilación que las produce. El modo de fallo analizado en este trabajo ha sido el deslizamiento del espaldón. Los resultados muestran que las funciones de densidad de las fuerzas sobre la pared del dique pueden ser obtenidas directamente de la altura de ola total en esta localización y, por lo tanto, la ecuación de verificación también puede ser formulada en términos de ésta. A partir de ahí puede calcularse la probabilidad de fallo asociada a este modo de fallo en el estado considerado, así como el margen de seguridad. Si se procede de forma análoga con el resto de modos de fallo, puede realizarse la verificación de la obra atendiendo a las condiciones de simultaneidad del agente solicitante, en este caso el oleaje.

Contents

List of Symbols	xvii
List of Figures	xxiii
List of Tables	xxix
1 Introduction	1
1.1 Motivation for the proposed work	1
1.2 Backgrounds	2
1.3 Objectives	2
1.3.1 Main objective	2
1.3.2 Specific objectives	3
1.4 Outline of the Thesis	3
1.5 Publications derived from this Thesis	4
2 Problem definition and parameter list	5
2.1 Wind wave-breakwater interaction. Wave energy distribution	5
2.1.1 Definition of the wave energy distribution processes	5
2.1.2 Energy conservation equation	7
2.2 State of the art	7
2.3 Breakwater typologies. Classification	8
2.3.1 Type A: Porous vertical breakwater (PVB)	9
2.3.2 Type B: Composite breakwater (CB)	9
2.3.3 Type C: Mixed breakwater with a berm below or at S.W.L. (LMB, HMB and HMCB)	9
2.3.4 Type D: Mixed breakwater with a berm above S.W.L. (RMB-CW)	10
2.3.5 Type E: Rubble mound breakwater (RMB)	10
2.3.6 Type F: Berm or S-shaped breakwater (SB)	10
2.4 Parameter list	11
3 Experimental and numerical setups	15
3.1 Physical experiments set-up	15
3.1.1 Model characteristics and wave conditions	15
3.1.2 Data acquisition and analysis	18
3.1.3 Wave breaking analysis	21
3.2 Numerical experiments set-up	23
3.2.1 Description of the model	23
3.2.2 Numerical experiments description	25
4 Hydraulic performance of different breakwater types under 2D wave attack	27
4.1 Governing equation and fitting criteria	27
4.2 Hydraulic performance of different breakwater types	28

4.2.1	Type A: Porous vertical breakwater (PVB)	29
4.2.2	Type B: Composite breakwater (CB)	30
4.2.3	Type C: Mixed breakwater with a berm below or at S.W.L. [$F_{MT}/h \leq 1.1$] (LMB, HMB and HMCB)	32
4.2.4	Type D: Mixed breakwater with a berm above the S.W.L. [$F_{MT}/h > 1.1$] (RMB-CW)	35
4.2.5	Type E and F: Undefined slope breakwater without crown wall (RMB, plane slope) and S-shaped breakwater (SB)	36
4.2.6	Other breakwater types	39
4.2.7	Comparison with other formulas	41
4.3	Application of the hydraulic performance curves	43
4.3.1	Sequence of application	43
4.3.2	Example of application to a non-overtoppable low-mound breakwater (Type C, LMB)	44
4.3.3	Reflection coefficient modulus of various breakwaters in Spain	47
4.3.4	Adaptive design method for breakwaters and optimization	48
4.4	Discussion and limitations of the hydraulic performance curves	50
4.5	Conclusions	52
5	Numerical quantification of the hydraulic performance	55
5.1	Introduction	55
5.2	Methodology	56
5.3	Results	60
5.3.1	Dependence on D_k and breakwater typology	61
5.3.2	Dependence on breakwater geometry	61
5.3.3	Dependence on wave characteristics	61
5.3.4	Comparison of the experimental and numerical hydraulic performance	62
5.3.5	Importance of the phase in the friction forces	63
5.4	Example to obtain the hydraulic performance by numerical modelling	64
5.5	Conclusions	65
6	An approximation to the statistical behavior of wind waves in front and on the face of the breakwater	67
6.1	Introduction	67
6.2	An approximation to the pdf of the linear superposition of incident and reflected narrow-banded wave trains	69
6.2.1	Wave height pdf in front of and at the toe of the breakwater	70
6.2.2	Wave height pdf on the breakwater face	73
6.3	Data analysis	73
6.4	Results	74
6.4.1	Statistical behavior of the wave train in front of and at the toe of the breakwater	74
6.4.2	Statistical behavior of the total wave train on the breakwater face	77
6.4.3	Calculation of the pdf of the total wave height at the toe and on the face of a given breakwater type	80
6.5	Example of application: variation of the total wave height at the front of different breakwater types	84
6.6	Conclusions	85
7	Breakwater design based on its hydraulic performance	87
7.1	Introduction	87

7.2	Verification equations in terms of the kinematic and dynamic variables in front of the breakwater	88
7.3	Kinematic and dynamic variables of a irregular wave train in front of a breakwater	89
7.4	Crown wall stability analysis	90
7.4.1	Methodology	92
7.4.2	Results	93
7.4.3	Calculation scheme	109
7.5	Conclusions	111
8	Conclusions and future research	113
8.1	Conclusions	113
8.2	Future research	115
A	Fitting of sigmoid function for reflection (modulus and phase) and transmission coefficients and wave energy dissipation rate	117
B	Obtaining the effective depth for waves propagating over a porous structure (Losada et al., 1997b)	133
	Bibliography	135

List of Symbols

Roman letters

a, b	Darcy-Forchheimer equation coefficients
a_1, b_1	Seelig and Ahrens (1981) formula coefficients
A_{eq}	Area per unit section of a porous medium under the mean water level
A_n	Amplitude of the spectral component
a_r, b_r	Coefficients (wave breaking)
a_{Xi}	Inflection point of the sigmoid curve ($i = K_R, K_T, \phi_R$)
a_Z, b_Z	Zanuttigh and van der Meer (2008) formula coefficient
B	Structure width
B_b	Berm width
B_{eq}	Equivalent width
b_{swl}	Width of the emerged rubble mound (Liu and Faraci, 2014)
C	Wave phase speed
c_A	Added mass coefficient
C_g	Linear theory wave group speed
D	Grain size
d	Submerged caisson height ($h - h_b$)
D^*	Wave energy dissipation rate
D'_*	Wave energy dissipation rate per unit of time
d_s	Width of the central slope (Type F)
dt	Distance between the toe and wall of the breakwater
E_i	Mean special energy per unit of the horizontal area
f	Frequency component of the wave spectrum

f_0	Frequency in which most of the energy in the wave spectrum is concentrated
F_c	Freeboard
f_c	Characteristic friction coefficient
F_G	Friction forces
F_i	Wave energy flux ($i = I, R, T$ incident, reflected, transmitted)
$F_{L,NL}$	L=Linear and NL=non-linear form of the drag forces
f_L, f_T, f_I	Laminar, turbulent and inertial frictional resistance forces
F_{MT}	Berm height
f_r	Friction coefficient of the porous medium
F_t	Transfer function
F_H	Horizontal force
F_h	Horizontal force in the wave crest
F_V	Vertical force
F_v	Vertical force in the wave crest
g	Gravitational acceleration
H	Wave height
h	Water depth
h_b	Caisson foundation depth
h_{ef}	Effective depth
H_i	Wave height ($i = I, R, T, t$ incident, reflected, transmitted and total)
$H_{p,w}$	Wave height ($i = p, w$ breakwater toe and breakwater wall)
h_{swl}	Submerged depth of the front wall (Liu and Faraci, 2014)
h_s	Height of the central slope (Type F)
I_c^*	Time-dependent amplitude of the cosine term
I_s^*	Time-dependent amplitude of the sine term
I_r	Iribarren number
K	Complex wave number ($k_r - ik_i$)
k	Wave number
k_0	Wave number for the peak frequency
K_f	Fourier asperity roughness parameter

K_R	Modulus reflection coefficient
K_T	Modulus transmission coefficient
KC_p	Local Keulegan-Carpenter number of the porous medium
KR	Complex reflection coefficient
KT	Complex transmission coefficient
L	Wave length
m_0	Zero-order moment
m_n	n-order moment
n	Porosity of the central body of the breakwater
n_s	Porosity of the main layer of the breakwater
P	Pressure in the wave crest
p	Pressure
P_{12}	Pressure at the berm top location
P_1	Pressure at the mean water level
P_2	Pressure at the bottom of the caisson
P_{u1}	Pressure at the entrance of the porous medium
P_{u2}	Pressure at the exit of the porous medium
Q_p	Type of unit, placement density and number of layers parameter
Q_t	Slope profile parameter
r	Height of a representative step
R^2	Determination coefficient
R_i	Envelope amplitude ($i = I, t$ incident and total wave train)
Re_p	Pore Reynolds number for oscillatory flow
S	Safety margin
s	Inertial coefficient of the porous medium
$S_{I,t}$	I=incident, t=total wave spectrum
S_p	Pressure spectrum
s_p	Wave steepness related to T_p
T	Wave period
t	Time

T_d	Design wave period
U	Volume-average ensemble-average velocity
u	Seepage velocity
u_d	Discharge velocity
V	Control volume
W	Stone weight
W_1	Submerged weight of the caisson
x	Horizontal axes with origin of coordinates at the toe of the structure
x'	Local coordinate with $x' = 0$ at the entrance of the porous medium and positive in the leeward direction
x_0/L	Non-dimensional phase
Y, Y_i	Phase-averaged quantity of wave-breakwater interaction ($i = K_R, K_T, \phi_R$)
Y_{i0}, Y_{i1}	Final and initial value of the sigmoid curve ($i = K_R, K_T, \phi_R$)
Y_{i2}	Central value of the sigmoid curve ($i = K_R, K_T, \phi_R$)
z	Vertical axes with origin of coordinates at S.W.L.
Z_1	Favorable terms in verification equation
Z_2	Unfavorable terms in verification equation

Greek letters

α, β	Coefficients defining a and b in the Darcy-Forchheimer equation
$\alpha_I, \alpha_1, \alpha_2, \alpha_3, \alpha_4$	Coefficient to calculate pressure laws and the vertical force
α_T	Seaward slope angle
α_w	Local scale parameter of the Weibull distribution, multiplying $H_{trms}(x = 0)$
β_{SB}, γ_{SB}	Slope angles for S breakwater (Type F)
β_T	Leeward slope angle
β_w	Shape parameter of the Weibull distribution
δ_w	Scale parameter of the Weibull distribution
ϵ_n	Random phase of the spectral component
$\eta_{I,R,t}$	Vertical displacement of the free surface (I=Incident, R=Reflected, and t=total)
η_w	Vertical displacement of the free surface at the breakwater wall
γ_c	Specific weight of the caisson

γ_i	Blending coefficient of the sigmoid curve ($i = K_R, K_T, \phi_R$)
γ_p	Constant in the added mass coefficient
γ_w	Specific weight of the water
λ	Empiric coefficient (overtopping)
λ_1, λ_2	Coefficient defining the friction coefficient equation
μ_c	Friction coefficient between the caisson base and the bedding layer
ν	Kinematic viscosity of the fluid
ϕ	Reflection phase
ϕ_T	Transmission phase
ρ	Water density
ρ_0	Stone dry density
ρ_{IR}	Correlation between incident and reflected wave series
ρ_r	Linear correlation coefficient between horizontal and vertical forces in the wave crest
σ	Angular frequency
σ_s	Standard deviation
ε	Mean quadratic error
φ	Time-dependent phase of the wave envelope
ξ_0	Breaker parameter (Iribarren number)

Subscripts

*	Denote a local variable
01	Mean
0	Associated with the representative frequency, f_0
cr	Critical referred to critical wave steepness to determine wave breaking
exp	Experimental
I,R,t	Incident, reflected and total wave train
max	Maximum
min	Minimum
num	Numerical
p	Peak
rms	Root-mean square

<i>s</i>	Significant
<i>teo</i>	Theoretical
<i>x</i>	Concomitant force

Breakwater types

CB	Composite breakwater (Type B)
HMB	High mound breakwater (Type C)
HMCB	High mound composite breakwater (Type C)
LMB	Low mound breakwater (Type C)
PVB	Porous vertical breakwater (Type A)
RMB	Rubble mound breakwater (Type E)
RMB-CW	Rubble mound breakwater with crown wall (Type D)
SB	S-breakwater (Type F)

List of Figures

2.1	Wave energy distribution.	5
2.2	Breakwater types: A) Porous vertical breakwater (PVB); B) Composite breakwater (CB); C) Low and high mound breakwater and high mound composite breakwater (LMB, HMB and HMCB) [$F_{MT}/h \leq 1.1$]; D) Rubble mound breakwater with crown wall (RMB-CW) [$F_{MT}/h > 1.1$]; E) Rubble mound breakwater (RMB); F) S-shaped breakwater (SB).	8
3.1	Breakwater types tested.	16
3.2	Importance of the resistance forces (diagram from Gu and Wang, 1991) in the performed tests.	17
3.3	Scheme of the wave flume and location of wave gauges.	19
3.4	Pressure sensors locations.	20
3.5	Pressure variables definition.	21
3.6	Maximum horizontal and vertical force and their concomitants of a sea state.	22
3.7	Scheme to identify the wave breaking type (Adapted from Kortenhaus and Oumeraci, 1998).	23
3.8	Wave breaking type (type C and D).	24
4.1	Sigmoid curve variation based on parameter γ (left panel) and a_X (right panel).	28
4.2	Type A (PVB). K_R , K_T and D^* as compared to the 2D scattering parameter, A_{eq}/L^2 , and various ranges of Dk . Experimental data and best-fitted curves.	30
4.3	Identification of performance regions, TR and DR for type A and B. In each region, the curve that best fits the sigmoid function is represented.	30
4.4	Composite breakwater (CB). K_R , K_T , D^* and x_0/L as compared to the 2D scattering parameter, A_{eq}/L^2 , various ranges of h_b/h and $Dk < 0.05$. Experimental data and best-fitted curves.	31
4.5	Identification of performance regions, TR and DR for type C, D, E and F. In each region, the curve that best fits the sigmoid function is represented.	33
4.6	Type C (LMB, HMB and HMCB). K_R , K_T , D^* and x_0/L as compared to the 2D scattering parameter, A_{eq}/L^2 , depending on B_b/h , F_{MT}/h , $H_{I_{rms}}/L$, for $Dk < 0.06$ and $h_b/h = 0.50$. Experimental data and best-fitted curves.	34
4.7	Type C (HMB). K_R , K_T and D^* as compared to the 2D scattering parameter, A_{eq}/L^2 , depending on B_b/h , Dk and $h_b/h = 0.50$. Experimental data and best-fitted curves.	35
4.8	Type D (RMB-CW). K_R , K_T , D^* and x_0/L as compared to the 2D scattering parameter, A_{eq}/L^2 , depending on B_b/h , F_{MT}/h , $H_{I_{rms}}/L$, for $Dk < 0.06$ and $h_b/h = 0.50$. Experimental data and best-fitted curves.	37
4.9	Type E (RMB with core and core + armor layer). K_R , D^* and x_0/L as compared to the 2D scattering parameter, A_{eq}/L^2 , as a function of $H_{I_{rms}}/L$ and section type: core (quarry run); core + armor layer (core protected with material of a uniform grain-size distribution). Experimental data and best-fitted curves.	38
4.10	Concrete armor units: a) dolosse, b) cube and c) cubipod.	39

4.11	K_R and D^* as compared to the 2D scattering parameter, A_{eq}/L^2 , and the type of armor unit with the following parameters: Core (Benedicto, 2004); S = Cubes and S = Cubipods (Medina and Gómez-Martín, 2007); S = Armor stones (Benedicto, 2004); S = Dolosse (Ruíz et al., 2013). Experimental data and best-fitted curves, depending on the porosity of the armor layer.	39
4.12	HMCB breakwater with $F_{MT}/h=1$ and without a superstructure (Allshop and Channel, 1989). K_R as compared to the 2D scattering parameter, A_{eq}/L^2 , relative width, B_b/h , and slope gradient, $\cot\alpha_T$. Experimental data and best-fitted curves.	40
4.13	K_R as compared to the 2D scattering parameter, A_{eq}/L^2 , under quasi-resonant conditions, $b_{swl}/h=0.292$, $h_{swl}/h=0.167$, $\cot\alpha_T=2$, $B=15$ cm, $h=24$ cm (Liu and Faraci, 2014). Experimental data and fit to a sigmoid curve with the following parameters: $\gamma_R=2.24$; $a_{XR}=0.008$; $K_{R1}=0.90$; $K_{R0}=0.17$	41
4.14	Comparison of K_R obtained with the sigmoid function (SF) and the formulas of Zanuttigh and van der Meer (Z&M) and Seelig and Ahrens (S&A). Type E (RMB) composed of: 1) Core and 2) Core + armor units.	42
4.15	Methodological sequence for applying the curves to obtain coefficients, K_R , ϕ , K_T , and D^*	44
4.16	Geometric dimensions.	45
4.17	Spanish breakwaters location and classification.	48
4.18	Location of the Spanish breakwaters on the fitted curves for the analysed breakwater typologies. A_{eq}/L^2 obtained: a) for the design period, T_d (upper graphs); b) for a time period equal to $0.5T_d$ (lower graphs).	49
4.19	Contour lines of K_R for the different breakwater types, depending on the parameter list.	50
4.20	Variation of K_R with the wave breaking type (Benedicto, 2004).	51
5.1	Methodology for the friction coefficient calibration.	59
5.2	Friction coefficient diagram.	60
5.3	Influence of the wave steepness on the friction coefficient.	61
5.4	Experimental versus numerical K_R , K_T and ϕ for the breakwater typologies.	62
5.5	Experimental versus numerical D^* for the breakwater typologies.	62
5.6	Mean square error, depending on the friction coefficient of the LMB ($F_{MT}/h = 0.50$) with $B_b=0.25$ m, $D=40$ mm, $H_{Is}=0.031$ m and $T_p=1.12$ s.	63
5.7	Comparison between the numerical and experimental values of K_R , K_T and ϕ , depending on the f_r of the LMB ($F_{MT}/h = 0.50$) with $B_b=0.25$ m, $D=40$ mm, $H_{Is}=0.031$ m and $T_p=1.12$ s.	63
5.8	Hydraulic performance curves obtained numerically.	65
6.1	Definition sketch.	70
6.2	Location of the wave gauges along the breakwater.	74
6.3	Probability density function of the non-dimensional incident, reflected, and total (at the toe) free surface elevation obtained by the linear superposition of the incident and reflected wave trains and measured with gauge S4. Type B with three relative foundation depths, h_b/h , $T_{p\ teo}=2$ s, $H_{Is\ teo}=0.04$ m, $D=40$ mm, and $B_b/h=0.625$. Empirical and Gaussian fit.	75
6.4	Probability density function of the non-dimensional incident, reflected, and total (at the toe) free surface elevation obtained by the linear superposition of the incident and reflected wave train and measured with gauge S4. Type C with three relative berm heights, F_{MT}/h , $T_{p\ teo}=2$ s, $H_{Is\ teo}=0.04$ m, $D=40$ mm, and $B_b/h=0.625$. Empirical and Gaussian fit.	76

6.5	Probability density function of the non-dimensional incident, reflected, and total (at the toe) free surface elevation obtained by the linear superposition of the incident and reflected wave train and measured with gauge S4. Type D with two relative berm heights, F_{MT}/h , $T_{p\ teo}=2$ s, $H_{Is\ teo}=0.04$ m, and $D=40$ mm. Empirical and Gaussian fit.	77
6.6	Probability density function of the non-dimensional total wave height at the toe ($x=0$) for Type B (three relative foundation depths h_b/h), C (three relative berm heights, F_{MT}/h), and D (two relative berm heights, F_{MT}/h), $T_{p\ teo}=2$ s, $H_{Is\ teo}=0.04$ m, $D=40$ mm, and $B_b/h=0.625$. Empirical and theoretical fit (Rayleigh distribution).	78
6.7	Probability density function of the non-dimensional total wave height in different positions along the breakwater slope (x_1 , x_2 , x_3 , and x_4) for type C and D. $T_{p\ teo}=1.05$ s, $H_{Is\ teo}=0.04$ m, $D=40$ mm, and $B_b/h=0.625$. Empirical and theoretical fit (Weibull distribution).	80
6.8	α_w and β_w as a function of k_0h for different positions along the breakwater slope (x_1 , x_2 , x_3 , and x_4) for two ranges of incident wave steepness, and for three relative berm heights (F_{MT}/h), $Dk < 0.06$, and $B_b/h = 0.250$. Type C.	81
6.9	α_w and β_w as a function of k_0h for different positions along the breakwater slope (x_1 , x_2 , x_3 , and x_4) for two ranges of incident wave steepness, and for two relative berm heights (F_{MT}/h), $Dk < 0.06$, and $B_b/h = 0.250$. Type D.	81
6.10	Comparison of the total root-mean-square wave height at the toe ($x = 0$) of different breakwater typologies, measured (gauge 4) and predicted (Approximate) with equation 6.25.	82
6.11	Comparison of the root mean square wave height at the front of the different breakwater typologies for two sea states.	84
7.1	Scheme of pressure laws and analysed variables.	92
7.2	Comparison between numerical and theoretical value of the pressure at the S.W.L. for type B as a function of h_b/h	93
7.3	Comparison between numerical and theoretical value of the pressure at the S.W.L. for type C and D as a function of F_{MT}/h and B_b/h	93
7.4	Impulsive pressure coefficient, α_I , for typology HMCB as a function of B_b/L and $H_{I\ rms}/h$	94
7.5	Relationship between non-dimensional pressure at the S.W.L., $P_{1\ rms}$, and the pressure at the bottom of the caisson, $P_{2\ rms}$, for type B as a function of h_b/h and kh	95
7.6	Comparison between non-dimensional pressure at the bottom of the caisson, experimental, $P_{2\ rms}$, and theoretical, $P_{2\ rms\ teo}$, for type B as a function of h_b/h	96
7.7	Comparison between pressure at the bottom of the caisson, numerical, $P_{2\ rms}$, and theoretical, $P_{2\ rms\ teo}$, for type C and D as a function of F_{MT}/h and B_b/h	96
7.8	Comparison between horizontal pressure laws for type C and D as a function of F_{MT}/h . $T_{p\ teo} = 2.50$ s, $H_{Is\ teo} = 0.08$ m and $B_b/h = 0.250$	97
7.9	Uplift pressure laws for type C and D as a function of F_{MT}/h and kh . $B_b/h = 0.250$	98
7.10	Uplift pressure laws for type C and D as a function of F_{MT}/h and kh . $B_b/h = 0.625$	99
7.11	Relationship between non-dimensional pressure at the bottom of the caisson, $P_{2\ rms}$, and pressure at the entrance of the porous medium, $P_{u1\ rms}$, for type B as a function of h_b/h , Dk , and B/L	100
7.12	Relationship between non-dimensional pressure at the bottom of the caisson, $P_{2\ rms}$, and pressure at the entrance of the porous medium, $P_{u1\ rms}$, for type C and D as a function of F_{MT}/h and B_b/h	100
7.13	α_3 as a function of B/L , Dk and h_b/h . Type B.	101
7.14	α_3 as a function of B/L , F_{MT}/h and B_b/h . Type C and D.	101
7.15	Classification of the uplift pressure law.	102

7.16	Relationship between r.m.s value of the non-dimensional horizontal and vertical forces as a function of h_b/h and Dk . Type B.	102
7.17	Relationship between r.m.s value of the non-dimensional horizontal and vertical forces as a function of F_{MT}/h and B_b/h . Type C and D.	103
7.18	Simultaneous vertical and horizontal forces for HMB typology.	103
7.19	Probability density function of the non-dimensional horizontal (left figure) and vertical (right figure) force in the wave crest. Type B, $B=0.14$ m, $h_b/h=0.25$, $D=40$ mm, $T_p\ teo=2.25$ s and $H_{Is\ teo}=0.06$ m. Empirical and theoretical fit (Weibull distribution).104	
7.20	Non-dimensional value of δ_w compared with the non-dimensional value the r.m.s of Fh and Fv as a function of B/L and h_b/h . Type B.	105
7.21	Relationship between β_w in Weibull pfd of Fh or Fv and H_w as a function of k_0h , B/L and h_b/h . Type B.	106
7.24	Joint probability function of Fh and Fv . Type C, $F_{MT}/h=0.75$, $B_b/h=0.25$, $T_p\ teo=1.05$ s, $H_{Is\ teo}=0.04$ m and $D=40$ mm. Empirical and theoretical fit (equation 7.19).	106
7.22	Non-dimensional value of δ_w compared with the non-dimensional value the r.m.s of Fh and Fv as a function of F_{MT}/h and B_b/h . Type C and D.	107
7.23	Relationship between β_w in Weibull pfd of Fh or Fv and H_w as a function of k_0h , F_{MT}/h and B_b/h . Type C and D.	107
7.25	Linear correlation coefficient between Fh and Fv as a function of k_0h and B/L . Type B.108	
7.26	Linear correlation coefficient between Fh and Fv as a function of k_0h . Type C and D. 108	
7.27	Scheme of pressure.	110
A.1	Type A (PVB). K_R , K_T and D^* as a function of A_{eq}/L^2 , and various ranges of Dk . Experimental data and best-fitted curves.	119
A.2	Type B (CB). K_R as a function of A_{eq}/L^2 , Dk and h_b/h . Experimental data and best-fitted curves.	120
A.3	Type B (CB). K_T as a function of A_{eq}/L^2 , Dk and h_b/h . Experimental data and best-fitted curves.	120
A.4	Type B (CB). D^* as a function of A_{eq}/L^2 , Dk and h_b/h . Experimental data and best-fitted curves.	121
A.5	Type B (CB). x_0/L ($\phi = 4\pi x_0/L$) as a function of A_{eq}/L^2 and h_b/h for all ranges of Dk . Experimental data and best-fitted curves.	121
A.6	Type B (CB). Sigmoid curve parameters for obtaining K_R and K_T . Parameters obtained and best-fitted curves.	122
A.7	Type C (LMB, HMB and HMCB). K_R as a function of A_{eq}/L^2 , Dk , B_b/h and F_{MT}/h ($h_b/h = 0.50$). Experimental data and best-fitted curves.	123
A.8	Type C (LMB, HMB and HMCB). K_T as a function of A_{eq}/L^2 , Dk , B_b/h and F_{MT}/h ($h_b/h = 0.50$). Experimental data and best-fitted curves.	124
A.9	Type C (LMB, HMB and HMCB). D^* as a function of A_{eq}/L^2 , Dk , B_b/h and F_{MT}/h ($h_b/h = 0.50$). Experimental data and best-fitted curves.	124
A.10	Type C (LMB, HMB and HMCB). x_0/L ($\phi = 4\pi x_0/L$) as a function of A_{eq}/L^2 and F_{MT}/h for all ranges of Dk and both two B_b/h . Experimental data and best-fitted curves.	125
A.11	Type C (LMB, HMB and HMCB). Sigmoid curve parameters for obtaining K_R . Parameters obtained and best-fitted curves.	126
A.12	Type C (LMB, HMB and HMCB). Sigmoid curve parameters for obtaining K_T . Parameters obtained and best-fitted curves.	126
A.13	Type D (RMB-CW). K_R as a function of A_{eq}/L^2 , Dk , B_b/h and F_{MT}/h ($h_b/h = 0.50$). Experimental data and best-fitted curves.	127
A.14	Type D (RMB-CW). K_T as a function of A_{eq}/L^2 , Dk , B_b/h and F_{MT}/h ($h_b/h = 0.50$). Experimental data and best-fitted curves.	128

A.15	Type D (RMB-CW). D^* as a function of A_{eq}/L^2 , Dk , B_b/h and F_{MT}/h ($h_b/h = 0.50$). Experimental data and best-fitted curves.	128
A.16	Type D (RMB-CW). x_0/L ($\phi = 4\pi x_0/L$) as a function of A_{eq}/L^2 and F_{MT}/h for all ranges of Dk and both two B_b/h . Experimental data and best-fitted curves.	129
A.17	Type E and F (RMB and SB). K_R as a function of A_{eq}/L^2 and section type: core (quarry run); core + armor layer (core protected with material of a uniform grain-size distribution). Experimental data and best-fitted curves.	130
A.18	Type E and F (RMB and SB). K_R as a function of A_{eq}/L^2 and type of armor unit. Experimental data and best-fitted curves.	130
A.19	Type E and F (RMB and SB). ($\phi = 4\pi x_0/L$) as a function of A_{eq}/L^2 and section type: core (quarry run); core + armor layer (core protected with material of a uniform grain-size distribution). Experimental data and best-fitted curves.	131

List of Tables

2.1	Parameter list.	13
3.1	Material characteristics: porosity, Fourier Asperity Roughness Parameter, characteristic diameter, sorting parameter, and dry density.	17
3.2	Wave conditions in experimental tests.	18
3.3	Non-dimensional parameters intervals in experimental tests.	18
3.4	Pressure sensors coordinates.	20
3.5	Wave breaking classification.	24
4.1	Fit parameters of the sigmoid curve for an HMCB breakwater with $F_{MT}/h = 1$ and without a superstructure (Allshop and Channel, 1989), depending on relative berm width, B_b/h , and slope gradient, $\cot\alpha_T$	40
4.2	Test used for comparison with the formulas of Zanuttigh and van der Meer (Z&M) and Seelig and Ahrens (S&A). FS and exp represent the sigmoid function and experimental values respectively.	42
4.3	Values of the non-dimensional parameters.	45
4.4	Sigmoid curve parameters for K_R , ϕ and K_T	45
4.5	Values obtained for K_R and ϕ	46
4.6	Analysis of the presence of wave breaking at the front of the breakwater.	46
4.7	Analysis of the presence of wave breaking on the berm.	46
4.8	Analysis of the presence of overtopping.	47
4.9	Sigmoid curve parameters of K_T	47
4.10	Value of D^*	47
4.11	Spanish breakwaters characteristics.	49
5.1	Overview of Forchheimer equation coefficients. M.T.F = Mainly turbulent flow; F.T.F = Fully turbulent flow.	57
5.2	Target parameters for simulated cases.	59
5.3	Characteristic friction coefficient fits.	60
5.4	Non-dimensional parameters.	64
5.5	Value of the coefficients of reflection (modulus and phase), transmission, and dissipation.	64
5.6	Fit parameters of the sigmoid equation.	65
6.1	Goodness of fit of the Gaussian distribution for the incident, reflected, and the measured and calculated total free surface elevation at the toe of the breakwater ($x=0$). Type B.	76
6.2	Goodness of fit of the Gaussian distribution for the incident, reflected, and the measured and calculated total free surface elevation at the toe of breakwater ($x=0$). Type C and D.	77
6.3	Goodness of fit coefficients to the Rayleigh distribution for the empirical probability density function of the total wave height at the toe of the breakwater. Types B, C, and D.	79

6.4	Goodness of fit for the probability density function of the total wave height at the face of the breakwater in the three locations (x_2 , x_3 , and x_4) to the Weibull distribution. Type C and D.	82
6.5	Coefficients used to calculate α_w and β_w in the bi-parametric Weibull probability density function of the total wave height at location x_2	83
6.6	Coefficients used to calculate α_w and β_w in the bi-parametric Weibull probability density function of the total wave height at location x_3	83
6.7	Coefficients used to calculate α_w and β_w in the bi-parametric Weibull probability density function of the total wave height at location x_4	84
7.1	Target parameters for simulated cases to breakwater stability analysis.	92
7.2	α_2 values for the different typologies.	97
7.3	α_3 values for the different typologies.	99
7.4	α_4 values for the different typologies.	104
7.5	Best fit to calculate the relationship between β_w in Weibull pfd of Fh or Fv and H_w	108
7.6	Best fit to calculate the linear correlation coefficient between Fh and Fv as a function of k_0h and B/L	109
A.1	Summary of the functional, curves, parameters and error of the hydraulic performance curves for the different breakwater types.	118
A.2	Type A (PVB). Sigmoid curve parameters for obtaining K_R and K_T	119
A.3	Type A (PVB). Goodness of fit of the sigmoid curves for obtaining K_R and K_T	119
A.4	Type B (CB). Sigmoid curve parameters for obtaining K_R , K_T and ϕ	122
A.5	Type B (CB). Goodness of fit of the sigmoid curves for obtaining K_R , K_T and ϕ	123
A.6	Type C (LMB, HMB and HMCB). Sigmoid curve parameters for obtaining K_R , K_T and ϕ	125
A.7	Type C (LMB, HMB and HMCB). Goodness of fit of the sigmoid curves for obtaining K_R and K_T	127
A.8	Type C (LMB, HMB and HMCB). Goodness of fit of the sigmoid curves for obtaining ϕ	127
A.9	Type D (RMB-CW). Sigmoid curve parameters for obtaining K_R , K_T and ϕ	129
A.10	Type D (RMB-CW). Goodness of fit of the sigmoid curves for obtaining K_R and K_T	130
A.11	Type D (RMB-CW). Goodness of fit of the sigmoid curves for obtaining ϕ	130
A.12	Type E and F (RMB and SB). Sigmoid curve parameters for obtaining K_R and ϕ	131
A.13	Type E (RMB). Goodness of fit of the sigmoid curves for obtaining K_R and ϕ . Note: For SB, there is not sufficient experimental data available to calculate R^2	131

Introduction

1.1 Motivation for the proposed work

The increase of maritime traffic has always gone in parallel with the growth of international economy, entailing an increase of the ship dimensions and the demand of harbor zones. This implies the need to design breakwaters in deeper areas and with severer climate conditions. Therefore, maritime structures, and particularly breakwaters, must be designed to satisfy the project requirements and to control wind-wave actions.

Depending on their typology, breakwaters reflect, dissipate, transmit, and radiate incident wave energy. This alters the distribution of the components of the frequency and directional wave spectra (Losada et al., 1993a; Losada et al., 1997b; Klopman and van der Meer, 1999). Partial standing wave patterns are likely to occur at all types of breakwater. Thus, wave transformation (i.e. wave reflection, wave transmission and wave energy dissipation) plays an important role in defining the wave regime in front of, near (seaward and leeward), and inside the breakwater (Hughes and Fowler, 1995; Losada et al., 1997a; Sutherland and O'Donoghue, 1998). In the case of regular waves, a pattern of nodes and antinodes in the wave height occurs in front of the structure. However, in the case of random waves, significant wave height only appears as a partial standing wave pattern close to the structure. According to Lamberti (1994), this pattern is a consequence of the effect of the coherence between incident and reflected components, which become evanescent as their distance from the reflecting surface increases. Thus, the superposition of incident waves and of those generated and transformed by the presence of the breakwater constitutes the set of oscillation patterns that affects the hydraulic performance of the structure. This evidently signifies that the understanding of the different processes involved in random wave interaction with structures is the basis for the development of reliable engineering design procedures.

Three type of breakwaters are usually considered in the breakwater design: mound, vertical and composite breakwater. The election of a typology depends on the materials and constructive elements availability, local experience, cost and possibility to justify its stability. In case of mound breakwaters, the calculation begins applying an empirical formula (Losada and Giménez-Curto, 1979; van der Meer, 1992) that provides the armor units weight of the main layer, and using this value the remaining elements of the section, underlying layers, core and, in case, wave wall are calculated. In case of a vertical or composite breakwater, the calculation is done applying a semi-empirical law of maximum horizontal and uplift pressures (Goda, 1985; Takahashi, 1996), and the breakwater dimensions are the necessary to delimit the failure by slide and overturn. These formulations are independent for each typology. Therefore, the comparison between alternatives of different breakwater types for the same wave conditions and project requirements is very difficult and unclear. Moreover, with the current knowledge, there is not a methodology that allows the design and verification of other different typologies from the three traditional ones, or the

quantification of changes in their behavior by using other materials or changing the geometry of the section. The consequences could be an oversizing of the breakwater geometry, an the inadequate selection of the typology, increasing costs, and uncertainty of the breakwater behavior in its useful life. The aim of this dissertation is to deepen the knowledge of the hydraulic performance results of the wave-breakwater interaction and to develop a tool that allows a unified breakwater design. For this purposed the study will be based on the wave energy transformation by the presence of the structure.

1.2 Backgrounds

For several years the *Environmental Fluid Dynamics Group* of the University of Granada has been working to quantify the behavior of various breakwater typologies designed as geometrical evolutions of the three traditional ones.

López (1998) analysed the importance of the reflection processes in the behavior of a rubble mound breakwater, specially in its stability. Since then, researches have focus on the study of breakwater behavior based on wave energy distribution resulting from the wave-breakwater interaction. Follow with the same typology, Benedicto (2004) studied the influence of the wave breaking type and characteristics of the layers (number, porosity) in the reflection process. These results were applied by Clavero (2007) to characterize the overtopping process in this breakwater typology and concluded that the dissipation by the wave breaking condition strongly the phenomenon. Experimental and theoretical results for this type of typology took Benedicto (2004) and Clavero (2007) to define a new breakwater with maximum stability, the S breakwater typology.

For a porous vertical breakwater, Pérez-Romero et al. (2009) performed a wide range of experimental tests and showed the influence of the breakwater relative width and the granular material characteristics in the wave energy balance. These results were completed by Correa (2009) for a larger range of relative breakwater widths.

For a impermeable vertical breakwater, the wave transformation processes are bounded because, when there is not any wave breaking, almost total reflection is obtained. Vílchez et al. (2011b) studied the pressure laws in a vertical breakwater measured in situ (in a prototype). Results indicated a direct relation between the total oscillation in front of the breakwater (incident + reflected waves) and the loads acting on the crown wall. Moreover, it was proved that the maximum horizontal and vertical force in a sea state are not always in phase.

These studies are the starting point of this Thesis. Results and data obtained from the experiments have been re-analysed for the completion of this research.

1.3 Objectives

1.3.1 Main objective

The main objective of this Thesis is to develop an unified methodology for verifying breakwaters design based on the hydraulic performance under perpendicularly impinging wind waves.

1.3.2 Specific objectives

To accomplish the main objective, the following specific objectives have been defined:

- 1 To obtain a parameter list that includes all the variables involved in the wave-breakwater interaction and to analyse their influence in the hydraulic performance of different breakwater typologies.
- 2 To derive an unified expression to calculate the variables that define the hydraulic performance: reflection coefficient (modulus and phase), transmission coefficient and wave energy dissipation rate, depending on the parameters identified in the previous specific objective.
- 3 To design a tool that allows the reliable use of a numerical model based on VARANS equations to quantify the hydraulic performance of different breakwater types.
- 4 To find an approximation to calculate the total oscillation in front or in the face of the breakwater applying the hydraulic performance curves.
- 5 To verify the breakwater stability as a function of the total oscillation in front or at the face of the breakwater.

1.4 Outline of the Thesis

Apart from the introduction (Chapter 1), this Thesis is organized as follows:

In Chapter 2, a definition of the processes resulting from the wave-breakwater interaction is done. A parameter list containing the principal non-dimensional parameters that control this interaction is also presented along with a brief description and classification of the breakwater typologies included in this research.

Chapter 3 is dedicated to describe the physical experimental and numerical setups. Both methods have been used to obtain the data analysed in this research. Data acquisition and analysis are also presented.

Chapter 4 focuses on the evaluation of the hydraulic performance resulting from the interaction of perpendicularly impinging wind water waves on various types of non-overtoppable breakwaters. The logistic sigmoid function has been found to define the hydraulic performance of the most common breakwater types. Moreover, the methodology of the application of the hydraulic performance curves is shown and some practical examples are included in order to show their efficiency.

In Chapter 5, a tool to numerically characterize the hydraulic performance is presented. For that, an analysis of the flow in the porous medium has been done and a linearised solution has been proposed. In this section an example of how the result can be applied is also included.

Chapter 6 presents an approximate solution of the total wave height distribution in front of the breakwater, caused by the linear superposition of the incident and reflected wave trains. The problem has been formulated and an approximate solution is provided.

In Chapter 7 an analysis of the breakwater stability has been done including the flow characteristics in front and at the face of the breakwater. The sliding of the superstructure failure mode has been analysed. The results shows the variables that quantify the breakwater stability can be calculated using the total oscillation in front and at the face of the breakwater.

Finally, in Chapter 8 the main conclusions and future research are summarized.

1.5 Publications derived from this Thesis

Journal Papers

- Vílchez, M., Clavero, M. and Losada, M. A, (2016c). Hydraulic performance of different non-overtopped breakwater types under 2D wave attack. *Coastal Engineering* 107, pp.34-52.
- Vílchez, M., Clavero, M., Lara, J. L., and M. and Losada, M. A, (2016a). A characteristic friction diagram for the numerical quantification of the hydraulic performance of different breakwater types. *Coastal Engineering* (Under review).
- Vílchez, M., Clavero, M., Baquerizo, A., and M. and Losada, M. A, (2016b). An approximation to the statistical behavior of wind waves in frint and on the face of non-overtoppend breakwaters. *Coastal Engineering* (Under review).

Proceeding in international conferences

- Clavero, M., Vílchez, M., Pérez, D., Benedicto, M. I., and M. and Losada, M. A, (2012). An unified design method of maritime works against waves. *Coastal Engineering Proceedings* 1(33), pp. 1-9. Santander (Spain).
- Vílchez, M., Díaz-Carrasco, P., Clavero, M., and Losada, M. A, (2016d). Verification of the crown wall stability taking into account the hydraulic performance curves. *Coastal Engineering Proceedings*. Accepted. Estambul (Turkey).

Proceeding in national conferences

- Vílchez, M., Clavero, M., Pérez, D., Izaskum, M.B., and Losada, M. A, (2011a). Evolución de tipologías de diques y comportamiento frente al reparto de flujos de energía. *XI Jornadas Españolas de Ingeniería de Costas y Puertos* Las Palmas, Spain (in spanish).
- Vílchez, M., Clavero, and Losada, M. A, (2015). Cálculo del comportamiento hidráulico de un dique de abrigo en talud con espaldón. *XIII Jornadas Españolas de Ingeniería de Costas y Puertos* Avilés, Spain (in spanish).

In this chapter, the wave energy distribution processes have been described, as well as the relationship between them, by means of the energy conservation equation. In addition, a classification of the different breakwater typologies considered in this study is presented. Finally, a parameter list including the main dimensionless monomials that describe the wave conditions, breakwater geometry and porous medium characteristics is obtained.

2.1 Wind wave-breakwater interaction. Wave energy distribution

This section describes the interaction between a breakwater section and sea oscillations according to ROM 1.0 (2009). The presence of the structure transforms the wave energy of sea oscillations, altering the distribution of the components of the frequency and directional spectra. The incident energy is distributed when the breakwater section interacts with the wind waves in (a) energy reflected and returned to the sea; (b) energy that is transmitted through or over the section; and (c) energy that is dissipated and thus extinguished (figure 2.1).

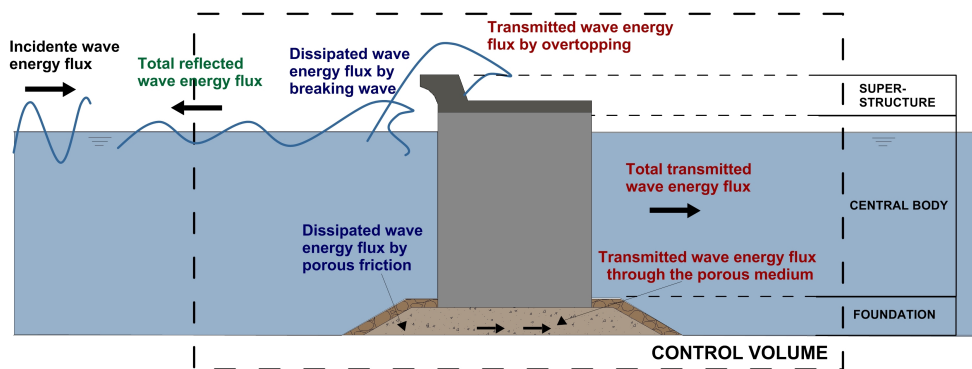


Figure 2.1.: Wave energy distribution.

2.1.1 Definition of the wave energy distribution processes

A breakwater reflects, dissipates and transmits the incident wave energy according to its type and the characteristics of the oscillation. These processes can be defined as follows:

2.1.1.1. Reflection

Wave energy reflection occurs due to a sudden change in the geometrical properties of the medium whereby the wave train is propagated. Consequently, abrupt changes in the water depth over a toe berm or in the hydraulic characteristics of the central portion of a rubble-mound breakwater as well as the presence of an impermeable wall in a vertical breakwater can cause the seaward reflection of part of the incident energy. In general, reflection at breakwaters does not occur at a fixed point or surface. Instead, there are numerous simultaneous reflection contributions throughout the propagation process. The last of these occurs when the wave train moves away from the breakwater section and propagates landward from the breakwater.

According to linear theory, the reflected energy can be evaluated through the bulk reflection coefficient (Hughes and Fowler, 1995) defined, similarly to regular waves, as a complex number with information regarding both the amplitude and phase of reflection (equation 2.1). K_R is the modulus of the reflection coefficient, which globally quantifies all the specific reflection processes. This can be defined by equation 2.2, where H_R and H_I are the reflected and incident wave height respectively. ϕ is the phase which represents the non-dimensional distance to a point in the inner part of the structure where an equivalent reflector would be found, which is capable of generating the same reflection effect as the total effect produced by all of the individual reflectors at their respective locations.

$$KR = K_R e^{(i\phi)} \quad (2.1)$$

$$K_R = \frac{H_R}{H_I} \quad (2.2)$$

2.1.1.2. Transmission

The transmission of wave energy landward from the breakwater can occur because of either wave overtopping at the crest or propagation through the porous medium. During its propagation through the breakwater or its foundation, part of the wave energy is consumed. If the breakwater is sufficiently wide enough, all of the energy may be dissipated. In such circumstances the wave energy transmitted through the breakwater is negligible. The transmitted energy can be evaluated by the bulk transmission coefficients (equation 2.3) similarly to the reflection coefficient, by a modulus, K_T (equation 2.4), and a phase, ϕ_T . In this case, H_T represents the transmitted wave height.

$$KT = K_T e^{(i\phi_T)} \quad (2.3)$$

$$K_T = \frac{H_T}{H_I} \quad (2.4)$$

2.1.1.3. Dissipation

The dissipation of wave energy is largely produced by two mechanisms: wave breaking on the front or face of the breakwater (including the turbulent flow through the voids of the armour units) and the shear stresses inside the porous medium. The rate of wave energy dissipation per unit of time, D'^* , produced by the breakwater can be calculated by equation 2.5, where D^* is the wave energy dissipation rate, ρ is the water density, g is the gravitational acceleration and C_g is the wave group speed. However, the evaluation of D'^* during the process is extremely complex and uncertain. An

indirect way for calculating the dissipated energy, which is applicable to breakwaters, is to resolve the wave energy conservation equation (equation 2.10), once the reflected and transmitted energy flux radiated from the control volume (figure 2.1) have been evaluated.

$$D^* = \frac{D'^*}{\frac{1}{8}\rho g C_g H_I^2} \quad (2.5)$$

2.1.2 Energy conservation equation

The analysis of these wave transformation processes can be achieved by establishing wave energy balance in a unit width control volume including the breakwater section (figure 2.1). The incoming and outgoing energy flows are evaluated as well as the dissipation processes inside it. The wave energy conservation equation in the control volume is given by equation 2.6 when linear theory is applied and when the transfer of wave energy to higher harmonics is considered negligible (Losada et al., 1997b). In this case the wave energy is expressed per unit of horizontal surface and unit of time as the most energetic wave frequency of the spectrum.

$$F_I - F_R - F_T - D'^* = 0 \quad (2.6)$$

$F_{I,R,T}$ represent the average incident, reflected (in front of) and transmitted (leeward) wave energy flows perpendicular to the breakwater per unit of area.. The minus sign represents energy extraction or loss from the control volume. The plus sign expresses the contribution or entry of energy in the control volume. These energy flows can be obtained as:

$$F_i = E_i C_{g,i} = \frac{1}{8} \rho g H_i^2 C_{g,i} \quad i = I, R, T (\text{incident, reflected and transmitted}) \quad (2.7)$$

The linear theory group speed is the following:

$$C_{g,i} = \frac{1}{2} C_i \left(1 + \frac{2k_i h}{\sinh(2k_i h)} \right) \quad (2.8)$$

where C_i , k , and h are the wave phase speed, wave number, and water depth, respectively. h and k are related to the angular frequency $\sigma = 2\pi/T$ by means of the dispersion equation (equation 2.9). F_i , E_i , and $C_{g,i}$ are phased-averaged quantities.

$$\sigma^2 = gk \tanh kh \quad (2.9)$$

Equation 2.6 can be expressed in terms of K_R , K_T , and D^* as shown in the energy conservation equation (constant depth):

$$K_R^2 + K_T^2 + D^* = 1 \quad (2.10)$$

2.2 State of the art

The dependence of wave regimes on the complex reflection and transmission coefficients and on the wave energy dissipation rate has been the focus of theoretical considerations, dimensional analysis, and experiments (Dalrymple et al., 1991; Losada et al., 1993b; Pérez-Romero et al., 2009).

Since the pioneering work of Iribarren (1949), which introduced the Iribarren number in the analysis of the stability of mound breakwaters, and its application by Battjes (1974) to the analysis of flow characteristics on sloping structures, many journal and conference papers have focused on the calculation of wave reflection by breakwaters (e.g. Seelig and Ahrens, 1981; Losada and Giménez-Curto, 1981; Allshop and Channel, 1989; Zanuttigh and van der Meer, 2008; Altomare and Gironella, 2014). Moreover, Garrido and Medina (2012), Iglesias et al. (2008), and Zanuttigh et al. (2013) demonstrate the efficiency of an Artificial Neural Network (ANN) for the prediction of the wave reflection coefficient for a wide range of coastal and harbor structures.

Unfortunately, most of these formulas and ANN methods analyze the reflection coefficient modulus without simultaneously evaluating the other hydraulic processes taking part in the wave-structure interaction, namely, the transmission coefficient and the wave energy dissipation rate. Furthermore, most databases, such as EU-project DELOS (www.delos.unibo.it) and CLASH (www.clash-eu.org), only provide the modulus of the reflection coefficient but not its phase. Actually, most databases do not supply the phase at all, and this type of information is extremely difficult to recover. As previously mentioned, the phase is essential in the evaluation of the flow characteristic in front of the breakwater. Flow characteristics include run-up, run-down, and overtopping, among other engineering magnitudes, which are crucial for breakwater design as it will be proven later.

2.3 Breakwater typologies. Classification

A gravity breakwater is composed of three main sections (ROM 1.0, 2009): (a) a foundation, which determines how the structure transmits forces to the seabed; (b) a central (or main) body, which controls the transformation of the incident wave energy and transmits the actions result of these processes to the foundation; and (c) a superstructure, which controls the wave overtopping rate and, if necessary, provides an access path.

Breakwater typologies can be classified according to the configuration and geometric dimensions of their components as well as the construction material. In this work the typologies choice has been done to get an uniform transition between one type and the next type for varying some parts or elements. It includes the typologies proposed by Kortenhaus and Oumeraci (1998) and the ROM 1.0 (2009) (figure 2.2):

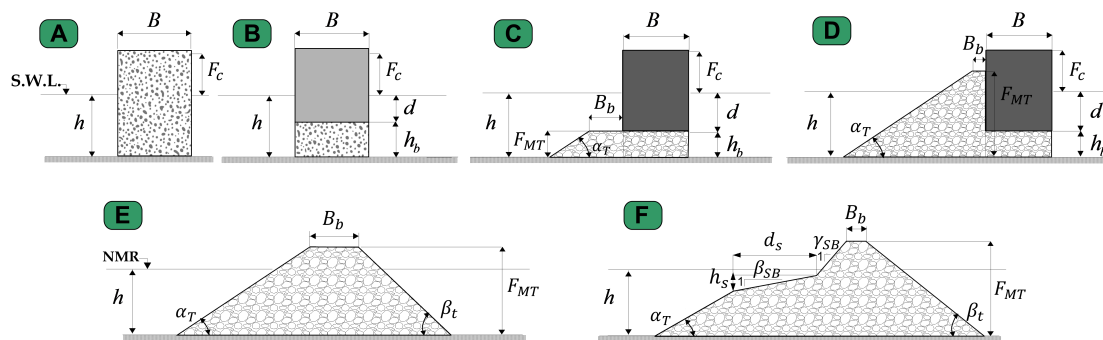


Figure 2.2.: Breakwater types: A) Porous vertical breakwater (PVB); B) Composite breakwater (CB); C) Low and high mound breakwater and high mound composite breakwater (LMB, HMB and HMCB) [$F_{MT}/h \leq 1.1$]; D) Rubble mound breakwater with crown wall (RMB-CW) [$F_{MT}/h > 1.1$]; E) Rubble mound breakwater (RMB); F) S-shaped breakwater (SB).

2.3.1 Type A: Porous vertical breakwater (PVB)

In a vertical breakwater typology (figure 2.2A), a single structural element includes both the central portion and the superstructure. Traditionally, the seaward face of the breakwater is vertical (thus, its name). It can be constructed with prefabricated caissons, massive concrete blocks, sheet piles, etc. The central portion of the breakwater is usually built on a foundation berm, made of granular material, adequately protected in order to guarantee its stability against sea oscillations. In the case of a impermeable vertical breakwater typology, the breakwater essentially behaves like a reflector of the incident wave energy and landwards energy transmission only occurs because of wave overtopping or, in very small quantities, because of the permeability of the foundation. When the section is composed of granular material, the transmission through the foundation and the energy dissipation rate in the porous medium increase. The permeable vertical breakwater is the case studied in this work. The geometric variables that define this typology are the following:

- B : The structure width
- D : The granular diameter
- F_c : The freeboard

2.3.2 Type B: Composite breakwater (CB)

When the foundation of the vertical breakwater occupies a large proportion of the water depth such that it significantly modifies the kinematics and the dynamics of the sea oscillations, it is called composite breakwater (figure 2.2B). Protection is provided by the lower subset (which also provides a foundation) and central body extends above the water to become part of the superstructure. Its performance can be predominantly reflecting, dissipative or a combination of both, depending on the water level, the characteristics of the incident wave and the geometrical dimension of the breakwater. Therefore, it can be partially reflecting and partially dissipative. The geometric variables that define this typology are, in addition to those for the vertical breakwater, the following:

- h_b : The caisson foundation depth

2.3.3 Type C: Mixed breakwater with a berm below or at S.W.L. (LMB, HMB and HMCB)

This type consists of a rubble mound layer of various thickness [$F_{MT}/h \leq 1.1$] and a caisson structure sitting on top of this mound (figure 2.2C). Inside this type, three different typologies can be distinguished as a function of the berm height (F_{MT}):

- **Low and high mound breakwater (LMB and HMB):** The relative berm height, F_{MT}/h (h is the water depth), varies from 0.3-0.6 for LMB to 0.6-0.9 for HMB. This type of breakwater can produce breaking wave at the breakwater wall.
- **High mound composite breakwater (HMCB):** A composite breakwater type with a very high rubble foundation and a smaller superstructure than standard vertical breakwater. This type has a berm close to the still water level (S.W.L.), $0.9 < F_{MT}/h < 1.1$. Depending on the water level at the structure, breaking waves or already broken waves can be observed at the breakwater.

The geometric variables that define this typology are, in addition to the previous one, the following:

- F_{MT} : The berm height or thickness
- B_b : The berm width
- α_T : The seaward slope angle

2.3.4 Type D: Mixed breakwater with a berm above S.W.L. (RMB-CW)

This type is defined as **rubble mound breakwater with crown wall (RMB-CW)** following Kortenhuis and Oumeraci (1998) (figure 2.2D). The crown walls are located on top of a rubble mound layer and the water level is below the berm [$F_{MT}/h > 1.1$]. In this typology only broken waves will reach the structure. The geometrical variables that defined this typology are the same as for type C.

2.3.5 Type E: Rubble mound breakwater (RMB)

This type is a traditional (Iribarren) breakwater (figure 2.2E). The central portion of the breakwater consists of a series of layers, which form a transition between the quarry run core and the main layer. The latter is made of natural or artificial pieces, and is the most resistant element to the wave action. The breakwater can be partially reflecting as well as partially dissipative depending on the characteristics of the incident wave action. Energy transmission landwards from the breakwater can be produced by wave overtopping at the crown, and through the foundation and central portion. The geometric variables that define this typology are the following:

- D : The diameter of the core material
- F_{MT} : The rubble mound height
- B_b : The rubble mound width
- α_T : The seaward slope angle
- β_T : The leeward slope angle
- Q_p : Variable to represent the armour unit type and placement density of the armor layer
- n_s : The armor layer porosity

2.3.6 Type F: Berm or S-shaped breakwater (SB)

This type of breakwater (figure 2.2F) is vulnerable to deformation because the units at the middle level of the structure can suffer extensive displacement in the same way as sand in a beach profile. The geometry of the profile is polygonal with three slopes. The length of the central polygon depends on the weight of the rock. The central portion of the breakwater can be made of any type of material, but it should provide adequate support so that the rocks in the main armour layer can be arranged with the prescribed orientation. This breakwater has absolute stability for all wave heights lesser than or equal to the design wave height. The geometric variables that define this typology are the following:

- F_{MT} : The rubble mound height
- B_b : The rubble mound width
- α_T , β_{SB} and γ_{SB} : The seaward three different slope angles
- β_T : The leeward slope angle
- h_s : The central slope height
- d_s : The central slope width
- Q_p : Variable to represent the armour unit type and placement density of the armor layer
- n_s : The armor layer porosity

2.4 Parameter list

This section presents the analysis of the main dimensionless monomials that determine the wind wave-breakwater interaction. According to this analysis, a parameter list has been performed including the parameters describing the wave motion and the geometric parameters necessary to unambiguously characterize breakwater types (section 2.3).

This parameter list contains the following subsets:

1 Related to the wave conditions:

- h/L : Relative water depth (L is the wavelength)
- H_I/L : Wave steepness of the incident wave train
- H_I/h : Relative incident wave height
- H_t/L : Wave steepness of the total wave height (incident and reflected train)

2 Related to breakwater geometry:

- B/L : Relative width of the caisson (1D scattering parameter)
- A_{eq}/L^2 : Relative area of the porous medium under the still water level (2D scattering parameter)
- h_b/h : Relative caisson foundation depth
- B_b/h : Relative berm width
- F_{MT}/h : Relative berm height
- $(F_c + h)/h$: Relative height of the breakwater
- α_T : Seaward slope angle
- Q_p : Type of unit and placement density of the armour layer
- Q_t : Slope profile: plane or S-shape

3 Related to porous medium characteristics:

- Dk or D/L : Relative grain diameter
- Re_p : Pore Reynolds number
- KC_p : Pore Keulegan-Carpenter number

Based on the theoretical background as well as numerical and experimental work, the 2D hydraulic performance for different breakwater types (Y) can be expressed by the following function:

$$Y = f \left(\frac{A_{eq}}{L^2}, Dk, \text{breakwater typology}, \frac{H_I}{L} \right) \quad (2.11)$$

where Y characterizes the wave regime resulting from the interaction between the breakwater and the incoming wave train. It represents the modulus of the reflection coefficient, K_R , the modulus of the transmission coefficient, K_T , the phase of the reflection coefficient, ϕ , and the wave energy dissipation rate, D^* .

The ratio B/L is a scattering parameter that controls 1D wave propagation in the porous medium (Dalrymple et al., 1991; Losada et al., 1993b; Pérez-Romero et al., 2009; Clavero et al., 2012, among others). However, for breakwaters consisting of different parts and units (some of which are composed of granular material), it is more convenient to define a 2D scattering parameter, A_{eq}/L^2 , where A_{eq} is the area per unit section under the S.W.L. This choice is consistent with the applicability domain of linear theory, which extends from the sea bottom to the still water level. The scattering parameter is related to the averaged transformation of the wave inside the porous medium. For a vertical porous breakwater (type A) A_{eq} is simply $B \cdot h$ and for a constant depth the scattering parameter is reduced to B/L , which is the relative breakwater width.

The relative grain diameter, Dk , controls the flow regime inside the porous medium, where k is the wave number, $k = 2\pi/L$. The nature of flow in a porous medium depend on the importance of frictional resistance forces (laminar, f_L , turbulent, f_T , and inertial, f_I). It can be analysed by evaluating two non-dimensional parameters, the Reynolds number (Re_p) and Keulegan-Carpenter number (KC_p) following Gu and Wang (1991). $Re_p = UD/\nu$, where U is the volume-average ensemble-average velocity and ν is the kinematic viscosity. $KC_p = UT/D$, where T is a characteristic period. KC_p tends to be large when the drag effect is important. Depending on the value of the pore Reynolds number and of the grain diameter, Burcharth and Andersen (1995), (following Dybbs and Edwards, 1984; Fand et al., 1987; Burcharth and Christensen, 1991) identified the following four hydraulic flow regimes: (1) Darcy flow regime (DFR) for $Re_p < 1$; (2) Forchheimer flow regime (FFR) for $1 < Re_p < 150$; (3) Transitional flow regime (TTR) for $150 < Re_p < 300$; and (4) Fully turbulent flow regime (FTFR) for $Re_p > 300$. For real breakwaters, the hydraulic regime within the structure is generally the fully turbulent flow (FTFR) and Re_p and KC_p can be omitted.

Moreover, *breakwater typology* includes the non-dimensional parameters that describe the breakwater geometry: h_b/h , F_{MT}/h , B_b/h , Q_p , and Q_t . In this work, the analyzed breakwater types are non-overtopped structures, therefore $(F_c + h)/h$ has not been considered. In the case of sloping breakwaters, the Iribarren number, $Ir = \tan\alpha_T/\sqrt{H/L}$, (Iribarren, 1938; Battjes, 1974; Losada and Giménez-Curto, 1981) is generally acknowledged to be an effective parameter that can be used to define the type of wave breaking against the breakwater slope. Wave breaking type can vary by modifying the wave steepness and maintaining the breakwater slope angle, by modifying the slope angle and maintaining the wave steepness, or by modifying both slope angle and wave steepness. This study applied the first option and the slope angle remained constant ($\cot\alpha_T = 1.5$).

According to the previous considerations, the hydraulic performance of the different breakwater types can be described in terms of the non-dimensional parameters given in table 2.1.

Typology	Parameters
Type A (PVB)	$A_{eq}/L^2, Dk, H_I/L$
Type B (CB)	$A_{eq}/L^2, Dk, h_b/h, H_I/L$
Type C and Type D (LMB, HMB, HMCB and RMB-CW)	$A_{eq}/L^2, Dk, h_b/h, B_b/h, F_{MT}/h, H_I/L$
Type E and Type F (RMB and SB)	$A_{eq}/L^2, Dk, Q_p, Q_t, H_I/L$

Table 2.1.: Parameter list.

In order to test the different breakwater typologies defined in section 2.3 two methods were implemented: 1) experimental and 2) numerical approaches. One part of the experimental data (type A, E and F) were obtained from previous works (section 1.2). New tests were performed in this work for type B, C and D. Numerical results were obtained by means of the IH-2VOF model, based on Navier-Stokes equations. In this chapter, both methods are described including model geometry, granular material characteristics and wave conditions. Wave breaking analysis is done as a function of wave conditions and breakwater characteristics. Finally, the variables obtained are presented.

3.1 Physical experiments set-up

The experiments were performed during a time period of over ten years with a total of 1575 experiments. The data for the A, E and F typologies were taken from previous studies in the *Environmental Fluid Dynamics Group* (Pérez, 2008; Correa, 2009; Benedicto, 2004; Clavero, 2007, respectively). Additional specific tests were carried out in this work for types B, C, and D.

Most of the experiments were performed in the wave flume at the CEAMA-University of Granada. The dimensions of the wave flume are 23 m in length, 0.65 m in width and 1 m in height. Data for type E and F were done in other labs, CITEEC in A Coruña, Spain, (33.8x0.58x0.80 m) and II-UNAM in Mexico (38x0.80x1m).

3.1.1 Model characteristics and wave conditions

3.1.1.1. Model characteristics

The following configurations were tested for the different breakwater types:

Type A model (figure 3.1A) consisted of a vertical porous breakwater with rectangular cross section. Three different model lengths ($B=0.02, 0.14$ and 0.50 m) and five different stone diameters ($D=12, 26, 40, 52$ and 110 mm) for $B=0.14$ and 0.50 m were tested.

Type B model (figure 3.1B) consisted of a composite breakwater with a rectangular parallelepiped shape above a foundation of granular material, both with the same width. Three different model widths ($B=0.14, 0.50$ and 1.50 m), four different foundation heights ($h_b=0.10, 0.20, 0.34$ and 0.40 m) and five different stone diameters ($D=12, 26, 40, 52$ and 110 mm) were tested.

Type C model (figure 3.1C) consisted of a composite breakwater protected by a berm of granular material. The granular material was the same as for the foundation. In this type the width and

foundation height of the composite breakwater were kept constant, $B=0.50$ m and $h_b=0.20$ m. The berm characteristics changed and three different berm heights ($F_{MT}=0.20, 0.30$ and 0.40 m), two different berm widths ($B_b=0.10$ and 0.25 m) and four different stone diameters ($D=12, 26, 40$ and 52 mm) were tested.

Type D model (figure 3.1D) consisted of a composite breakwater protected by a slope of granular material. The granular material was the same as for the foundation. In this type the characteristics of the composite breakwater were the same as for type C. The berm characteristic changed and two different berm heights ($F_{MT}=0.50$ and 0.60 m), two different berm widths ($B_b=0.10$ and 0.25 m) and four different stone diameters ($D=12, 26, 40$ and 52 mm) were tested.

Type E model (figure 3.1E) consisted of a rubble mound breakwater with seaward slope angle constant ($\cot\alpha_T=1.5$). Two section were tested. The first one was composed solely of a core (C) with a single granular material. The second one was built with the same core material but was protected by a main layer of armor stones (S).

Type F model (figure 3.1F) consisted of a S-shaped profile with the following three seaward slope angles: $\cot\alpha_T=1.6$, $\cot\beta_{SB}=5.6$ and $\cot\gamma_{SB}=0.75$. The height and width of the middle slope were $h_s=0.018$ m and $d_s=0.90$ m respectively.

Water depth was kept constant and equal to 0.4 m except for the case of type E and F, in which it was 0.5 and 0.54 m respectively. All the test were done for non-overtopping conditions.

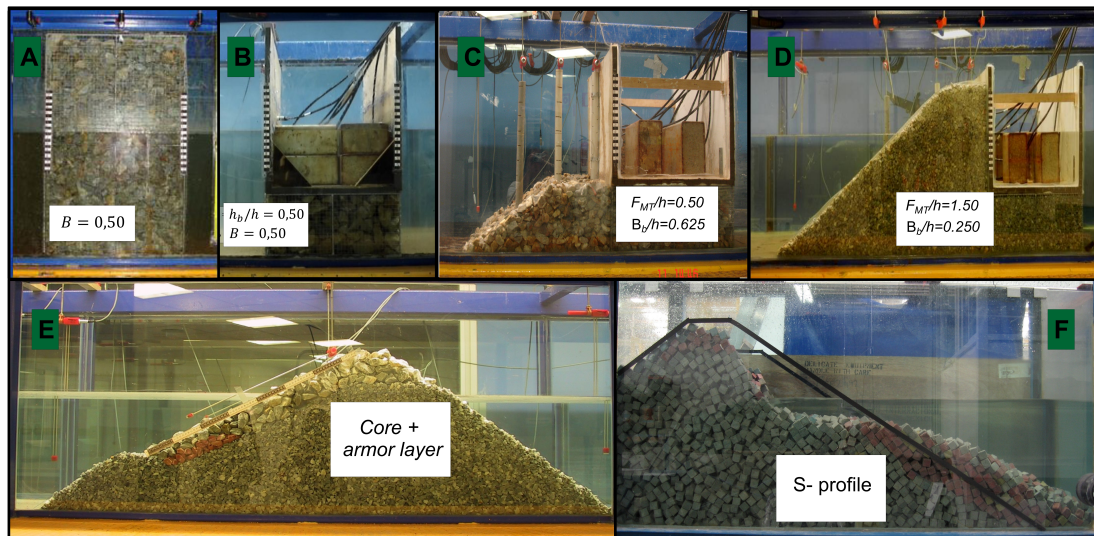


Figure 3.1.: Breakwater types tested.

Granular material characteristics

The granular materials for type A, B, C and D were classified according to CIRIA-CUR-CETMEF (2007). Their characteristics are shown in table 3.1. A Fourier Asperity Roughness Parameter (K_f) was assigned to each material depending on the axial dimension of the number of units. Finally, based on K_f , the average stone weight (W) and dry density (ρ_0), the characteristic diameter, D , was calculated with the following equation: $D = K_f \cdot (W/\rho_0)^{1/3}$. For a more detailed description, see Scarcella et al. (2006) and Pérez-Romero et al. (2009).

$D(m)$	n	K_f	D_{50}	D_{85}/D_{15}	$\rho_0 (tn/m^3)$
110	0.471	1.03	115	1.21	2.57
52	0.474	1.03	75	1.21	2.57
40	0.473	1.03	45	1.44	2.69
26	0.462	1.02	30	1.54	2.84
12	0.391	1.02	10	1.71	2.83

Table 3.1.: Material characteristics: porosity, Fourier Asperity Roughness Parameter, characteristic diameter, sorting parameter, and dry density.

For type E, the core material was fine gravel with a median size, $D=6.95$ mm, and porosity $n=0.42$. The relation D_{85}/D_{15} was 1.60 and the density was $\rho_0=2.7$ tn/m³. The armor units were angular stones with a diameter of 2.95 cm whereas the armor layer consisted of two layers of units. The porosity of the armor layer was $n_s=0.48$. When necessary, the stability of the armor stones in all of the breakwater types was assured by means of a fine wire mesh, which did not modify their hydrodynamic behavior.

The flow regime in the cases analyzed was evaluated, following the methodology proposed by Pérez-Romero et al. (2009), by using the diagram proposed in Gu and Wang (1991) and subsequently in van Gent (1995) (see section 2.4). The velocity, U , was approximated as $U \sim nH/T$, where H is the average of the root mean square wave height at the entry and exit of the porous medium and T is the mean period, T_{01} . Figure 3.2 shows the results. In all cases, Re_p/KC_p was larger than 10 and Re larger than 10^1 . Data are located in the region where the three forces are of similar importance.

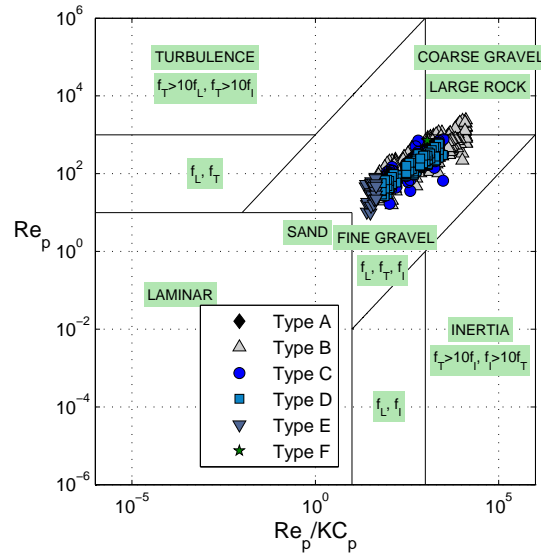


Figure 3.2.: Importance of the resistance forces (diagram from Gu and Wang, 1991) in the performed tests.

3.1.1.2. Wave conditions

For all tests, irregular waves were generated with the wave absorption system (AWACS®) activated. They then impinged perpendicularly onto the breakwater. These irregular waves were generated with a Jonswap type spectrum, and a peak enhancement factor of 3.3. Waves only broke when the wave train impacted against the breakwater wall or when they broke on the berm or slope because

of the change in depth. In no case did depth-limited breaking occur, and so the waves did not break before reaching the breakwater. Wave period was varied to test a wide range of relative depth, h/L . Deep, intermediate and moderate shallow water conditions were analyzed. The target wave parameters used in the laboratory are included in table 3.2, where $T_{p\ teo}$ is the peak period; $H_{Is\ teo}$ is the significant incident wave height and s_p is the wave steepness calculated as $s_p = 2\pi H_{Is} / gT_p^2$. For single-peak spectra, it is approximately $T_{01} = 0.8T_p$ (Goda, 1985).

Typology	$T_{p\ teo}$ (s)	$H_{Is\ teo}$ (m)	s_p
Type A	1.05-3.00	0.04-0.08	0.003-0.047
Type B	1.05-3.00	0.04-0.08	0.003-0.047
Type C	1.05-2.50	0.04-0.06	0.004-0.035
Type D	1.05-2.50	0.04-0.06	0.004-0.035
Type E	1.40-2.7	0.12-0.20	0.011-0.065
Type F	1.31-1.58	0.18	0.046-0.067

Table 3.2.: Wave conditions in experimental tests.

Table 3.3 sums up the variation intervals of the non-dimensional parameters included in the parameter list for the experimental tests. For their calculation the measured mean period has been used (T_{01}).

Typology	$\frac{A_{eq}}{L^2}$	$\frac{h_b}{h}$	$\frac{F_{MT}}{h}$	$\frac{B_b}{h}$	$cot\alpha_T$	Dk	n_s	$\frac{H_{I_{rms}}}{L}$	$\frac{h}{L}$
Type A	0.056- 0.200	-	-	-	-	0.01- 0.70	-	0.011- 0.050	0.10- 0.37
Type B	0.0005- 0.36	0.25 0.50 0.85 1.00	-	-	-	0.01- 0.53	-	0.003- 0.05	0.07- 0.39
Type C	0.008- 0.26	0.50	0.50 0.75 1.00	0.250 0.625	1.5	0.02- 0.30	-	0.005- 0.04	0.09- 0.36
Type D	0.018- 0.330	0.50	1.25 1.50	0.250 0.625	1.5	0.02- 0.40	-	0.005- 0.03	0.09- 0.36
Type E	0.040- 0.300	-	1.36 1.60	0.48 0.202	1.5	0.004- 0.009	- 0.48	0.0052- 0.03	0.12- 0.30
Type F	0.180- 0.220	-	1.59	0.31	1.5 2	0.108	-	0.063- 0.065	0.025

Table 3.3.: Non-dimensional parameters intervals in experimental tests.

3.1.2 Data acquisition and analysis

3.1.2.1. Free surface analysis

Ten resistance wave gauges (S1 to S10, figure 3.3) were located along the flume and used to measure free surface elevations with a sampling frequency of 20 Hz. The distances between the gauges are also shown in figure 3.3. The positions of gauges S1, S2, S3, and S8 were the same for all the typologies. Gauges S9 y S10 were used only for type A and B in order to remove the reflection from the dissipation ramp. Gauges S4, S5 and S6 were only considered in the case of

type C, D, and E because typologies A and B did not have a protection berm. Regarding the type E, gauges S6 and S7 were located at the beginning and the end of the berm, respectively.

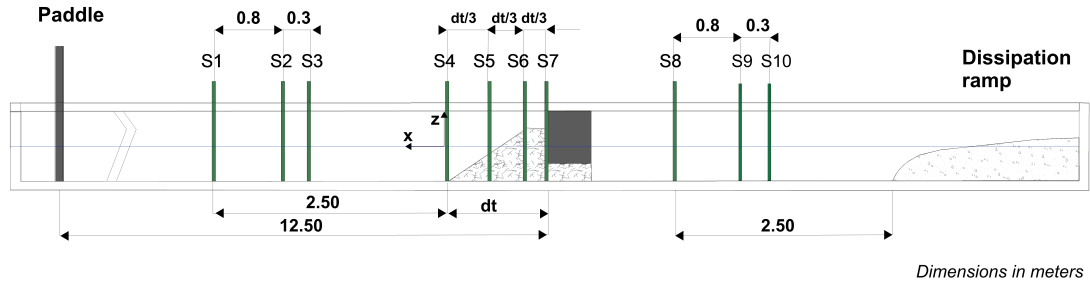


Figure 3.3.: Scheme of the wave flume and location of wave gauges.

Data obtained from the free surface measured were the following:

1. Instantaneous values of the free surface elevation:

- $\eta_I(t)$ and $\eta_R(t)$, incident and reflected wave train. The incident and reflected wave trains were separated by applying Baquerizo method (Baquerizo, 1995) to the data measured by gauges S1, S2, and S3. This method is based on linear theory.
- $\eta_t(t, x_i)$, total free surface time series in each position of the wave gauges (x_i).

2. Statistical parameters obtained from the free surface time series analysis:

- $H_{I_{rms}}$, T_{01} , K_R and ϕ : Incident root-mean-square wave height, mean period and reflection coefficient modulus and phase respectively. These variables were calculated with the data measured by gauges S1, S2 and S3. The incident and reflected wave trains were separated by applying Baquerizo (1995).
- $H_{T_{rms}}$ and K_T : Transmitted root-mean-square wave height and transmission coefficient. When wave energy transmission through the breakwater was significant (type A and B, and $K_T > 0.5$), $H_{T_{rms}}$ was calculated by applying Baquerizo method to the data obtained from gauges S8, S9, and S10, and by separating the reflected energy flow from the ramp. In the rest of the cases, since $H_{T_{rms}}$ was small and the transmission phase was not relevant, $H_{T_{rms}}$ was obtained only with gauge S8. The transmission coefficient was computed as the ratio of the incident root-mean square wave height, $H_{I_{rms}}$, and the transmitted root-mean-square wave height, $H_{T_{rms}}$ (Equation 2.4).
- D^* : Wave energy dissipation rate. By applying equation 2.10, the overall energy dissipation was calculated for each type of breakwater tested.
- H_{prms} or $H_{trms}(x=0)$: Root-mean-square total wave height (due to the interaction of the incident and reflected wave trains) at the breakwater toe. This variable was calculated with gauge S4, located at the toe of the structure ($x=0$).
- H_{wrms} and η_{wrms} : Root-mean-square total wave height at the wall and root-mean-square free surface at the wall. These variables were calculated with gauge S7 located seaward the superstructure $x = -dt = -(B_b + F_{MT} \cot \alpha_T)$.
- H_{S5rms} and H_{S6rms} : Root-mean-square total wave height in other two locations along the breakwater slope ($x_{S5} = -dt/3$ and $x_{S6} = -2dt/3$) that were calculated with measurement from sensor S5 and S6 respectively.

3.1.2.2. Pressure analysis

Pressure sensors were installed to obtain the pressures and loads acting on the breakwater for type B (figure 3.4). Sensors were distributed along the wall and the bottom of the caisson. The locations for the different breakwater widths are present in table 3.4 following the reference system shown in figure 3.4.

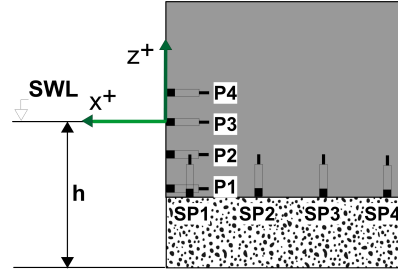


Figure 3.4.: Pressure sensors locations.

Sensor	Coordinates	$B = 0.14$ m	$B = 0.50$ m	$B = 1.50$ m
P1	z_1	-0.20	-0.20	-0.20
P2	z_2	-0.09	-0.09	-0.10
P3	z_3	0	0	0
P4	z_4	0.07	0.07	–
SP1	x_1	0	0	-0.1
SP2	x_2	-0.14	-0.25	-0.26
SP3	x_3	–	-0.50	-0.75
SP4	x_4	–	–	-1.4

Table 3.4.: Pressure sensors coordinates.

The data obtained from the pressure gauges have been the following (figure 3.5):

1. Instantaneous values of the pressure:
 - $p(z_i, t)$: Pressure time series at the wall of the caisson (z_i location).
 - $p(x_i, t)$: Pressure time series at the bottom of the caisson (x_i location).
2. Statistical parameters obtained from the pressure time series analysis:
 - $P(x, z)$: Pressure in the wave crest (for each wave of a sea state).
 - P_{1rms} : Root-mean-square value of pressure in the mean water level from the data measured by pressure sensor P3.
 - P_{2rms} : Root-mean-square value of pressure at the toe of the caisson from the data measured by pressure sensor P1.
 - P_{u1rms} : Root-mean-square value of uplift pressure at the entrance of the porous medium from the data measured by pressure sensor SP1.
 - P_{u2rms} : Root-mean-square value of uplift pressure at the exit of the porous medium from the data measured by pressure sensor SP4.

The data of forces obtained from the pressure measurement have been the following:

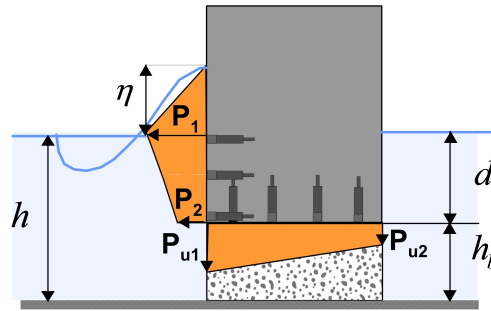


Figure 3.5.: Pressure variables definition.

1. Instantaneous values of horizontal and vertical forces:

- $FH(t)$: Horizontal force time series.
- $FV(t)$: Vertical force time series

The dynamic horizontal and vertical forces time series were obtained by integrating pressure and uplift pressure laws respectively. It has been assumed that the pressure law above the S.W.L. follows a linear law between the pressure at S.W.L. and $P=0$ for $z = \eta_w$. Moreover, a linear law has been assume between each consecutive sensor.

2. Statistical parameter obtained from the force time series analysis are:

- Fh : Horizontal force in the wave crest (for each wave of a sea state).
- Fv : Vertical force in the wave crest (for each wave of a sea state).
- Fh_{rms} : Root-mean-square value of horizontal force in the wave crest.
- Fv_{rms} : Root-mean-square value of vertical force in the wave crest.
- Fh_{max} and Fv_x : The maximum horizontal force in the wave crest and its concomitant vertical force (see figure 3.6).
- Fh_x and Fv_{max} : The maximum vertical force in the wave crest and its concomitant horizontal force (see figure 3.6).

3.1.3 Wave breaking analysis

The breaking types may be classified by the force time series characteristics (Nagai, 1973; Oumeraci and Kortenhaus, 1997). These authors distinguished four breaking type based on the force time evolution on a vertical wall, under different relative wave height (figure 3.7):

- **Quasi-standing waves (QSW)**: This type is produced by smaller wave heights so that the incident waves are approximately fully reflected by the wall and do not break. The wave rises above the structure without breaking and their horizontal speed field is transformed in vertical speed field. The typical force history at the wall do not show significant peaks but alters slowly over the time.

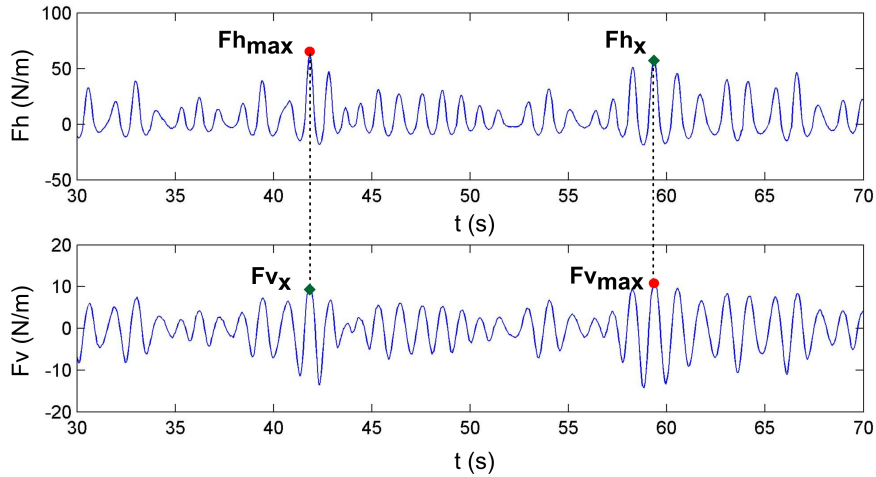


Figure 3.6.: Maximum horizontal and vertical force and their concomitants of a sea state.

- **Slightly breaking waves (SBW):** This type occur when the wave height is slightly increased and the waves start to break in front of the breakwater. Sometimes this breaking occurs at the wall, thus inducing the double peak of the force time series becomes asymmetric. Oumeraci et al. (1993) pointed out that the asymmetry of the double peak indicates that a transition from the standing wave to a breaking wave system is taking place. The first peak is higher than the second one (quasi-static) peak, but with less duration.
- **Wave impacts (IL):** This type generally occurs when the berm in front of the structure induces a breaker with the breaking point just in front of the wall. It provokes a strong impact including trapped air between the water column and the breakwater wall. The force history shows a clear and high first peak with a very short duration. The subsequent peak has relatively slow time variation although its duration is larger than the first peak.
- **Broken waves (BW):** The breaking point is far enough from the wall and only broken waves reach the structure. In this case a force history is obtained which is generally superimposed by high frequency oscillations due to a large air content in the water. The order of magnitude of the forces is the same as for slightly breaking waves.

Kortenhaus and Oumeraci (1998) proposed a method (figure 3.7) to define the wave breaking type based on three parameters: 1) the relative berm height (F_{MT}/h); 2) the relative total wave height ($H_{ts}^* = H_{ts}/h$), where H_{ts} is the significant total wave height at the toe of the breakwater; and 3) the relative berm width ($B_{eq}^* = B_{eq}/L$). The authors define B_{eq} as $B_{eq} = B_b + (0.5h_b \cot \alpha_T)$. The wave breaking classification (table 3.5) has been made following this method and the observations derived from photographs and video frames of the tests. There was almost not wave breaking for type A and B tests. Figure 3.8 shows the wave breaking observed for type C (LMB, HMB, HMCB) and type D (RMB-CW) as a function of the relative berm width and total wave steepness in front of the breakwater ($x = 0$). In the most of the LMB tests, no wave breaking occurred. Instead, a quasi-standing wave train was formed in front of the structure. In the case of HMB and HMCB tests, the waves began to break in front of the structure, and some finally broke on the crown wall. For HMB and HMCB tests, impulsive pressures were measured on the wall for the largest wave steepness and relative berm width. In the case of RMB-CW tests, only broken waves occurred. It was also the case of type E and F.

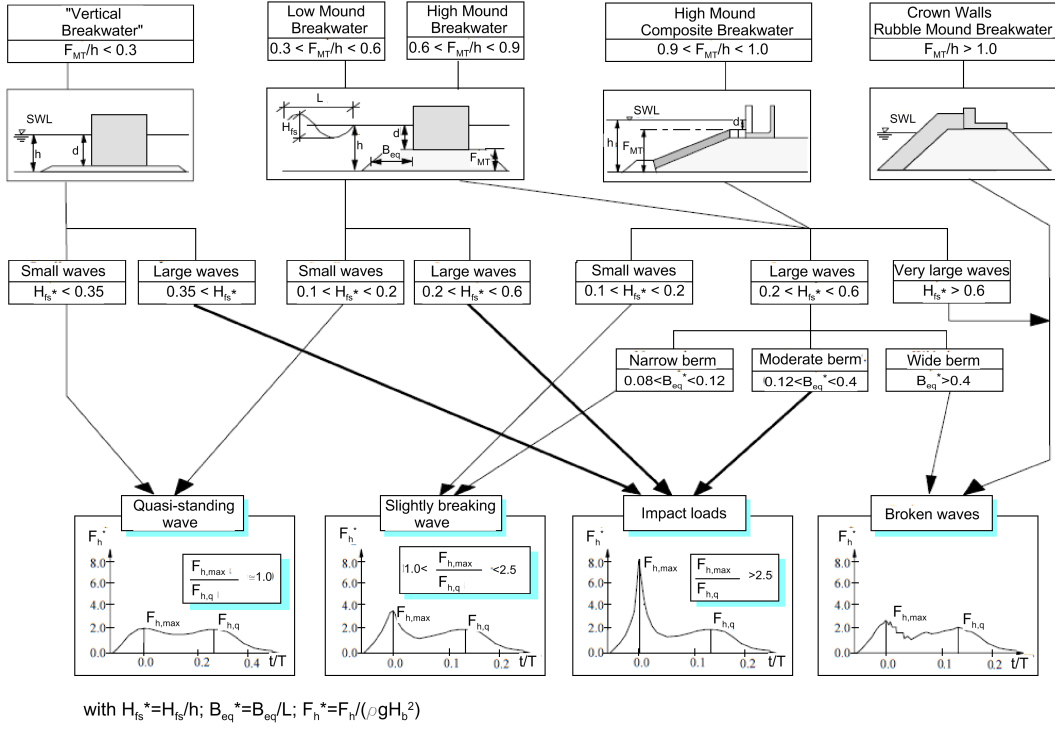


Figure 3.7.: Scheme to identify the wave breaking type (Adapted from Kortenhaus and Oumeraci, 1998).

3.2 Numerical experiments set-up

3.2.1 Description of the model

The IH-2VOF numerical model (Lara et al., 2008) solves the flow both inside and outside the porous medium. It is based on the Volume-Averaged/Reynolds Averaged Navier-Stokes equations (VARANS) in a two-dimensional domain. These equations are obtained when the RANS equations are integrated in a control volume, both inside and outside the porous medium. The final form of these equations is presented in equations 3.1 and 3.2. A more detailed description can be found in Hsu et al. (2002).

$$\frac{\partial \bar{u}_i}{\partial x_i} = 0 \quad (3.1)$$

$$\frac{1 + c_A}{n} \frac{\partial \bar{u}_i}{\partial t} + \frac{\bar{u}_j}{n^2} \frac{\partial \bar{u}_i}{\partial x_j} = -\frac{1}{\rho} \frac{\partial \bar{p}}{\partial x_i} + \frac{\nu}{n} \frac{\partial^2 \bar{u}_i}{\partial x_j \partial x_j} - \frac{1}{n} \frac{\partial \bar{u}'_i \bar{u}'_j}{\partial x_j} - F_{Gi} \quad (3.2)$$

In these equations, t denotes time; u is the Reynolds-averaged velocity; p is pressure; n is the porosity; ν is the kinematic viscosity; $i, j = 1, 2$ where 1 denote horizontal and 2 vertical directions. The over-bar represents the volume-averaged and single primes are the Reynolds-averaged fluctuation. F_{Gi} represents the resistive or friction forces created by the solid skeleton of the porous medium. The mass added term appears on the left side of the equation, which affects the acceleration term, where $c_A = \gamma_p(1 - n)/n$ is the added mass coefficient. The value of $\gamma_p = 0.34$ (van Gent, 1995) is considered to be constant because the results are practically insensitive to its variation (Losada et al., 2008). Numerical simulations in this study did not take into account the Reynolds stresses

Breakwater type		Breaker type
Type A		Quasi-standing waves
Type B		Quasi-standing waves
Type C	LMB	Quasi-standing waves
	HMB	Slightly breaking wave-Impact loads
	HMCB	Slightly breaking wave-Impact loads
Type D		Broken waves
Type E		Broken waves
Type F		Broken waves

Table 3.5.: Wave breaking classification.

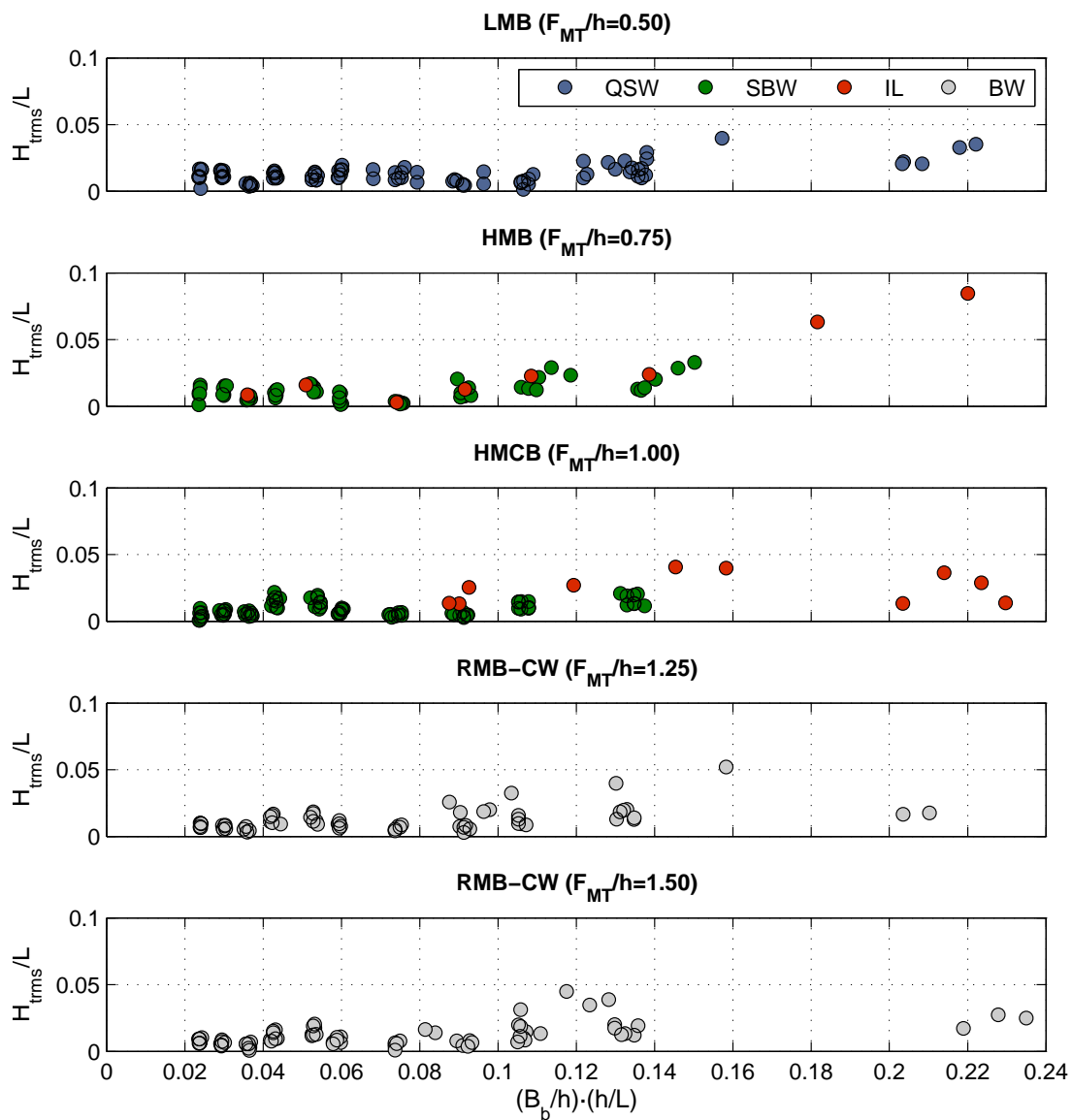


Figure 3.8.: Wave breaking type (type C and D).

term. The friction term in the porous medium is a closed model because this cannot be resolved directly in the model. This also corresponds to the concept of a closure model for turbulence modelling. As the coefficient in the friction forces is calibrated by direct comparison with the experimental data, it is considered to already include the turbulence effect. This can be regarded as a valid approximation for engineering applications (Jensen et al., 2014).

Volume of fluid (VOF) method is followed to compute free surface. IH-2VOF uses a finite difference scheme to discretize the equations. A forward time difference and a combined central difference and upwind schemes are considered for the time and spatial derivations respectively. Wave conditions are introduced in the model imposing a velocity field and a free surface time evolution on one side of the numerical domain. Active wave absorption was also considered.

3.2.2 Numerical experiments description

The wave flume was reproduced in the IH2-VOF model using a 2DV domain. A uniform grid on the z axis was used with a grid cell size of 0.5 cm. Horizontally (in the x axis), three regions were defined: (i) a center region, 5 meters long and containing the breakwater section with the finest resolution and a cell size of 1 cm; (ii) two regions at the beginning and at the rear end of the numerical wave flow with a cell size of 2 cm. A mesh sensitivity analysis was performed to assess the computational cost and the accuracy of the results. The total number of cells in the numerical domain was 1304 x 162. Active wave absorption was considered at the generation boundary, and the dissipative ramp at the final of the flume was reproduced with a porous medium. The characteristics of this porous medium were previously calibrated by comparison between the reflection coefficient measured experimentally and calculated numerically in the wave flume in absence of the breakwater for different wave conditions following Higuera et al. (2014).

Because of the computational cost of the model, a representative number of typologies and wave conditions were selected to simulate. The cases have been selected depending on the analysis carried out. They will be described in the corresponding section (chapter 5 and 7).

Hydraulic performance of different breakwater types under 2D wave attack

This chapter deals with the influence of the non-dimensional parameters (parameter list) on the hydraulic performance (reflection, modulus and phase, and transmission coefficients, and wave energy dissipation rate) of the breakwater types described in section 2.3. The study was based on data obtained from the experimental tests detailed in the previous chapter. The results confirm that the variation of those coefficients depends on the dimensions and properties of the parts and elements of the breakwater as well as on the wave characteristics. The logistic sigmoid function is found to accurately describe the behavior of these coefficients. The analysis of the sigmoid curve parameters are also included in this chapter. A summary of their values for the different breakwater typologies can be found in Appendix A.

4.1 Governing equation and fitting criteria

The sigmoid function is defined by Churchill and Usagi (1972) as following: if $Y(X)$ is a physical entity describing a transport phenomenon and $Y_0(X)$ and $Y_1(X)$ are known asymptotes to $Y(X)$ for small and large values of the independent variable X ,

$$Y(X) = (Y_1 - Y_0) \left[1 + \left(\frac{X}{a_X} \right)^\gamma \right]^{-1} + Y_0 \quad X > 0 \quad (4.1)$$

which describes a uniform transition between the asymptotes with γ , a blending coefficient, and a_X , a parameter of the process inherent to the sigmoid shape. The Churchill-Usagi method has been successfully used to describe various transport phenomena in fluid mechanics, heat transfer, and chemical engineering (Sivanesapillai et al., 2014). Curve definition requires four parameters: Y_0 , Y_1 , a_X , and γ . Figure 4.1 shows how the variation of these parameters affects the form of the sigmoid curve.

In this research, the phase-averaged quantities [K_R , K_T , ϕ_R , D^*] are physical entities describing a wave energy transport phenomenon. Following Churchill and Usagi (1972), and for a given breakwater typology, these quantities should adapt to a sigmoid shape for a specific independent variable and other non-dimensional parameters, as given by equation 2.11 and summarized in table 2.1. A logistic sigmoid curve should fix uniform transitions of Y_i , between Y_{i0} and Y_{i1} ,

$$Y_i = (Y_{i1} - Y_{i0}) \left[1 + \left(\frac{A_{eq}/L^2}{a_{Xi}} \right)^{\gamma_i} \right]^{-1} + Y_{i0} \quad \left\{ \begin{array}{l} A_{eq}/L^2 > 0 \\ Y_{i0} < Y_i < Y_{i1} \text{ or } Y_{i1} < Y_i < Y_{i0} \end{array} \right. \quad (4.2)$$

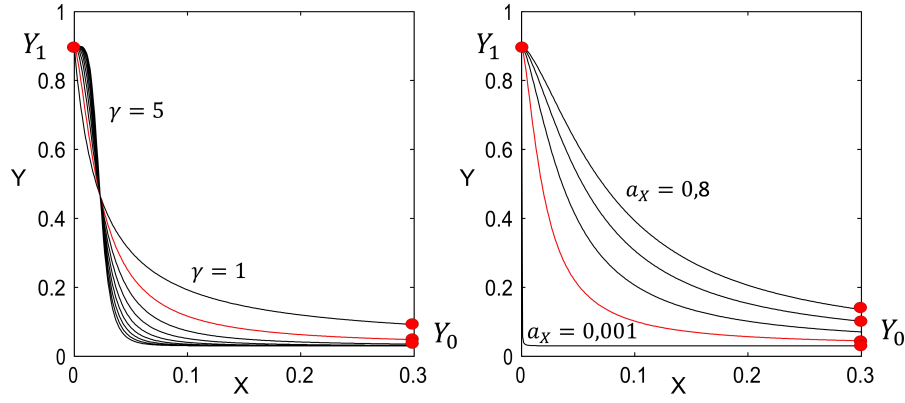


Figure 4.1.: Sigmoid curve variation based on parameter γ (left panel) and a_X (right panel).

where i is the index denoting the modulus of the reflection coefficient, K_R , modulus of the transmission coefficient, K_T , phase of the reflection coefficients, ϕ , or the wave energy dissipation rate, D^* . The selected independent variable is the relative volume of granular material per unit of breakwater width, or 2D scattering parameter, $X = A_{eq}/L^2$. The other two fit parameters of the curve (γ_i and a_{X_i}) depends on granular material characteristics, the breakwater typology, and incoming wave train conditions.

Based on the experimental data, the least squares method can be applied to obtain the four fit parameters (Y_{0i} , Y_{1i} , γ_i , a_{X_i}) of the sigmoid curve for the phase-averaged quantities [K_R , K_T , ϕ , D^*] for each breakwater typology. The error in the experimental data, y_{exp} , and theoretical data, y_{teo} , is calculated by means of the determination coefficient, R^2 :

$$R^2 = 1 - \frac{\sum (y_{exp}(i) - y_{teo}(i))^2}{\sum (y_{exp}(i) - \bar{y}_{exp})^2} \quad (4.3)$$

In the case of breakwater typologies with reflection coefficients that experience little variation and whose value is practically constant in regards to the main variable, the quantification of the error is based on the following mean quadratic error, ε :

$$\varepsilon = \sqrt{\frac{\sum (y_{exp}(i) - y_{teo}(i))^2}{\sum y_{exp}(i)^2}} \quad (4.4)$$

4.2 Hydraulic performance of different breakwater types

This section presents the fitted curves for the modulus and phase of the reflection coefficient, transmission coefficient as well as the energy dissipation rate obtained from the experimental data pertaining to wind wave action for non-overtoppable breakwaters analysed in this work (section 2.3). Parameters of the fitted curves are presented in Appendix A for these breakwater typologies and the range of analysed variables.

4.2.1 Type A: Porous vertical breakwater (PVB)

In a porous vertical breakwater (PVB), the modulus and phase of the reflection coefficient, transmission coefficient as well as the energy dissipation rate mainly depend on the 2D scattering parameter (A_{eq}/L^2) and the relative diameter of the porous medium (D/L or Dk):

$$Y = [K_R, K_T, \phi, D^*] = f(A_{eq}/L^2, Dk, H_I/L) \quad (4.5)$$

Figure 4.2 portrays the variation of Y with the 2D scattering parameter, A_{eq}/L^2 , and four ranges of relative diameter, Dk .

- The performance of this breakwater type in regards to wave action is organized in two regions (see the scheme in figure 4.3): (i) the transition region (TR) and (ii) the transmission, decay and stabilization region (DR). In the transition region, the reflection coefficient grows with the 2D scattering parameter until a maximum value (K_{Rmax}) associated with a critical value of A_{eq}/L^2 , $(A_{eq}/L^2)_{K_{Rmax}}$. The reflection process is then saturated. This maximum value decreases as Dk increases. When the relative width of the breakwater is greater than the critical value, $A_{eq}/L^2 > (A_{eq}/L^2)_{K_{Rmax}}$, the performance of the breakwater enters the transmission, decay and stabilization region. From here on, the value of the reflection coefficient remains stable or vary negligibly and only depends on Dk . Can be observed that the reflection coefficient modulus can oscillate under resonant conditions in this region, depending on the value of A_{eq}/L^2 (Requejo et al., 2002; Pérez-Romero et al., 2009). This behaviour can be seen in figure 4.2 for $Dk \geq 0.07$.

Each of these two regions can be defined by a sigmoid curve. The initial value in the TR, K_{R1} (TR), corresponds to $A_{eq}/L^2 \rightarrow 0$ and the final value, K_{R1} (TR), is the maximum value of K_R corresponding to $A_{eq}/L^2 = (A_{eq}/L^2)_{K_{Rmax}}$. The initial value in the second curve for DR is the same that the final value in TR curve, K_{R1} (TR) = K_{R0} (DR), and the final value, K_{R0} (DR), corresponds to the stabilization value of the reflection coefficient modulus.

Due to K_R does not significantly vary in the transmission, decay and stabilization region with a value closer to K_{Rmax} , it is possible to use the same sigmoid curve to define the two regions (see the best-fitted curves in figure 4.2) with $K_{R1} = K_{R1}$ (TR) and $K_{R0} = K_{R0}$ (DR).

For this type, the initial and final values of the sigmoid curve are a function of Dk . The smallest and largest values of K_R (K_{R1} and K_{R0} respectively) are associated with the minimum and maximum values of the reflection coefficient. The value of K_{R1} ($A_{eq}/L^2 \rightarrow 0$) defines the breakwater response when the transmission process is dominant. It is usually associated with large wave periods (shortest wave steepness). On the other hand, the value for the largest A_{eq}/L^2 , K_{R0} , corresponds with processes in which the reflection and dissipation processes are dominant. Generally speaking, it is associated with short wave periods (largest wave steepness).

- In contrast, the transmission coefficient modulus decrease monotonically for A_{eq}/L^2 and a decreasing Dk .
- Strictly speaking, the wave energy dissipation rate, D^* , is the complementary value of the sum of the squares of the two sigmoid curves. Its performance can also be represented by a sigmoid curve. The performance of the wave energy dissipation rate in this type follows a

similar pattern that the reflection coefficient modulus. In this case, the dissipation is only by friction in the porous medium because not wave-breaking occur during the tests.

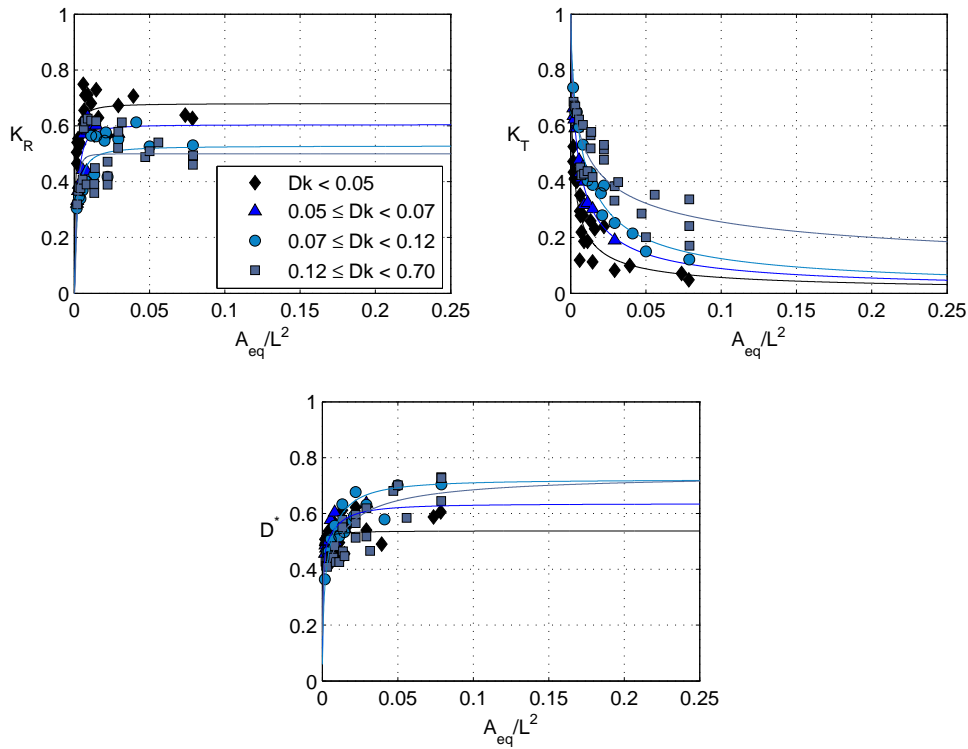


Figure 4.2.: Type A (PVB). K_R , K_T and D^* as compared to the 2D scattering parameter, A_{eq}/L^2 , and various ranges of Dk . Experimental data and best-fitted curves.

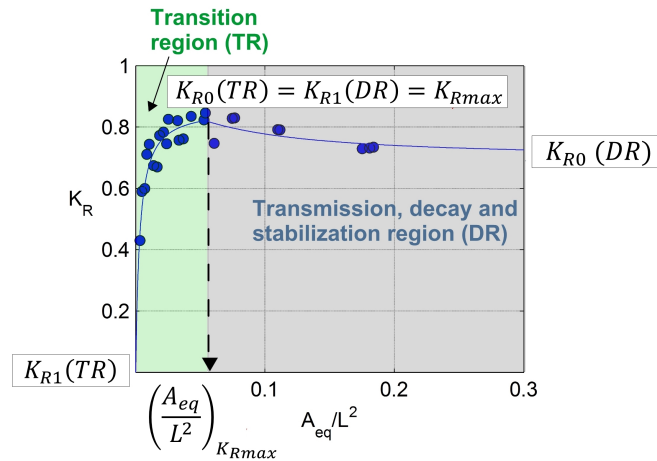


Figure 4.3.: Identification of performance regions, TR and DR for type A and B. In each region, the curve that best fits the sigmoid function is represented.

4.2.2 Type B: Composite breakwater (CB)

When an impermeable caisson is added to a porous vertical breakwater (CB), the modulus and phase of the reflection and transmission coefficients as well as the energy dissipation rate follow

the same behaviour pattern that type A (PVB) but depends also of the relative foundation depth, h_b/h . The functional for this type is present in equation 4.6:

$$Y = [K_R, K_T, \phi, D^*] = f(A_{eq}/L^2, Dk, h_b/h, H_I/L) \quad (4.6)$$

Figure 4.4 portrays the variation of Y with the 2D scattering parameter, A_{eq}/L^2 , four relative foundation depths, h_b/h , and one range of relative diameter, Dk . The results for the other range of parameters are presented in Appendix A. The variation of ϕ (represented by the non-dimensional phase, $x_0/L = \phi/4\pi$) with the 2D scattering parameter, A_{eq}/L^2 , is shown for the four ranges of relative diameter, Dk . They reflect the following:

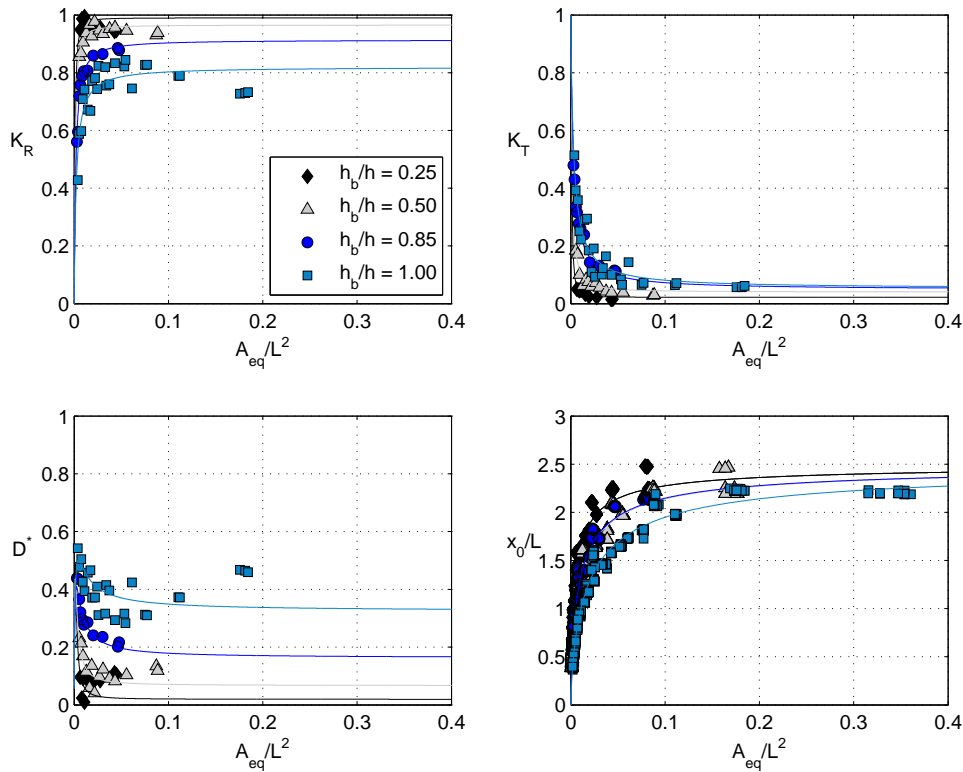


Figure 4.4.: Composite breakwater (CB). K_R , K_T , D^* and x_0/L as compared to the 2D scattering parameter, A_{eq}/L^2 , various ranges of h_b/h and $Dk < 0.05$. Experimental data and best-fitted curves.

- The behavior of the energy dissipation rate and reflection and transmission modulus, depending on the A_{eq}/L^2 and Dk , is segregated in different curves, based on the value of h_b/h . The presence of the caisson modifies the initial and final values necessary for the fitting.
- When $h_b/h \rightarrow 0$, the breakwater behaves similarly to an impermeable vertical breakwater (full reflection regime). In this case the impermeable caisson dominates the reflection processes and the transmission and dissipation in the porous medium is negligible. In contrast, for $h_b/h = 1$, the foundation of the crown is at still water level (S.W.L.) and the behavior is similar to type A (PVB). In this case the porous medium dominates the reflection processes because the transmission and dissipation in porous medium increase. In addition, for large values of Dk the across-breakwater modulation of K_R under resonant conditions becomes apparent.

- The transmission coefficient modulus decrease monotonically with A_{eq}/L^2 and decreasing h_b/h . It can be assumed that for A_{eq}/L^2 greater than approximately 0.15, and irrespectively of Dk , the reflection process and wave energy dissipation are in equilibrium. This yields an almost constant value of K_R , and energy transmission is thus negligible.
- The dimensionless phase of the reflection coefficient, x_0/L , follows the same pattern as the modulus. Following Sutherland and O'Donoghue (1998), the points in the figure are the experimental values that have been obtained by adding multiples of 2π to the phase though without modifying the results obtained because of the cyclical nature of the phase. The behaviour of x_0/L can be also described by a sigmoid curve fitted between the initial and final values: $(x_0/L)_1$ and $(x_0/L)_0$. The stabilization occurs approximately after the same values of A_{eq}/L^2 at which the reflection coefficient modulus become stable. The influence of Dk is not significant in the non-dimensional phase value, while h_b/h tempers the increase of the phase with the 2D scattering parameter.

4.2.3 Type C: Mixed breakwater with a berm below or at S.W.L.

$[F_{MT}/h \leq 1.1]$ (LMB, HMB and HMCB)

The construction of a porous submerged berm with relative width, B_b/h , and a relative height from the seabed of $F_{MT}/h \leq 1.1$, increases the relative width of the breakwater and reinforces its dissipation power with respect to the mixed breakwater without a berm (type B). This can eventually cause the wave to break on the front face of the breakwater and on the berm. The reflection (modulus and phase) and transmission coefficients as well as the energy dissipation rate vary, depending also on the geometric characteristics of the berm (the experimental berm was constructed with granular material of the same diameter as that in the foundation), in accordance with equation 4.7:

$$Y = [K_R, K_T, \phi, D^*] = f(A_{eq}/L^2, Dk, h_b/h, F_{MT}/h, B_b/h, H_I/L) \quad (4.7)$$

For this type, the reflection and transmission coefficient and energy dissipation rate vary essentially in the transmission, decay and stabilization region (DR) (see scheme for K_R in figure 4.5). For all practical purposes, the transition region is not relevant for this type (for construction reasons, these breakwaters have a minimum equivalent area, that generally corresponds to the maximum possible value of the reflection coefficient). Because of that, for this type only one sigmoid curve was fit in the DR.

Figure 4.6 portrays the variation of Y with the 2D scattering parameter; one relative caisson foundation depth, h_b/h ; two relative berm widths, B_b/h ; three relative berm heights, F_{MT}/h ; one range of relative diameter, Dk ; and two incident wave steepness, $H_{I_{rms}}/L$. To analyse the influence of the relative diameter, Dk , in this type, figure 4.7 shows the variation of Y with the 2D scattering parameter for one relative berm height, $F_{MT}/h = 0.75$ (HMB), with two relative berm widths, B_b/h , and two ranges of the relative diameter, Dk . The variation of the non-dimensional phase, x_0/L with the 2D scattering parameter is shown for both two ranges of Dk in figure 4.6. They reflect the following:

- For the reflection process, the largest and smallest values of K_R (K_{R1} and K_{R0} , respectively) are associated with the maximum and minimum values of the reflection coefficient. The value of K_{R1} defines the breakwater response when the reflection process is dominant, and when the wave energy dissipated, mostly by porous friction, is negligible. It is usually

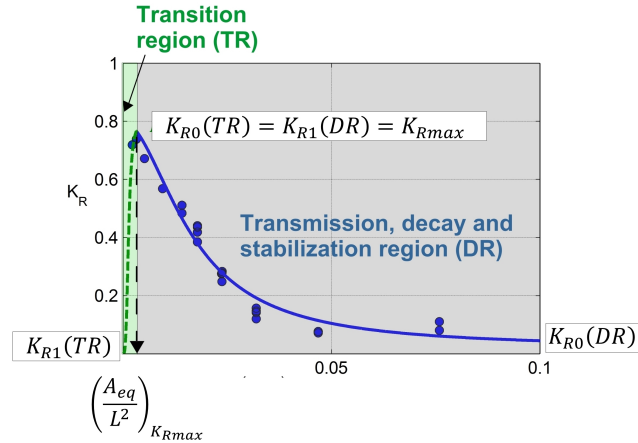


Figure 4.5.: Identification of performance regions, TR and DR for type C, D, E and F. In each region, the curve that best fits the sigmoid function is represented.

associated with large wave periods (largest wavelengths) and the smallest wave steepness. On the other hand, the smallest value, K_{R0} , determines the reflection coefficient when the energy dissipation rate tends to be maximal. Generally speaking, it is associated with short wave periods (shortest wavelengths) and the largest wave steepness. Moreover, under such conditions the dissipation process can dominate the wave-structure interaction.

The wave transmission, K_T , for non-overtoppable permeable breakwaters decreases with A_{eq}/L^2 . For large A_{eq}/L^2 , $K_{T0} \rightarrow 0$, whereas for $A_{eq}/L^2 \rightarrow 0$, K_{T1} must fulfil the energy conservation equation and can be approximated by means of $K_{T1}^2 \sim 1 - K_{R1}^2$. The wave energy dissipation rate in this type could occur due to one or all of the following mechanisms: porous friction and wave breaking onto the structure.

- For $F_{MT}/h = 0.50$ (LMB) and with no wave breaking, the relative berm width, B_b/h , the relative diameter of its granular material, Dk , and the relative height of the superstructure foundation, h_b/h , determine the dissipation rate, mostly by friction, and the variation of the reflection and transmission coefficients as A_{eq}/L^2 increases. It should be highlighted that for $A_{eq}/L^2 > 0.05$ the variation of the reflection and transmission coefficient modulus, and energy dissipation rate is negligible. Thus, from an engineering point of view, K_R can be regarded as practically constant with a value resulting from the largest expected steepness of incoming waves.

For $F_{MT}/h = 0.75$ (HMB), the dissipation rate increases because few waves break (largest wave steepness). This causes a decrease in the modulus of the reflection coefficient. However, the dissipation rate is mostly due to friction, and the widest berm is more dissipative than the shortest one. In this case, the modulus of K_R decreases more rapidly (the dissipation rate increases). Again, for $A_{eq}/L^2 > 0.05$, K_R can be considered constant although its value is lower than the corresponding non-wave-breaking value ($F_{MT}/h = 0.50$). The relative berm geometry, height and width, and the relative diameter control the value of Y_{i0} and the other parameters of the sigmoid curve. It can be seen (figure 4.6) that the modulus of K_T increases with Dk whereas the modulus of the reflection coefficient decreases slightly.

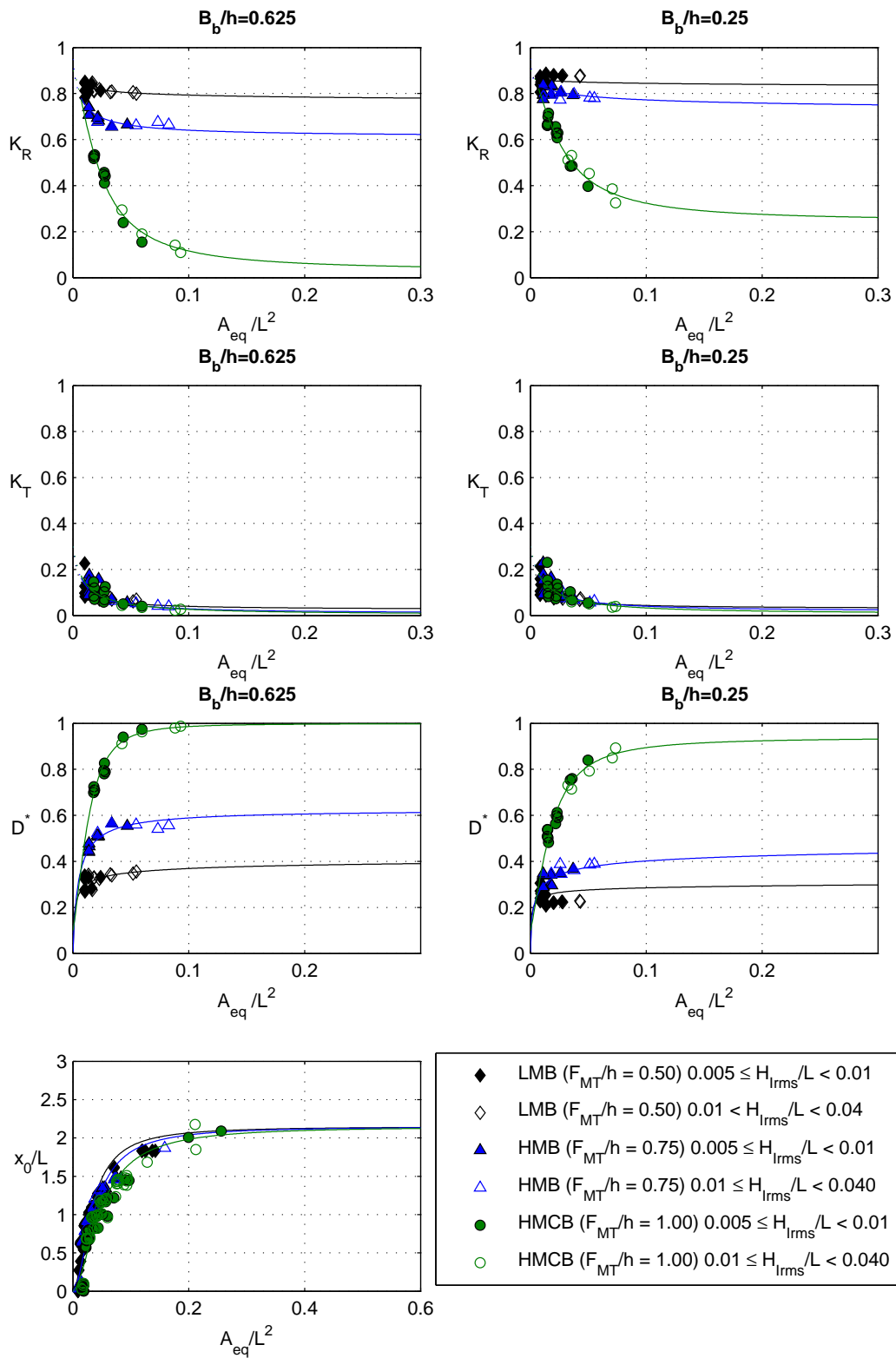


Figure 4.6.: Type C (LMB, HMB and HMCB). K_R , K_T , D^* and x_0/L as compared to the 2D scattering parameter, A_{eq}/L^2 , depending on B_b/h , F_{MT}/h , $H_{I_{rms}}/L$, for $Dk < 0.06$ and $h_b/h = 0.50$. Experimental data and best-fitted curves.

For $F_{MT}/h = 1.00$ (HMCB), almost all the waves break onto the slope or the berm, which enhances the wave energy dissipation rate by breaking and turbulence. As A_{eq}/L^2 grows, there is a rapid decrease in the modulus of the reflection coefficient (and a corresponding increase in the energy dissipation rate). For $A_{eq}/L^2 > 0.15$, K_R can be considered constant, but its value is much lower than the corresponding non-wave-breaking value ($F_{MT}/h = 0.50$) and strongly depends on the relative berm width. Thus, the relative berm width controls the value of Y_{i0} and the shape of the sigmoid curve. Once again, this behavior is weakly dependent on wave steepness. It can be assumed that an HMCB breakwater, con $F_{MT}/h = 1.00$ y $B_b/h > 0.625$, is totally dissipative for $A_{eq}/L^2 > 0.123$, independently of wave steepness and with negligible wave reflection and transmission.

- The general behavior of the non-dimensional phase x_0/L in regards to A_{eq}/L^2 is approximately the same as that of breakwaters with no berm, and follow the same pattern as the modulus. However, the height of the berm and, to a lesser extent, its width, regardless of wave breaking, tempers the increase of the phase with the 2D scattering parameter.

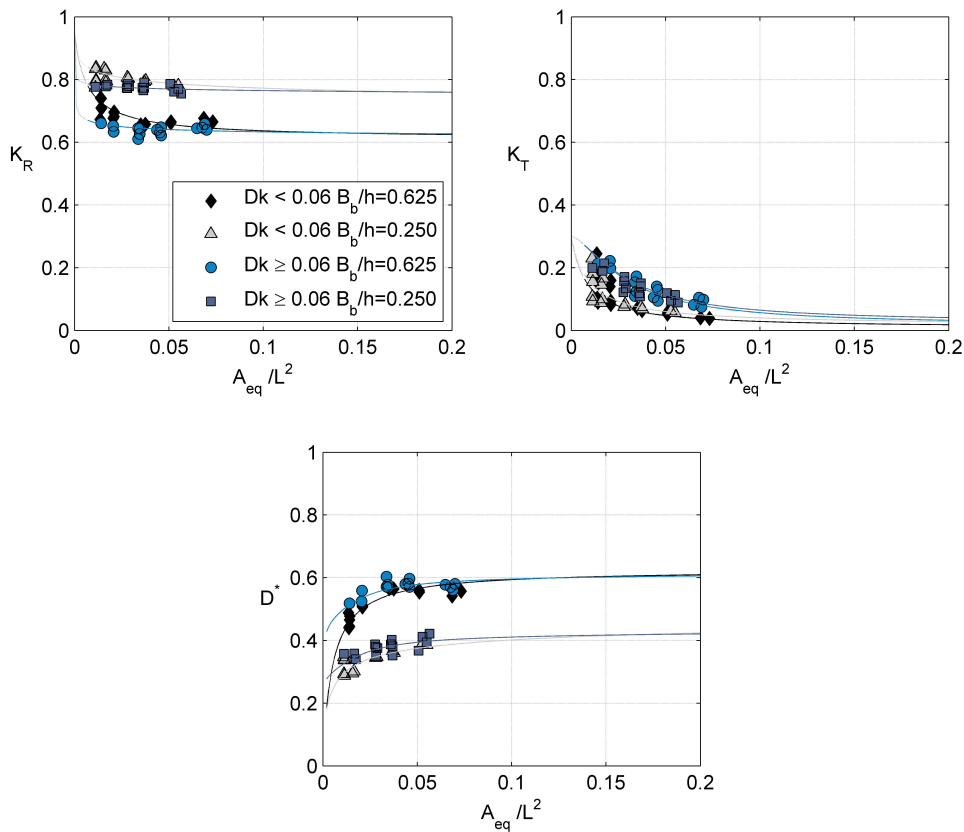


Figure 4.7.: Type C (HMB). K_R , K_T and D^* as compared to the 2D scattering parameter, A_{eq}/L^2 , depending on B_b/h , Dk and $h_b/h = 0.50$. Experimental data and best-fitted curves.

4.2.4 Type D: Mixed breakwater with a berm above the S.W.L. [$F_{MT}/h > 1.1$] (RMB-CW)

When the berm is above the S.W.L., the breakwater behaves like a traditional slope breakwater. The waves break on the slope and eventually reach the superstructure. The modulus and phase of

the reflections coefficient and transmission coefficient as well as the energy dissipation rate depend on the following non-dimensional parameters (Equation 4.8):

$$Y = [K_R, K_T, \phi, D^*] = f(A_{eq}/L^2, Dk, h_b/h, F_{MT}/h, B_b/h, H_I/L) \quad (4.8)$$

Figure 4.8 portrays the variation of Y with the 2D scattering parameter; one relative caisson foundation depth, h_b/h ; two relative berm widths, B_b/h ; two relative berm heights, F_{MT}/h ; one range of relative diameter, Dk ; and two incident wave steepness, $H_{I\text{rms}}/L$. Furthermore, the variation of the non-dimensional phase, x_0/L with the 2D scattering parameter is shown for both two ranges of Dk . They reflect the following:

- The modulus of the reflection coefficient decrease with the 2D scattering parameter, A_{eq}/L^2 , until a constant value, associated with the largest wave steepness and thus waves break on the slope. In this case, with a berm sufficient height from the foundation the waves, whether broken or not, run up and down the slope. This means that a superstructure is not required unless it is necessary to build access road. It can be seen that the influence of the coefficients weakly depend on the height of the berm, F_{MT}/h .
- The behavior of the non-dimensional phase follows the same pattern as that of Type C.

4.2.5 Type E and F: Undefined slope breakwater without crown wall (RMB, plane slope) and S-shaped breakwater (SB)

The tilt of the front face of the breakwater may eventually cause the wave to break onto the structure, thus increasing the wave energy dissipation rate. For an undefined plane-slope breakwater without a crown wall, the modulus and phase of the reflection and transmission coefficients, as well as the energy dissipation rate, are determined with equation 4.9:

$$Y = [K_R, K_T, \phi, D^*] = f(A_{eq}/L^2, Dk, Q_p, Q_t, H_I/L) \quad (4.9)$$

Figure 4.9 shows the variation of Y with the 2D scattering parameter; a seaward slope, Q_t , a slope angle, $\cot\alpha_T$, and two intervals of incident wave steepness, $H_{I\text{rms}}/L$. Results of two different sections are shown: one built only with the core, and the other one with the same core material but protected with a main layer of armor stones. Furthermore, data for S-breakwater have been added. They reflect the following:

- For the undefined sloping breakwater only composed of the core, the modulus of the reflection coefficient decrease with the 2D scattering parameter, A_{eq}/L^2 , and for values larger than 0.20, K_R and D^* can be regarded as constant. This region is associated with the largest wave steepness and thus waves break on the slope.
- If one or more upper layers are added to the breakwater section, wave dissipation increases because of the turbulence flow through the armor layer. The addition of a main layer causes the final fit value of the reflection, K_{R0} , to decrease. Again, for $A_{eq}/L^2 > 0.20$, K_R can be regarded as constant, but its value is lower for the protected slope with an armor layer than for the slope built only with the core. Correspondingly, the rate of energy dissipation is also constant but greater for the protected slope. It was found that the experimental values for the interval of the greatest wave steepnesses were slightly lower than those obtained for the smaller wave steepness intervals. Nevertheless, the difference was not sufficiently significant to be taken into account in the practical application.

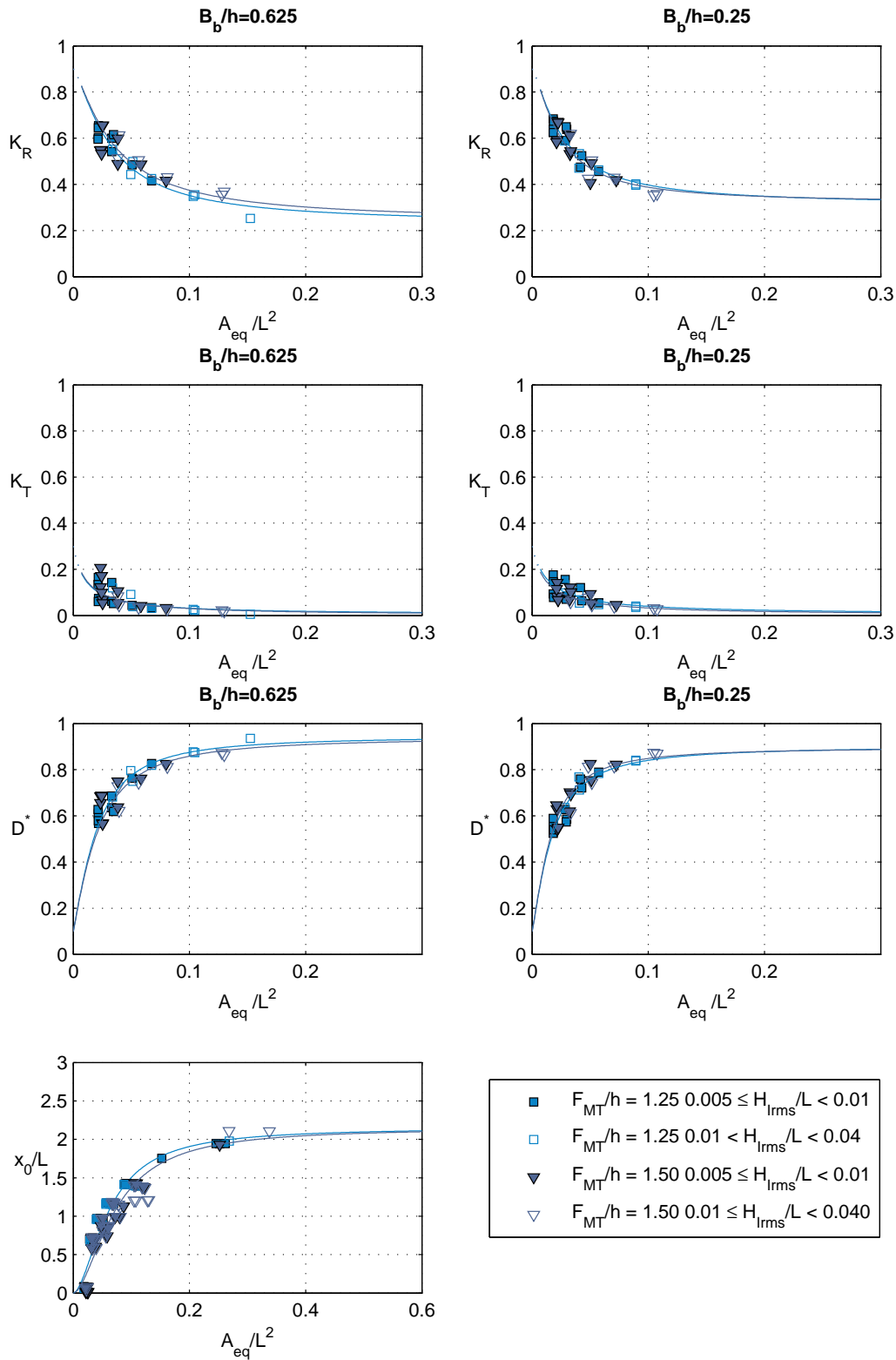


Figure 4.8.: Type D (RMB-CW). K_R , K_T , D^* and x_0/L as compared to the 2D scattering parameter, A_{eq}/L^2 , depending on B_b/h , F_{MT}/h , $H_{I_{rms}}/L$, for $Dk < 0.06$ and $h_b/h = 0.50$. Experimental data and best-fitted curves.

- Available data to SB show that this type minimizes the reflected energy flow. Its effectiveness stem from the fact that practically all breakers have an Ir minor than 2.5. However more data will be necessary for fitting the sigmoid curve in this type.
- Since in this study, wave transmission in these breakwater types was practically negligible, the wave energy dissipation rate was computed by using $K_T = 0$.
- The behavior of the non-dimensional phase follows the same pattern as the previous types of breakwater, but depends on the characteristics of the armor layer, as can be observed in figure 4.9. The presence of the main layer modifies the phase for $A_{eq}/L^2 > 0.05$, by changing its rate of variation as the 2D scattering parameter grows, at least until $A_{eq}/L^2 < 0.3$.

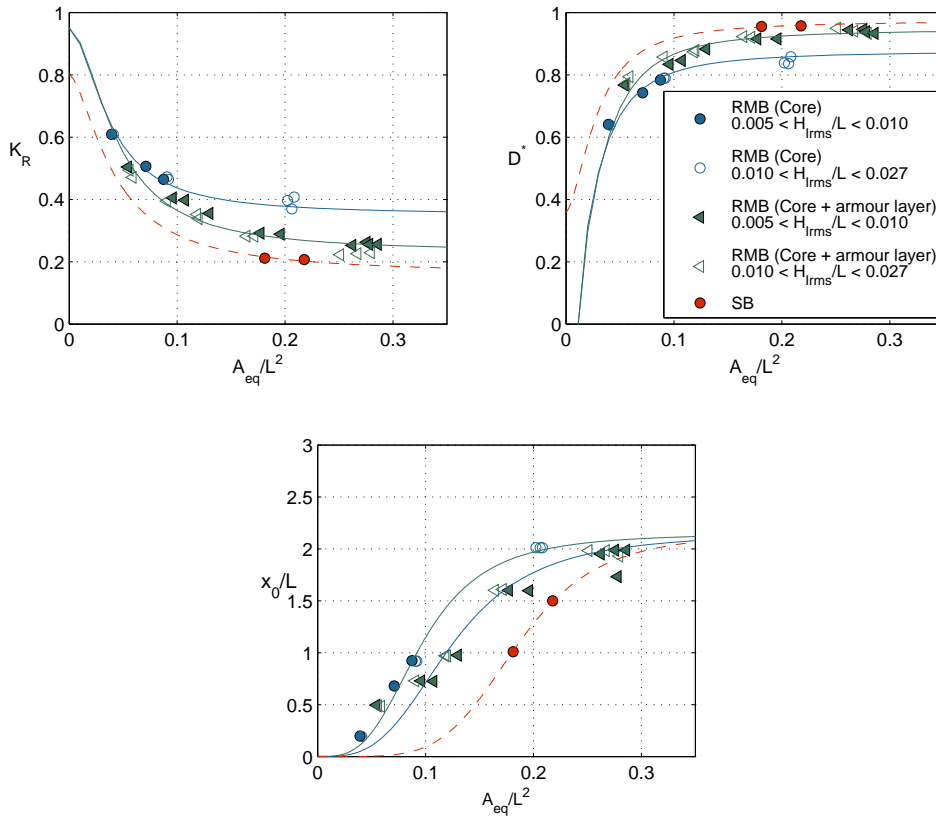


Figure 4.9.: Type E (RMB with core and core + armor layer). K_R , D^* and x_0/L as compared to the 2D scattering parameter, A_{eq}/L^2 , as a function of $H_{I_{rms}}/L$ and section type: core (quarry run); core + armor layer (core protected with material of a uniform grain-size distribution). Experimental data and best-fitted curves.

4.2.5.1. Effect of main layer units and porosities in the hydraulic performance

For the sake of completeness, this study analyzed the performance of non-overtoppable breakwaters with an armor layer composed of different units and placement density, Q_p . Two data sources were analyzed: (i) dolosse (figure 4.10a) breakwater (Ruíz et al., 2013) with $n_s = 0.49$; (ii) cube (figure 4.10b) and cubipod (figure 4.10c) breakwaters (Medina and Gómez-Martín, 2007) with $n_s = 0.37$ and 0.40 , respectively. Figure 4.11 shows these experimental data and the best-fitted curves (modulus of the reflection coefficient and wave energy dissipation rate) along with those of the section composed only of a core (Core) or of a core and a rubble layer (Core + armor layer) with armor stones (see figure 4.9). As can be observed, increasing the porosity of the main

layer caused the final fit value of K_R , K_{R0} , to decrease. Although some of these data depart from the fitted curve, it is also true that the data regarding cubes and cubipods include all the results obtained, namely, those for plane slopes as well as those for fault (or non-planar) slopes.

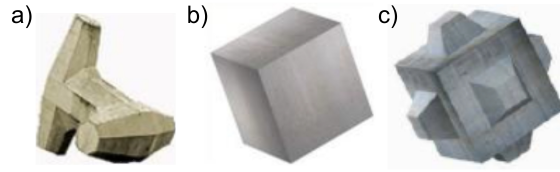


Figure 4.10.: Concrete armor units: a) dolosse, b) cube and c) cubipod.

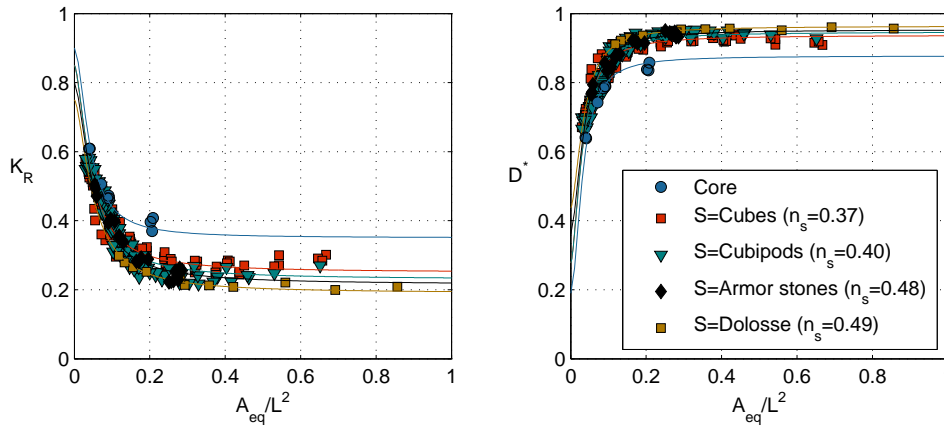


Figure 4.11.: K_R and D^* as compared to the 2D scattering parameter, A_{eq}/L^2 , and the type of armor unit with the following parameters: Core (Benedicto, 2004); S = Cubes and S = Cubipods (Medina and Gómez-Martín, 2007); S = Armor stones (Benedicto, 2004); S = Dolosse (Ruíz et al., 2013). Experimental data and best-fitted curves, depending on the porosity of the armor layer.

These results confirm that for armored non-overtoppable slope breakwaters, the reflection coefficient (modulus and phase) and the wave energy dissipation rate (by wave breaking, turbulence, and porous friction) are accurately represented by a sigmoidal function with a principal variable, the 2D scattering parameter. Moreover the sigmoid curve parameters mainly depend on the porosity and placement density of the armor unit, and weakly depend on the incident wave steepness.

4.2.6 Other breakwater types

This section provides the fitted curves for other breakwater types similar to the previous ones, but based on data obtained and published by other researchers. The objective is prove the accuracy of the sigmoid curve to reproduce the behaviour of the reflection coefficient modulus in other breakwater types. Unfortunately, none of these studied cases provided information regarding the phase of the reflected wave train. The cases that were selected permitted the analysis of the dependence of the reflection coefficient modulus on the slope angle and on the quasi-resonant conditions in special structures.

4.2.6.1. HMCB with superstructure (Allshop and Channel, 1989)

According to Kortenhaus and Oumeraci (1998), this breakwater is an HMCB (section 4.2.3) with $F_{MT}/h=1$, although in this case the breakwater has not superstructure (impermeable caisson). Its lack of superstructure is compensated by a rubble mound slope made of material of uniform

diameter, $D=0.056$ m. The freeboard of the breakwater prevents it from being overtopped. The parameter list are the same as those of the HMCB, except for h_b/h , and including the possible dependence of the emerged slope, and the slope angle.

Figure 4.12 shows the data and fitted curve for the slope: (a) $\cot\alpha_T = 1.5$ (left graph); (b) $\cot\alpha_T=2.0$ (right graph) and three relative berm widths, $B_b/h=0.523, 1.053, 2.105$. Also included is the curve derived from the experiments for the HMCB with superstructure (section 4.2.3) with $B_b/h=0.625, h_b/h=0.50$, and $Dk \leq 0.06$, because the breakwater's crown wall makes it geometrically similar to the profile in Allshop and Channel (1989). The figure shows that the performance of the two breakwater types is similar though the lack of caisson slightly reduces the coefficient value in comparison to the HMCB with an impermeable caisson. The setting values selected for the fit (table 4.1) weakly depend on the berm width. For the flattest slope, the curve moves towards the y-axis, attains the final value of reflection coefficient, K_{R0} , and slightly decreases although the difference are not very significant.

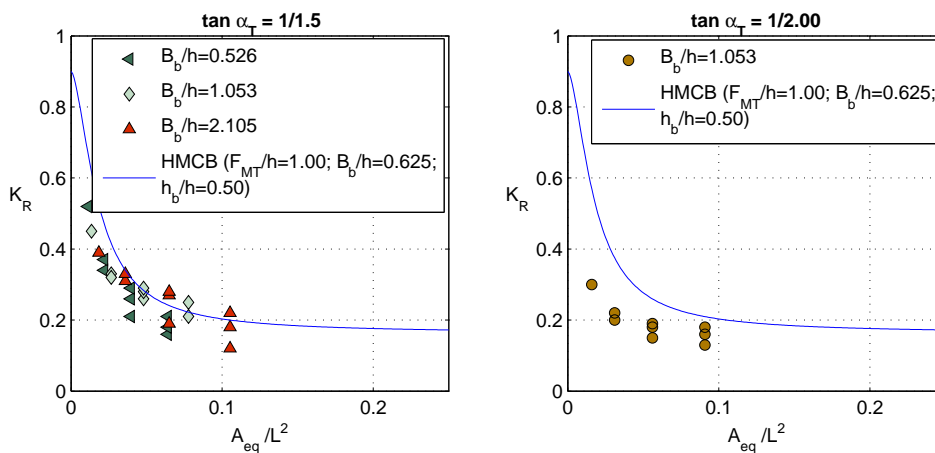


Figure 4.12.: HMCB breakwater with $F_{MT}/h=1$ and without a superstructure (Allshop and Channel, 1989). K_R as compared to the 2D scattering parameter, A_{eq}/L^2 , relative width, B_b/h , and slope gradient, $\cot\alpha_T$. Experimental data and best-fitted curves.

$\cot\alpha_T$	B_b/h	γ_R	a_{XR}	K_{R1}	K_{R0}
1.5	0.526	1.40	0.0111	0.90	0.18
	1.053	1.40	0.0107	0.90	0.18
	2.105	1.40	0.0109	0.90	0.14
2	1.053	1.40	0.0061	0.90	0.14

Table 4.1.: Fit parameters of the sigmoid curve for an HMCB breakwater with $F_{MT}/h = 1$ and without a superstructure (Allshop and Channel, 1989), depending on relative berm width, B_b/h , and slope gradient, $\cot\alpha_T$.

4.2.6.2. Special structures with quasi-resonant conditions (Liu and Faraci, 2014)

Under certain engineering conditions, it is necessary to design breakwaters, with specific geometries and materials, which at certain values of A_{eq}/L^2 have quasi-resonant conditions. The performance of these special breakwaters is characterized by maximum and minimum values of the reflection coefficient, transmission coefficient, or dissipation rate. One example is the performance of a caisson with an open front chamber filled with sloping rubble mound (figure 4.13). This type of structure has been studied by Liu and Faraci (2014). This work report two extensive campaigns of

experimental work involving such a caisson, in which several geometrical elements were changed, namely the submerged depth of the open front wall, h_{swl} , the slope, and the width of the emerged rubble mound, b_{swl} , to evaluate their influence on the reflection coefficient. The behavior of this structure is accurately reproduced by the sigmoid curve, which reflects the experimental data, thus enhancing the value of the scattering parameter under quasi-resonant conditions (figure 4.13). These conditions are closely related to the geometry and materials of the breakwater.

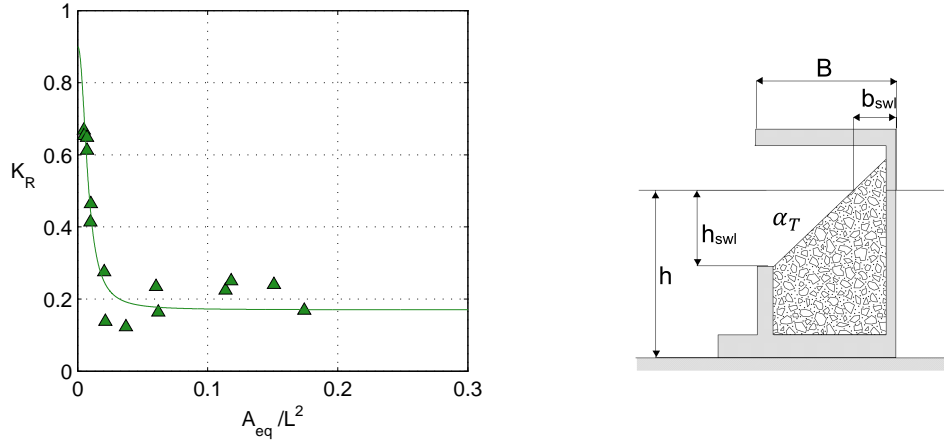


Figure 4.13.: K_R as compared to the 2D scattering parameter, A_{eq}/L^2 , under quasi-resonant conditions, $b_{swl}/h=0.292$, $h_{swl}/h=0.167$, $\cot\alpha_T=2$, $B=15$ cm, $h=24$ cm (Liu and Faraci, 2014). Experimental data and fit to a sigmoid curve with the following parameters: $\gamma_R=2.24$; $a_{XR}=0.008$; $K_{R1}=0.90$; $K_{R0}=0.17$.

4.2.7 Comparison with other formulas

It is not a simple task to compare the results of this study with those obtained by other researchers. There are two reasons for this. Firstly, the phase of the reflection coefficients is rarely provided in the results of such work. Secondly, some research studies do not show the complete breakwater section, which hinders the calculation of the 2D scattering parameter, A_{eq}/L^2 , and blocks the application of the wave energy conservation equation. For undefined sloped breakwaters (non-overtopped), Losada and Giménez-Curto (1979) and Zanuttigh and van der Meer (2008), among others, showed that the modulus of the reflection coefficient roughly depends on the Iribarren number, I_r , and type of armor unit. All the formulas predict a larger reflection coefficient for the largest Iribarren number. Moreover, the deviation between the predicted and measured values also increases with I_r .

Figure 4.14 shows a comparison of the measured and predicted values of K_R for an RMB with different sections (section 4.2.5). Predicted data have been calculated with 1) the sigmoid function (SF), 2) Zanuttigh and van der Meer (2008) equation (Z&M), and 3) Seelig and Ahrens (1981) equation (S&A). Data with an Iribarren number greater than 4 were considered. Equation 4.10 and 4.11 show the formulae given by Zanuttigh and van der Meer (2008) and Seelig and Ahrens (1981) respectively. Data with a wave steepness value, s_p , of greater than 0.012 were selected because Zanuttigh and van der Meer's formula is restricted to this condition.

$$K_R = \tanh(a_Z \xi_0^{b_Z}) \quad (4.10)$$

$$K_R = \frac{a_1 \xi_0^2}{\xi_0^2 + b_1} \quad (4.11)$$

ξ_0 is the breaker parameter (Iribarren number) based on the spectral wave period at the breakwater toe. The values of the coefficients are the following: (1) for permeable rock, $a_Z=0.12$, $b_Z=0.87$, $a_1=0.49$ and $b_1=5.456$; (2) for permeable rock with armor units, $a_Z=0.105$, $b_Z=0.87$, $a_1=0.49$ and $b_1=5.456$. The data used for the comparison are included in table 4.2. As can be observed, with the exception of the sigmoid curve, none of the formulas matches the experimental values. In fact, they predict an almost constant value.

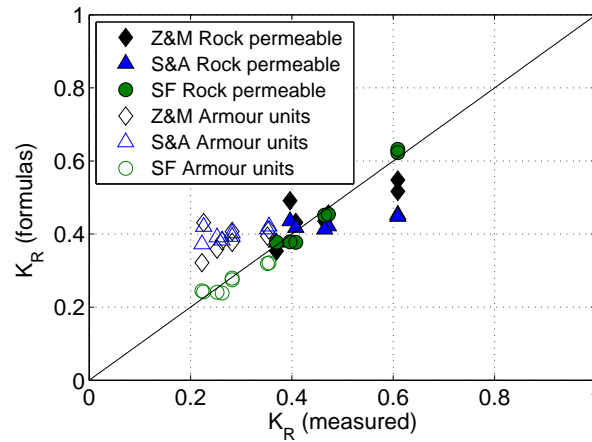


Figure 4.14.: Comparison of K_R obtained with the sigmoid function (SF) and the formulas of Zanuttigh and van der Meer (Z&M) and Seelig and Ahrens (S&A). Type E (RMB) composed of: 1) Core and 2) Core + armor units.

Permeable rock						
$cot\alpha_T$	T_p	$H_{I_s}(m)$	$K_R(Z\&M)$	$K_R(S\&A)$	$K_R(FS)$	$K_R(exp)$
1.5	2.600	0.058	0.548	0.453	0.632	0.609
1.5	2.559	0.065	0.517	0.448	0.623	0.609
1.5	2.868	0.059	0.455	0.422	0.454	0.472
1.5	2.857	0.068	0.435	0.413	0.425	0.465
1.5	2.429	0.027	0.491	0.435	0.379	0.396
1.5	2.416	0.037	0.432	0.417	0.377	0.408
1.5	2.420	0.064	0.353	0.377	0.378	0.370
Armor units						
$cot\alpha_T$	T_p	$H_{I_s}(m)$	$K_R(Z\&M)$	$K_R(S\&A)$	$K_R(FS)$	$K_R(exp)$
1.5	1.811	0.057	0.411	0.421	0.321	0.355
1.5	1.802	0.064	0.394	0.413	0.319	0.352
1.5	1.617	0.068	0.377	0.393	0.279	0.282
1.5	1.593	0.058	0.407	0.402	0.275	0.282
1.5	1.413	0.066	0.322	0.372	0.244	0.223
1.5	1.395	0.034	0.431	0.420	0.242	0.226
1.5	1.388	0.051	0.359	0.391	0.241	0.252
1.5	1.369	0.055	0.381	0.383	0.238	0.262

Table 4.2.: Test used for comparison with the formulas of Zanuttigh and van der Meer (Z&M) and Seelig and Ahrens (S&A). *FS* and *exp* represent the sigmoid function and experimental values respectively.

4.3 Application of the hydraulic performance curves

This section describes the methodology for obtaining the reflection coefficient (modulus and phase), transmission coefficient, and wave energy dissipation rate, based on the hydraulic performance curves obtained in previous section. For this purpose, a practical example is presented, which explains how performance curves can be used to verify certain project requirements or conditioning factors related to the oscillatory regime because of wind wave-breakwater interaction for non-overtoppable or occasionally overtoppable maritime structures. Furthermore, other applications has been included in order to show the efficiency of the hydraulic performance curves to (i) explore the cost-effective of the entire parametric list in a very short time, (ii) analyse the sensitivity of the breakwater type to different agents, materials, and geometries and (iii) determine its viability.

4.3.1 Sequence of application

The general application sequence involves doing the following (figure 4.15):

- 1 Selecting the pair of values representative of the design requirements from the joint probability distribution of (H_{Itrms}, T_{01}) at the breakwater location, and choosing the most probable values of the smallest and largest incident wave steepness.
- 2 Designing a preliminary section of the chosen breakwater type, calculating the equivalent area, A_{eq} , the corresponding values of scattering parameter, A_{eq}/L^2 , and subsequently selecting the non-dimensional parameter specific to the breakwater type and to the wave action of the parameter list.
- 3 Selecting the sigmoid curve parameters for the reflection coefficient $[K_{R1}, K_{R0}, \gamma_R, a_{XR}]$, non-dimensional phase $[(x_0/L)_1, (x_0/L)_0, \gamma_\phi, a_{X\phi}]$, and transmission coefficient $[K_{T1}, K_{T0}, \gamma_T, a_{XT}]$. Then, calculating the reflection coefficient for the two extreme sea state conditions, depending on A_{eq}/L^2 , and other non-dimensional parameters.
- 4 Calculating the most probable values of the smallest and largest total (incident plus reflected) wave steepness values, $[(A_{eq}/L^2)_{min}, (H_{trms}/L)_{min}]$, $[(A_{eq}/L^2)_{max}, (H_{trms}/L)_{max}]$, at the toe of the breakwater.
- 5 Verifying wave breaking at the front of the breakwater, on the berm, or on the slope, by applying an appropriate breaking criterion, and adjusting, if necessary, the largest total wave steepness values and the sigmoid curve parameters.
- 6 Verifying that the breakwater is impervious to overtopping (limit freeboard).
- 7 Calculating the transmitted waves based on the expressions of K_T .
- 8 Calculating the dissipation rate of the waves and the variation of other state variables, for example, the root mean square velocity, or pressure, in any location at the front of the breakwater.

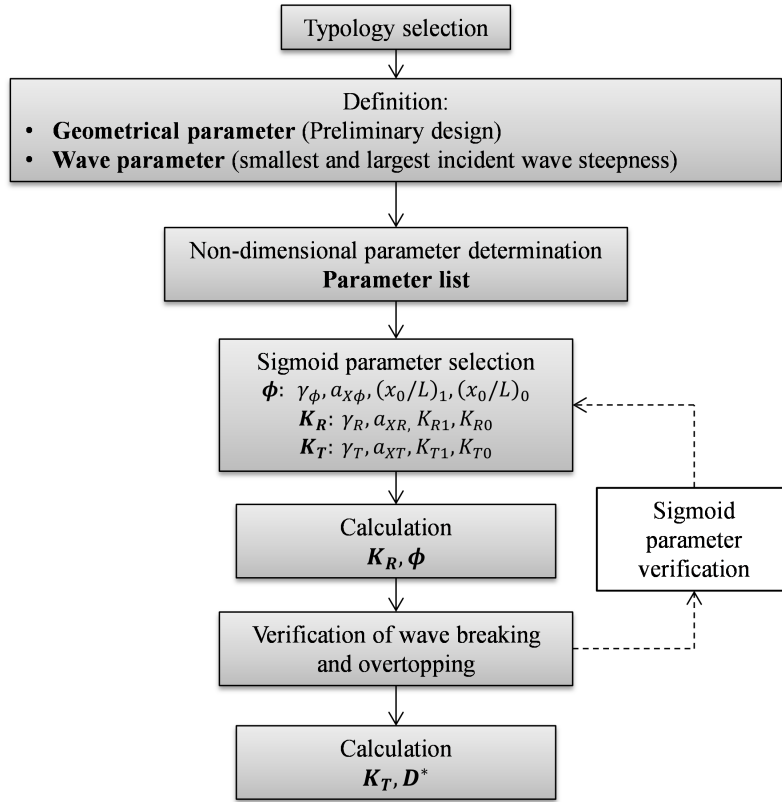


Figure 4.15.: Methodological sequence for applying the curves to obtain coefficients, K_R , ϕ , K_T , and D^* .

4.3.2 Example of application to a non-overtoppable low-mound breakwater (Type C, LMB)

In this section, the sigmoid curve is used to determine the wave transformation of the incident wave train resulting from the interaction with a given (preliminary) breakwater design. The steps are the following:

Step 1: Selecting the pair of values representative of the design requirements from the joint probability distribution of (H_{Irms}, T_{01}) at the breakwater location. The following sea states impinging on the breakwater were selected:

- State 1: $H_{Irms} = 3$ m; $T_{01min} = 7$ s; normal incidence
- State 2: $H_{Irms} = 3$ m; $T_{01max} = 12$ s; normal incidence

Step 2: Preliminary breakwater design, scattering parameter, and other non-dimensional parameters. An LMB is planned at a depth of $h=16$ m, with the following geometric dimensions (preliminary design) (see figure 4.16): $h_b=8$ m; $B=19$ m; $F_{MT}=8$ m; $B_b=10$ m; $F_c=3$ m; $cot\alpha_T=1.5$; $D=0.30$ m.

The equivalent area, A_{eq} (red-colored section in figure 4.16), which corresponds to the area of porous material below the still water level, is calculated as follows:

$$A_{eq} = Bh_b + (B_b + 0.5F_{MT}cot\alpha_T)F_{MT} = 280 \text{ m}^2 \quad (4.12)$$

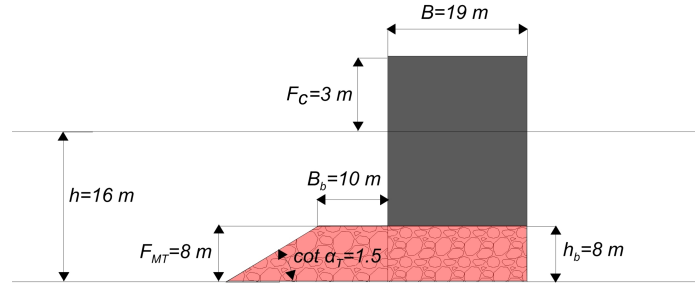


Figure 4.16.: Geometric dimensions.

Table 4.3 shows the scattering parameter and other non-dimensional parameters (A_{eq}/L^2 , h_b/h , F_{MT}/h , B_b/h , Dk) for the two sea states, namely, the probable maximum period, T_{01max} , and probable minimum period, T_{01min} , their wavelengths, and the respective steepness of the incident wave train.

Sea State	h/L	$H_{I_{rms}}/L$	A_{eq}/L^2	h_b/h	F_{MT}/h	B_b/h	Dk
$H_{I_{rms}}, T_{01min}$	0.233	0.044	0.059	0.50	0.50	0.625	0.027
$H_{I_{rms}}, T_{01max}$	0.115	0.022	0.015	0.50	0.50	0.625	0.014

Table 4.3.: Values of the non-dimensional parameters.

Step 3: Sigmoid curve parameters for the reflection coefficient, modulus and phase, and transmission coefficient (see table A.6). The sigmoid curve parameters are shown in table 4.4.

Variable	Sigmoid parameter			
	γ_R	a_{XR}	K_{R0}	K_{R1}
K_R	0.4282	0.0019	0.75	0.95
x_0/L	γ_ϕ	$a_{X\phi}$	$(x_0/L)_0$	$(x_0/L)_1$
	1.75	0.0296	2.15	0
K_T	γ_T	a_{XT}	K_{T0}	K_{T1}
	1	0.0065	0.0211	0.30

Table 4.4.: Sigmoid curve parameters for K_R , ϕ and K_T .

The values of K_R and ϕ are determined for the two sea states with equation 4.1 (table 4.5).

Steps 4 and 5: Largest wave steepness and breaking criterion at the front of the breakwater and on the berm. The values of H_{trms} are obtained by using the reflection coefficient and phase for each sea state as calculated with the following equation (see chapter 6):

$$H_{trms}(x) = H_{I_{rms}} \sqrt{1 + K_R^2 + 2K_R \cos(2kx + \phi)} \quad (4.13)$$

In this work, the maximum wave steepness at the front of the breakwater is estimated by applying the following breaking criterion for partial standing wave trains (ROM 1.0, 2009),

$$(H_{trms}/L)_{cr} \leq [a_r + b_r \{(1 - K_R)/(1 + K_R)\}] \tanh(kh) \quad (4.14)$$

Sea State	K_R	ϕ
$H_{I_{rms}}, T_{01min}$	0.787	20.84
$H_{I_{rms}}, T_{01max}$	0.809	6.00

Table 4.5.: Values obtained for K_R and ϕ .

where $a_r=0.08$ and $b_r=0.03$. Since the critical wave steepness value is never exceeded, there are no breaking waves at the front of the breakwater (table 4.6).

Sea State	H_{trms}/L	$(H_{trms}/L)_{cr}$	$H_{trms}/L > (H_{trms}/L)_{cr}$
$H_{I_{rms}}, T_{01min}$	0.043	0.075	No \rightarrow No breaking
$H_{I_{rms}}, T_{01max}$	0.039	0.052	No \rightarrow No breaking

Table 4.6.: Analysis of the presence of wave breaking at the front of the breakwater.

By following the same procedure, wave breaking on the berm is verified. However, it is necessary to previously calculate the wavelength on the berm. Here the method in Losada et al. (1997b) (Appendix B) based on the effective depth of the wave train, h_{ef} , is used. Values for $n=0.40$, $s=1$ and $f_r=3.17$ and 6.29 are chosen for sea states 1 and 2, respectively (s is the inertial coefficient and f_r is the linear friction coefficient, Sollitt and Cross, 1972). The election of the friction coefficient will be presented in chapter 5. The results are given in table 4.7.

Sea State	k_r	h_{ef}	H_{trms}/L	$(H_{trms}/L)_{cr}$	$H_{trms}/L > (H_{trms}/L)_{cr}$
$H_{I_{rms}}, T_{01min}$	0.112	8.323	0.053	0.061	No \rightarrow No breaking
$H_{I_{rms}}, T_{01max}$	0.610	8.124	0.052	0.040	Yes \rightarrow Breaking

Table 4.7.: Analysis of the presence of wave breaking on the berm.

It is plausible that the sea state with the minimum period causes waves to break on the berm. In regard to the LMB, breaking waves do not significantly modify the reflection coefficient. Nonetheless, this calculation can help to predict if the breaker can reach the caisson and produce impulsive loads.

Step 6: Verification of wave overtopping. In this work, to verify that the design breakwater is not overtopped by the waves, the following criterion is applied: the freeboard of the breakwater should be larger than the root-mean-square vertical total displacement of the free surface on the wall, η_{trms} , affected by a coefficient λ , ($F_c - \lambda\eta_{trms} > 0$) (Clavero, 2007). The value of η_{trms} is approximate with equation 4.13 as $H_{trms}/2$. The fact that the wall is located at $x = -(B_b + F_{MT} \cot \alpha_T)$ from the toe of the breakwater is also taken into account. A value of $\lambda = 2$ is used to ascertain whether overtopping occurs in the two sea states. The results are given in table 4.8.

Step 7: Calculation of transmission coefficient with equation 4.1 and parameters selected in step 3 (table 4.9).

Sea State	η_{trms}	$F_c - \lambda\eta_{trms}$	$F_c - \lambda\eta_{trms} > 0$
$H_{I_{rms}}, T_{01min}$	1.354	0.291	Yes → Non overtopping
$H_{I_{rms}}, T_{01max}$	1.115	0.771	Yes → Non overtopping

Table 4.8.: Analysis of the presence of overtopping.

Sea State	K_T
$H_{I_{rms}}, T_{01min}$	0.049
$H_{I_{rms}}, T_{01max}$	0.107

Table 4.9.: Sigmoid curve parameters of K_T .

Step 8: Calculation of wave energy dissipation. D^* is calculated with the energy conservation equation (equation 2.10). The results are shown in table 4.10.

Sea State	D^*
$H_{I_{rms}}, T_{01min}$	0.378
$H_{I_{rms}}, T_{01max}$	0.334

Table 4.10.: Value of D^* .

4.3.3 Reflection coefficient modulus of various breakwaters in Spain

Figure 4.17 shows the type and location of various breakwaters along the Spanish coastline defined in table 4.11. Their geometric and wave characteristics were obtained from the Atlas de Diques Españoles (Puertos del Estado, 2012). The four parameters needed to define the curves, Y_0 , Y_1 , a_X , and γ , were taken from the sigmoid curves proposed in this work (Appendix A). Figure 4.18 shows the breakwaters and the sigmoid curves for each breakwater typology analyzed. After the curve values obtained were assigned to the reflection coefficients, it was found that the range of the scattering parameter covered most of the values characteristic of real breakwaters.

For the set of breakwaters analyzed, the scattering parameter showed a wide range of variation, $0.005 < A_{eq}/L^2 < 0.4$. The three upper graphs correspond to the design wave period, T_d , (safety limit states). The three lower graphs were calculated with half that period and are representative of operational limit states. As can be observed, for design conditions, sloping breakwaters (type E, RMB) could presumably reflect more than 40% of the incident root-mean-square wave height, whereas in normal operational conditions, reflection would lessen to 20-30% of the root-mean-square wave height. Low and high berm breakwaters with a superstructure (LMB and HMB, type C) would reflect more than 70% of the root-mean-square wave height for design (safety) conditions and operability.



Figure 4.17.: Spanish breakwaters location and classification.

4.3.4 Adaptive design method for breakwaters and optimization

The application of the results of this research facilitates the formulation of different design alternatives that satisfy the same conditions or project requirements, such as limiting the reflection produced by the breakwater in its interaction with the waves. With this tool, the breakwater design can be adapted to safety and operability requirements. Figure 4.19 shows the contour lines of K_R for the different breakwater types, depending on the parameter list. For example, in the design of a breakwater in which the reflection modulus is limited to a maximum value of 0.5 (or where the root mean square wave height at the toe of the breakwater does not exceed a certain value), two options can be considered:

- HMB, HMCB, or RMB-CW with width $B_b/h \sim 0.625$, as long as the scattering parameter remains higher than approximately 0.025 for a slope $F_{MT}/h > 0.75$ and $F_{MT}/h \leq 1.00$ and higher than 0.040 if the slope increases $F_{MT}/h > 1.00$.
- If the relative width of the berm is reduced, $B_b/h \sim 0.250$, in breakwater typologies HMB, HMCB, or RMB-CW, it is then necessary to raise the height of the crown, $F_{MT}/h > 1.00$. In this case, it would be possible to select an HMCB and RMB as long as the scattering parameter remains more or less greater than 0.045.
- RMB or SB, depending on the scattering parameter. It should be greater than 0.06 for an RMB and greater than 0.05 for an SB.

If more than one breakwater typology satisfies all the project requirements, it is best to choose the least expensive option. The economic evaluation should consider the initial investment and costs, which in this case would include maintenance and repair as well as the effects of this work on harbor operations. Furthermore, the availability of sufficient amounts of high-quality material in all project phases as well as sea and land construction equipment significantly condition the choice of breakwater typology.

Nº Id.	Breakwater Name	Typology	Harbor	Sea
1	Punta Langosteira	LMB	A Coruña	Atlantic Ocean
2	Prioriño cape	LMB	Ferrol Port	Atlantic Ocean
3	Osa	RMB	Gijón	Cantabric Sea
4	Punta Lucero	RMB	Bilbao	Cantabric Sea
5	Zierbera	HMB	Bilbao	Cantabric Sea
6	North	RMB	Barcelona	Mediterranean Sea
7	West	LMB	Tarragona	Mediterranean Sea
8	South	RMB	Valencia	Mediterranean Sea
9	Botafoc (I)	LMB	Eivissa	Mediterranean Sea
10	Botafoc (II)	LMB	Eivissa	Mediterranean Sea
11	South	RMB	Alicante	Mediterranean Sea
12	East	LMB	Motril	Mediterranean Sea
13	Exterior	RMB	Algeciras	Mediterranean Sea
14	Reina Sofía	LMB	Las Palmas	Atlantic Ocean

Table 4.11.: Spanish breakwaters characteristics.

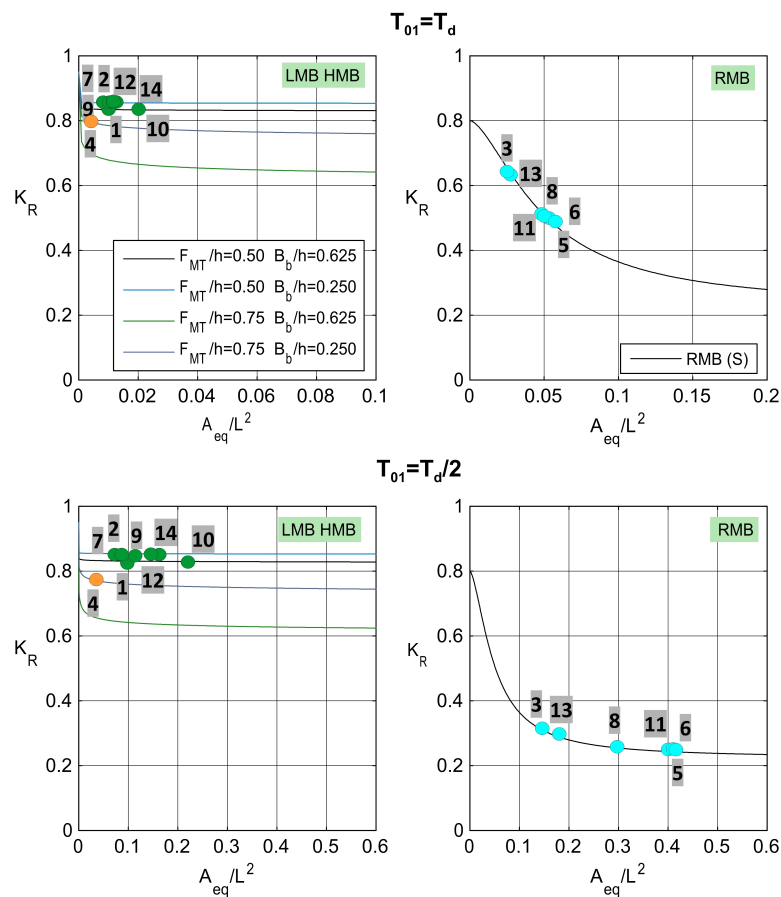


Figure 4.18.: Location of the Spanish breakwaters on the fitted curves for the analysed breakwater typologies. A_{eq}/L^2 obtained: a) for the design period, T_d (upper graphs); b) for a time period equal to $0.5T_d$ (lower graphs).

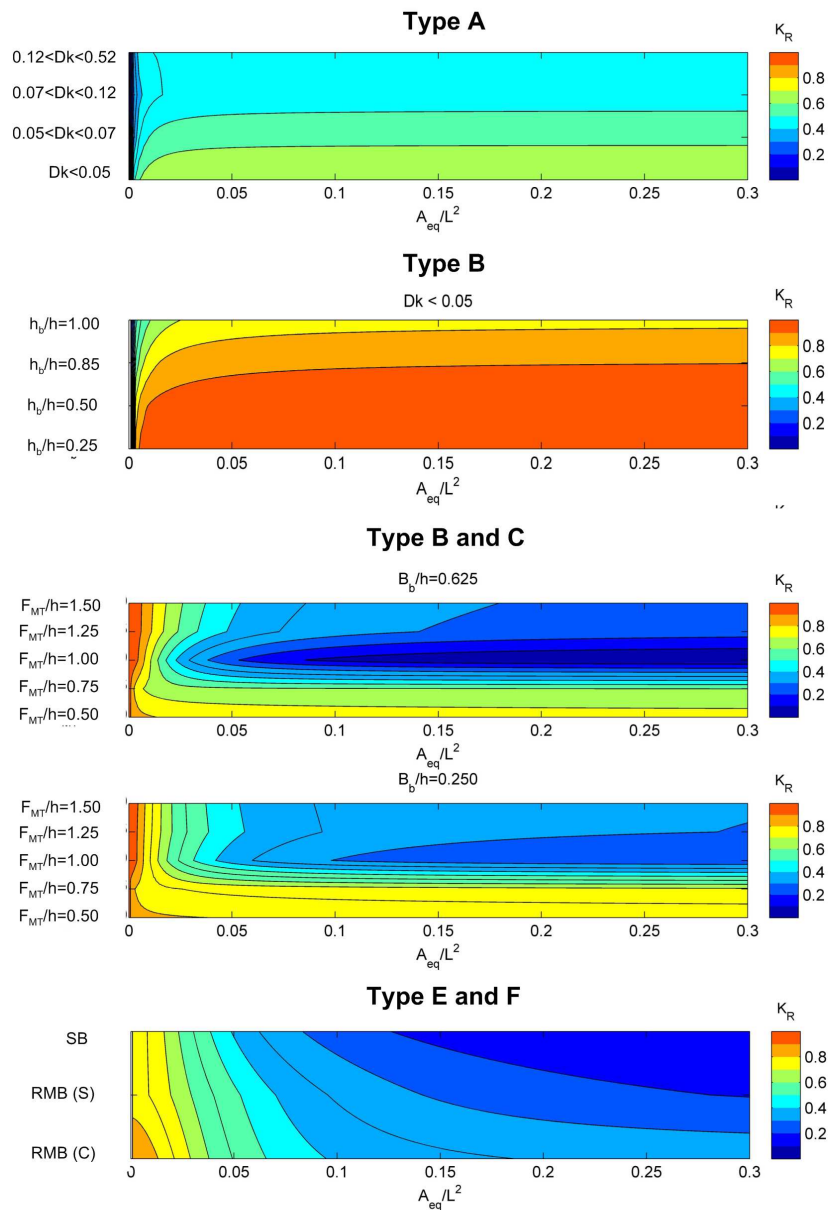


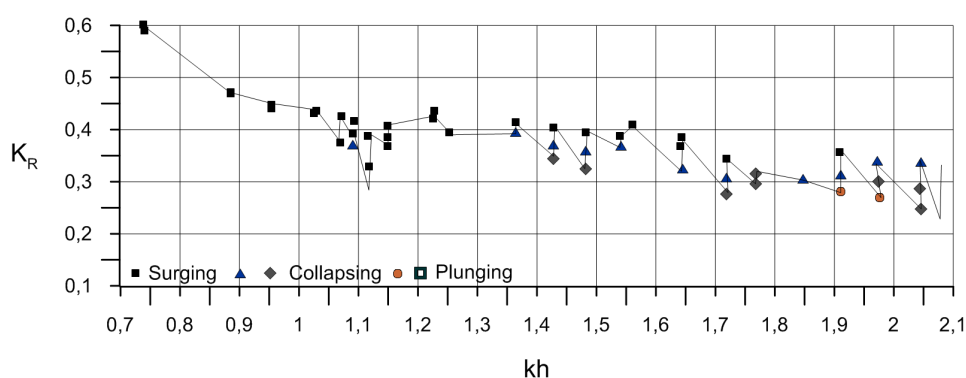
Figure 4.19.: Contour lines of K_R for the different breakwater types, depending on the parameter list.

4.4 Discussion and limitations of the hydraulic performance curves

Despite the large number of experimental tests and the wide range of breakwater types covered, the results of this study also have limitations stemming from the theoretical background applied to analyse the results. Some of these limitations are succinctly addressed in what follows.

All of the breakwater experiments were performed with the same slope gradient, $\cot\alpha_T = 1.5$. It is well known that the reflection coefficient is only dependent on Ir when the main wave transformation is due to wave breaking by plunging and spilling, generally speaking, when $Ir < 1.5$. Indeed, it can be assumed that in this range, the modulus of the reflection coefficient linearly increases with

Ir (Losada, 1990). For larger values of Ir , wave reflection becomes the dominant process of wave transformation. As shown in this research, under such conditions, other parameters play a major role in controlling wave-structure interaction. When $Ir < 1.5$ and $1.5 < \cot\alpha_T < 2.0$, the incident wave steepness $H_I/L_0 \leq (\tan\alpha_T/Ir)^2$ is physically limited by generation or by wave instability. As reflected in the results of previous work, for large values of A_{eq}/L^2 , when the slope is modified within the previously mentioned interval, a small variation in the value of K_{R0} should be expected. This can be observed in figure 4.20 (taken from Benedicto, 2004) which shows how the reflection coefficient modulus varies with the relative depth (for a given breakwater typology and constant depth, it is equivalent to parameter A_{eq}/L^2) for different types of wave breaking calculated with the Iribarren number. The experiments were performed on an RMB (core) breakwater impinged by regular waves. Consequently for the analysis of the hydraulic performance of a slope breakwater, the information obtained with the slope $\cot\alpha_T = 1.5$ is valid for milder slopes, possibly up to $\cot\alpha_T < 2.5$. It should be highlighted that because of costs and construction-related considerations, the majority of breakwaters designed for harbor protection have steep slopes $1.3 < \cot\alpha_T < 2.0$.



1981). van Gent (2014) confirmed this result in their analysis of mound breakwater stability under oblique wave attack. This limitation cannot be too restrictive because the main alignment of the breakwater should be oriented parallel to the design wave crests. In addition, perpendicular incidence provides the highest expected value of the reflection coefficients.

This study was carried out on non-overtoppable breakwaters. Nevertheless, generally speaking, breakwaters in port installations are designed so as not to be overtoppable. For this reason, the study of their interaction with incident waves is a necessity in practical engineering. Furthermore, it is well known that overtopping should be significant for it to affect the reflection coefficient (van der Meer et al., 2005).

4.5 Conclusions

After the analysis of the hydraulic performance of different breakwater types, the following conclusions can be derived:

- 1 The complex wave reflection and transmission coefficients as well as the overall dissipation rate caused by the structure are engineering quantities that can be used to evaluate the hydraulic performance of common typologies of non-overtoppable breakwaters typologies. The data confirm that the variation of those coefficients (as well as the energy dissipation rate) depends on the dimensions and properties of the parts and elements of the breakwater as well as on the wave characteristics.
- 2 In this paper, the logistic sigmoid function (Churchill and Usagi, 1972) has been found to define the domain of the hydraulic performance of the most common breakwaters. It relates the modulus and phase of the reflection coefficient, the modulus of the transmission coefficient and the overall energy dissipation rate to the non-dimensional parameters that represent the breakwater geometry, construction materials, and the incoming irregular wave train. It provides smooth performance transitions between different breakwater types and discriminates the full spectrum of wave oscillatory regimes resulting from wind wave-structure interaction.
- 3 It is shown that the principal variable of the sigmoid function is the 2D scattering parameter A_{eq}/L^2 , where A_{eq} is the area of a porous medium under the mean water level and L is the wavelength. The curve is defined by the following four parameters: Y_0 , Y_1 , a_X , and γ .
- 4 Two behavior regions can be distinguished: (i) the transition region (TR), and (ii) the transmission, decay and stabilization region (DR).
 - **Reflection coefficient behavior:** For types A and B a sigmoid curve has been defined to represent the variation of the coefficient in the two regions. K_{R1} and K_{R0} are associated with the minimum and maximum values of the reflection coefficient respectively. The value of K_{R1} defines the breakwater response when the transmission process is dominant. It is usually associated with large wave periods (largest wavelengths) and the smallest wave steepness. On the other hand, K_{R0} , determines the reflection coefficient when the reflection coefficient tends to be large. Generally speaking it is associated with short wave periods (shortest wavelengths) and the largest wave steepness. For types C, D, E and F the reflection, transmission and energy dissipation rate vary essentially in DR. In this case, K_{R1} and K_{R0} are associated with the maximum and minimum values of the

reflection coefficient respectively. The value of K_{R1} defines the breakwater response when the reflection process is dominant and K_{R0} determines the reflection coefficient when the energy dissipation rate tend to be larger.

- **Transmission coefficient behavior:** For all breakwater types, the wave transmission decreases with A_{eq}/L^2 . For large A_{eq}/L^2 , $K_{T0} \rightarrow 0$, whereas for $A_{eq}/L^2 \rightarrow 0$, K_{T1} must fulfil the energy conservation equation and can be approximated by means of $K_{T1}^2 \sim 1 - K_{R1}^2$.
- **Reflection phase behavior:** The dimensionless phase of the reflection coefficient, x_0/L follows the same pattern as the modulus. $(x_0/L)_1$ and $(x_0/L)_0$ are associated with the minimum and maximum values of the non-dimensional phase.

5 Parameters K_{R1} , K_{R0} , a_X and γ depend on the non-dimensional parameters of the parameter list which define the breakwater typology, the relative grain size of the porous medium, Dk , and others non-dimensional parameters representing the breakwater geometry.

Numerical quantification of the hydraulic performance

This chapter develops a method for numerically calculating the hydraulic performance in the analysed breakwater typologies. For this purpose, a characteristic friction diagram was obtained to evaluate the wave transformation inside the porous medium. The friction diagram is based on a linear coefficient that is constant for the whole porous medium volume and stationary in the wave cycle. It was calibrated by minimizing the error in the hydraulic performance between experimental measurements and numerical calculations (IH-2VOF numerical model).

5.1 Introduction

The sigmoid curves obtained in the previous chapter to evaluate the hydraulic performance of a breakwater can be defined with a reduced number of data. These are usually obtained testing scale models physically in a laboratory. However, numerical models are being increasingly used in last years to solve this type of problems because of its computing power and versatility. Since most breakwaters are either partially or totally composed of granular material, the quality of the numerical results depends on correctly defining the wave transformation inside the porous medium.

The representation of the flow resistance forces inside the porous medium is generally based on the extended Darcy-Forchheimer equation:

$$F_{NL} = aun + bu|u|n^2 + c_A \frac{d(un)}{dt} \quad (5.1)$$

where u is the seepage velocity through the voids, which is related to the discharge velocity by means of the expression $u_d = un$ (where n is the porosity); and a , b , and c_A are local coefficients. This expression includes a linear term, which represents a Darcy's type of flow for a laminar flow behavior, a non-linear term, which considers the turbulent flow characteristics, and an inertial term that accounts for the added mass effect due to transient effects (Polubarinova-Kochina, 1962). The added mass defines the extra momentum needed to accelerate the same volume of water in a porous medium (van Gent, 1995). Since the inertial term represents the effect of the porous medium on the acceleration of the fluid, it is usually combined with the acceleration term in the Navier-Stokes equations as it was seen in equation 3.2. Accordingly, the flow resistance forces equation can be written as following:

$$F_{NL} = aun + bu|u|n^2 \quad (5.2)$$

Several approaches to determine the Darcy-Forchheimer coefficients can be found in literature. Ward (1964) established coefficients in term of porosity, turbulent friction, and the intrinsic permeability. However, the preferred formula for a uniform porous medium is based on porosity and fluid viscosity (Hannoura and Barends, 1981; Smith, 1990). Following Ergun (1952) and Engelund (1953), Burcharth and Andersen (1995) analyzed these coefficients and established their relationship with the flow conditions for different hydraulic regimes. They proposed analytical expressions to calculate a and b :

$$a = \alpha \frac{\nu(1-n)^2}{n^3 D} \quad (5.3)$$

$$b = \beta \frac{1-n}{n^3 D} \quad (5.4)$$

α and β are two empirical parameters and ν is the kinematic viscosity. van Gent (1995) developed a model based on the Navier-Stokes equations, which expressed the coefficients as a function of porosity, diameter, and the Keulegan-Carpenter number. Most of numerical models based on the Volume-Averaged/Reynolds Averaged Navier-Stokes equations (VARANS) include the Darcy-Forchheimer equation to evaluate the flow in the porous medium. In this context, it is necessary to calibrate the coefficient values based on laboratory data (see Liu et al., 1999; Hsu et al., 2002; Losada et al., 2008; del Jesus et al., 2012; Jensen et al., 2014; Higuera et al., 2014).

Despite the previously mentioned research, the problem of the flow in a porous medium has not been definitively solved. Forchheimer coefficients have to be chosen depending on breakwater typology, materials characteristics and flow conditions. However, different authors have proposed different coefficients for the same wave and breakwater conditions (see table 5.1). Therefore, there is not any demonstrate robust method to properly select the coefficients in the resistive forces.

The main objective of this chapter was to propose a method that provides a reliable use of a numerical model based on VARANS equations (e.g. the IH-2VOF model) to quantify the hydraulic performance of the different breakwater types. This method is based on a characteristic friction diagram that uses a linear approximation to calculate the friction forces inside a porous medium. It was obtained by minimizing the error between the wave reflection coefficient (modulus and phase) and the transmission coefficient, obtained experimentally (section 3.1), and calculated numerically with the IH-2VOF numerical model (section 3.2).

5.2 Methodology

To apply a VARANS model such as IH-2VOF (Lara et al., 2008) values of the Forchheimer coefficients must be chosen. Sollitt and Cross (1972) simplified the Forchheimer equation terms (equation 5.1) with a linear expression (equation 5.5) and proposed to determine the linear coefficient, f_r , using Lorentz's hypothesis of equivalent work.

$$F_L = f_r \sigma u \quad (5.5)$$

f_r is a non-dimensional linear friction coefficient and σ is the angular frequency ($\sigma = 2\pi/T$). In this case the mean period, T_{01} , was used. The role of the friction coefficient is to represent the wave transformation in the porous medium, which determines the hydraulic performance due to the wind wave-breakwater interaction. Depending on its value, the structure becomes

Authors	Breakwater typology	Porous medium characteristics	Reynold number	Forchheimer coefficients	
				α	β
Engelund (1953)	-	Sands	Low Re_p	1500	3.6
van Gent (1995)	Permeable vertical breakwater	5 types of rock-spheres; $D=0.02-0.06$ m; $n = 0.388 - 0.476$	5000-66000	1000	$1.1 \left[1 + \frac{7.5}{KC_p} \right]$
		Round rock $D_{85}/D_{15}=1.4$	< 2100 – 8050	10000	2.2
Burcharth and Andersen (1995)	-	Semi-round rock $D_{85}/D_{15}=1.9$	800-2100	3000	2.7
		Irregular rock $D_{85}/D_{15}=1.4-1.8$	600-10300	1400-13000	2.4-3
		Crushed rocks $D=0.016$ m; $n=0.49$	F.T.F	1000	1.1
Liu et al. (1999)	Permeable vertical breakwater	Uniform glass beads $D=0.03$ m; $n=0.39$	100	200	1.1
Garcia et al. (2004)	Rubble-mound low-crested breakwater	Gravel core $n=0.49$	M.T.F	1000	1.2
		External layer (Gravel) $n=0.39$	M.T.F	1000	0.8
Lara et al. (2008)	Low mound breakwater	Gravel foundation $D=0.035$ cm; $n=0.48$	M.T.F	200	0.8
		External layer (Gravel) $D=3.5$ cm; $n=0.50$	M.T.F	200	1.1
Losada et al. (2008)	Rubble mound breakwater	Gravel core $D=0.01$ m; $n=0.48$	M.T.F	200	0.8
		External layer (Gravel) $D=0.035$ m; $n=0.50$	M.T.F	200	1.1
		External layer (Gravel) $D=0.135$ m; $n=0.50$	M.T.F	200	0.7
Lara et al. (2011)	Porous underwater step	$D=0.0307$ m; $n=0.4$	-	985.89	2.45
Lara et al. (2012)	Permeable vertical breakwater	Gravel $D=0.0083$ m; $n=0.43$	M.T.F $Re_p=1000$	10000	3
		Crushed stones $D=0.0159$ cm; $n=0.49$	325	10000	3
del Jesus et al. (2012)	Porous dam (Lin, 1998)	Glass beads $D=0.003$ cm; $n=0.39$	9.6	700	0.5
		Crushed rock $D=0.0159$ m $n=0.49$	M.T.F	1000	3
Higuera et al. (2014)	Rubble mound breakwater (Guanche et al., 2009)	Primary armor layer $D=0.12$ m $n=0.50$	M.T.F	5000	2
		Secondary layer $D=0.035$ m $n=0.49$	M.T.F	5000	3
		Core $D=0.01$ m $n=0.53$	M.T.F	5000	1
	Vertical porous breakwater (Lara et al., 2012)	$D=0.015$ m $n=0.51$	M.T.F	20000	1.5
Jensen et al. (2014)	Permeable vertical breakwater	Spherical glass beads (S.G.B) $D=0.002$ m $n=0.34$	$Re_p=62$	500	2
		S.G.B. $D=0.016$ m $n=0.49$	$Re_p=325$	500	2
		S.G.B. $D=0.025$ m $n=0.41$	$Re_p=2750$	500	2

Table 5.1.: Overview of Forchheimer equation coefficients. M.T.F = Mainly turbulent flow; F.T.F = Fully turbulent flow.

almost full reflective with phase zero or π (f_r very large) or the wave propagates almost without transformation (f_r close to zero). The main advantage of this approach is that the flow inside the porous medium can be represented by only one coefficient, which is stationary in the wave cycle and constant inside the porous medium. This theory has been used previously to solve various types of coastal engineering problems (Madsen and White, 1976; Dalrymple et al., 1991; Losada et al., 1993b). It has been also experimentally validated by various authors (Losada et al., 1995; Scarcella et al., 2006; Pérez-Romero et al., 2009).

In this study, a characteristic linear friction coefficient (f_c) was obtained for different breakwater typologies. This was achieved by minimizing the error in the comparison between the hydraulic performance, obtained experimentally and calculated numerically. Experimental data were detailed in section 3.1. Numerical results were calculated with IH-2VOF (section 3.2). The friction forces (F_G , equation 3.2) were modeled by the linearized expression (equation 5.5) in terms of the friction coefficient, f_r . Range of numerical simulations are described below.

The characteristic friction coefficient of each experiment was determined as follows (figure 5.1):

- 1 Reflection coefficient, K_R , transmission coefficient, K_T , and phase, ϕ , were obtained numerically for different values of the friction coefficient, $f_r = [f_{r1}, ..f_{rj} \dots f_{rn}]$.
- 2 The error for K_R , K_T and ϕ was calculated with equation 5.6 for each f_{rj} values by comparison between experimental (*exp*) and numerical (*num*) data.

$$\varepsilon_i(f_{rj}) = \sqrt{\frac{(Y_{inum}(f_{rj}) - Y_{iexp})^2}{Y_{iexp}^2}} \quad i = K_R, K_T, \phi \quad (5.6)$$

- 3 A total error for each f_{rj} values was defined as the sum of the individual error obtained in step 2:

$$\varepsilon(f_{rj}) = \varepsilon_{K_R}(f_{rj}) + \varepsilon_{K_T}(f_{rj}) + \varepsilon_{\phi}(f_{rj}) \quad (5.7)$$

- 4 The characteristic friction coefficient, f_c , was obtained as the one which produces the minimum value of the total error, $\varepsilon(f_{rj})$.
- 5 Once the characteristic friction coefficient was obtained, an additional check of the consistency and robustness of the applied method was done by comparing the experimental and numerical wave energy dissipation rate. It was evaluated from the energy conservation equation 2.10.

Numerical simulations

The numerical simulations were designed to cover the whole range of parameters defined in section 3.1. Simulated cases are shown in table 5.2, where $H_{I_{steo}}$ and $T_{p_{teo}}$ are target wave values used in laboratory, significant incident wave height and peak period respectively. However, the simulated wave data in each case correspond to laboratory measurements. Results were obtained for the typologies shown in the table. Results for the rest of typologies can be determined by interpolation.

Numerical wave gauges were placed in the same location as the ones used in the physical experiments. The methodology used to obtain the wave reflection (modulus and phase) and transmission coefficients was the same followed for the experimental analysis. Wave dissipation rate was also calculated using equation 2.1.

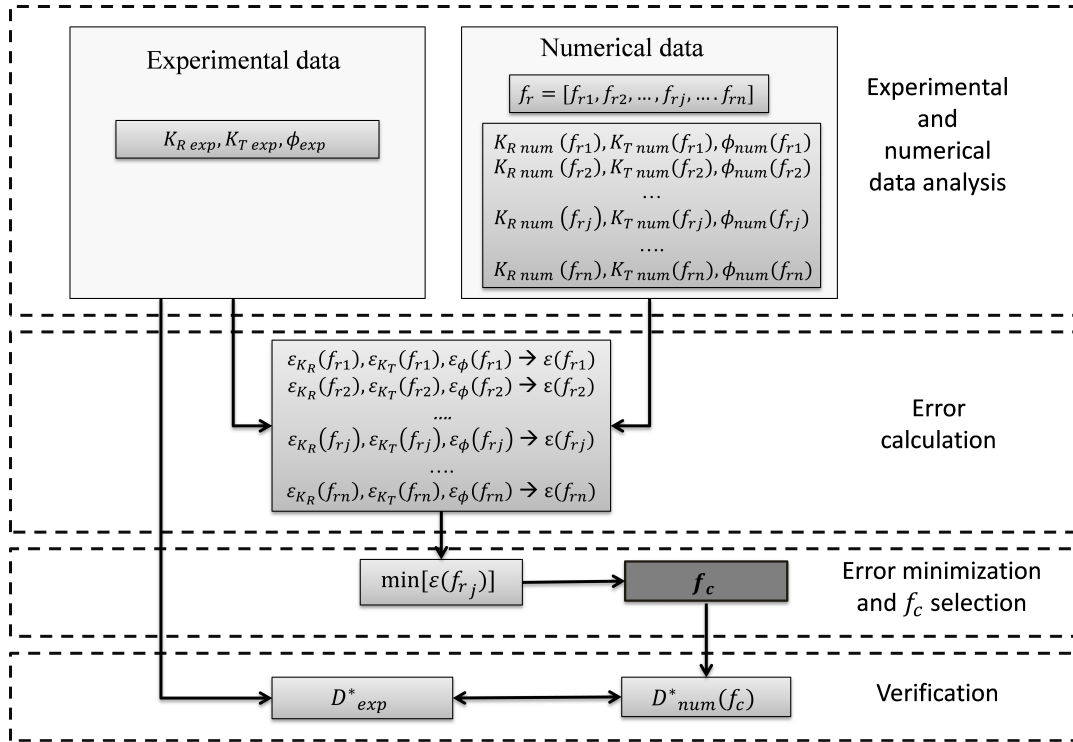


Figure 5.1.: Methodology for the friction coefficient calibration.

Type	$B(m)$	$h_b(m)$	$F_{MT}(m)$	$B_b(m)$	$cot\alpha_T$	$D(m)$	$H_{I_s\ teo}$	$T_{p\ teo}$
A	PVB	0.14	-	-	-	12	0.04	1.05
		0.50	-	-	-	40, 110	0.04	1.05, 3.00
		0.14	0.10, 0.20, 0.40	-	-	12, 40	0.04	1.05, 3.00
		B	CB	0.10	-	-	-	12, 40
0.50	-			-	-	52	0.04	1.05, 1.50
		0.20, 0.40	-	-	-	12, 40	0.04	1.05, 2.50
			-	-	-	110	0.04	1.05, 1.50
			0.10	1.5	-	12	0.04	1.05, 2.00, 2.50
					-	40	0.04	1.05, 1.50, 2.00, 2.50
C	LMB	0.50	0.20	0.20	-	12	0.04	1.05, 1.75, 2.50
					0.25	1.5	0.06	1.05, 2.50
					40	0.04	1.05, 1.50, 1.75	
					-	-	0.06	1.05
					0.10	1.5	0.04	1.50
					0.25	1.5	0.04	1.05, 2.50
					40	0.04	1.05, 2.50	
					-	-	0.04	1.05
					0.10	1.5	0.04	1.05, 1.50
					0.25	1.5	0.04	1.05, 2.00, 2.50
D	RMB-CW	0.50	0.20	0.60	-	12	0.04	1.05
					0.25	1.5	0.06	1.05, 2.50
					40	0.04	1.05, 1.50, 1.75	
					-	-	0.06	1.05
					-	0.04,	2.50	
					-	-	0.05	
E	RMB	-	-	0.68	0.19	1.5	7	0.03, 2
								0.04,
								0.05

Table 5.2.: Target parameters for simulated cases.

5.3 Results

Figure 5.2 presents the characteristic friction diagram. It shows the value of f_c against Dk for different breakwater typologies. The best fitting curves to obtain the value of f_c are also included. These curves correspond to a potential function as follows:

$$f_c = \lambda_1(Dk)^{\lambda_2} \quad (5.8)$$

For each breakwater typology, coefficients λ_1 and λ_2 for the best fitting curve and the upper and lower 95% confidence bounds are listed in table 5.3. They depends on the geometric characteristics of the breakwater, h_b/h , B_b/h and F_{MT}/h . This dependence is analysed in this section. Furthermore, the influence of the incident wave steepness is studied.

Next, it is shown the comparison between the experimental reflection (modulus and phase) and transmission coefficients and those calculated with the numerical model using the optimum friction coefficient, f_c . The experimental and numerical wave energy dissipation rate are also presented.

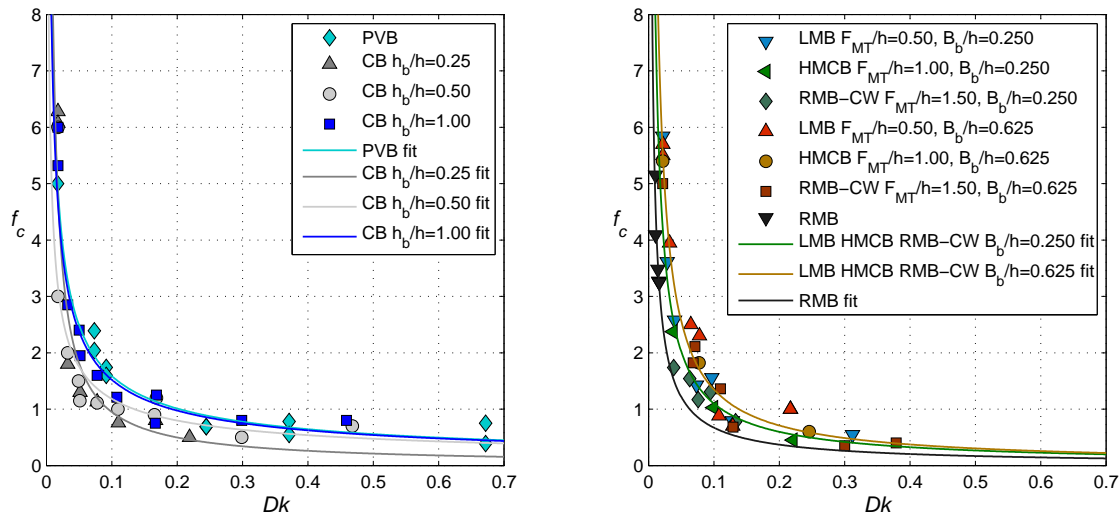


Figure 5.2.: Friction coefficient diagram.

Typology	Fit curve	$f = \lambda_1(Dk)^{\lambda_2}$					
		Best fitting curve		Upper 95% conf. bound		Lower 95% conf. bound	
		λ_1	λ_2	λ_1	λ_2	λ_1	λ_2
PVB (Type A)		0.535	-0.650	0.486	-0.800	0.260	-0.450
CB (Type B)	$h_b/h = 0.25$	0.111	-0.932	0.253	-1.210	0.049	-0.653
	$h_b/h = 0.50$	0.320	-0.568	0.574	-0.782	0.179	-0.354
	$h_b/h = 1.00$	0.348	-0.643	0.518	-0.790	0.232	-0.495
LMB, HMxCB and RMB-CW (Type C and D)	$B_b/h = 0.250$	0.145	-0.790	0.225	-1.042	0.094	-0.717
	$B_b/h = 0.625$	0.160	-0.927	0.231	-1.066	0.111	-0.788
RMB (Type E)		0.093	-0.860	* More information is needed			

Table 5.3.: Characteristic friction coefficient fits.

5.3.1 Dependence on Dk and breakwater typology

The left panel of figure 5.2 shows data for PVB (type A) and CB (type B), which have no berm or protection slope. The right panel shows data for LMB and HMCB (type C), RMB-CW (type D) and RMB (type E). The same trend is observed for the different breakwater typologies. The diagram indicates that the friction coefficient mainly depends on the non-dimensional parameter, Dk , which decreases exponentially as the friction coefficient increases. Three different regions can be observed from the results, bounded by the intervals $Dk < 0.05$, $0.05 < Dk < 0.25$ and $Dk > 0.25$. The first interval shows the highest friction coefficients. When Dk tend to zero the characteristic friction coefficient grows rapidly and the wave reflection dominates to the wave transmission, independently of the breakwater typology. That yields that fluid flow reaches very low Reynolds numbers and the porous medium behaves like an almost impermeable media. However, results shown in the second interval are strongly influenced by Dk . Friction clearly decreases when Dk increases. Results within the third interval show an almost constant friction value, revealing a clear influence of the breakwater geometry on the hydrodynamics.

5.3.2 Dependence on breakwater geometry

For each breakwater typology, figure 5.2 also shows the influence of other non-dimensional parameters on the f_c value related to the breakwater geometry. In the case of the CB, the friction coefficient experiences a slight increase as the relative submergence of the breakwater, h_b/h , increases. In the case of berm breakwaters, the relative height of the berm does not have a significant impact on the value of f_c , though an increase in the relative width, B_b/h , produces a slight increase in the friction coefficient.

5.3.3 Dependence on wave characteristics

Figure 5.3 shows the influence of the wave steepness, $H_{I_{rms}}/L$, on f_c . It presents the value of f_c obtained for the LMB and RMB-CW, with $B_b/h=0.625$ and for two different wave steepness intervals. The best-fit to results for these breakwater typologies is also plotted. As can be observed, the wave steepness does not significantly affect the value of the friction coefficient.

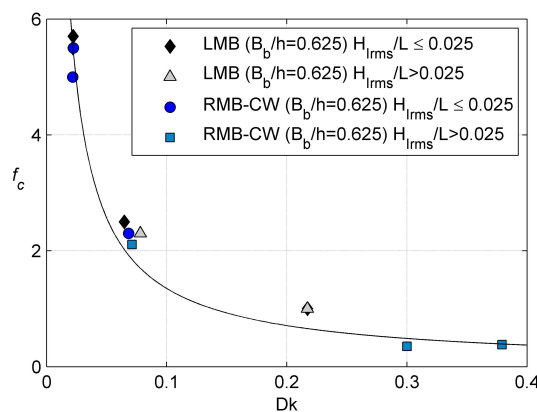


Figure 5.3.: Influence of the wave steepness on the friction coefficient.

5.3.4 Comparison of the experimental and numerical hydraulic performance

Figure 5.4 compares the experimental and numerical data of the coefficients of wave reflection (modulus and phase) and transmission obtained for the characteristic friction coefficient. The goodness between experimental and numerical data has been also included through the determination coefficient (equation 4.3). For all cases the value of R^2 is larger than 0.92. Moreover, the experimental and numerical wave energy dissipation rate is shown in figure 5.5 with a value of R^2 greater than 0.95. Generally speaking, the comparison is quite satisfactory.

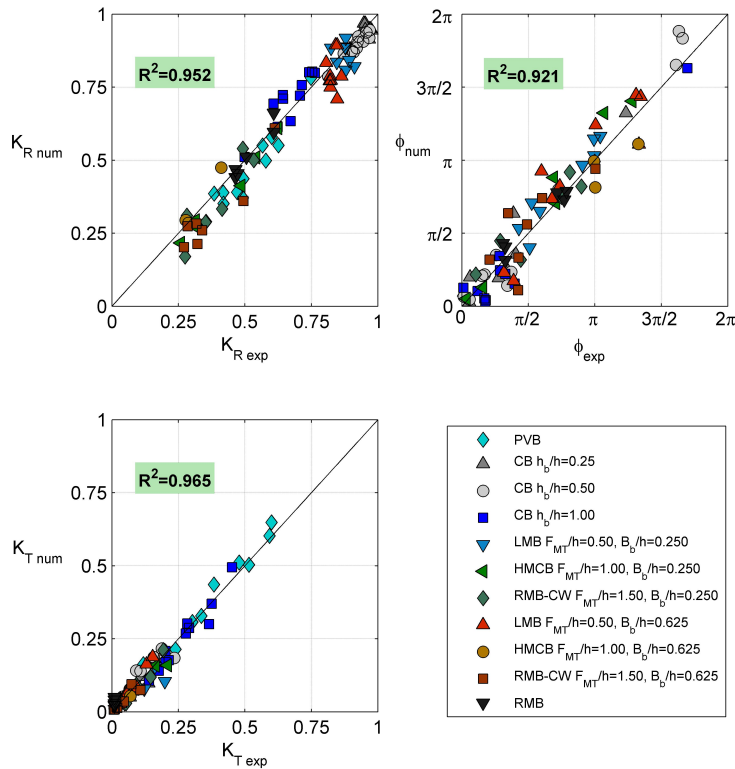


Figure 5.4.: Experimental versus numerical K_R , K_T and ϕ for the breakwater typologies.

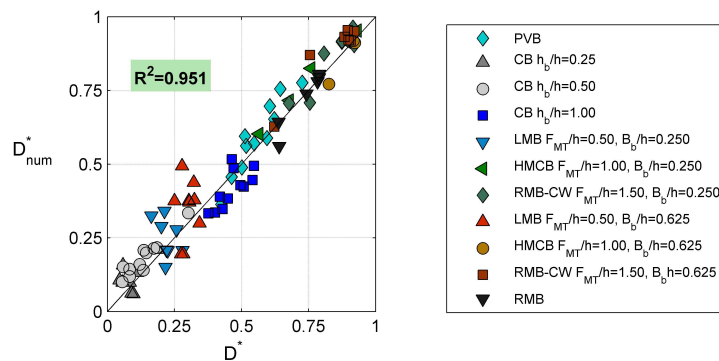


Figure 5.5.: Experimental versus numerical D^* for the breakwater typologies.

5.3.5 Importance of the phase in the friction forces

Figure 5.6 shows an example of the total error variation for different f_r values in a LMB ($F_{MT}/h=0.50$) with $B_b=0.25$ m, $D=40$ mm, and wave conditions of $H_{Is}=0.031$ m and $T_p=1.12$ s. The green triangles show the total error, taking into account both the modulus and phase of the wave reflection coefficient and the modulus of the transmission coefficient. In contrast, the red circles show the total error without including the error in the phase. In the first case, $f_r=1$ provides the minimum error with similar experimental and numerical values of K_R , K_T , and ϕ (figure 5.7). In the second case, $f_r=1.4$ induced the minimum error with very similar experimental and numerical values of K_R , and K_T . However, the corresponding experimental and numerical phases are different, $\phi_{exp}=4.12$ rad and $\phi_{num}=0.28$ rad, respectively (figure 5.7). Notice the importance of including the phase of the reflection coefficient in friction coefficient calibration. The accurate selection of this coefficient is essential for correctly calculating the hydraulic performance and for evaluating the localization of nodes and anti-nodes in front of the structure (Hughes and Fowler, 1995).

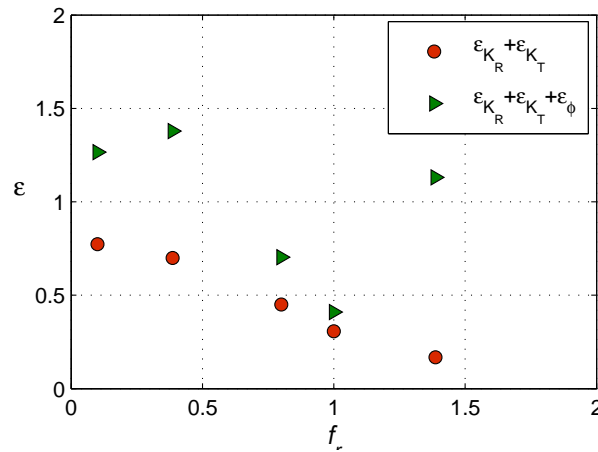


Figure 5.6.: Mean square error, depending on the friction coefficient of the LMB ($F_{MT}/h = 0.50$) with $B_b=0.25$ m, $D=40$ mm, $H_{Is}=0.031$ m and $T_p=1.12$ s.

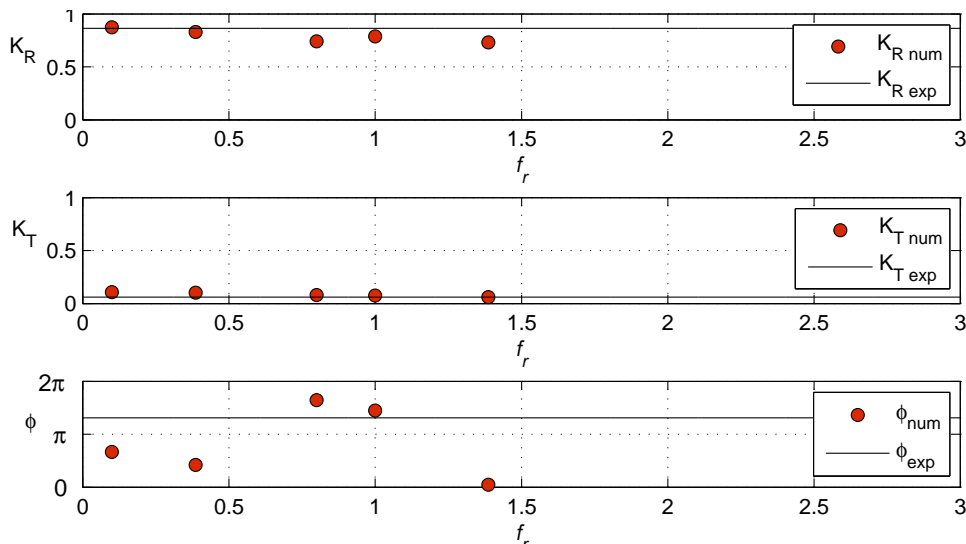


Figure 5.7.: Comparison between the numerical and experimental values of K_R , K_T and ϕ , depending on the f_r of the LMB ($F_{MT}/h = 0.50$) with $B_b=0.25$ m, $D=40$ mm, $H_{Is}=0.031$ m and $T_p=1.12$ s.

5.4 Example to obtain the hydraulic performance by numerical modelling

A RMB-CW breakwater is designed for a depth of $h=16$ m with the following geometric characteristics:

$$B=20 \text{ m}; h_b=8 \text{ m}; F_c=12 \text{ m}; D=0.48 \text{ m}; \cot\alpha_T=1.5; F_{MT}=24 \text{ m}; B_b=4 \text{ m}.$$

The values of Y_i (where i denotes wave reflection, modulus and phase, and transmission coefficients) is calculated in four points, two asymptotic values, $Y_{i,1}$ and $Y_{i,2}$ and two center values in the intermediate region $Y_{i,21}$ and $Y_{i,22}$.

Firstly, the set of wave parameters is defined. In this case, $H_{I_{rms}}$ varies between 1.5 and 3.5 m whereas T_{01} oscillate between 6 and 12 s. Next, a value of $A_{eq}=608 \text{ m}^2$ is obtained. Regarding the geometric characteristics of the breakwater and the sea states, the rest of the non-dimensional parameters are determined for every point (table 5.4). The friction coefficient has been calculated with the friction diagram (table 5.3), based on Dk .

Point	$H_{I_{rms}}$	T_{01}	$H_{I_{rms}}/L$	A_{eq}/L^2	Dk	B_b/h	f_c	n
Y_{i0}	1.5	12	0.0108	0.0314	0.0217	0.25	4.22	0.478
Y_{i21}	3.5	10	0.0313	0.0487	0.0270	0.25	3.48	0.478
Y_{i22}	3.5	7.5	0.0460	0.1049	0.0396	0.25	2.27	0.478
Y_{i1}	3.5	6.0	0.0653	0.2114	0.0562	0.25	1.83	0.478

Table 5.4.: Non-dimensional parameters.

K_R , K_T , D^* , and the non-dimensional phase, x_0/L , are calculated with the numerical model IH-2VOF (table 5.5).

Point	K_R	K_T	x_0/L	D^*
Y_{i0}	0.510	0.044	0.228	0.738
Y_{i21}	0.409	0.035	0.432	0.832
Y_{i22}	0.195	0.040	1.868	0.961
Y_{i1}	0.164	0.023	2.169	0.973

Table 5.5.: Value of the coefficients of reflection (modulus and phase), transmission, and dissipation.

Finally, following the methodology proposed in chapter 4, the best fit parameters of the sigmoid functions have been obtained and listed in table 5.6. The numerical data and the theoretical curves are shown in figure 5.8. The energy dissipation rate are also included.

Fit parameters	K_R	K_T	x_0/L
γ_i	3.901	0.118	0.084
a_i	0.063	1.674	4.090

Table 5.6.: Fit parameters of the sigmoid equation.

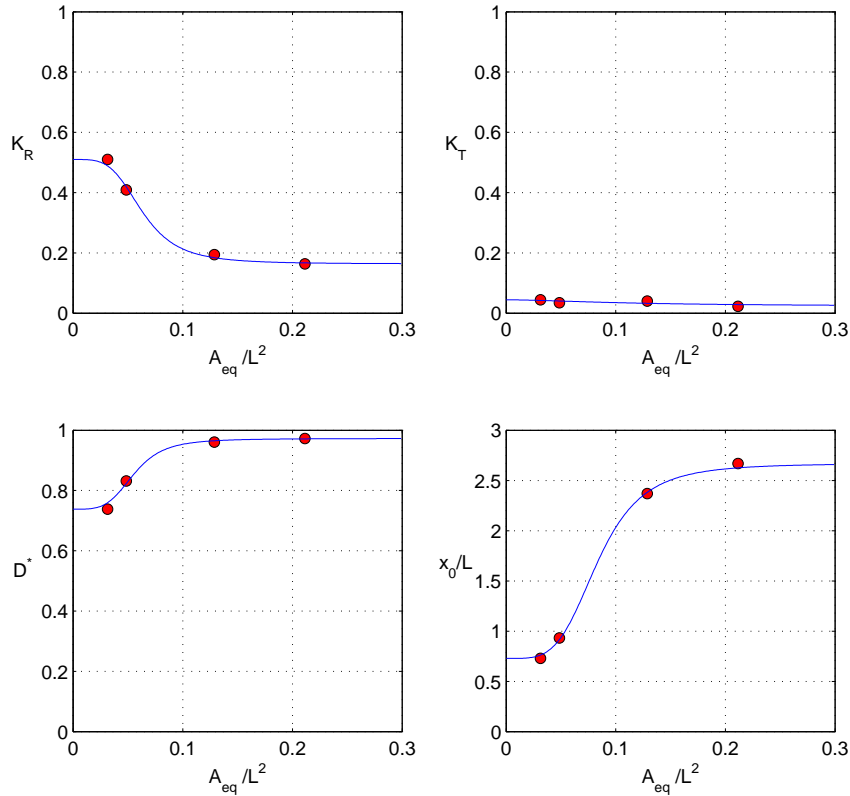


Figure 5.8.: Hydraulic performance curves obtained numerically.

5.5 Conclusions

A method has been developed to calculate numerically the hydraulic performance of different breakwater types. For this purpose, a characteristic friction diagram for evaluating the wave transformation inside the porous medium has been obtained. The diagram is based on a characteristic friction coefficient, f_c , that is constant in space and stationary in the wave cycle. The main conclusions that can be derived from this results are the following:

- 1 Results showed that even for breakwater typologies in which the dissipation in the porous medium is only a small percentage of the total dissipation resulting from the wave-structure interaction, the accurate evaluation of the friction forces in the porous medium is a determining factor in the calculation of the hydraulic performance.
- 2 The characteristic friction coefficient depends on the following parameters:
 - The breakwater typology and the granular material characteristics, mainly of the non-dimensional parameter, Dk . For all typologies a similar trend is observed and three

regions can be distinguish: 1) a first region ($Dk < 0.05$) in which the characteristic friction coefficient decreases rapidly with Dk and the dependence with the breakwater geometry is minimum; 2) a second interval ($0.05 < Dk < 0.25$) where the coefficient is strongly influenced by Dk ; and 3) a third region ($Dk > 0.25$) with an almost constant value of the characteristic friction coefficient depending on the breakwater geometry.

- The geometric characteristics of the breakwater also influence the value of f_c although to a lesser extent. The characteristic friction coefficient increases with the relative foundation depth, h_b/h , and the relative berm with, B_b/h . However, the relative berm height, F_{MT}/h , does not have a significant impact on the value of f_c .
- The wave steepness has not a significant influence in the value of f_c .
- RMB typology shows the same trend that the other typologies, but a wider range of Dk would be necessary to confirm this behavior.

3 The experimental and numerical total dissipation fit fairly well. This confirms that the IH-2VOF is able to accurately evaluate the hydraulic performance applying the characteristic friction coefficient to represent the friction forces in the porous medium. This simple engineering method can improve the efficiency of numerical modeling in combination with laboratory tests and semi-empirical formulations, thus reducing costs and saving time in the breakwater pre-design stage.

An approximation to the statistical behavior of wind waves in front and on the face of the breakwater

In this chapter, the statistical behavior of the total wave height, H_t , resulting from the interaction of wind waves and different breakwaters is analysed. Two regions were studied: 1) in front of the breakwater and 2) at the face of the breakwater. The results confirm that the probability density function of H_t correspond to a Rayleigh distribution in front of the breakwater and, from the toe of the structure to the toe of the crown, it evolves to a Weibull distribution. The scale parameter of this distribution can be calculated in terms of the root mean square value of H_t . An approximation to calculate this value has been proposed using the modulus and phase of the reflection coefficient as given by the logistic sigmoid function (chapter 4). The results show good agreement with the experimental data.

6.1 Introduction

The prediction of the characteristics of wave height and water velocity in front of breakwaters and other coastal structures is crucial for their design, construction and maintenance. Depending on their typology, breakwaters reflect, dissipate, transmit, and radiate incident wave energy and partial standing wave patterns are thus likely to occur in front of them as it has been seen in section 4. To calculate flow characteristics (e.g. run-up, run-down, overtopping, etc.), and the structural response of the different breakwater sections and elements, an in-depth understanding of wave-structure interaction is required.

In maritime engineering problems it is often assumed that the statistical behavior of wind waves is a stationary random process, and that the local water surface elevation, η_t , is normally distributed. However, depending on the hydraulic performance of different types of breakwater and the large number of processes involved in wave-structure interaction, the validity of these assumptions is subject to reasonable doubt. Wave nonlinearities, correlation between successive waves, wave reflection, and wave energy dissipation by friction and breaking, among other things, can cause the probability density function of the water surface displacement to depart from a Gaussian distribution.

Longuet-Higgins (1952) first applied Rice's theory (Rice, 1944) to ocean (progressive) waves under the hypothesis of a narrow-band spectrum with component frequencies concentrated around a central frequency, f_0 . Under such conditions, the resulting variation of η_t corresponds to a regular sinusoid, whose random amplitude (envelope) and phase slowly vary in comparison to the central frequency wave. Assuming that η_t has a Gaussian distribution or that the phase is uniformly

distributed, since one condition implies the other (Rice, 1944), the wave amplitude can be shown to follow a Rayleigh distribution, where the parameter is the zeroth spectral moment, m_0 , which is equal to variance of η_t .

The height of each wave is nearly twice its amplitude, and in all likelihood, is also Rayleigh distributed. Moreover, the variance of η_t may be expressed as the average of integrals taken over each wave. This results in a relationship between the root-mean-square wave height, H_{rms} , the variance of η_t , and the zeroth spectral moment. Any of these is a suitable parameter that can be used to characterize the Rayleigh probability function of the individual wave heights. The underlying premise is that the individual wave heights are independent.

Cartwright and Longuet-Higgins (1956) derived the theoretical distribution of the wave amplitude for a broad wave spectrum. Longuet-Higgins (1963) analyzed the effects of wave nonlinearities on the probability distribution of η_t and concluded that under such conditions and for breaking waves, the Gaussian assumption of η_t is not realistic.

Baquerizo et al. (1997) and Baquerizo and Losada (1999) studied the wave height-to-depth ratio in front of reflective coastal structures, including the effects of wave reflection and dissipation by wave breaking. For non-breaking waves, the water surface displacement is the result of the superposition of two Gaussian random variables, namely, the incident and the reflected wave trains. It is thus also Gaussian distributed. Accordingly, for waves with a narrow band spectrum, the peaks or amplitudes and the wave heights are Rayleigh distributed. The parameter is the root-mean-square wave height of the total wave train (incident and the reflected wave trains), H_{trms} , given by:

$$H_{trms} = H_{IRms} \sqrt{1 + K_{*R}^2 + 2K_{*R} \rho_{IR}} \quad (6.1)$$

where $-1 \leq \rho_{IR} \leq 1$ is the correlation coefficient between both series, $\rho_{IR} = \cos(2kx + \phi_*)$, which depends on the phase lag between each component of the incident wave train and the corresponding reflected component; H_{IRms} is the root-mean-square incident wave height; and K_{*R} is the module of the local reflection coefficient such that K_{*R}^2 is the ratio of seaward to shoreward propagating wave energy, and ϕ_* the local phase lag. $k^* = 2\pi/L^*$ is the wave number, where L^* is the wave length of a characteristic wave period of the train, and x is the horizontal distance to the coastline. For breaking waves the Gaussian model is not strictly applicable, and as a result, the distribution of peaks, amplitudes, wave height, and the wave height-to-depth ratio, H/h , depart from a Rayleigh distribution. Based on experiments under non-negligible short-wave reflective conditions, Baquerizo and Losada (1999) showed that the local wave height-to-depth ratio follows a bi-parametric Weibull distribution, where the scale parameter can be expressed in terms of the root-mean-square of the total wave height (equation 6.1). The shape parameter, β_w , indicates the departure of the probability density function (pdf) from the Rayleigh distribution, and is a kind of spreading factor that increases as the wave height decreases by breaking or friction, that is, as the water surface displacement smooths out. $\beta_w = 1$ corresponds to an exponential distribution, and $\beta_w = 2$ to a Rayleigh distribution. The analysis was based on Supertank experiments (Kraus et al., 1992) of swell waves propagating along monotonic, barred, and terraced reflective beach profiles.

Battjes and Groenendijk (2000) analyzed the wave height distribution on shallow foreshores and proposed a model distribution consisting of a Rayleigh distribution for the lower wave heights, and a Weibull distribution with a higher exponent for higher wave heights. The parameters of this distribution were estimated from laboratory data of wave heights on shallow foreshores of different impermeable slopes, and expressed in terms of local wave energy, depth and bottom slope.

This result seems to confirm the evolution of the Rayleigh distribution to a Weibull distribution, depending on the wave transformation in the neighborhood of coastal structures and coastal zones. Yu et al. (2014) also studied the statistical behavior of the wave height in front of and propagating over a mild slope, and concluded that it obeys the Rayleigh distribution at the offshore location, whereas in the surf zone, the wave height distribution can be approximate by the composite Weibull distribution.

Losada et al. (1997a) used linear wave theory to calculate the evolution of the total spectrum (incident and reflected wave trains) in front of a vertical permeable and impermeable coastal structure on a horizontal bottom. Seaward of the vertical dissipative structure, the total spectrum contains nodal and antinodal frequencies resulting from the interaction of incident and reflected components. The distance between the two adjacent nodal frequencies decreases with movement offshore, and depends on the incoming wave train, breakwater geometry, and the characteristics of the porous material. For long-crested random waves, the zero-order momentum of the total wave field has upper and lower limits at the front face of the vertical structure and moving off the structure. Klopman and van der Meer (1999) obtained a similar spatial evolution of the spectrum in front of a vertical impermeable wall with a foreland (sloping bottom).

Summarising, although there might be some support for the validity of the Gaussian assumption at a certain location in front of the breakwater, once the wave propagates through and onto the breakwater, the occurrence of friction and wave breaking weakens this hypothesis.

To clarify the statistical behavior of water waves in the proximity of breakwaters, this chapter addressed the following questions:

- 1 Whether the water surface elevation in front and at the toe of the structure has a Gaussian distribution.
- 2 Whether the wave height in this same area follows a Rayleigh distribution in which the parameter is the variance of the local water surface displacement.
- 3 Whether the statistical behavior of the wave height depends on the hydraulic performance of the breakwater, and if so, what is the nature of this dependence.
- 4 Whether the statistical behavior of the wave height on the breakwater face changes and, if so, in what way.
- 5 Finally, whether the Weibull distribution provide an accurate description of the total wave height on the breakwater face.

6.2 An approximation to the pdf of the linear superposition of incident and reflected narrow-banded wave trains

A train of long-crested waves was considered impinging perpendicularly onto a breakwater, which is the only source of the reflected wave train. The origin of the coordinates (see figure 6.1) is set at the toe of the breakwater at the still water level (S.W.L.) with the cross-breakwater coordinate, x ,

positive seawards and the vertical axis pointing upwards. Offshore from the breakwater, the water depth is constant. The instantaneous free surface elevation at any location in front of the coastal structure, $\eta_t(x, t)$, is the result of the linear superposition of the incident and reflected wave trains denoted by $\eta_I(x, t)$ and $\eta_R(x, t)$, respectively.

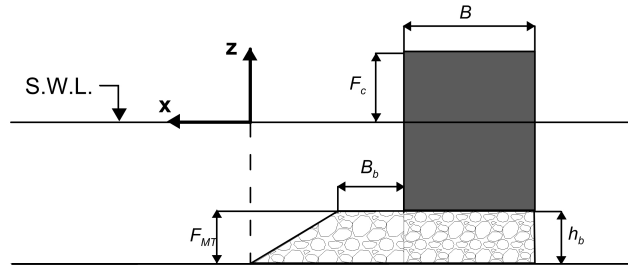


Figure 6.1.: Definition sketch.

6.2.1 Wave height pdf in front of and at the toe of the breakwater

The incident and reflected wave trains are assumed to be both narrow-banded Gaussian processes with a zero mean. In the framework of linear wave theory, their component frequencies are concentrated over a narrow range around the same central representative frequency, f_0 . Consequently, the variation of η_I , η_R and η_t corresponds to a regular sinusoid with a slowly varying envelope and phase, and the individual waves in each wave train have almost the same period but gradually varying amplitudes.

The local root-mean-square wave height based on the variance of the instantaneous free surface elevation is given by the following equation (Baquerizo et al., 1997):

$$\overline{\eta_t^2} = \overline{(\eta_I + \eta_R)^2} = \overline{\eta_I^2} + \overline{\eta_R^2} + 2\overline{\eta_I\eta_R} \quad (6.2)$$

where the overbar denotes time averaging, and $(\overline{\eta_I\eta_R})$ represents the correlation between the incident, η_I , and reflected, η_R , waves. Although this term tends to zero far away from the breakwater, it is not negligible closer to the reflective structure. Consequently, for the purposes of this study this term had to be considered. Equation 6.2 can be written in terms of the root-mean-square wave heights of the wave trains:

$$H_{trms}^2 = H_{Itrms}^2 + H_{Rtrms}^2 + a\overline{\eta_I\eta_R} \quad (6.3)$$

H_{trms} , H_{Itrms} , and H_{Rtrms} are the root-mean-square wave height of the total, incident, and reflected wave fields, respectively. For a Gaussian and narrow-band process, the parameter $a = 16$.

The local wave spectrum in front of the breakwater, $S_t(f)$, is given by:

$$S_t(f, x) = F_t^2(f, x)S_I(f) \quad (6.4)$$

where

$$F_t^2(f, x) = 1 + K_R^2(f) + 2K_R(f) [\cos(2k(f)x + \phi(f))] \quad (6.5)$$

$F_t^2(f, x)$ is the modulus of the transfer function (Losada et al., 1997a). In equation 6.5, $K_R(f)$ and $\phi(f)$ are, respectively, the modulus and phase of the reflection coefficient for each of the frequency components f . $S_I(f)$ is the incident wave spectrum. The n th-order momentum for the wave spectrum is given by:

$$m_{nt}(x) = \int_0^{\infty} f^n S_t(f, x) df \quad (6.6)$$

Offshore from the breakwater, the zero-order momentum (m_0) with the horizontal sea bottom can be expressed as:

$$m_{0t}(x) = m_{0I} + m_{0R} + m_{0IR}(x) \quad (6.7)$$

where m_{0I} and m_{0R} correspond to the zero-order moment of the incident and reflected spectra, respectively:

$$m_{0I} = \int_0^{\infty} S_I(f) df \quad (6.8)$$

$$m_{0R} = \int_0^{\infty} K_R^2(f) S_I(f) df \quad (6.9)$$

and m_{0IR} can be calculated by using the equation:

$$m_{0IR}(x) = 2 \int_0^{\infty} K_R(f) [\cos(2k(f)x + \phi(f))] S_I(f) df \quad (6.10)$$

Following Rice (1944), any wave profile satisfying the previous assumptions can be expressed as follows:

$$\eta(t) = \sum_{n=1}^{\infty} A_n \cos(2\pi f_n t + \epsilon_n) = I_c^*(t) \cos(2\pi f_0 t) - I_s^* \sin(2\pi f_0 t) \quad (6.11)$$

where $I_c^*(t)$ and $I_s^*(t)$ are given by:

$$\begin{cases} I_c^*(t) = \sum_{n=1}^{\infty} A_n \cos(2\pi(f_n - f_0)t + \epsilon_n) \\ I_s^*(t) = \sum_{n=1}^{\infty} A_n \sin(2\pi(f_n - f_0)t + \epsilon_n) \end{cases} \quad (6.12)$$

The central frequency f_0 can be any representative frequency in the wave spectrum, where most of the energy is concentrated. Here, $f_0 = f_p$, the peak frequency.

The envelope amplitude $R_I(t)$ and phase angle $\varphi(t)$ can be defined in terms of $I_c^*(t)$ and $I_s^*(t)$:

$$\begin{cases} R_I = \sqrt{(I_c^*)^2 + (I_s^*)^2} \\ \varphi(t) = \tan^{-1} \left[\frac{I_s^*}{I_c^*} \right] \end{cases} \quad (6.13)$$

The wave profile is then given by:

$$\eta(t) = R_I(t) \cos[2\pi f_0 t + \varphi(t)] \quad (6.14)$$

Based on the characteristic modulus and phase of the reflection coefficient, denoted by K_R and ϕ , and associated with the representative frequency f_0 , a global transfer function is defined as follows:

$$F_{0t}^2(x) = [1 + K_R^2 + 2K_R \cos(2k_0x + \phi)] \quad (6.15)$$

and the zero-order moment of the total wave spectrum is given by:

$$\hat{m}_{0t}(x) = F_{0t}^2(x)m_{0I} \quad (6.16)$$

The symbol $\hat{}$ denotes the moment calculated with K_R and ϕ . It should be highlighted that in front of the breakwater, K_R and ϕ have constant values that depend on the breakwater typology and wave conditions.

Next, $I_c(t, x)$ and $I_s(t, x)$ are calculated in terms of $I_c^*(t)$ and $I_s^*(t)$, and then multiplied by the square root of the transfer function (equation 6.5):

$$\begin{cases} I_c(t, x) = [1 + K_R^2 + 2K_R \cos(2k_0x + \phi)]^{\frac{1}{2}} I_c^*(t) \\ I_s(t, x) = [1 + K_R^2 + 2K_R \cos(2k_0x + \phi)]^{\frac{1}{2}} I_s^*(t) \end{cases} \quad (6.17)$$

The amplitude $R_t(t, x)$ and the phase angle $\varphi_t(t)$ of the total wave train are given by:

$$\begin{aligned} R_t(t, x) &= \sqrt{I_c^2(t, x) + I_s^2(t, x)} \\ &= [1 + K_R^2 + 2K_R \cos(2k_0x + \phi)]^{\frac{1}{2}} \sqrt{(I_c^*)^2 + (I_s^*)^2} = F_{0t}(x)R_I(t) \end{aligned} \quad (6.18)$$

$$\varphi_t(t) = \varphi(t) = \text{atan} \left[\frac{I_s^*(t)}{I_c^*(t)} \right] \quad (6.19)$$

The total wave profile, $\eta_t(t, x)$, can then be written as follows:

$$\eta_t(t, x) = R_t(t, x) \cos [2\pi f_0 t + \varphi_t(t)] \quad (6.20)$$

If the incident wave train is a stationary Gaussian stochastic process that is represented by the amplitudes $I_c^*(t)$ and $I_s^*(t)$, the variances of the components of $R_t(t, x)$ are:

$$\begin{aligned} E[(I_c^*)^2] &= E[(I_s^*)^2] = E[\overline{\eta_I^2}] = m_{0I} \\ E[K_R^2(I_c^*)^2] &= E[K_R^2(I_s^*)^2] = E[\overline{\eta_R^2}] = \hat{m}_{0R} \\ E[K_R \cos(2k_0x + \phi)(I_c^*)^2] &= E[K_R \cos(2k_0x + \phi)(I_s^*)^2] = E[\overline{\eta_{IR}^2}] = \hat{m}_{0IR} \end{aligned} \quad (6.21)$$

and the total variance of $\eta_t(t, x)$ is equal to the total variance of the total water surface displacement at any point in front of the breakwater. From equation 6.21, the moment of the total wave surface in front of the breakwater follows as:

$$\hat{m}_{0t}(x) = m_{0I} + \hat{m}_{0R} + \hat{m}_{0IR}(x) \quad (6.22)$$

Considering that at any location x , $R_t(t, x)$ and $\varphi_t(t)$ are uncorrelated independent variables, the probability density function of $R_t(t, x)$ is given by:

$$p(R_t(x)) = \frac{R_t(x)}{m_{0t}(x)} \exp - \frac{R_t^2(x)}{2m_{0t}(x)} \quad (6.23)$$

Moreover, invoking the symmetry of the wave profile, the wave height of the total wave train in front of the breakwater, $H_t = 2R_t$, follows a Rayleigh distribution with parameter $H_{trms}(x) = \sqrt{8m_{0t}(x)}$,

$$p(H_t(x)) = \frac{2H_t(x)}{H_{trms}^2(x)} \exp - \frac{H_t^2(x)}{H_{trms}^2(x)} \quad (6.24)$$

which varies with the distance to the breakwater. The value of H_{trms} can be calculated from equation 6.22 as:

$$H_{trms}(x) = H_{Itrms} \sqrt{1 + K_R^2 + 2K_R \cos(2k_0x + \phi)} \quad (6.25)$$

6.2.2 Wave height pdf on the breakwater face

For locations on the breakwater face ($x < 0$), because of wave energy dissipation by friction and wave breaking, the probability density function of the total wave height should depart from the Rayleigh density function, and consequently, its behavior is better represented by a bi-parametric Weibull distribution (Baquerizo and Losada, 1999). The general expression of the probability density function of a bi-parametric Weibull distribution for a random variable, y , is:

$$p(y) = \frac{\beta_w}{\delta_w} \left(\frac{y}{\delta_w} \right)^{\beta_w - 1} \exp - \left(\frac{y}{\delta_w} \right)^{\beta_w} \quad (6.26)$$

In equation 6.26, δ_w and β_w are the scale and shape parameters, respectively. They depend on the breakwater typology and the specific location ($x < 0$) on the breakwater face under consideration. For the sake of convenience, this study calculated the scale parameter (δ_w) in terms of the root mean square of the total wave height at the toe of the breakwater: $\delta_w = \alpha_w H_{trms}(x = 0)$. Accordingly, equation 6.26 is expressed in terms of the total local wave height (incident and reflected wave trains) at the toe of the breakwater, $x = 0$:

$$p(H_t(x < 0)) = \frac{\beta_w}{\alpha_w H_{trms}(x = 0)} \left(\frac{H_t(x < 0)}{\alpha_w H_{trms}(x = 0)} \right)^{\beta_w - 1} \exp - \left(\frac{H_t(x < 0)}{\alpha_w H_{trms}(x = 0)} \right)^{\beta_w} \quad (6.27)$$

As shown, for $\alpha_w = 1$ and $\beta_w = 2$, equation 6.27 is the Rayleigh probability density function.

6.3 Data analysis

This study was done for breakwater type B, C and D. To address the analysis the following variables were taken into account (see section 3.1 for detail about data acquisition):

1. Instantaneous value of free surface elevations:

- $\eta_I(t)$ and $\eta_R(t)$, incident and reflected wave train. The incident and reflected wave trains were separated by applying Baquerizo (1995) to the data measured by gauges S1, S2, and S3.
- $\eta_t(t, x_i)$, total (incident and reflected) wave train in front of the breakwater. i represents the location of the measurements with $i=1, 2, 3$ and 4 for S4, S5, S6, and S7, respectively (figure 6.2).

2. Statistical parameters:

- $H_{I_{rms}}$, incident root-mean-square wave height obtained as $\sqrt{8m_{0I}}$.
- $H_{trms}(x_i)$, total root-mean-square wave height obtained at each i position as: $H_{trms}(x_i) = \sqrt{8m_{0t}(x_i)}$

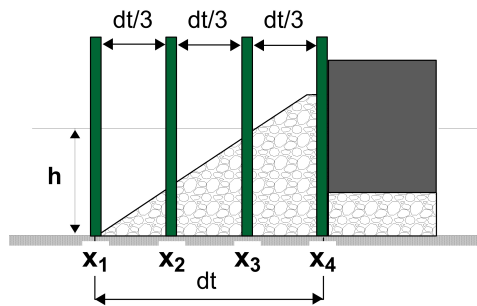


Figure 6.2.: Location of the wave gauges along the breakwater.

6.4 Results

6.4.1 Statistical behavior of the wave train in front of and at the toe of the breakwater

Figures 6.3-6.5 display the measured histogram of the non-dimensional total water surface displacement juxtaposed with the calculated histograms of the incident and reflected water surface displacements, and their linear superposition at the toe of the breakwater for:

- Type B (CB) with three different relative foundation depths, $h_b/h = 0.25, 0.50,$ and 1.00 ; $T_{p\ teo} = 2$ s, $H_{Is\ teo} = 0.04$ m, and $D = 40$ mm (figure 6.3).
- Type C (LMB, HMB, HMCB) with three different relative berm heights, $F_{MT}/h = 0.50, 0.75,$ and 1.00 ; $T_{p\ teo} = 2$ s, $H_{Is\ teo} = 0.04$ m, $D = 40$ mm, and $B_b/h = 0.625$ (figure 6.4).
- Type D (RMB-CW) with two different relative berm heights, $F_{MT}/h = 1.25$ and 1.50 ; $T_{p\ teo} = 2$ s, $H_{Is\ teo} = 0.04$ m, $D = 40$ mm, and $B_b/h = 0.625$ (figure 6.5).

The theoretical Gaussian probability density functions are included for comparison. The measured total free surface elevation histograms faithfully replicate major features of the Gaussian probability density functions. The data regarding the goodness of fit to the Gaussian distribution for all tests are shown in table 6.1 for type B and 6.2 for type C and D respectively. This was calculated by

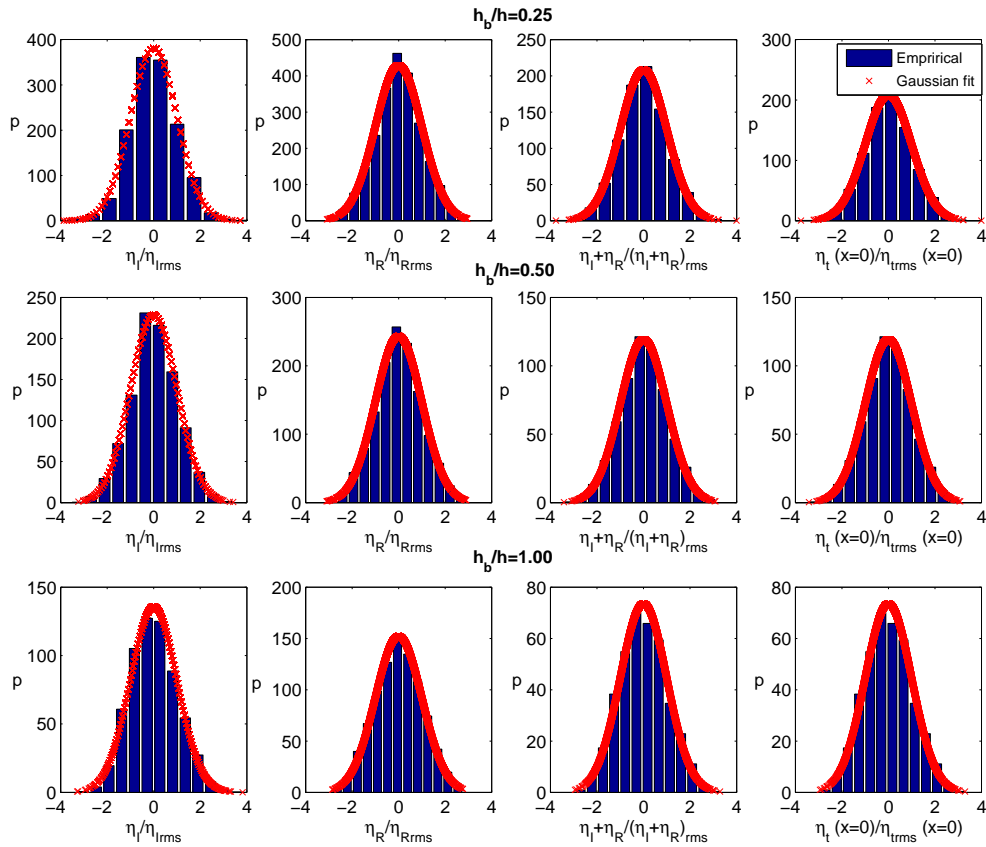


Figure 6.3.: Probability density function of the non-dimensional incident, reflected, and total (at the toe) free surface elevation obtained by the linear superposition of the incident and reflected wave trains and measured with gauge S4. Type B with three relative foundation depths, h_b/h , $T_{p\ teo} = 2$ s, $H_{Is\ teo} = 0.04$ m, $D = 40$ mm, and $B_b/h = 0.625$. Empirical and Gaussian fit.

means of the determination coefficient, R^2 (equation 4.3) and the standard deviation, σ_s . The subscripts, *emp* and *teo*, denote empirical and theoretical data, respectively. Thus, for engineering applications, it can be safely assumed that the total wave trains, measured and calculated, and the incident and reflected wave trains at the toe of the breakwater are Gaussian processes with a zero mean.

Figure 6.6 displays the measured histograms of the total wave height juxtaposed with the Rayleigh probability density function with parameter the root-mean-square wave height at the toe, $H_{trms}(x = 0)$, of the following types of breakwater:

- (a) Type B (CB) with three different relative foundation depths, $h_b/h = 0.25, 0.50, \text{ and } 1.00$; $T_{p\ teo} = 2$ s, $H_{Is\ teo} = 0.04$ m, and $D = 40$ mm.
- (b) Type C (LMB, HMB, HMCB) with three different relative berm heights, $F_{MT}/h = 0.50, 0.75, \text{ and } 1.00$; $T_{p\ teo} = 2$ s, $H_{Is\ teo} = 0.04$ m, $D = 40$ mm, and $B_b/h = 0.625$.
- (c) Type D (RMB-CW) with two different relative berm heights, $F_{MT}/h = 1.25 \text{ and } 1.50$; $T_{p\ teo} = 2$ s, $H_{Is\ teo} = 0.04$ m, $D = 40$ mm, and $B_b/h = 0.625$.

For all tests, the goodness of fit to the Rayleigh distribution is given in table 6.3. Again, it can be safely assumed that the total wave height in front of the breakwater is a random variable following a Rayleigh distribution in which the parameter is the root mean square of the total wave height.

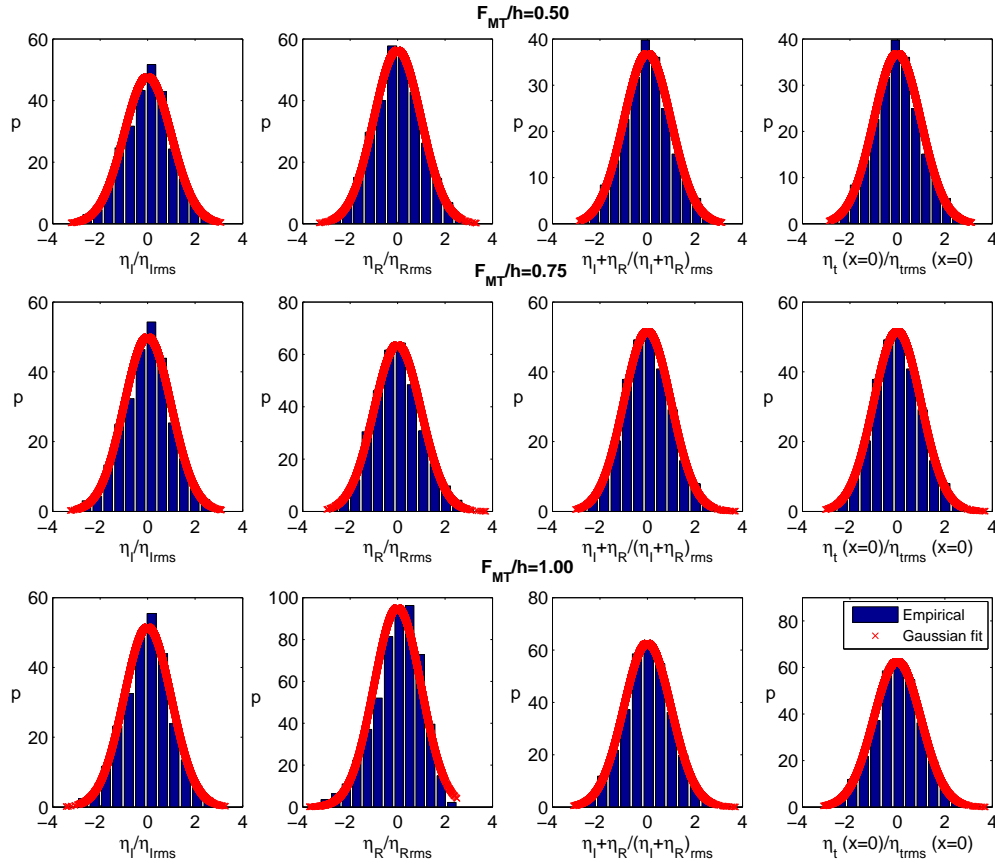


Figure 6.4.: Probability density function of the non-dimensional incident, reflected, and total (at the toe) free surface elevation obtained by the linear superposition of the incident and reflected wave train and measured with gauge S4. Type C with three relative berm heights, F_{MT}/h , $T_p \text{ teo} = 2$ s, $H_{Is \text{ teo}} = 0.04$ m, $D = 40$ mm, and $B_b/h = 0.625$. Empirical and Gaussian fit.

Type	h_b/h	Dk	η_I		η_R		$\eta_I + \eta_R$		η_t	
			R^2	σ_s	R^2	σ_s	R^2	σ_s	R^2	σ_s
B	0.25	$Dk < 0.05$	0.97	0.04	0.98	0.02	0.98	0.02	0.98	0.01
		$0.05 \leq Dk < 0.07$	0.98	0.02	0.98	0.01	0.99	0.02	0.98	0.01
		$0.07 \leq Dk < 0.12$	0.97	0.03	0.99	0.01	0.99	0.01	0.99	0.01
		$0.12 \leq Dk < 0.52$	0.97	0.03	0.99	0.01	0.99	0.01	0.98	0.01
B	0.50	$Dk < 0.05$	0.97	0.02	0.98	0.01	0.98	0.01	0.98	0.02
		$0.05 \leq Dk < 0.07$	0.98	0.01	0.99	0.01	0.99	0.01	0.98	0.02
		$0.07 \leq Dk < 0.12$	0.98	0.01	0.99	0.01	0.99	0.01	0.98	0.02
		$0.12 \leq Dk < 0.52$	0.99	0.01	0.99	0.01	0.99	0.01	0.98	0.01
B	1.00	$Dk < 0.05$	0.95	0.03	0.97	0.03	0.96	0.02	0.96	0.02
		$0.05 \leq Dk < 0.07$	0.95	0.03	0.98	0.02	0.97	0.02	0.96	0.02
		$0.07 \leq Dk < 0.12$	0.97	0.03	0.97	0.03	0.97	0.02	0.96	0.02
		$0.12 \leq Dk < 0.52$	0.97	0.11	0.97	0.12	0.97	0.12	0.95	0.12

Table 6.1.: Goodness of fit of the Gaussian distribution for the incident, reflected, and the measured and calculated total free surface elevation at the toe of the breakwater ($x=0$). Type B.

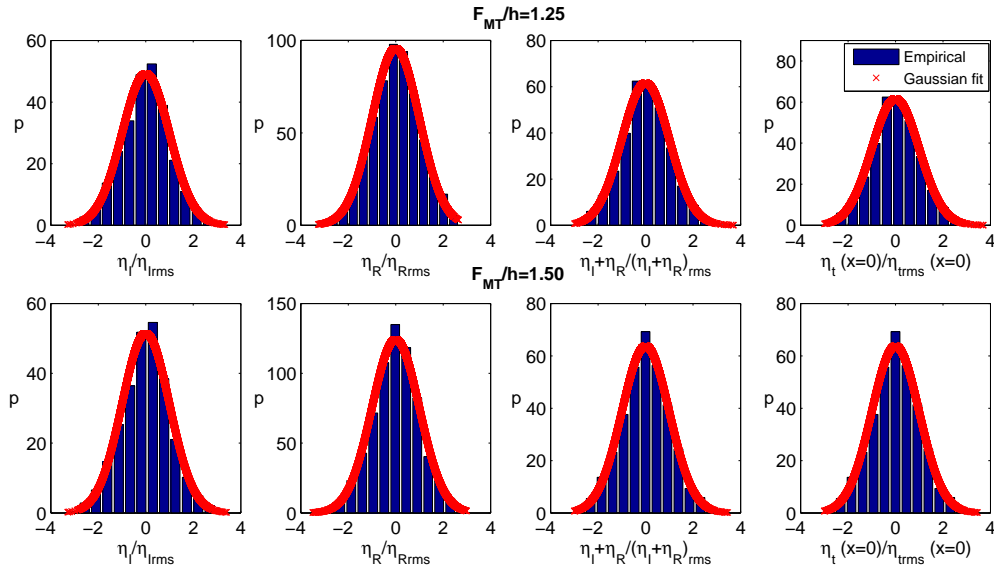


Figure 6.5.: Probability density function of the non-dimensional incident, reflected, and total (at the toe) free surface elevation obtained by the linear superposition of the incident and reflected wave train and measured with gauge S4. Type D with two relative berm heights, F_{MT}/h , $T_{p\ teo}=2$ s, $H_{Is\ teo}=0.04$ m, and $D=40$ mm. Empirical and Gaussian fit.

Type	B_b/h	F_{MT}/h	Dk	η_I		η_R		$\eta_I + \eta_R$		η_t	
				R^2	σ_s	R^2	σ_s	R^2	σ_s	R^2	σ_s
C	0.250	0.50	$Dk < 0.06$	0.99	0.01	0.99	0.01	0.99	0.01	0.99	0.01
			$Dk \geq 0.06$	0.99	0.01	0.99	0.01	0.99	0.01	0.99	0.01
		0.75	$Dk < 0.06$	0.99	0.01	0.99	0.01	0.98	0.01	0.99	0.01
			$Dk \geq 0.06$	0.99	0.01	0.99	0.01	0.99	0.01	0.99	0.01
	0.625	0.50	$Dk < 0.06$	0.99	0.01	0.99	0.01	0.98	0.01	0.99	0.01
			$Dk \geq 0.06$	0.99	0.01	0.99	0.01	0.99	0.01	0.99	0.01
		0.75	$Dk < 0.06$	0.99	0.01	0.99	0.01	0.98	0.01	0.99	0.01
			$Dk \geq 0.06$	0.99	0.01	0.98	0.01	0.99	0.01	0.99	0.01
D	0.250	1.25	$Dk < 0.06$	0.99	0.01	0.98	0.01	0.98	0.01	0.99	0.01
			$Dk \geq 0.06$	0.99	0.01	0.99	0.01	0.99	0.01	0.99	0.01
		1.50	$Dk < 0.06$	0.98	0.01	0.98	0.01	0.98	0.01	0.99	0.01
			$Dk \geq 0.06$	0.99	0.01	0.98	0.01	0.99	0.01	0.99	0.01
	0.625	1.25	$Dk < 0.06$	0.93	0.23	0.93	0.23	0.93	0.23	0.94	0.24
			$Dk \geq 0.06$	0.99	0.01	0.99	0.01	0.99	0.01	0.99	0.01
		1.50	$Dk < 0.06$	0.99	0.01	0.98	0.01	0.99	0.01	0.99	0.01
			$Dk \geq 0.06$	0.99	0.01	0.99	0.01	0.99	0.01	0.99	0.01

Table 6.2.: Goodness of fit of the Gaussian distribution for the incident, reflected, and the measured and calculated total free surface elevation at the toe of breakwater ($x=0$). Type C and D.

6.4.2 Statistical behavior of the total wave train on the breakwater face

Figure 6.7 displays the measured histograms of the total wave height at three positions along the breakwater slope (x_2 , x_3 , and x_4) juxtaposed with the theoretical bi-parametric Weibull probability

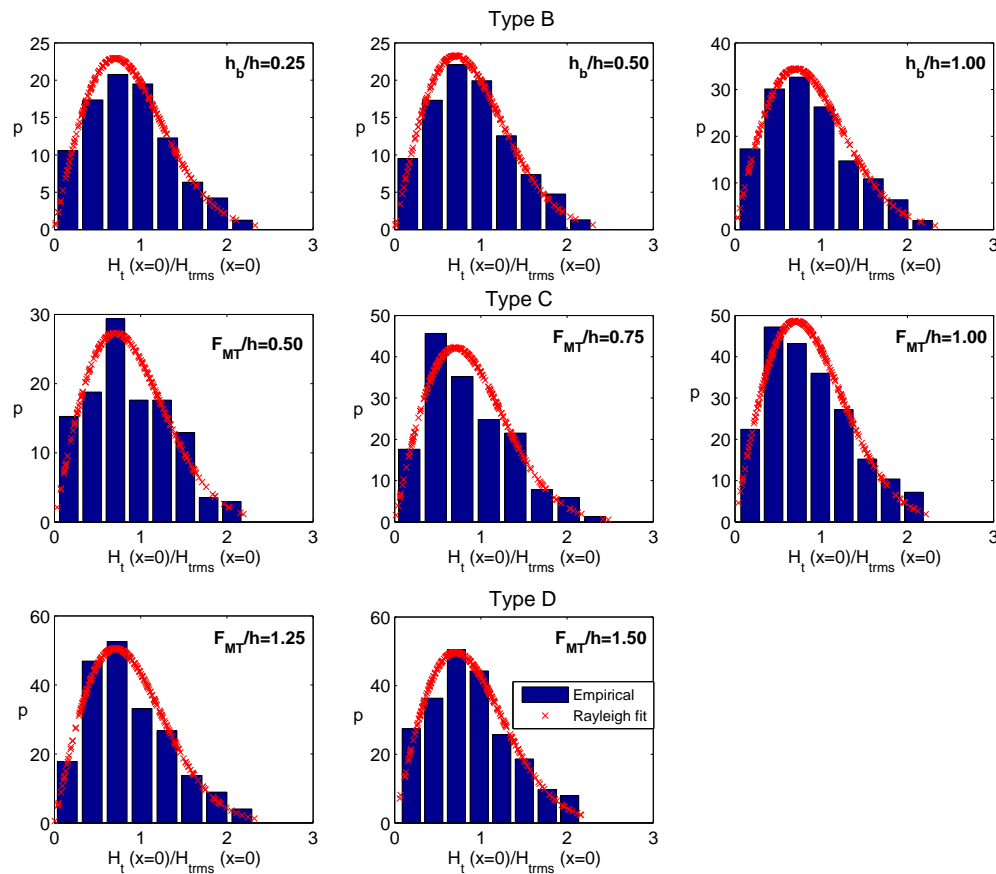


Figure 6.6.: Probability density function of the non-dimensional total wave height at the toe ($x=0$) for Type B (three relative foundation depths h_b/h), C (three relative berm heights, F_{MT}/h), and D (two relative berm heights, F_{MT}/h), $T_{p\ teo}=2$ s, $H_{I\ s\ teo}=0.04$ m, $D=40$ mm, and $B_b/h=0.625$. Empirical and theoretical fit (Rayleigh distribution).

density function (equation 6.27) for breakwater types, C and D. For purposes of comparison, the total wave height values at the toe of the breakwater ($x = x_1 = 0$) are included. The coefficients of the goodness of fit to the Weibull distribution at the three locations (x_2 , x_3 , and x_4) are given in table 6.4. The results show that the probability density function of the wave height in front of the breakwater face ($x < 0$) fits a bi-parametric Weibull function. For all breakwater types, the relative distance between the toe of the structure and the crown face is $dt/L < 1.12$. Shoreward of the toe, the wave-structure interaction evolves rapidly.

Type	h_b/h	Dk	R^2	σ_s	
B	0.25	$Dk < 0.05$	0.91	0.06	
		$0.05 \leq Dk < 0.07$	0.90	0.06	
		$0.07 \leq Dk < 0.12$	0.91	0.05	
		$0.12 \leq Dk < 0.52$	0.92	0.06	
	0.50	$Dk < 0.05$	0.91	0.06	
		$0.05 \leq Dk < 0.07$	0.89	0.07	
		$0.07 \leq Dk < 0.12$	0.91	0.06	
		$0.12 \leq Dk < 0.52$	0.91	0.06	
	1.00	$Dk < 0.05$	0.86	0.09	
		$0.05 \leq Dk < 0.07$	0.85	0.11	
		$0.07 \leq Dk < 0.12$	0.91	0.08	
		$0.12 \leq Dk < 0.52$	0.88	0.14	
Type	B_b/h	F_{MT}/h	Dk	R^2	σ_s
C	0.50	0.50	$Dk < 0.06$	0.88	0.08
			$Dk \geq 0.06$	0.89	0.06
	0.250	0.75	$Dk < 0.06$	0.90	0.05
			$Dk \geq 0.06$	0.93	0.04
	1.00	1.00	$Dk < 0.06$	0.93	0.03
			$Dk \geq 0.06$	0.92	0.07
	0.625	0.50	$Dk < 0.06$	0.90	0.07
			$Dk \geq 0.06$	0.90	0.06
		0.75	$Dk < 0.06$	0.90	0.06
			$Dk \geq 0.06$	0.92	0.05
	1.00	0.75	$Dk < 0.06$	0.88	0.18
			$Dk \geq 0.06$	0.88	0.17
1.25		$Dk < 0.06$	0.90	0.08	
		$Dk \geq 0.06$	0.94	0.06	
0.250	1.50	$Dk < 0.06$	0.89	0.10	
		$Dk \geq 0.06$	0.92	0.06	
	1.25	$Dk < 0.06$	0.83	0.23	
		$Dk \geq 0.06$	0.93	0.04	
0.625	1.50	$Dk < 0.06$	0.90	0.08	
		$Dk \geq 0.06$	0.89	0.07	

Table 6.3.: Goodness of fit coefficients to the Rayleigh distribution for the empirical probability density function of the total wave height at the toe of the breakwater. Types B, C, and D.

Regarding the different breakwater types, figure 6.8 and figure 6.9 show the variation of Weibull parameters, α_w and β_w , on the breakwater face (x_1, x_2, x_3) as a function of k_0h , for three relative berm heights (F_{MT}/h), two ranges of the incident wave steepness ($H_{I_{rms}}/L$), $Dk < 0.06$, and relative berm width, $B_b/h = 0.250$. k_0 is the wave number at the toe of the breakwater (x_1). As shown, the value of β_w remains almost constant with k_0h , having an approximate value of 2 for LMB and HMB at all locations. In contrast, it increases with k_0h for HMCB and RMB-CW ($F_{MT}/h \geq 1$), growing with the distance to the breakwater toe.

For all breakwater typologies, α_w depends slightly on k_0h at x_1 , and this dependence strengthens with movement off the toe up the wall. As k_0h increases, α_w also increases until it achieves a maximum value for k_0h closer to 0.75. This maximum value depends on the wave breaking type, and the largest one was obtained for $F_{MT}/h=1.00$. Furthermore, α_w and β_w weakly depend on the incident wave steepness.

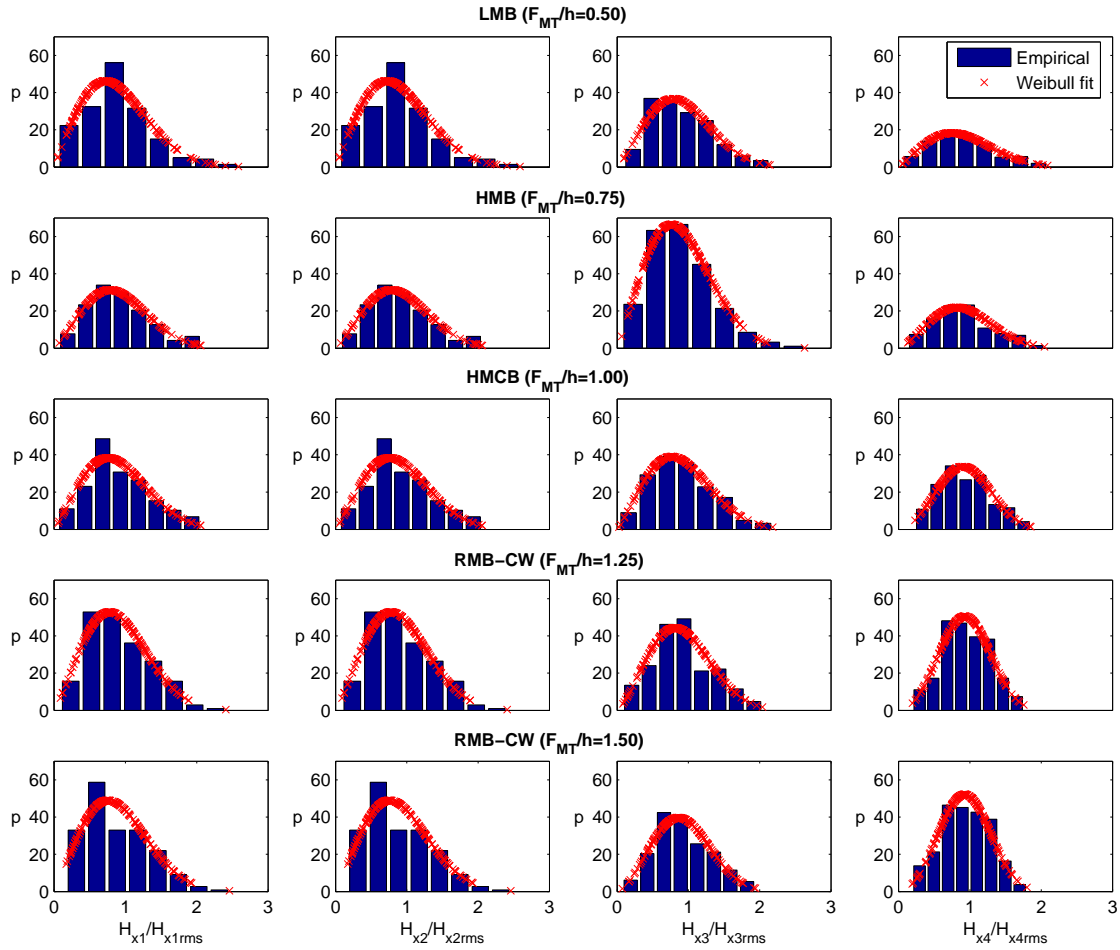


Figure 6.7.: Probability density function of the non-dimensional total wave height in different positions along the breakwater slope (x_1 , x_2 , x_3 , and x_4) for type C and D. $T_{p\ teo}=1.05$ s, $H_{I\ s\ teo}=0.04$ m, $D=40$ mm, and $B_b/h=0.625$. Empirical and theoretical fit (Weibull distribution).

Best fit curves for α_w and β_w at each location and for different breakwater typologies are also shown in figure 6.8 and figure 6.9. They are calculated as follows:

$$\beta_w = b_{\beta 1}(k_0 h)^2 + b_{\beta 2}(k_0 h) + b_{\beta 3} \quad (6.28)$$

$$\alpha_w = a_{\alpha 1}(k_0 h)^2 + a_{\alpha 2}(k_0 h) + a_{\alpha 3} \quad (6.29)$$

Values of the fit parameters are presented in tables 6.5-6.7 for all the tests. Notice that coefficients $(a_{\alpha 1}, a_{\alpha 2}, a_{\alpha 3}, b_{\beta 1}, b_{\beta 2}, b_{\beta 3}) = f(F_{MT}/h, B_b/h, Dk, x)$.

6.4.3 Calculation of the pdf of the total wave height at the toe and on the face of a given breakwater type

To estimate the pdf of the total wave height at the toe of a given breakwater ($x = 0$), it is necessary to have the root mean square of the total wave height, H_{trms} . Given the incident root-mean-square wave height $H_{I\ rms}$ and a representative wave period (single-peaked wave spectrum with period T_p),

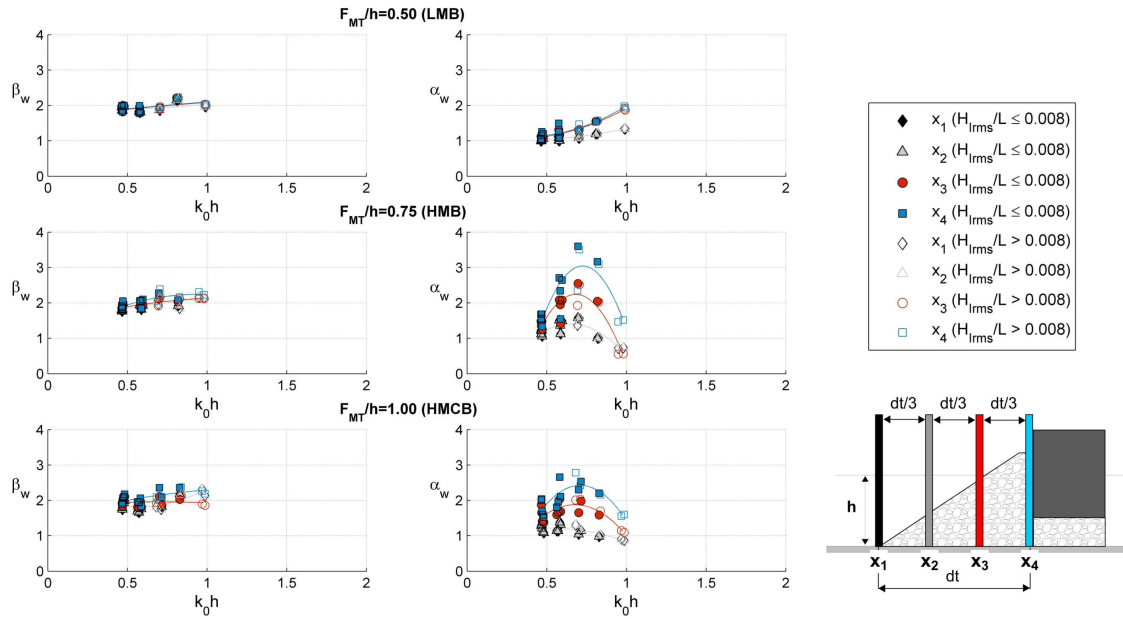


Figure 6.8.: α_w and β_w as a function of $k_0 h$ for different positions along the breakwater slope (x_1 , x_2 , x_3 , and x_4) for two ranges of incident wave steepness, and for three relative berm heights (F_{MT}/h), $Dk < 0.06$, and $B_b/h = 0.250$. Type C.

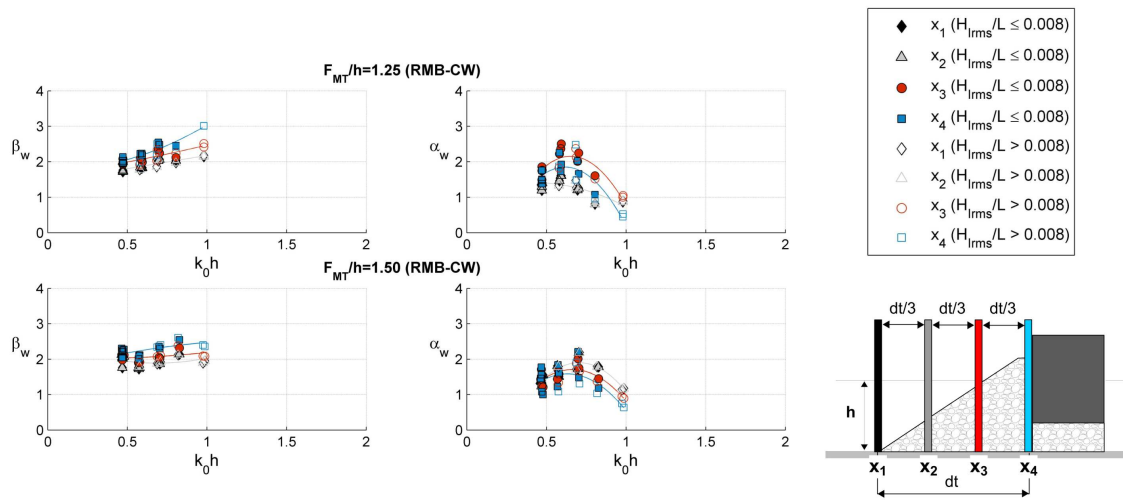


Figure 6.9.: α_w and β_w as a function of $k_0 h$ for different positions along the breakwater slope (x_1 , x_2 , x_3 , and x_4) for two ranges of incident wave steepness, and for two relative berm heights (F_{MT}/h), $Dk < 0.06$, and $B_b/h = 0.250$. Type D.

it can be obtained by applying equation 6.25. The modulus and phase of the reflection coefficient (K_R and ϕ) for a specific breakwater type can be calculated with the hydraulic performance curves obtained in chapter 4. For different breakwater typologies, figure 6.10 shows the comparison of H_{trms} at the toe ($x = 0$), measured at gauge 4 and calculated with equation 6.25. The performance of the approximation is evaluated, based on the determination coefficient that is also included in the figure. The comparison is fairly good.

Type	B_b/h	F_{MT}/h	Dk	$R^2(x_2)$	$\sigma_s(x_2)$	$R^2(x_3)$	$\sigma_s(x_3)$	$R^2(x_4)$	$\sigma_s(x_4)$
C	0.250	0.50	$Dk < 0.06$	0.91	0.48	0.86	0.48	0.84	0.47
			$Dk \geq 0.06$	0.78	0.40	0.87	0.40	0.89	0.35
		0.75	$Dk < 0.06$	0.96	0.01	0.95	0.04	0.93	0.01
			$Dk \geq 0.06$	0.95	0.01	0.94	0.03	0.94	0.01
		1.00	$Dk < 0.06$	0.96	0.01	0.92	0.02	0.92	0.01
			$Dk \geq 0.06$	0.95	0.18	0.93	0.04	0.92	0.18
	0.625	0.50	$Dk < 0.06$	0.94	0.01	0.93	0.01	0.97	0.01
			$Dk \geq 0.06$	0.94	0.01	0.93	0.01	0.94	0.01
		0.75	$Dk < 0.06$	0.95	0.01	0.94	0.01	0.93	0.01
			$Dk \geq 0.06$	0.91	0.01	0.96	0.02	0.92	0.01
		1.00	$Dk < 0.06$	0.96	0.01	0.94	0.03	0.94	0.01
			$Dk \geq 0.06$	0.96	0.01	0.94	0.07	0.94	0.01
D	0.250	1.25	$Dk < 0.06$	0.93	0.23	0.92	0.11	0.92	0.23
			$Dk \geq 0.06$	0.96	0.01	0.93	0.01	0.91	0.01
		1.50	$Dk < 0.06$	0.94	0.01	0.94	0.01	0.86	0.01
			$Dk \geq 0.06$	0.95	0.01	0.94	0.02	0.91	0.01
	0.625	1.25	$Dk < 0.06$	0.95	0.01	0.91	0.01	0.94	0.01
			$Dk \geq 0.06$	0.96	0.01	0.94	0.07	0.94	0.01
		1.50	$Dk < 0.06$	0.93	0.01	0.91	0.01	0.91	0.01
			$Dk \geq 0.06$	0.96	0.01	0.94	0.01	0.92	0.01

Table 6.4.: Goodness of fit for the probability density function of the total wave height at the face of the breakwater in the three locations (x_2 , x_3 , and x_4) to the Weibull distribution. Type C and D.

Parameters β_w and α_w of the bi-parametric Weibull distribution on the slope of the breakwater ($x < 0$) depend on k_0h , the breakwater geometry, and Dk . Their values can be calculated by applying equations 6.28 and 6.29 with the coefficients given in tables 6.5-6.7. Once the value of $H_{trms}(x = 0)$ is known at the toe of the breakwater, the Weibull pdf of the total wave height at any point on the slope is given by equation 6.27 and, in particular, at the crownface.

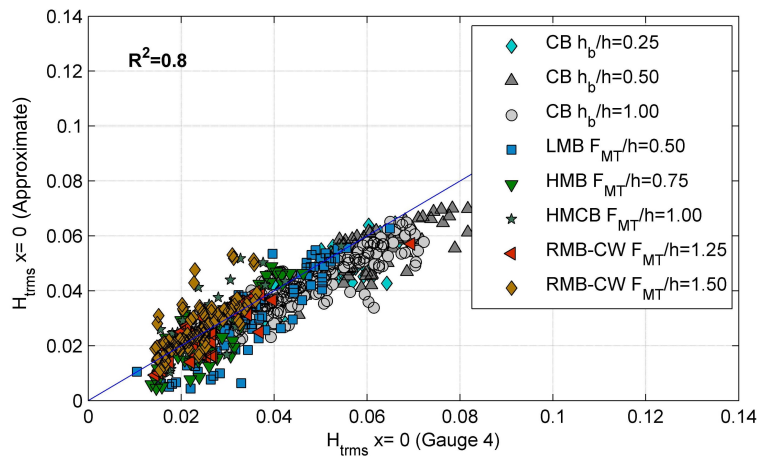


Figure 6.10.: Comparison of the total root-mean-square wave height at the toe ($x = 0$) of different breakwater typologies, measured (gauge 4) and predicted (Approximate) with equation 6.25.

Type	F_{MT}/h	B_b/h	Dk	b_{β_1}	b_{β_2}	b_{β_3}	a_{α_1}	a_{α_2}	a_{α_3}	
C	0.50	0.250	$Dk < 0.06$	0.21	-0.04	1.86	0.74	-0.50	1.10	
			$Dk \geq 0.06$	-1.28	2.24	1.12	-2.50	4.16	-0.48	
		0.625	$Dk < 0.06$	-1.31	2.04	1.22	-4.46	6.37	-0.73	
			$Dk \geq 0.06$	-0.03	0.19	1.87	-0.92	1.37	0.82	
		0.75	0.250	$Dk < 0.06$	-0.19	0.79	1.52	-7.37	9.59	-1.71
				$Dk \geq 0.06$	-0.16	0.48	1.75	0.82	-2.11	2.31
	0.625	$Dk < 0.06$	0.28	0.41	1.59	3.45	-5.39	3.00		
		$Dk \geq 0.06$	-0.15	1.16	1.21	2.45	-4.67	2.98		
	1.00	0.250	$Dk < 0.06$	2.85	-3.28	2.76	-1.68	1.74	0.77	
			$Dk \geq 0.06$	-0.39	1.13	1.39	0.97	-2.21	2.17	
		0.625	$Dk < 0.06$	1.28	-1.39	2.23	0.41	-1.15	1.77	
			$Dk \geq 0.06$	-0.21	0.67	1.60	0.86	-2.11	2.22	
1.25		0.250	$Dk < 0.06$	-0.03	0.79	1.42	-2.01	1.68	1.06	
			$Dk \geq 0.06$	-0.34	0.93	1.46	1.16	-2.63	2.35	
0.625	$Dk < 0.06$	-0.15	0.63	1.57	-0.44	-0.16	1.59			
	$Dk \geq 0.06$	-0.37	0.96	1.45	1.20	-3.26	3.01			
1.50	0.250	$Dk < 0.06$	1.42	-1.95	2.56	-9.40	13.24	-2.76		
		$Dk \geq 0.06$	-0.26	0.78	1.5	0.07	-0.81	1.77		
	0.625	$Dk < 0.06$	1.11	-0.8	2.09	-7.45	10.97	-2.13		
		$Dk \geq 0.06$	-0.40	1.41	1.15	0.15	-1.10	2.26		

Table 6.5.: Coefficients used to calculate α_w and β_w in the bi-parametric Weibull probability density function of the total wave height at location x_2 .

Type	F_{MT}/h	B_b/h	Dk	b_{β_1}	b_{β_2}	b_{β_3}	a_{α_1}	a_{α_2}	a_{α_3}	
C	0.50	0.250	$Dk < 0.06$	-0.07	0.49	1.67	1.75	-1.05	1.22	
			$Dk \geq 0.06$	-1.26	2.30	1.09	-0.84	2.74	-0.11	
		0.625	$Dk < 0.06$	-0.20	0.63	1.67	-3.69	8.2	-1.78	
			$Dk \geq 0.06$	-0.39	1.04	1.54	-2.41	4.43	-0.24	
		0.75	0.250	$Dk < 0.06$	-0.42	1.12	1.44	-19.58	26.72	-6.87
				$Dk \geq 0.06$	-0.54	1.3	1.41	-0.38	0.12	2.00
	0.625	$Dk < 0.06$	0.11	0.13	1.86	-1.58	0.12	2.22		
		$Dk \geq 0.06$	-2.31	3.63	0.71	-3.34	2.48	1.64		
	1.00	0.250	$Dk < 0.06$	-0.33	0.46	1.8	-8.28	11.19	-1.91	
			$Dk \geq 0.06$	0.02	0.06	2.01	0.24	-1.46	2.64	
		0.625	$Dk < 0.06$	-1.51	2.75	1.12	-1.71	1.24	1.52	
			$Dk \geq 0.06$	-0.09	0.36	1.93	0.72	-2.11	2.66	
1.25		0.250	$Dk < 0.06$	0.23	0.60	1.64	-11.44	14.91	-2.70	
			$Dk \geq 0.06$	-0.82	1.86	1.28	0.18	-0.96	2.33	
0.625	$Dk < 0.06$	-1.51	2.90	0.90	-1.19	0.85	1.44			
	$Dk \geq 0.06$	-0.20	0.62	1.80	1.61	-4.52	4.17			
1.50	0.250	$Dk < 0.06$	0.36	-0.23	2.06	-7.90	10.50	-1.78		
		$Dk \geq 0.06$	0.23	0.02	2.02	-0.52	-0.50	2.38		
	0.625	$Dk < 0.06$	-1.25	2.00	1.48	0.60	-2.34	2.28		
		$Dk \geq 0.06$	0.36	-0.16	2.13	2.46	-7.12	5.56		

Table 6.6.: Coefficients used to calculate α_w and β_w in the bi-parametric Weibull probability density function of the total wave height at location x_3 .

Type	F_{MT}/h	B_b/h	Dk	$b_{\beta 1}$	$b_{\beta 2}$	$b_{\beta 3}$	$a_{\alpha 1}$	$a_{\alpha 2}$	$a_{\alpha 3}$
C	0.50	0.250	$Dk < 0.06$	-0.07	0.5	1.67	2.1	-1.5	1.38
			$Dk \geq 0.06$	-1.09	1.99	1.24	0.48	1.67	0.17
		0.625	$Dk < 0.06$	-1.39	2.38	1.08	-4.17	11.14	-2.91
			$Dk \geq 0.06$	-0.43	1.02	1.57	-3.37	6.65	-0.80
	0.75	0.250	$Dk < 0.06$	-1.56	2.93	0.87	-23.85	34.61	-9.51
			$Dk \geq 0.06$	-0.9	1.93	1.26	-3.00	5.45	0.31
		0.625	$Dk < 0.06$	-0.09	1.14	1.46	-8.06	10.16	-0.48
			$Dk \geq 0.06$	-2.67	4.86	0.11	-6.35	7.84	0.26
	1.00	0.250	$Dk < 0.06$	-0.46	1.27	1.48	-11.89	16.88	-3.57
			$Dk \geq 0.06$	-0.75	2.05	1.19	-1.18	1.71	1.63
		0.625	$Dk < 0.06$	-1.36	2.39	1.21	-1.80	0.56	2.04
			$Dk \geq 0.06$	-0.67	1.76	1.38	0.35	-1.93	3.36
D	1.25	0.250	$Dk < 0.06$	1.36	-0.08	1.76	-11.29	13.92	-2.44
			$Dk \geq 0.06$	-1.97	4.62	0.13	-0.35	-0.13	2.28
		0.625	$Dk < 0.06$	-3.49	5.78	0.18	2.36	-4.56	3.03
			$Dk \geq 0.06$	-1.24	2.84	1.14	1.49	-4.60	4.43
	1.50	0.250	$Dk < 0.06$	-0.40	1.19	1.68	-7.63	9.62	-1.45
			$Dk \geq 0.06$	-1.42	3.61	0.67	-2.12	2.36	1.37
		0.625	$Dk < 0.06$	-2.25	3.50	1.14	1.88	-4.44	3.04
			$Dk \geq 0.06$	-1.11	2.77	1.25	2.52	-7.72	6.30

Table 6.7.: Coefficients used to calculate α_w and β_w in the bi-parametric Weibull probability density function of the total wave height at location x_4 .

6.5 Example of application: variation of the total wave height at the front of different breakwater types

The application of the results of this study can be used to determine the variation of the root mean square total wave height (incident and reflected waves) in front of the breakwater, depending on its typology. For that purpose, knowledge of the phase value is essential. Two incident sea states are considered. One state is associated with breakwater safety, ultimate limit state: $T_{01,s} = 14$ s, and $H_{I_{rms,s}} = 4$ m. In contrast, the less energetic state is associated with operational conditions and operational limit state: $T_{01,o} = 7$ s, and $H_{I_{rms,o}} = 1$ m. In both cases, the water depth is $h = 15$ m and the seabed slope is almost horizontal. The root-mean-square total wave height is calculated in front of the breakwater, at $x = 0$. All breakwater typologies have the same stone diameter $D = 1$ m. The freeboard is such that the possibility of overtopping the breakwater is negligible.

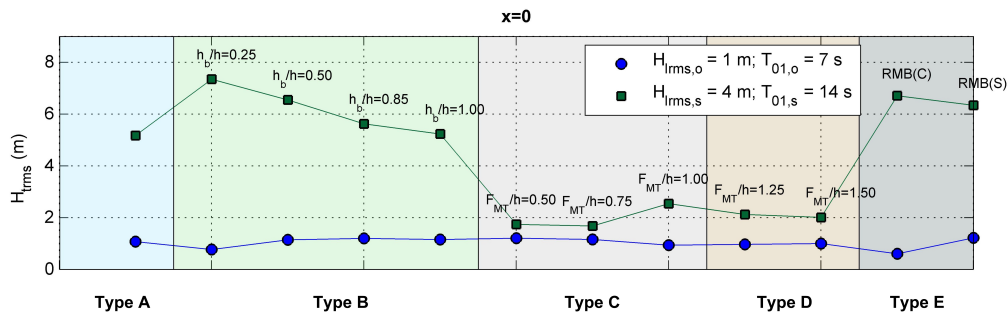


Figure 6.11.: Comparison of the root mean square wave height at the front of the different breakwater typologies for two sea states.

As shown in figure 6.11, the breakwater typology are represented on the x-axis, whereas the total root mean square wave heights at the front of the breakwater are represented on the y-axis. For the sea state with the shortest period, $T_{01,o} = 7$ s, the root mean square wave height is slightly higher than that of the impinging waves, except in the case of the rubble mound breakwater (type E).

For the most energetic sea state with the longest period, $T_{01,s} = 14$ s, the root mean square wave height at the front of the breakwater decreases to approximately half the $H_{I_{rms}}$ in the case of the types C and D. However, for types B and E, there is an increase in the root mean square wave height of roughly 50%. This result highlights the importance of the phase value and of its incidence in determining the total oscillation at the front of the breakwater, especially since it is responsible for actions on the structure.

6.6 Conclusions

This chapter analyzed the statistical behavior of wind waves that interact with different types of breakwater. Depending on their typology, these breakwaters reflect, dissipate, transmit, and radiate incident wave energy in varying proportions, and partial standing wave patterns are likely to occur in front of all types of them as it was seen in section 4. The objective of this chapter was to clarify the role played by the wind wave-structure interaction in the random behavior of the total surface elevation. For this purpose, Rice's theory of envelope amplitude was used to obtain an approximate solution of the total wave-height distribution in front of the breakwater caused by the linear superposition of the incident and reflected wave trains. Experiments presented in section 3.1 were used. The following conclusions can be derived from this research:

- 1 The incident, reflected and total wave train (resulting from the linear superposition of the incident and reflected irregular wave trains) can be treated as a Gaussian processes.
- 2 The total wave height of the linear superposition of narrow-banded incident and reflected wave trains in front of the breakwater followed a Rayleigh distribution in which the parameter was the root mean square of the total wave height. It can be calculated in terms of the modulus and phase of the reflection coefficient, due to the wave-structure interaction, as given by the logistic sigmoid function (chapter 4).
- 3 From the toe of the structure to the toe of the crown, the pdf of the total wave height on the surface of the breakwater evolves from a Rayleigh distribution to a Weibull bi-parametric distribution, depending on energy dissipation by wave breaking and friction in the porous medium, both of which are contingent on the breakwater typology.
- 4 The scale and the shape parameters of the Weibull distribution vary along the breakwater face, depending on breakwater typology, location, and relative water depth, $k_0 h$. The largest deviation from the Rayleigh distribution occurs at the toe of the crown.
- 5 The following probability density functions of the total wave height are proposed: (1) a Rayleigh distribution in front of the breakwater ($x \geq 0$); and (2) a bi-parametric Weibull distribution at the breakwater face ($x < 0$). The parameter of the Rayleigh distribution is the root mean square of the total wave height, which can be accurately calculated by using the modulus and phase of the reflection coefficient, given by the hydraulic performance curves (chapter 4). The bi-parametric Weibull distribution is described in terms of the root mean square of the total wave height at the toe ($x = 0$) of the structure. The scale and shape

parameters are both quadratic functions of $k_0 h$, also calculated at the toe of the structure. The coefficients of the proposed curves depend on breakwater typology, granular characteristics of the porous medium, and location on the breakwater face. Their values have been estimated and parameterised.

- 6 These findings are weakly dependent on the incident wave steepness and hold for narrow-banded incident wave trains impinging perpendicularly onto non-overtopped breakwaters, built with a short relative frontface $dt/L < 1.12$, which ensures a rapid evolution of the wave train on the breakwater face.

Breakwater design based on its hydraulic performance

The design of a breakwater requires that the failure modes which can affect its security, functionality and operability in its useful life are bounded. The failure modes can be verified by means of the corresponding verification equation. In this chapter, the main failure modes that can affect a breakwater are described. The verification equations of said failure modes forced by wind waves in the front or face of the breakwater have been formulated in terms of the kinematic and dynamic variables of the flow at these locations. These variables have been analysed for the failure mode that considers sliding of the crown wall. Results show that the parameters of the pdf of these variables depend on the total wave height at the same location and therefore, the verification equation can be also formulated in terms of this variable. Based on these results, a unified methodology to verify simultaneously the failure modes produce by wind waves in front or face of the breakwater is presented.

7.1 Introduction

According to the Recommendations for Maritime Works (ROM 0.0, 2001; ROM 1.0, 2009) of *Puertos del Estado* (and other similar recommendations and technical criteria), the design project of a breakwater must address the requirements that the joint probability of failure of the main failure modes attached for the ultimate and serviceability limit states in the useful life of the breakwater and other phases of the project, construction and maintenance are bounded. A failure or stoppage mode can be defined as the way, form, or mechanism in which an operational failure or stoppage happens. For each type of breakwater it is essential to consider the set of operational failure and stoppage modes that can affect the breakwater section, its components, elements and subelements. The mechanism or means by which the failure or stoppage occurs is described by evaluating its importance and consequences for the safety, service, and use and exploitation. To analyse a failure mode, all of the prevailing agents and other agents that can participate in the triggering and evolution of the failure or stoppage mode should be specified. The time period in which the failure or stoppage mode can occur is the state, it is crucial to define the descriptors of the agents, for example, r.m.s wave height, average wave period.

The occurrence of the operational failure or stoppage mode during a given state can be verified by means of the corresponding verification equation. This equation establishes the functional relations between the project factors that define the condition of the operational failure or stoppage. Currently, there are different verification equations for the main failure modes (in some cases it consists of only a general criteria, poorly verified). These equations have been formulated independently from each other, even in the case in which the failure modes are affected by the same atmospheric and maritime agents. The best state-of-the-art procedure consists on restricting the evolution of the failure modes assigned to an ultimate limit state by means of threshold values

(e.g. start of failure, damage and destruction). The breakwater failure is considered when the threshold value is reached in some of failure modes and the elements of the breakwater have to be rebuilt. However, to optimize the breakwater design, the main failure modes affected by the same wave conditions in the front of the breakwater should be verified simultaneously. Therefore, there is a necessity for a verification equation in which breakwater section, its parts and elements are considered as an interconnected and interdependent set.

In this work, the breakwater behavior resulting from the wind wave-breakwater interaction has been formulated in a unified way by means of the hydraulic performance curves based on the wave energy balance. These results make it possible to obtain the kinematic and dynamic characteristics of the flow in front and at the face of the breakwater (velocity, pressure), and the response of the structure (e.g. stone displacement, sliding of the superstructure) can be formulated as a function of them.

This chapter aims to develop a unified methodology for the verification of failure modes affecting the front of the breakwater by the wind wave. This has been achieved by means of the hydraulic performance curves results of the wave-breakwater interaction.

7.2 Verification equations in terms of the kinematic and dynamic variables in front of the breakwater

The failure modes produced by the wind wave - breakwater interaction are classified depending on the breakwater typology and the area where the failure or stoppage occurs or which is affected: section, elements and subelements (chapter 2). The main failure modes are described in ROM 1.0 (2009) and CEM (2002) as a function of the different breakwater types and parts affected:

- Vertical breakwater and composite breakwater with a protection berm (type B and C):
 - Central portion: (1) Central body-level berm sliding; (2) Sliding by layers; (3) Overturning of the caisson as a whole and by rows; (4) Structural failure of the breakwater section.
 - Superstructure: (1) Sliding of the superstructure; (2) Overturning of the superstructure; (3) Breaking because of the exhaustion of structural resistance of the crown parapet section.
 - Global section; (1) Overall loss of stability; (2) Settlement; (3) Overturning; (4) Local loss of stability.
 - Foundation berm and soil: (1) Displacement of stones in the toe berm; (2) Toe berm sinking or collapse.
- Rubble mound breakwater with and without crown-wall (type D and E):
 - Central portion: (1) Displacement of stones in the main layer; (2) Breakage of armor units.
 - Superstructure: (1) Sliding of the superstructure; (2) Overturning of the superstructure.
 - Global section; (1) Overall loss of stability; (2) Settlement; (3) Displacement of the main layer.

- Foundation berm and soil: (1) Displacement of stones in the toe berm; (2) Toe berm sinking or collapse.

The occurrence of the operational failure or stoppage mode during a given state can be verified by means of the corresponding verification equation (ROM 0.0, 2001; ROM 1.0, 2009). It is necessary to establish a verification equation for each failure mode assigned to an ultimate or serviceability limit state and for each operational mode belonging to an operational limit state. The verification equation consists in a set of terms. In general, this is a state equation, and therefore, it is applied with the hypothesis that the outcomes of the set of project factors are stationary and uniform from a statistical point of view. The terms of the equation are a combination of mathematical operations of project factors, parameters, agents, and actions. The terms can be classified as favorable (Z_1), and unfavorable (Z_2). Favorable and unfavorable terms are those that contribute in a favorable or unfavorable way to the non-occurrence or the prevention of the failure mode, respectively. The safety margin is thus defined as the difference between favorable terms and unfavorable terms:

$$S = Z_1 - Z_2 \quad (7.1)$$

According to this definition, the structure is safe and reliable, and will not fail for a given failure mode when $S > 0$, and therefore it will fail when $S \leq 0$. The value $S = 0$ separates the failure domain from the safety or reliability domain. Then, the verification equation is established with pairs of terms that can represent, for example, unit weight and actions due to wind waves, the freeboard of the dike and wave run-up, etc. In general, the terms of the equation [Z_1, Z_2] are a function mainly of:

- Breakwater typology
- Geometry of the parts and elements
- Parameter of the medium
- Agents, in this case wave conditions
- Failure level

In some failure modes, it is necessary to define the failure level considered, for example, when the armor layer stability is analyzed. To relate the failure level with the parameter defining the damage, some criteria should be established in terms of changes in the geometric characteristics such as the number of displaced stones in a concrete area.

7.3 Kinematic and dynamic variables of a irregular wave train in front of a breakwater

A train of long-crested waves impinges perpendicularly to a breakwater as was described in section 6.2. The instantaneous free surface elevation, $\eta_t(x, t)$ (results from the linear superposition of the incident and reflected wave trains), at any location in front of the coastal structure has a Gaussian probability density function (see chapter 6). Kinematic and dynamic variables of the total oscillation, for instance dynamic pressure, are shown to be statistically independent and to possess a Gaussian probability distribution (Borgman, 1967). In the following, the dynamic pressure, p ,

will be analysed. p at the breakwater wall can be calculated, in a complex form, in terms of the total free surface elevation by means of the transfer function, F_{tp} :

$$p(t, x = x_w, z) = F_{tp}(f, z)\eta_t(t, x = x_w) \quad (7.2)$$

where

$$F_{tp}(f, z) = \begin{cases} \rho g \frac{\cosh(k(h+z))}{\cosh(kh)} & \text{if } -(h - h_b) < z \leq 0 \\ \rho g & \text{if } 0 \leq z < \eta_t \end{cases} \quad (7.3)$$

The corresponding pressure spectra is given as:

$$S_p(f, x = x_w, z) = |F_{tp}(f, z)|^2 S_t(f, x = x_w) \quad (7.4)$$

When the incident waves have a narrow-band spectrum, the transfer functions can be approximated to a function of a representative central frequency (f_0) as shown in chapter 6 and pressure spectra can be obtained as:

$$S_p(f, x = x_w, z) = |F_{tp}(f_0, z)|^2 S_t(f, x = x_w) \quad (7.5)$$

Defining P as the pressure in the wave crest (for each wave of the sea state), the root mean square value of P , can be then calculated as a function of the r.m.s wave height at the breakwater wall, H_{wrms} , from equation 7.5 as follows:

$$P_{rms}(x = x_w, z) = \begin{cases} \rho g \frac{\cosh(k_0(h+z))}{\cosh(k_0h)} \frac{H_{wrms}}{2} & \text{if } -(h - h_b) < z \leq 0 \\ \rho g \left(\frac{H_{wrms}}{2} - z \right) & \text{if } 0 \leq z < \eta_t \end{cases} \quad (7.6)$$

In chapter 6 the r.m.s value of the total wave height at the breakwater wall, H_{wrms} , was calculated in terms of the r.m.s total wave height at the breakwater toe, H_{prms} . The latter was approximated as a function of K_R and ϕ , which can be obtained from the hydraulic performance curves.

7.4 Crown wall stability analysis

In this section, the sliding of the superstructure failure mode is analysed. This is one of the most important failure modes associated with the stability of this element. It occurs when the resulting wave force in the seaward direction exceeds the friction force between the caisson base and the bedding layer. The terms of the verification equation for this failure mode are the following:

- Favorable term: $Z_1 = \mu_c(W_1 - Fv)$
- Unfavorable term: $Z_2 = Fh$

where μ_c is the friction coefficient between the caisson base and the bedding layer and W_1 is the submerged weight of the caisson (equation 7.7). Horizontal and vertical forces in the wave crest can be obtained by integrating the pressure laws (equation 7.8 and 7.4).

$$W_1 = [F_c + (h - h_b)]B\gamma_c - [(h - h_b)B\gamma_w] \quad (7.7)$$

$$Fh = \int_{-(h-h_b)}^{\eta} P(x = x_w) dz \quad (7.8)$$

$$Fv = \int_{x_w}^{x_w+B} P(z = -(h-h_b)) dx \quad (7.9)$$

γ_c and γ_w are the specific weight of the caisson and water respectively.

In these equations, the terms of verification equation are a function of:

$$[P, Fh, Fv] = f(\text{breakwater typology}, Dk, \frac{H_I}{L}, kh) \quad (7.10)$$

Several authors have studied the pressure distribution through analytical, physical and numerical approaches. Formulas differ depending on the breakwater typology and the breaking type. For vertical or composite breakwaters and for non-breaking wave conditions, Fenton (1985) proposed a theoretical solution. When wave breaking occurs, most of formulae are based on empirical results (Sainflou, 1928; Goda, 1985; Nagai, 1973) and assume the following considerations:

- The maximum horizontal pressure is produced in the mean water level.
- The pressure below the still water level follows a hyperbolic cosine law or a linear law.
- The uplift pressure law is triangular with zero pressure at the leeward side of the caisson. However, other authors point out that uplift pressure at the exit of the caisson is not always zero and the law may not be lineal (Liu, 1985; Losada et al., 1993b; Pérez, 2008).

When impact pressures are caused by waves breaking directly onto a wall, the problem becomes more complex and the solution is often to increase the pressure in the proximity of the S.W.L. multiplying it by a constant value (Minikin, 1963; Cooker and Peregrine, 1990). Takahashi (1996) also proposed a method (Goda modified) to calculate the pressure in a composite breakwater under breaking waves and impact waves. This method also includes the effect of the protection berm, sloping top, and incident wave angle.

In the case of a rubble mound breakwater, the waves broke before they reach the wall. Iribarren and Nogales (1950) proposed a very conservative method with a triangular pressure law. Jensen (1984) analysed the influence of wave period and wave height concluding that the pressure increased when both variables increased as well. Günbak and Göcke (1984) and Martín et al. (1999) proposed to separate the action of the waves on the wall into two distributions: a hydrostatic one representing the mass of water that hit the wall and a rectangular one associated with the kinematic energy of the wave. The model by Pedersen (1996) presents two different rectangular pressure distributions, one in the protected zone by the porous material and other in the zone not protected. Norgaard et al. (2014) modified previous formula to adapt it for shallow water conditions. These authors assume a triangular law for the uplift pressure.

Present formulae are based on the incident wave conditions. In this section, the pressure laws and horizontal and vertical forces are analysed as a function of the total oscillation at the wall of the caisson.

7.4.1 Methodology

Experimental and numerical data has been used in order to analyse the pressure laws and forces in the crown wall. Experimental data were obtained for type B in the range of the parameters defined in table 3.3. Numerical data (section 3.2) were obtained for type C and D for the geometric and wave conditions described in table 7.1.

The analysed variables of pressure and force were presented in section 3.1.2.2 and are summarized as follows (figure 7.1):

- $p(t)$, $FH(t)$ and $FV(t)$: Time series of pressure in different locations along the wall and horizontal and vertical forces.
- H_{wrms} : Root mean square value of the free surface elevation at the wall.
- Horizontal pressure distribution: 1) P_{1rms} : Root mean square value of the pressure at the mean water level; 2) P_{2rms} : Root mean square value of the pressure at the bottom of the caisson.
- Vertical pressure distribution: 1) P_{u1rms} : Root mean square value of the pressure at the entrance of the porous medium; 2) P_{u2rms} : Root mean square value of the pressure at the end of the porous medium.
- Fh and Fv : Horizontal and vertical force in the wave crest for each wave of a sea state.
- Fh_{rms} and Fv_{rms} : Root mean square value of the horizontal and vertical forces respectively.

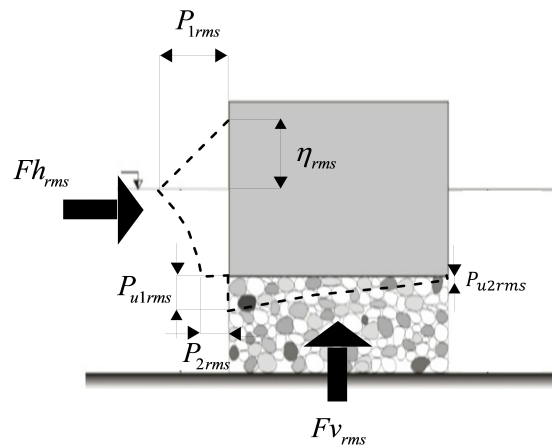


Figure 7.1.: Scheme of pressure laws and analysed variables.

Type	F_{MT}	$B_b(m)$	$D(m)$	$H_{Is\ teo}$ (m)	$T_{p\ teo}$ (s)	
LMB	0.25, 0.50	0.1, 0.25	40	0.04, 0.08	1.05, 1.50, 2.00, 2.50	
C	HMB	0.75	0.1, 0.25	40	0.04, 0.08	1.05, 1.50, 2.00, 2.50
	HMCB	1.00	0.1, 0.25	40	0.04, 0.08	1.05, 1.50, 2.00, 2.50
D	RMB-CW	1.25, 1.50	0.1, 0.25	40	0.04, 0.08	1.05, 1.50, 2.00, 2.50

Table 7.1.: Target parameters for simulated cases to breakwater stability analysis.

7.4.2 Results

7.4.2.1. Horizontal pressure distribution

Pressure over the mean water level

It is known (Goda, 1985; Takahashi, 1996) that the pressure law above S.W.L. follows a triangular distribution depending on the maximum sea water level elevation at the wall. Figures 7.2 and 7.3 show the r.m.s value of the pressure at the mean water level, P_{1rms} , compared with the hydrostatic pressure at this location calculated as given by equation 7.11, where ρ is the water density and g is the gravity acceleration. These results are presented for type B as a function of h_b/h (figure 7.2) and for type C and D as a function of F_{MT}/h and B_b/h (figure 7.3).

$$P_{1rms} = \rho g \frac{H_{wrms}}{2} \quad (7.11)$$

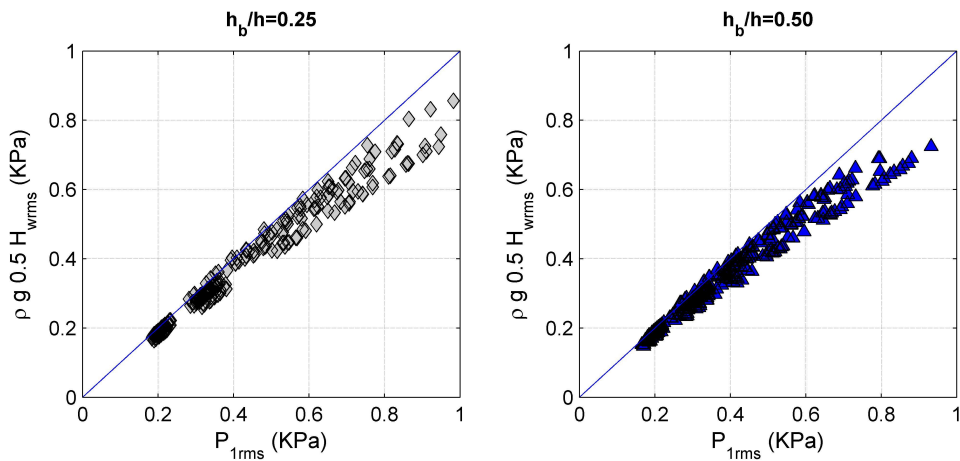


Figure 7.2.: Comparison between numerical and theoretical value of the pressure at the S.W.L. for type B as a function of h_b/h .

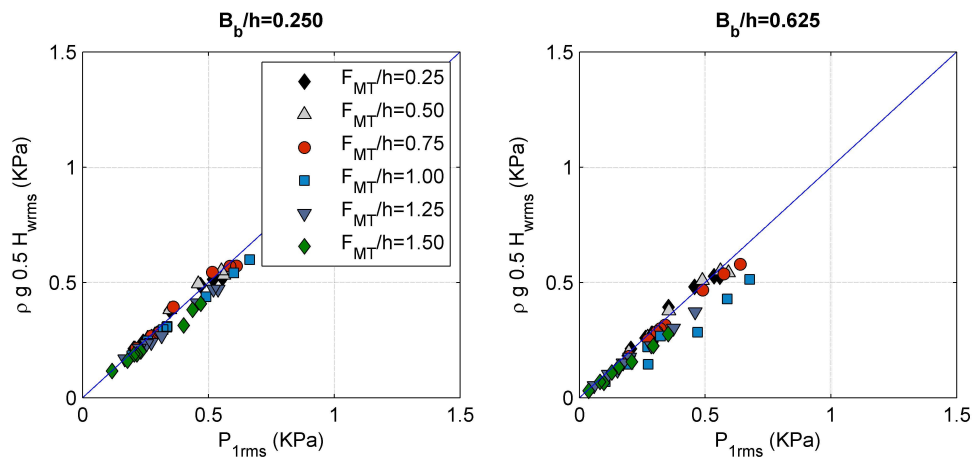


Figure 7.3.: Comparison between numerical and theoretical value of the pressure at the S.W.L. for type C and D as a function of F_{MT}/h and B_b/h .

For all typologies, it is verified that the pressure over the mean water level is directly proportional to the sea water elevation at the wall. For larger pressures, the theoretical expression underestimates the pressure at this location. This can be because of the nonlinear effects produced in the wave train when the wave reaches the wall. To correct this effect, a coefficient, α_1 , has been included (equation 7.12). $\alpha_1 = 1.14$ has been found for all breakwater typologies. Moreover, for HMCB, $F_{MT}/h = 1.00$ and the largest berm, $B_b/h = 0.625$, pressures greater than the ones obtained with equation 7.12 were observed. This overpressure can be due to impulsive pressures that were observed at the wall for the smallest wave period. In this case, the value of P_{1rms} can be calculated as the modified hydrostatic pressure affected by an empirical coefficient, α_I , to take into account this excess of pressure (equation 7.13).

$$P_{1rms} = \rho g \frac{H_{wrms}}{2} \alpha_1 \quad (7.12)$$

$$P_{1rms} = \left[\rho g \frac{H_{wrms}}{2} \alpha_1 \right] \alpha_I \quad (7.13)$$

α_I depends mainly on the parameter B_b/h and H_{Irms}/h (figure 7.4). The excess of pressure increases with the relative berm width and wave height increase. This result is in accordance with Takahashi (1996), but this author proposed higher values of α_I because the analysis was done without taking into account the reflection processes in the total wave height calculation. The best fits to calculate α_I for HMCB typology are also included in figure 7.4. For the rest of cases $\alpha_I = 1$.

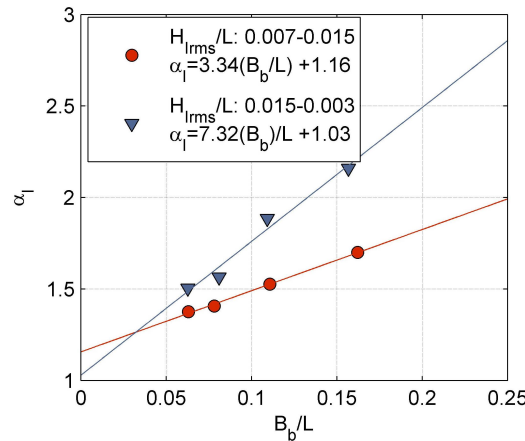


Figure 7.4.: Impulsive pressure coefficient, α_I , for typology HMCB as a function of B_b/L and H_{Irms}/h .

Pressure below the mean water level

Figure 7.5 shows the relationship between the root mean square of the non-dimensional values of the pressure at the mean water level, P_{1rms} , and at the bottom of the caisson, P_{2rms} , for type B. For the two analysed relative foundation depths, $h_b/h=0.25$ and 0.50 , P_{2rms} mainly depends on the relative depth, kh . Long waves produce the greater pressure at the bottom. P_{2rms} has been compared with the theoretical pressure at this location, $z = -(h - h_b)$, (equation 7.6).

$$P_{2rms} = P_{1rms} \frac{\cosh(k_0 h_b)}{\cosh k_0 h} \quad (7.14)$$

In this work, f_0 has been considered as the peak frequency. Non-dimensional results are shown in figure 7.6 for type B with two relative foundation depths. Equation 7.14 correctly represents the results but slightly overestimates the value of P_{2rms} for the largest pressures and the two relative foundation depths. This head loss could be due to the sudden increase of velocity at the entrance of the porous medium. Consequently, the pressure decreases in this location.

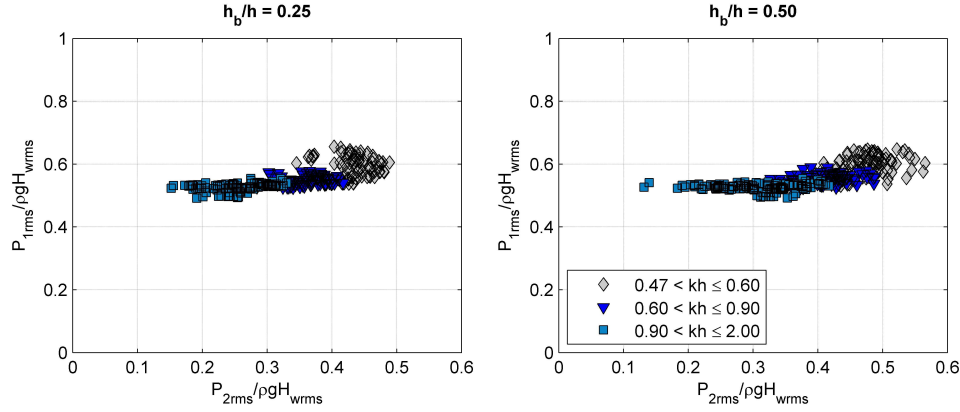


Figure 7.5.: Relationship between non-dimensional pressure at the S.W.L., P_{1rms} , and the pressure at the bottom of the caisson, P_{2rms} , for type B as a function of h_b/h and kh .

Figure 7.7 presents the results for type C and D as a function of F_{MT}/h . Moreover, the comparison of numerical and theoretical pressure laws below S.W.L. is shown in figure 7.8 for $T_{p\ teo}=2.5$ s and $H_{Is\ teo}=0.08$ m. The blue line represents the location of the breakwater berm coronation. For LMB, $F_{MT}/h=0.25$ and 0.50 , numerical pressure law below S.W.L. sets very successfully with theoretical law. In this case, the pressure reduction effect is not so pronounced than the one observed for type B. The presence of the berm could damp the sudden change in the stream line at the entrance of the porous medium. For $F_{MT}/h \geq 0.75$ the berm or slope is total or partially protecting the crown and the presence of the granular material attenuates the value of P_{2rms} . For HMB, $F_{MT}/h = 0.75$, the pressure law is well fitted to the hyperbolic cosine law (equation 7.14) until the point in which there is a change of medium (only water \rightarrow water + granular material) at $z/(h - h_b) = -0.5$. From this location the pressure is slightly lower than the one given by the theoretical law. The biggest difference is observed for HMCB, $F_{MT}/h = 1.00$. Finally, for RMB-CW, $F_{MT}/h > 1.00$, the complete pressure law from the S.W.L. to the bottom of the caisson is affected by the presence of the porous medium and the pressure deficit is reduced in comparison with the two previous typologies. In order to quantify this pressure deficit, a new coefficient α_2 has been introduced (Equation 7.15). $\alpha_2 = f(h_b/h, F_{MT}/h)$. Values of α_2 for the different typologies are presented in the table 7.2. The pressure law could be approximated by a linear distribution from the S.W.L. and the bottom of the caisson for all breakwater typologies, with P_{2rms} calculated as given in equation 7.15. In the case of $F_{MT}/h = 0.75$, the horizontal law would be composed by two different distributions: 1) a linear law between the S.W.L. and the berm coronation, in which pressure, P_{1rms} , can be calculated with equation 7.15 taken $\alpha_2 = 1$ and; 2) other linear law from this point to the bottom of the caisson where P_{2rms} can be calculated with equation 7.15 taken α_2 as given in table 7.2.

$$P_{2rms} = P_{1rms} \frac{\cosh(k_0 h_b)}{\cosh k_0 h} \alpha_2 \quad (7.15)$$

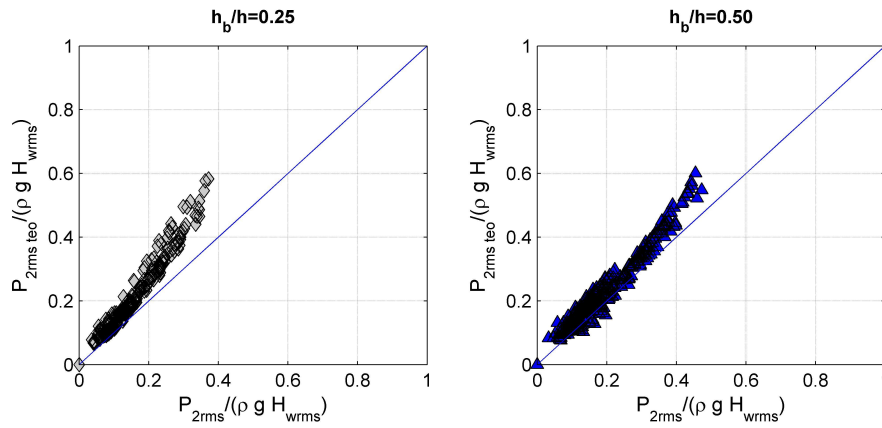


Figure 7.6.: Comparison between non-dimensional pressure at the bottom of the caisson, experimental, P_{2rms} , and theoretical, $P_{2rms\ teo}$, for type B as a function of h_b/h .

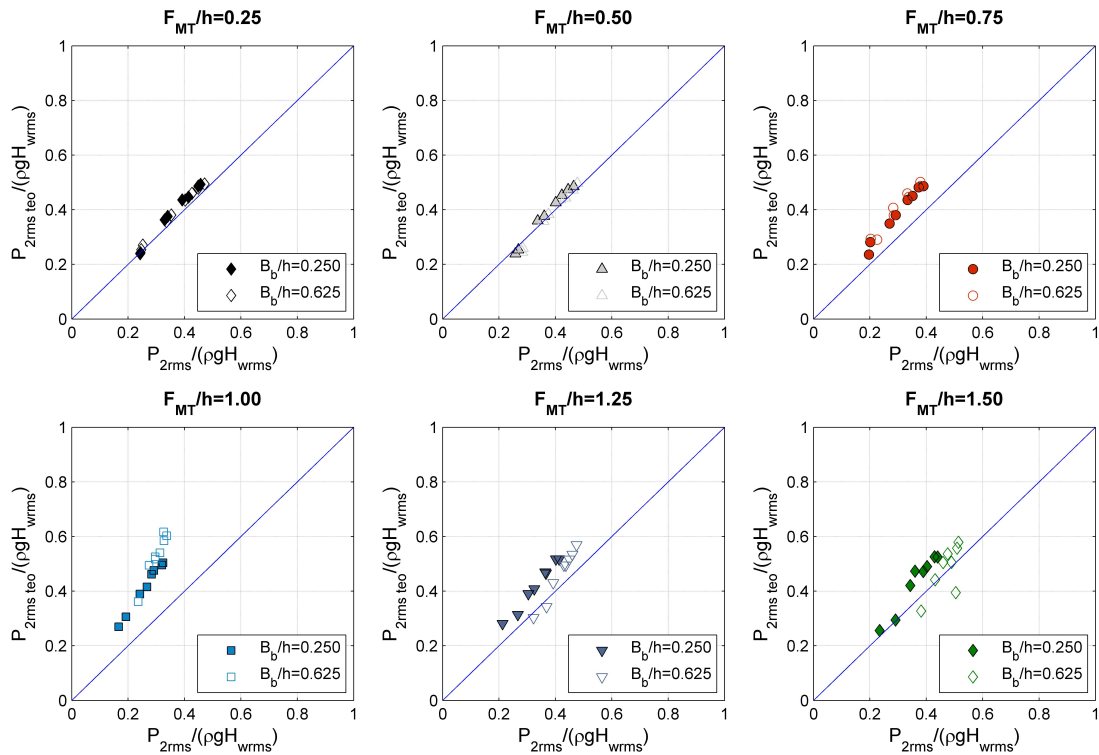


Figure 7.7.: Comparison between pressure at the bottom of the caisson, numerical, P_{2rms} , and theoretical, $P_{2rms\ teo}$, for type C and D as a function of F_{MT}/h and B_b/h .

7.4.2.2. Uplift pressure distribution

The uplift pressures will depend mainly on the wave transformation processes in the porous medium. Firstly, the shape of the uplift pressure law is analysed. Figures 7.9 and 7.10 show the non-dimensional uplift pressure along the bottom of the caisson for type C and D. Results are presented as a function of the coordinate x'/B (x' is the local coordinate, with $x' = 0$ at the entrance of the porous medium) in terms of F_{MT}/h and kh for $B_b/h = 0.250$ and $B_b/h = 0.625$ (figure 7.9 and 7.10 respectively). The uplift pressure law is nearly linear which indicates that the

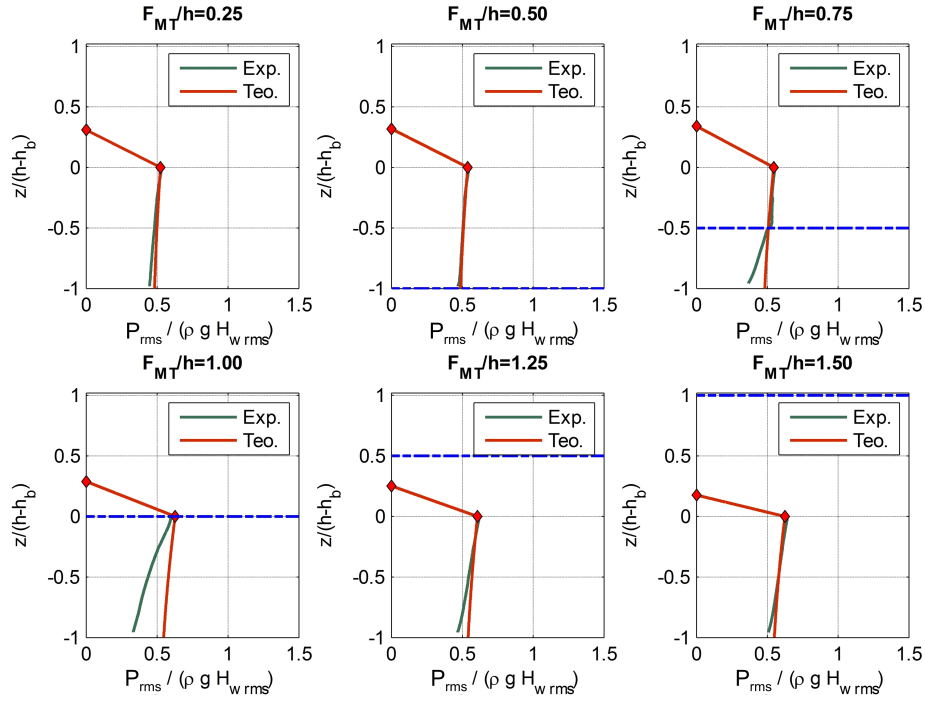


Figure 7.8.: Comparison between horizontal pressure laws for type C and D as a function of F_{MT}/h . $T_{p\ teo} = 2.50$ s, $H_{Is\ teo} = 0.08$ m and $B_b/h = 0.250$.

flow in the porous medium is fully developed (Losada et al., 1993b; Pérez, 2008). Long waves increase the uplift pressure at the entrance of the porous medium. Moreover, in the most of the cases uplift pressure at the exit is not zero. The behavior is the same for the two values of B_b/h .

The value of the non-dimensional uplift pressure at the entrance of the porous medium, P_{u1rms} , is compared with the non-dimensional pressure at the bottom of the caisson, P_{2rms} for type B (figure 7.11) and C and D (figure 7.12). For type B, results are shown for the two relative foundation depths, h_b/h , as a function of the relative width of the caisson, B/L and Dk . In general, there is a linear relationship between the pressure values, although P_{u1rms} is slightly lower than P_{2rms} because of the change in the stream line direction at the entrance of the porous medium. The head loss (value of P_{u1rms} relative to P_{2rms}) increases when B/L decreases and for the highest h_b/h . The influence of Dk is only significant when $B/L < 0.10$. Results are similar in the case of type C and D where B/L was tested in the range of $0.10 \leq B/L < 0.35$. For $B_b/h = 0.250$ the head

Typology	h_b/h or F_{MT}/h	α_2
CB	$h_b/h = 0.25$	1.38
	$h_b/h = 0.50$	1.17
LMB	$F_{MT}/h = 0.25$	1
	$F_{MT}/h = 0.50$	1
HMB	$F_{MT}/h = 0.75$	0.31
HMCB	$F_{MT}/h = 1.00$	1.70
RMB-CW	$F_{MT}/h = 1.25$	1.17
	$F_{MT}/h = 1.50$	1.09

Table 7.2.: α_2 values for the different typologies.

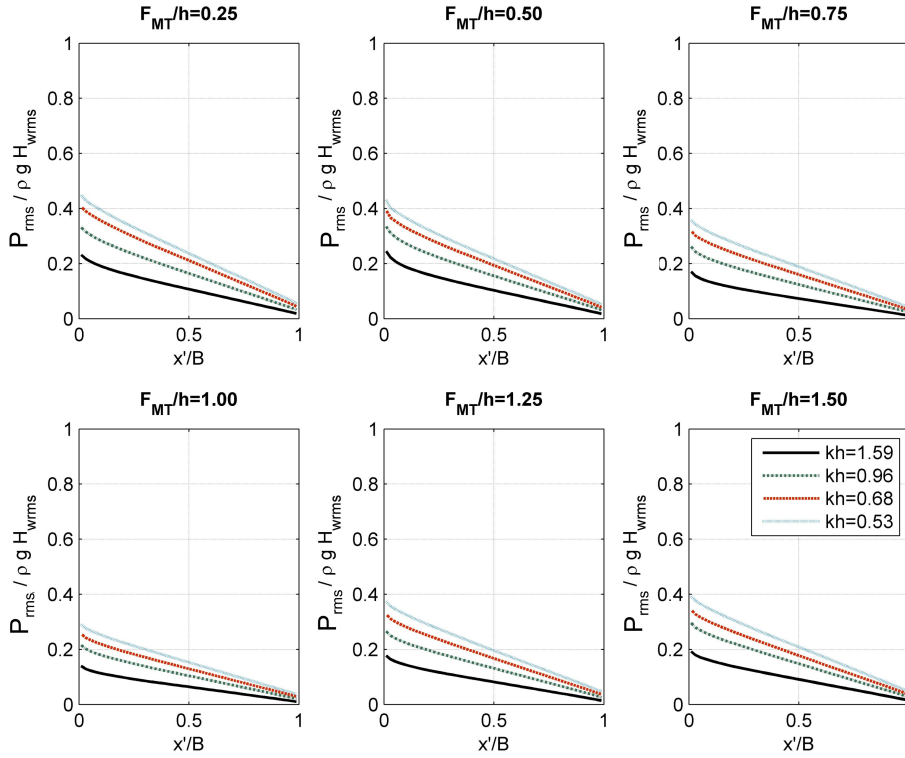


Figure 7.9.: Uplift pressure laws for type C and D as a function of F_{MT}/h and kh . $B_b/h = 0.250$.

loss is negligible in all cases whereas for $B_b/h = 0.625$ slightly increases for $F_{MT}/h \geq 1$. For the prediction of the uplift forces $P_{u1rms} = P_{2rms}$ can be assumed.

Finally, the uplift pressure at the exit of the porous medium is analysed. At previously stated, the pressure at this location cannot be considered zero. It should depend on the transmission coefficient through the porous medium. Therefore, the relation between P_{u1rms} and P_{u2rms} has been studied as a function of K_T as follows:

$$P_{u2rms}/P_{u1rms} = \alpha_3 K_T \quad (7.16)$$

with α_3 a empirical coefficient. It is presented in figures 7.13 and 7.14 for type B, and C and D respectively. This parameter depends mainly on the relative width of the caisson B/L . It decreases exponentially with B/L until a value $B/L = (B/L)_{min}$ from which α_3 is nearly zero. Therefore, three types of uplift pressure laws can be defined as a function of B/L (figure 7.15):

- Trapezoidal uplift pressure law for $B/L < (B/L)_{min}$ (figure 7.15 A) . In this case the wave is not completely dissipated by the porous medium and pass leeward the structure.
- Triangular uplift pressure law for $B/L = (B/L)_{min}$ (figure 7.15 B). In this case $P_{u2rms} = 0$.
- Triangular uplift pressure law with zero pressure before the exit of the caisson for $B/L > (B/L)_{min}$ (figure 7.15 C). In this case the wave dissipates completely in the porous medium and there is not any wave transmission leeward the breakwater.

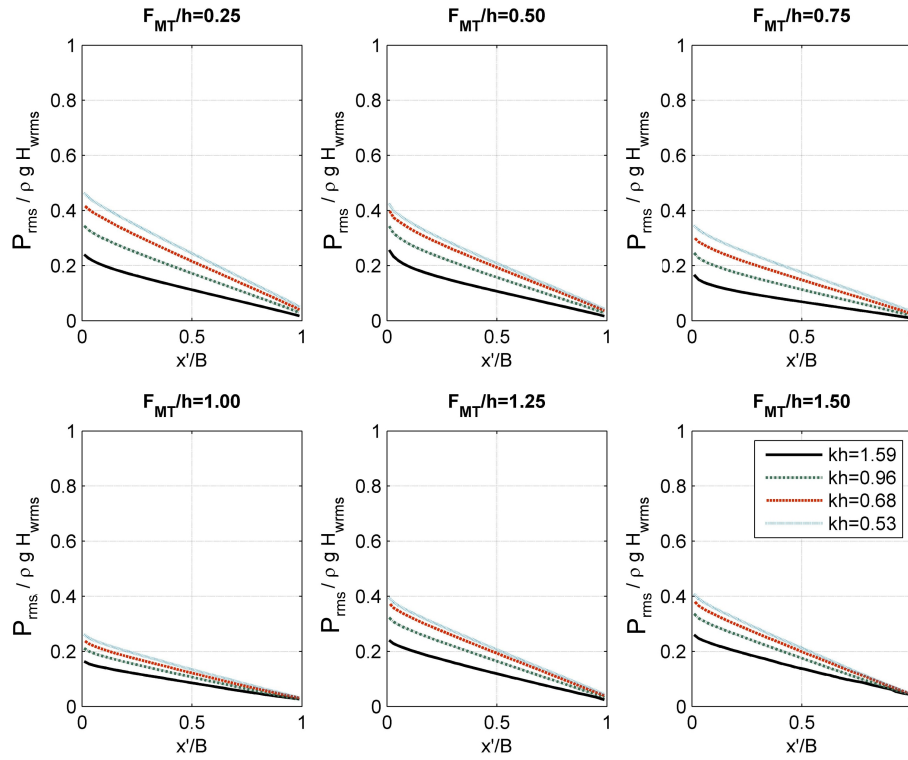


Figure 7.10.: Uplift pressure laws for type C and D as a function of F_{MT}/h and kh . $B_b/h = 0.625$.

The α_3 coefficient also depends on the breakwater typology (Dk , h_b/h , F_{MT}/h and B_b/h) although to a lesser extent. Table 7.3 presents the equation to obtain α_3 and $(B/L)_{min}$ for types B, C and D. Moreover, the best fit curves are presented in figures 7.13 and 7.14.

		$\alpha_3 = a_{\alpha_3}(B/L)^{b_{\alpha_3}}$			
Type	h_b/h	Dk	a_{α_3}	b_{α_3}	$(B/L)_{min}$
B	0.25	$Dk < 0.05$	0.0013	-1.26	0.89
		$0.05 < Dk < 0.07$	0.0020	-1.26	1.24
		$0.07 < Dk < 0.12$	0.0029	-1.26	1.50
		$0.12 < Dk < 0.52$	0.0042	-1.26	1.50
	0.50	$Dk < 0.05$	0.0027	-1.26	1.50
		$0.05 < Dk < 0.07$	0.0040	-1.26	1.50
		$0.07 < Dk < 0.12$	0.0061	-1.26	1.50
		$0.12 < Dk < 0.52$	0.0074	-1.26	1.50
Type	B_b/h	Dk	a_{α_3}	b_{α_3}	$(B/L)_{min}$
C and D	0.250	$0.05 < Dk < 0.16$	0.0019	-1.04	1.23
	0.625		0.0012	-1.04	0.80

Table 7.3.: α_3 values for the different typologies.

7.4.2.3. Horizontal and vertical forces

Figures 7.16 and 7.17 show the relationship between the non-dimensional r.m.s. values of the horizontal and vertical forces. For type B (figure 7.16) data are separated for the two relative foundation depths and have been plotted as a function of the relative width of the caisson. Results show that data can be grouped for different B/L intervals presenting a linear behavior. In all cases,

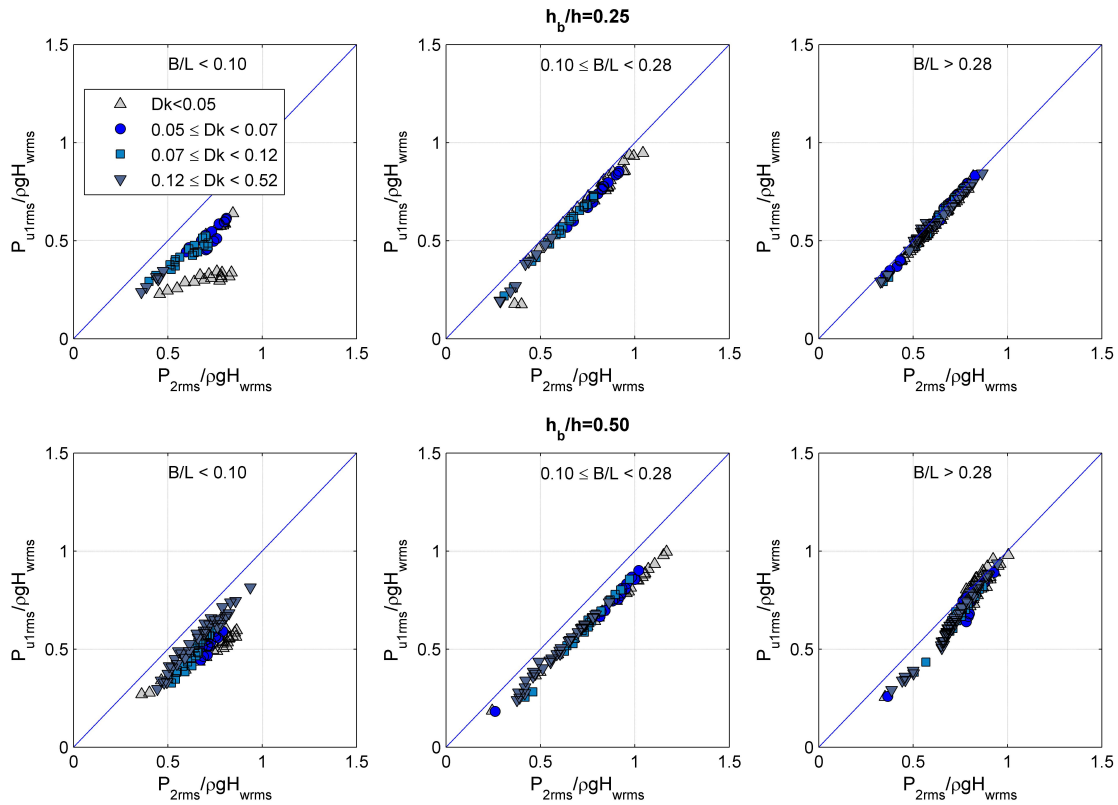


Figure 7.11.: Relationship between non-dimensional pressure at the bottom of the caisson, P_{2rms} , and pressure at the entrance of the porous medium, P_{u1rms} , for type B as a function of h_b/h , Dk , and B/L .

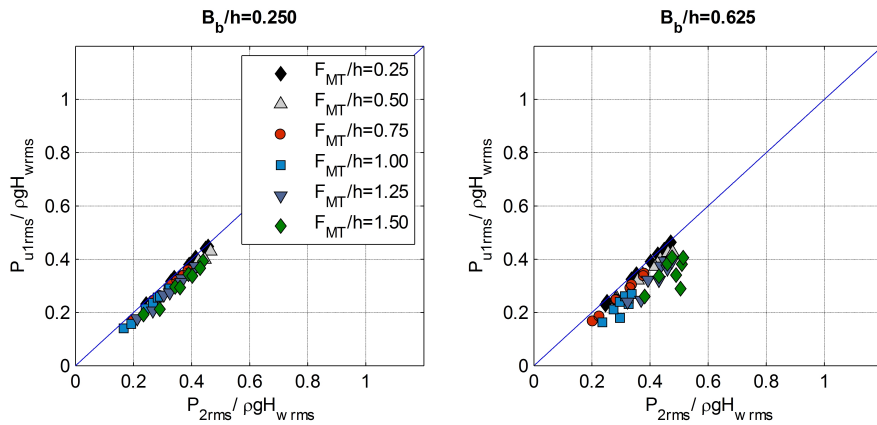


Figure 7.12.: Relationship between non-dimensional pressure at the bottom of the caisson, P_{2rms} , and pressure at the entrance of the porous medium, P_{u1rms} , for type C and D as a function of F_{MT}/h and B_b/h .

the slope of the line increases with B/L . Three force regimes can be distinguished as a function of this parameter for the two relative foundation depths:

- Regime in which the horizontal forces are dominants. This corresponds with the lowest range of B/L ($B/L < 0.10$).

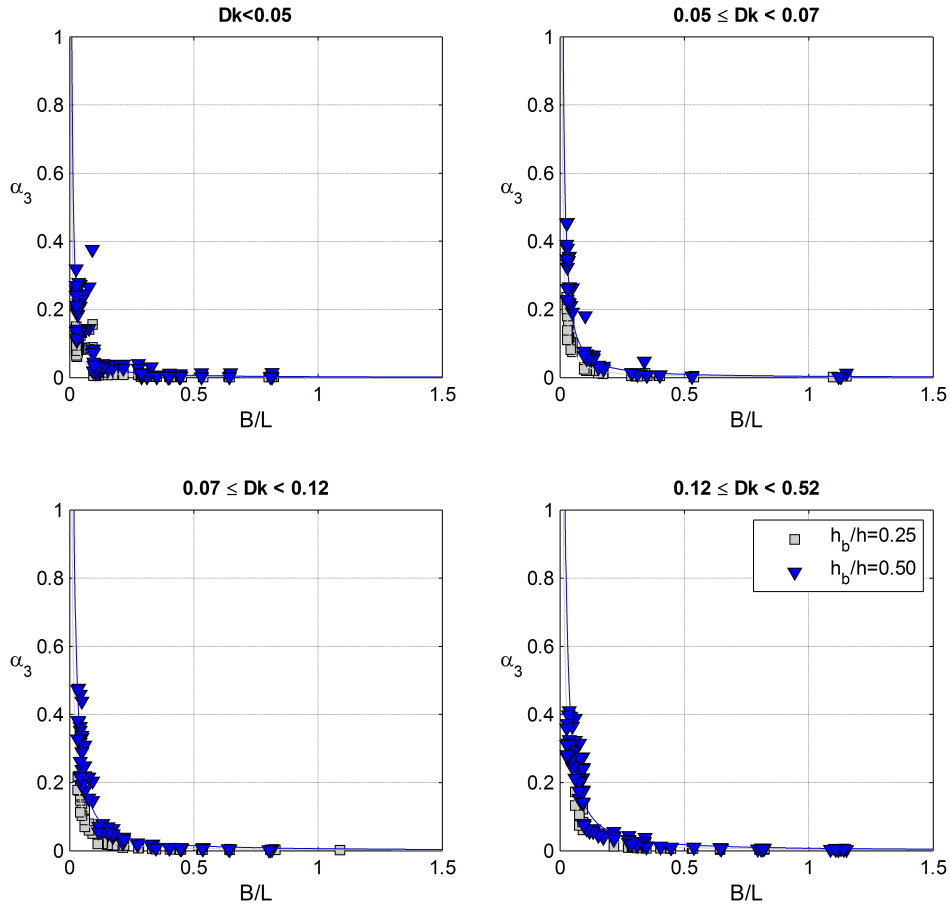


Figure 7.13.: α_3 as a function of B/L , Dk and h_b/h . Type B.

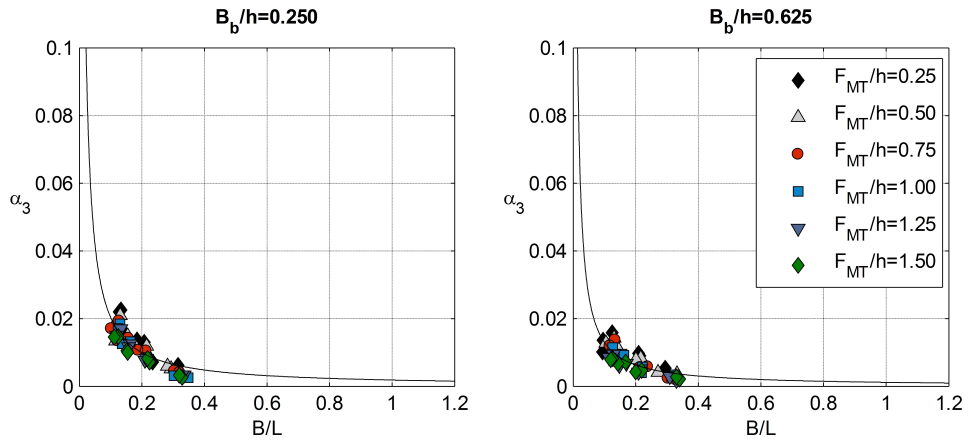


Figure 7.14.: α_3 as a function of B/L , F_{MT}/h and B_b/h . Type C and D.

- Regime in which the vertical forces are dominant corresponding with the highest range of B/L ($0.28 < B/L < 1.20$).
- Intermediate regime in which both forces have the same importance. This corresponds with the intermediate range of B/L ($0.10 < B/L < 0.28$).

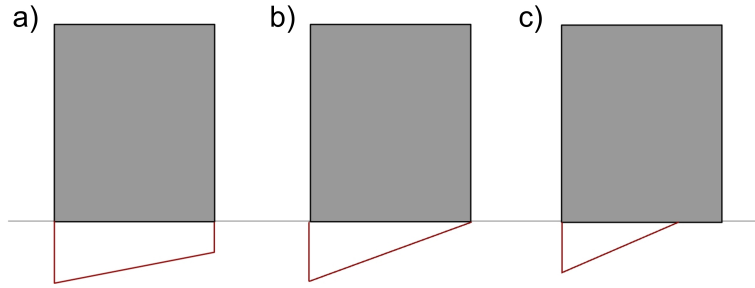


Figure 7.15.: Classification of the uplift pressure law.

Moreover, vertical forces increase with an increment of the foundation depth. For type C and D (figure 7.17) data are presented for the two relative berm widths and have been plotted as a function of the relative berm height. A linear relationship is also observed with the slope decreasing with an increase of F_{MT}/h . The dependence on this parameter is greater as the relative berm height increases. In these data the interval of B/L was $0.1 < B/L < 0.35$, which corresponds with the intermediate regime and both forces are important. The slope of the line has been obtained. This value is represent by α_4 (equation 7.17) which is included in table 7.4 for all typologies. This coefficient is a function of the *breakwater typology*.

$$Fv_{rms} = \alpha_4 Fh_{rms} \quad (7.17)$$

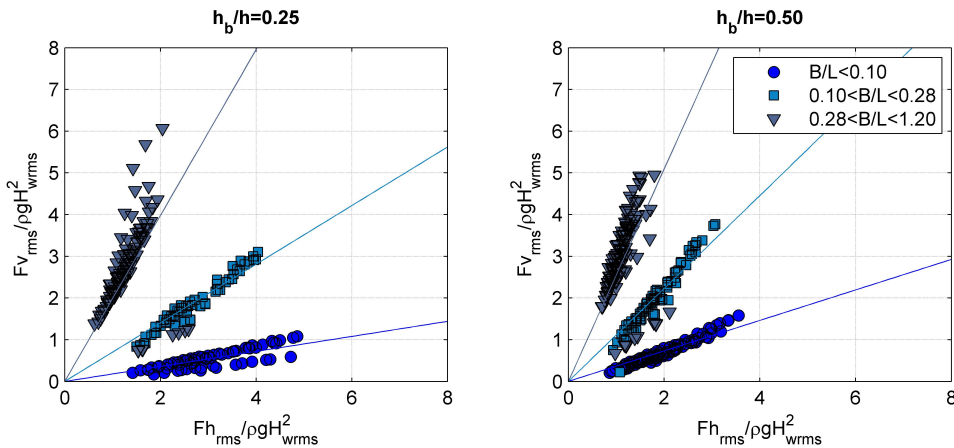


Figure 7.16.: Relationship between r.m.s value of the non-dimensional horizontal and vertical forces as a function of h_b/h and Dk . Type B.

7.4.2.4. Probability density function of the horizontal and vertical forces

In existing formulae in literature, it is assumed that the maximum horizontal and vertical forces in a sea state occur simultaneously. However, several authors have pointed out the invalidity of said hypothesis (Pérez, 2008; Vílchez et al., 2011b). This has also been proved in this research. Figure 7.18 shows the maximum horizontal force and its respective vertical force in the crest $[Fh_{max}, Fv_x]$ as well as the maximum vertical force and its respective horizontal force in the crest $[Fh_x, Fv_{max}]$ for every wave of a sea state tested for the HMB typology. It can be observed that the maximum horizontal and vertical forces are not in phase. The maximum horizontal force is associated with a given vertical force, and the maximum vertical force is associated with a given horizontal force. Moreover, there is a combination of forces whose effect on the structure could be equal or even more unfavorable than the two combinations of maximum and their concomitant

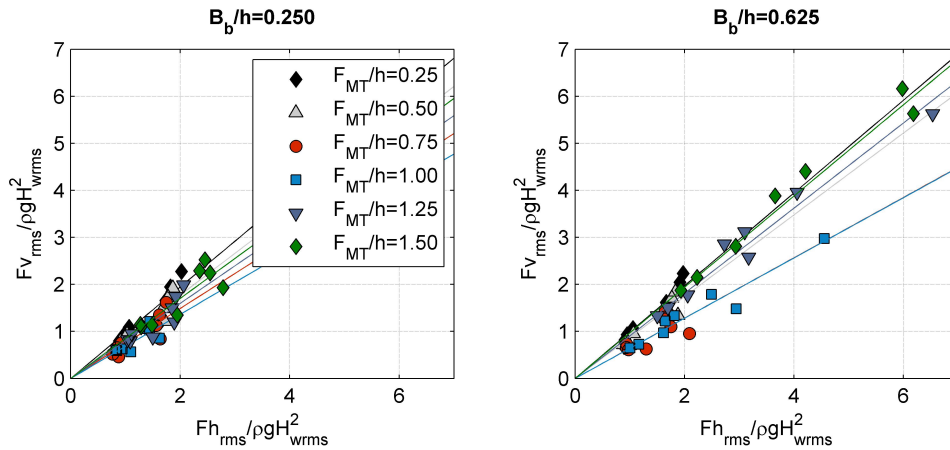


Figure 7.17.: Relationship between r.m.s value of the non-dimensional horizontal and vertical forces as a function of F_{MT}/h and B_b/h . Type C and D.

forces. Consequently, in order to design the crown of the breakwater different combinations of horizontal and vertical forces should be analysed.

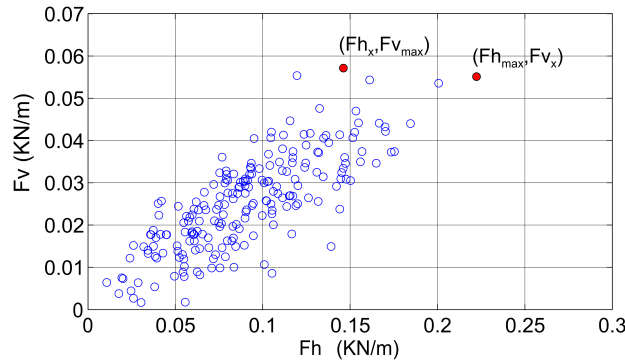


Figure 7.18.: Simultaneous vertical and horizontal forces for HMB typology.

In this subsection the probability density functions of the horizontal and vertical forces in the wave crest are studied. Then, the joint probability density function of these variables has been obtained.

Probability density function of the horizontal and vertical forces in the wave crest

The probability density functions of the horizontal and vertical forces in the wave crest (Fh and Fv respectively) have been calculated for each sea state. Based on these results, the theoretical pdf is then obtained. Figure 7.19 display the empirical histogram of the non-dimensional value of Fh (left) and Fv (right) juxtaposed with the calculated histogram for type B with $B=0.14$ m, $h_b/h=0.25$, $D=40$ mm, $T_{p\ teo}=2.25$ s and $H_{Is\ teo}=0.06$ m. The best fit for both variables, Fh and Fv , has been found to be the Weibull probability density function (Equation 6.26).

The Weibull parameters, β_w and δ_w for Fh y Fv are shown in figure 7.20 and 7.21 for type B and figure 7.22 and 7.23 for type C and D respectively. The scale parameter δ_w normalized with respect to the r.m.s value of the total wave height at the wall has been compared with the non-dimensional r.m.s of Fh or Fv . For all three breakwater typologies, these two variables have a linear relation with 1:1 slope. Therefore this parameter could be accurately approximated to the root mean square value of the variable. The shape parameter, β_w , has been related to the shape parameter of the total

Type	h_b/h	B/L	α_4	
B	0.25	$B/L < 0.10$	0.18	
		$0.10 \leq B/L < 0.28$	0.70	
		$0.28 \leq B/L < 1.20$	1.99	
	0.50	$B/L < 0.10$	0.37	
		$0.10 \leq B/L < 0.28$	1.11	
		$0.28 \leq B/L < 1.20$	2.54	
Type	B_b/h	B/L	F_{MT}/h	α_4
C and D	0.250	$0.10 < B/L < 0.35$	0.25	0.97
			0.50	0.89
			0.75	0.74
			1.00	0.68
			1.25	0.80
			1.50	0.85
	0.625	$0.10 < B/L < 0.35$	0.25	0.99
			0.50	0.87
			0.75	0.64
			1.00	0.64
			1.25	0.91
			1.50	0.97

Table 7.4.: α_4 values for the different typologies.

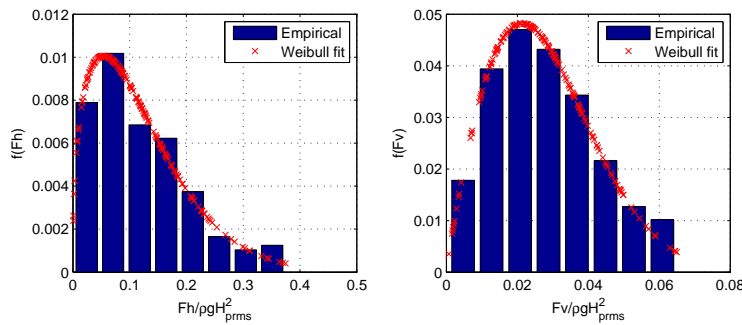


Figure 7.19.: Probability density function of the non-dimensional horizontal (left figure) and vertical (right figure) force in the wave crest. Type B, $B=0.14$ m, $h_b/h=0.25$, $D=40$ mm, $T_p\ teo=2.25$ s and $H_{Is\ teo}=0.06$ m. Empirical and theoretical fit (Weibull distribution).

wave height at the breakwater wall, $\beta_w(H_w)$, as a function of k_0h (with k_0 the wave number at the breakwater toe), h_b/h and Dk for type B. This relationship is approximately constant or increases slightly with k_0h for both variables, Fh and Fv , and for both relative foundation depths. However, for Fv data scattered increases. For type C and D results are shown as a function of F_{MT}/h and B_b/h . Two different behaviours are observed depending on the portion of the caisson that the berm is protecting. This parameter is constant or increases slightly with k_0h for $F_{MT}/h \leq 1.00$ and decreases for $F_{MT}/h > 1.00$. A weakly influence of B_b/h has been observed. The best fit for the relationship between the shape parameters of the pdf of these two variables is given in table 7.5.

Joint cumulative distribution of horizontal and vertical forces

If V_1 and V_2 are two variables with a Weibull pdf described by δ_{w1}, β_{w1} and δ_{w2}, β_{w2} , the scale and shape parameters respectively; and $0 \leq \rho_r \leq 1$ is the linear correlation coefficient defined as:

$$\rho_r = \frac{Cov(V_1, V_2)}{\sqrt{\sigma_s^2(V_1)\sigma_s^2(V_2)}} \quad (7.18)$$

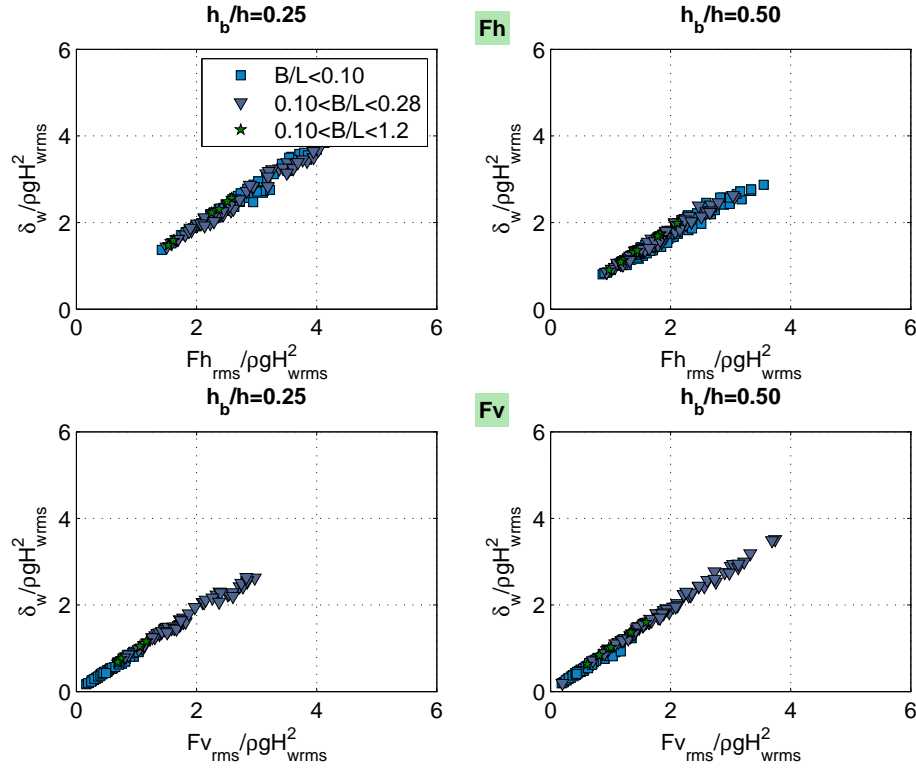


Figure 7.20.: Non-dimensional value of δ_w compared with the non-dimensional value the r.m.s of Fh and Fv as a function of B/L and h_b/h . Type B.

the joint probability density function of the normalized variables V_1/δ_{w1} and V_2/δ_{w2} can be defined as (Yacoub et al., 2005):

$$p(v_1, v_2) = \frac{\beta_{w1}\beta_{w2}v_1^{\beta_{w1}-1}v_2^{\beta_{w2}-1}}{1 - \rho_r} \exp\left(-\frac{v_1^{\beta_{w1}} + v_2^{\beta_{w2}}}{1 - \rho_r}\right) I_0\left(\frac{2\sqrt{\rho_r v_1^{\beta_{w1}} v_2^{\beta_{w2}}}}{1 - \rho_r}\right) \quad (7.19)$$

where I_0 is the modified Bessel function of the first kind and order 0 (Abramowitz and Stegun, 1972). Joint cumulative distribution can be obtain from 7.19 as:

$$P(v_1, v_2) = \int \int p(v_1, v_2) dv_1 dv_2 \quad (7.20)$$

Joint pdf of the normalized Fh and Fv ($Fh/\delta_w(Fh)$ and $Fv/\delta_w(Fv)$ respectively) has been obtained. Figure 7.24 shows the empirical joint pdf juxtaposed with the theoretical one calculated with equation 7.19 for a breakwater type B with $F_{MT}/h=0.75$, $B_b/h=0.25$, $T_{p\ teo}=1.05$ s, $H_{I_s\ teo}=0.04$ m and $D=40$ mm. Results show that the joint pdf of $Fh/\delta_w(Fh)$ and $Fv/\delta_w(Fv)$ fits fairly good to the theoretical pdf defined with equation 7.19. The value of ρ_r is presented in figures 7.25 and 7.26 for types B, and C and D respectively with the fit to calculate it given in table 7.6 as a function of the *breakwater typology*. Results show that ρ_r decreases whit the water depth increases for all breakwater typologies. Moreover, its value depends on the other parameters defining the *breakwater typology*.

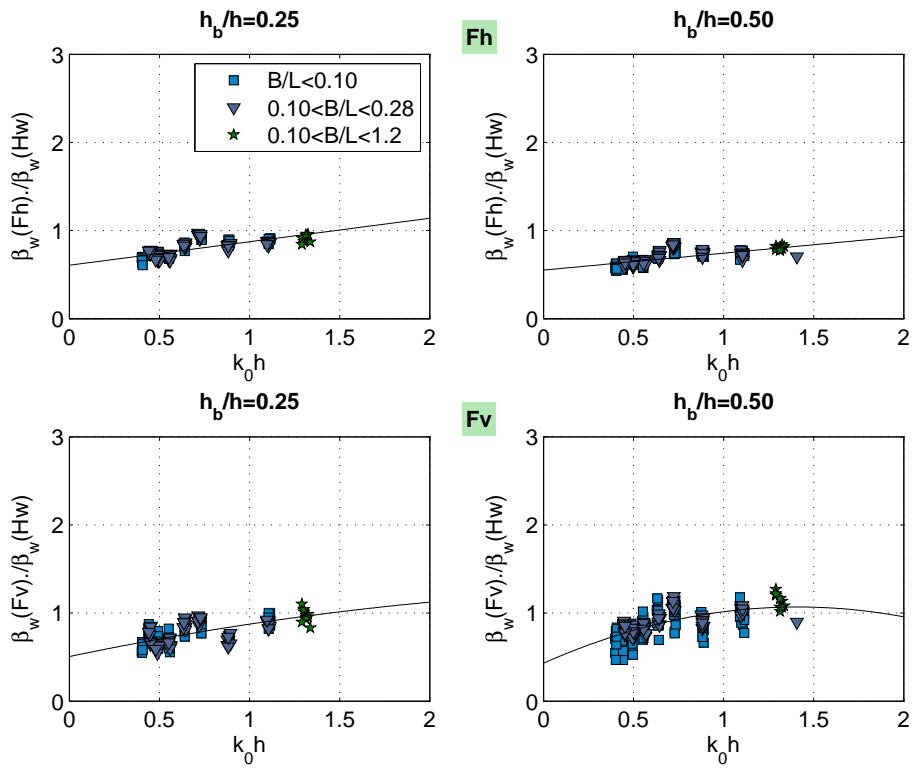


Figure 7.21.: Relationship between β_w in Weibull pfd of Fh or Fv and H_w as a function of $k_0 h$, B/L and h_b/h . Type B.

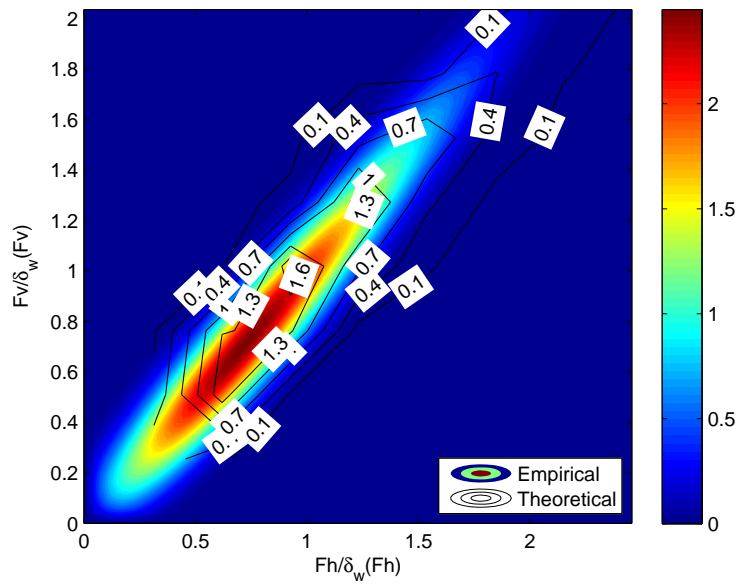


Figure 7.24.: Joint probability function of Fh and Fv . Type C, $F_{MT}/h=0.75$, $B_b/h=0.25$, $T_{p\ teo}=1.05$ s, $H_{Is\ teo}=0.04$ m and $D=40$ mm. Empirical and theoretical fit (equation 7.19).

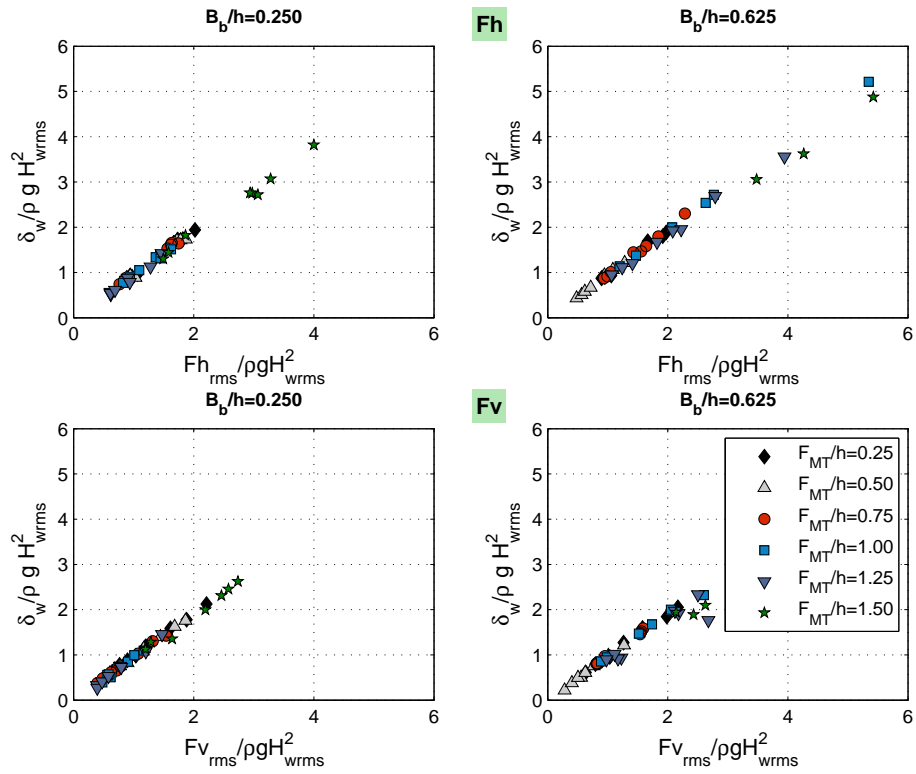


Figure 7.22.: Non-dimensional value of δ_w compared with the non-dimensional value the r.m.s of Fh and Fv as a function of F_{MT}/h and B_b/h . Type C and D.

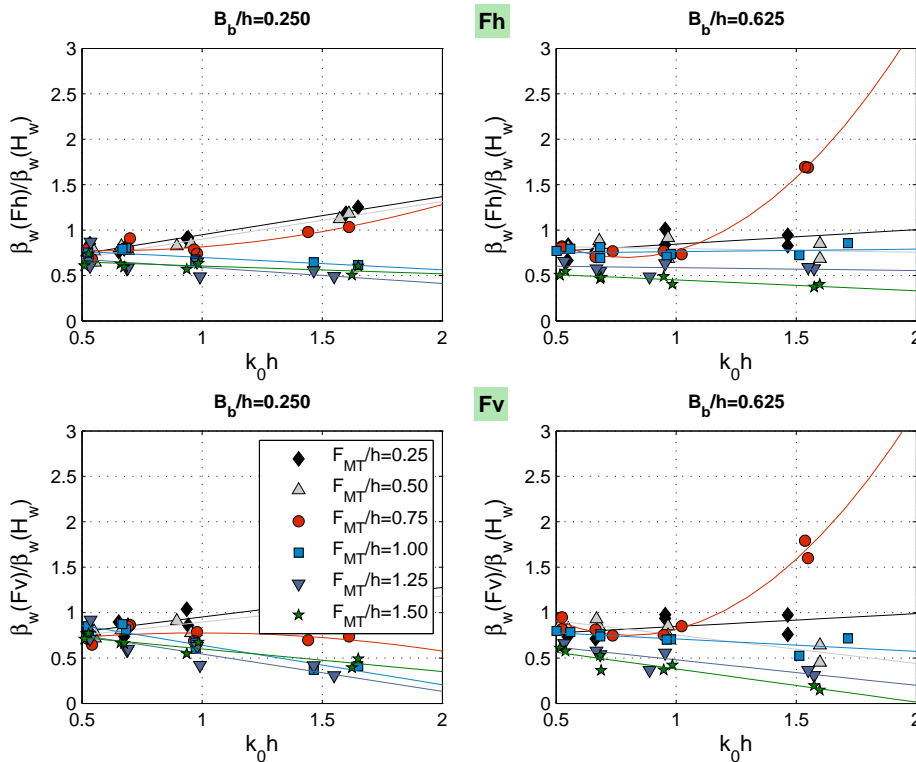


Figure 7.23.: Relationship between β_w in Weibull pfd of Fh or Fv and H_w as a function of $k_0 h$, F_{MT}/h and B_b/h . Type C and D.

$$\frac{\beta_w(Fh,v)}{\beta_w(H_w)} = a_{\beta F1}(k_0h)^2 + a_{\beta F2}(k_0h) + a_{\beta F3}$$

Type	h_b/h	Fh			Fv			
		$a_{\beta F1}$	$a_{\beta F2}$	$a_{\beta F3}$	$a_{\beta F1}$	$a_{\beta F2}$	$a_{\beta F3}$	
B	0.25	0.27	0.61	0	0.43	0.51	-0.06	
	0.50	0.19	0.55	0	0.90	0.43	-0.32	
Type	B_b/h	F_{MT}/h	$a_{\beta F1}$	$a_{\beta F2}$	$a_{\beta F3}$	$a_{\beta F1}$	$a_{\beta F2}$	$a_{\beta F3}$
C and D	0.250	0.25	0.42	0.53	0	0.33	0.63	0
		0.50	0.41	0.49	0	0.29	0.61	0
		0.75	-0.31	0.87	0.23	0.39	0.58	-0.20
	0.650	1.00	-0.13	0.83	0	-0.44	1.07	0
		1.25	-0.18	0.77	0	-0.41	0.96	0
		1.50	-0.09	0.69	0	-0.25	0.85	0
C and D	0.250	0.25	0.16	0.69	0	0.14	0.71	0
		0.50	-0.04	0.84	0	-0.31	1.06	0
		0.75	-2.78	1.80	1.75	-2.8	1.88	1.74
	0.650	1.00	0.03	0.74	0	-0.14	0.84	0
		1.25	-0.03	0.62	0	-0.28	0.76	0
		1.50	-0.12	0.57	0	-0.36	0.75	0

Table 7.5.: Best fit to calculate the relationship between β_w in Weibull pfd of Fh or Fv and H_w .

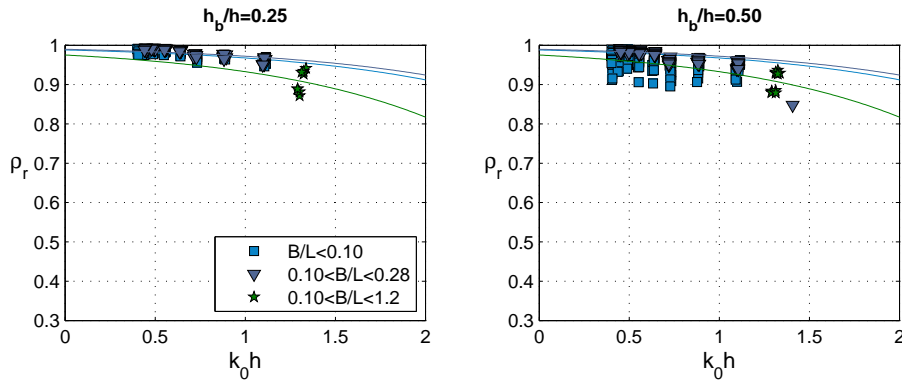


Figure 7.25.: Linear correlation coefficient between Fh and Fv as a function of k_0h and B/L . Type B.

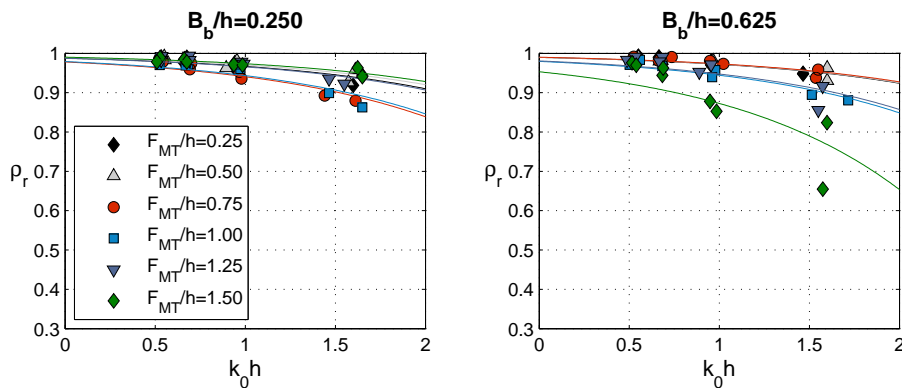


Figure 7.26.: Linear correlation coefficient between Fh and Fv as a function of k_0h . Type C and D.

				$\rho_r = a_{\rho_r} e^{k_0 h} + 1$
Type	h_b/h	B/L	a_{ρ_r}	
B	0.25	$B/L < 0.10$	-0.012	
		$0.10 \leq B/L < 0.28$	-0.010	
		$0.28 \leq B/L < 1.20$	-0.025	
	0.50	$B/L < 0.10$	-0.022	
		$0.10 \leq B/L < 0.28$	-0.026	
		$0.28 \leq B/L < 1.20$	-0.025	
Type	B_b/h	B/L	F_{MT}/h	a_{ρ_r}
C and D	0.250	$0.10 < B/L < 0.35$	0.25	-0.012
			0.50	-0.011
			0.75	-0.021
			1.00	-0.021
			1.25	-0.013
			1.50	-0.010
	0.625	$0.10 < B/L < 0.35$	0.25	-0.010
			0.50	-0.010
			0.75	-0.010
			1.00	-0.021
			1.25	-0.020
			1.50	-0.047

Table 7.6.: Best fit to calculate the linear correlation coefficient between Fh and Fv as a function of k_0h and B/L .

7.4.3 Calculation scheme

For a given sea state $[H_{I_{rms}}, T_{01}]$ with normal incidence, and a pre-design breakwater typology, the methodology to calculate the failure probability of the breakwater associated with this sea state is the following:

- 1 To calculate K_R and ϕ from the hydraulic performance curves.
- 2 To obtain the r.m.s value of the total wave height at the breakwater toe, H_{prms} as:

$$H_{prms}(x) = H_{I_{rms}} \sqrt{1 + K_R^2 + 2K_R \cos(2k_0x + \phi)} \quad (7.21)$$

- 3 To calculate the r.m.s value of the total wave height at the breakwater wall, H_{wrms} . This can be obtained from the Weibull pdf as a function of H_{prms} , α_w and β_w as:

$$H_{wrms} = \sqrt{(\alpha_w H_{prms})^2 \Gamma\left(1 + \frac{2}{\beta_w}\right) - \left[\alpha_w H_{prms} \Gamma\left(1 + \frac{1}{\beta_w}\right)\right]^2} \quad (7.22)$$

where Γ is the gamma function.

- 4 To obtain r.m.s value of the horizontal force by integrating the pressure law at the breakwater wall (figure 7.27). The final expression as a function of H_{wrms} is given by:

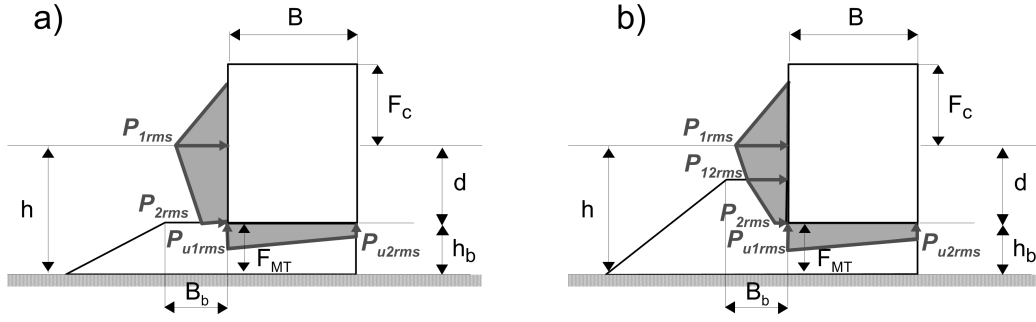


Figure 7.27.: Scheme of pressure.

- For type C and $F_{MT}/h = 0.75$ (Figure 7.27 b):

$$Fh_{rms} = \rho g \frac{H_{trms}(x_4)}{8} \left\{ H_{trms}(x_4) + 2(h - h_b) \left(1 + \frac{\cosh(k_0 h_b)}{\cosh(k_0 h)} \alpha_2 \right) \right\} \alpha_1 \alpha_I \quad (7.23)$$

- For the rest of the typologies (Figure 7.27 a):

$$Fh_{rms} = \rho g \frac{H_{trms}(x_4)}{8} \left\{ H_{trms}(x_4) + 2[(h - F_{MT}) + (h - h_b) \frac{\cosh(k_0 F_{MT})}{\cosh(k_0 h)} + (F_{MT} - h_b) \frac{\cosh(k_0 h_b)}{\cosh(k_0 h)}] \alpha_2 \alpha_1 \alpha_I \right\} \quad (7.24)$$

where $\alpha_1 = 1.14$; α_I is given in figure 7.4 for HMGB and $\alpha_I = 1$ for the rest of typologies; and α_2 is given in table 7.2.

5 To calculate Fv_{rms} as follows:

$$Fv_{rms} = Fh_{rms} \alpha_4 \quad (7.25)$$

α_4 can be obtained from table 7.4.

6 To evaluate the bi-parametric Weibul pdf of Fh and Fv (equation 6.26). The scale parameters are $\delta_w = Fh_{rms}$ or Fv_{rms} respectively. The shape parameter, β_w can be calculated as a function of $\beta_w(H_w)$ as given in table 7.5.

7 To obtain the joint pdf of $[Fh, Fv]$ with equation 7.19. The value of ρ_r can be calculated as given in table 7.6.

8 Applying simulation technique series of Fh and Fv can be obtained from its marginal and joint pdfs, and the pdf of the safety margin S can be obtained for this sea state.

The failure probability of the breakwater in its useful life for this failure mode can be estimated by repeating the previous process for the different sea states (with an associated probability of occurrence) that can occur in the useful life of the breakwater.

7.5 Conclusions

An unified method has been proposed to simultaneously verify the failure modes produced by the same wave conditions which affect the front or face of the breakwater. The methodology is based on the derivation of the pdf of the kinematic and dynamic variables of the total oscillation in front of the breakwater as a function of the total wave height at that same location. These variables define the actions in the breakwater and are necessary to formulate the verification equation of the failure modes.

This methodology has been developed for the failure mode that considers sliding of the superstructure. The following conclusions have been obtained:

- 1 The r.m.s of the dynamic pressure in the wave crest at the breakwater wall and at the bottom of the caisson is directly proportional to the r.m.s wave height at this location. An approximation to calculate the r.m.s of these pressure laws has been proposed based on the evaluation of the transfer function between these variables for a representative frequency. Results show that the pressure above the S.W.L. is hydrostatic except in the case of the highest pressures in which nonlinear effects can occur and when impact pressures take place. Under the S.W.L., the pressure law follows an hyperbolic cosine function, but this law is modified by the presence of the toe berm. The uplift pressure depends mainly on the transmission coefficient. Three types of uplift laws have been defined as a function of the relative width of the caisson. A simplified scheme has been proposed to obtain the pressure laws depending on the *breakwater typology*.
- 2 The r.m.s value of the horizontal and vertical forces in the crown wall have been obtained by integrating the horizontal and uplift pressure laws respectively. The relation between the non-dimensional values of these forces is linear. Three force regimes have been defined as a function of B/L depending on which force predominates.
- 3 The probability density functions of the horizontal and vertical forces in the wave crest have been calculated. These follow a bi-parametric Weibull distribution. The scale parameter is the r.m.s of these variables, which can be obtained directly from the total wave height at the wall applying the developed pressure scheme. The shape parameter depends on the relative depth and the *breakwater typology*. It has been calculated in terms of the shape parameter of the Weibull distribution of the total wave height at the breakwater wall.
- 4 It is noted that the maximum horizontal and uplift force are not always in phase. Moreover different combination of horizontal and vertical forces could produce even more unfavourable effects than the previous two combinations. Therefore, the joint probability density function of the horizontal and vertical forces in wave crest has been derived. This distribution can be calculated with parameters related to those of the marginal Weibull distribution of these variables and the linear correlation coefficient which depend on the relative depth and the *breakwater typology*.
- 5 The safety margin in the verification equation can be obtained from the horizontal and vertical forces in the wave crest of a given sea state. The failure probability of the breakwater in its useful life for this failure mode can be estimated by applying the previous process for the different sea states (with an associated probability of occurrence) that can occur in the useful life of a breakwater. The verification equation of the other failure modes produced by

the same agent, wind waves, in the front or face of the breakwater could be obtained in the same way, and to simultaneously verify all of these failure modes.

Conclusions and future research

8.1 Conclusions

The aim of this Thesis was to develop an unified methodology for verifying breakwaters design based on the hydraulic performance under perpendicularly impinging wind waves. To achieve this goal, a combination of experimental and numerical works has been performed. The main conclusions are organised according to the different specific objectives defined in section 1.3.2:

- Objectives 1 and 2: *To obtain a parameter list to represent all variables involved in the wave-breakwater interaction and to analyse their influence in the hydraulic performance of different breakwater typologies; and to derive an unified expression to calculate the variables that define the hydraulic performance: reflection coefficient (modulus and phase), transmission coefficient and wave energy dissipation rate, depending on the parameters identified in the previous specific objective.*

The hydraulic performance resulting from the wave breakwater interaction was analysed. This can be evaluated by means of the modulus and phase of the wave reflection coefficient, the wave transmission coefficient, and the rate of energy dissipation. A parameter list was designed containing the non-dimensional monomials that influence the hydraulic performance for different breakwater typologies: (A) porous vertical breakwater (PVB); (B) composite breakwater (CB); (C) mixed breakwater with a berm below or at S.W.L. (low and high mound breakwater, LMB and HMB, respectively, and a high mound composite breakwater, HMCB); (D) mixed breakwater with a berm above S.W.L. (rubble mound breakwater with crown walls, RMB-CW); (E) a rubble mound breakwater, plane slope (RMB) and (F) S-breakwater.

Experimental results have confirmed that the hydraulic performance depends on the dimensions and properties of the parts and elements of the breakwater as well as on the wind wave characteristics. When the characteristics of the wind wave train is modified, most of the structures transit between the following regimes: (a) the standing oscillatory regime (full wave reflection); (b) partial standing oscillatory regime (partial wave reflection); (c) dissipative regime; and (d) transmitted oscillatory regime. Indeed, all of the breakwater typologies cover a full spectrum of oscillatory regimes.

A unified expression (the logistic sigmoid function) was found to define the domain of the hydraulic performance of all of these breakwaters typologies. The main variable of the sigmoid function is the 2D scattering parameter A_{eq}/L^2 , where A_{eq} is the area of the porous medium below the S.W.L. and L is the wave length. This curve is defined with four parameters: the two asymptotic (initial and final) values and the blending and shape parameters. The initial and final values correspond to the representative values of the smallest and greatest expected

wave steepness and identify the dominant process: reflection, transmission or dissipation of energy. These four parameters depend on the relative grain diameter, D_k , and on the non-dimensional parameters that represent the breakwater geometry. These were obtained for all breakwater typologies analysed in this work.

- Objective 3: *To design a tool that allows the reliable use of a numerical model based on VARANS equations to quantify the hydraulic performance of different breakwater types.*

A method to numerically calculate the hydraulic performance of different breakwater typologies was developed. This method is based on the definition of the frictional forces in the porous medium by a linear coefficient that is constant in the porous medium volume and stationary in the wave cycle. A characteristic friction diagram was proposed to calculate this coefficient. Results show that the accurate evaluation of the friction forces in the porous medium is a determining factor to define the hydraulic performance. The characteristic friction coefficient depends on the breakwater typology and geometry, mainly on the relative diameter of the granular material, D_k . It is expected that this method reduces costs and saves time in the breakwater pre-design stage.

- Objective 4: *To find an approximation to calculate the total oscillation in front or in the face of the breakwater applying the hydraulic performance curves.*

An approximate solution to calculate the total oscillation in front of the breakwater was presented. This consists of defining the probability density function (pdf) of the wave height in front and at the face of the breakwater as a function of the root mean square value of the wave height at the breakwater toe. This value can be accurately calculated by using the modulus and phase of the reflection coefficient, given by the hydraulic performance curves. Results show that the total wave train in front of the breakwater followed a Rayleigh distribution in which the scale parameter is the root mean square of the total wave height. From the toe of the structure to the toe of the crown, the pdf of the total wave height evolves from a Rayleigh distribution to a Weibull bi-parametric distribution, depending on energy dissipation by wave breaking and friction in the porous medium, both of which are contingent on the breakwater typology. The scale and the shape parameters of the Weibull distribution vary along the breakwater face, depending on breakwater typology, granular characteristics of the porous medium, location, and relative water depth. The largest deviation from the Rayleigh distribution occurs at the toe of the crown.

Two theoretical pdf of the total wave height were proposed : (1) a Rayleigh distribution in front of the breakwater with parameter the approximated root mean square of the total wave height at the breakwater toe as scale parameter; and (2) a bi-parametric Weibull distribution at the breakwater face with parameters described in terms of the root mean square of the total wave height at the toe of the structure.

- Objective 5: *To verify the breakwater stability as a function of the total oscillation in front or at the face of the breakwater.*

An unified method has been proposed to simultaneously verify the failure modes produced by the same wave conditions which affect the face of the breakwater. The method is based on the derivation of the pdf of the kinematic and dynamic variables of the total oscillation in front of the breakwater as a function of the total wave height at the same location. These variables define the actions in the breakwater and are necessary to formulate the verification

equation of the failure modes. The methodology has been developed for the sliding of the superstructure failure mode, but can be applied in the same way to any failure modes produced by the wind wave at the face of the breakwater. Results show that the dynamic and kinematic variables, in this case dynamic pressures, are directly proportional to the total oscillation in the studied section. Therefore, the pdf of the total horizontal and vertical forces amplitude also fit to a Weibull distribution whose parameters can be derived as a function of the total wave height pdf parameters. The safety margin in the verification equation is formulated according to these variables of force and consequently, the pdf of the safety margin can be obtained and the failure probability of the breakwater for this failure mode and sea state calculated. The verification equation of the others failure modes produced by the same agent, wind waves, in the front or face of the breakwater could be obtained in the same way, and a simultaneously verification of these failure modes could be performed.

8.2 Future research

The ROM (ROM 1.0, 2009) methodology establishes that the breakwater design should be done considering all of the principal failure modes that can affect the breakwater stability during its useful life under ultimate and serviceability limit state. This work has intended to improve the knowledge in the breakwater design by proposing a scheme of work which linked directly the response of the breakwater to the wave action by means of the hydraulic performance resulting from this interaction. Therefore, different failure modes produced by the same agent can be analysed simultaneously. After these results, future researchs are required. Three main lines are proposed:

- 1 The first one should be focused on obtaining and calibrating expressions to verify other different failure modes. The pdfs of the variables involved in this failure modes would be obtained in the way proposed in this Thesis. This study should focus, in the first place, in three of the main failure modes that affect the security and operativity of a breakwater by the wave attack:
 - Wave overtopping. Several authors affirm that when wave action significantly overtops the structure, the reflection coefficient decreases in regards to the value of the non-overtoppable breakwater (Takahashi, 1996). It is less known the phase of the reflection coefficient also varies. As a result, the oscillatory pattern at the toe and at the face of the breakwater would change. The mean overtopping flow volume in the sea state or other equivalent statistical magnitude depends on this oscillatory regime in front of the breakwater (Clavero, 2007). Generally, breakwaters in port installations are designed so as not to be very overtoppable. Then, experimental works should be done to quantify this phenomenon for low overtoppable breakwaters.
 - Displacement of the armor stone in the main layer and in the toe berm. The current formulas to calculate the required rock size in the rubble or toe structure are based on the stability number. This is formulated as a function of the incident wave conditions (van der Meer, 1998; van Gent and van der Werf, 2014). Experimental tests should be performed with different granular materials (diameter and porosity) in order to relate the damage with the velocities and accelerations affecting these part of the breakwater.
- 2 The second line should be focused on developing techniques to quantify the main failure modes initiation and the response and evolution of the breakwater damage when different failure modes are produced simultaneously. Experimental tests for different breakwater

typologies subject to a loading cycle should be done, analysing the relationship with the hydraulic performance and considering the time scale of damage evolution following Castillo et al. (2012).

- 3 Finally, the third line should focus on how the hydraulic performance is modified when the incident wave angle increases. For not overly oblique waves ($15^\circ < \theta < \theta_{Brewster}$), it is well known that the reflection coefficient modulus decreases depending on the porosity of the medium (Dalrymple et al., 1991). The Brewster angle is the angle in which zero reflection is produced. For wave incidence more oblique than the Brewster angle, the linear reflection process does not hold, and the wave crest propagates along the breakwater, and diffraction inside the porous structure takes place (Dalrymple et al., 1991). Results for low incidence wave angles could be implemented analytically following the methodology proposed by Pérez (2008). For larger incidence angles, experimental work in 3D should be performed.

Fitting of sigmoid function for reflection (modulus and phase) and transmission coefficients and wave energy dissipation rate

This appendix includes the parametric expressions for obtaining the reflection and transmission coefficient modulus and reflection phase. The wave energy dissipation rate can be calculated from these results with the energy conservation equation (2.10). The sigmoid curve proposed is the following:

$$Y_i = (Y_{i1} - Y_{i0}) \left[1 + \left(\frac{A_{eq}/L^2}{a_{Xi}} \right)^{\gamma_i} \right]^{-1} + Y_{i0} \quad \left\{ \begin{array}{l} A_{eq}/L^2 > 0 \\ Y_{i0} < Y_i < Y_{i1} \text{ or } Y_{i1} < Y_i < Y_{i0} \end{array} \right. \quad (\text{A.1})$$

where i is the index denoting the modulus of the reflection coefficient, K_R , the modulus of the transmission coefficient, K_T , the phase of the reflection coefficient, ϕ , or the wave energy dissipation rate, D^* . The selected independent variable is the relative volume of granular material per unit of breakwater width, or 2D scattering parameter, $X = A_{eq}/L^2$. γ_i , a_{Xi} , Y_{i1} and Y_{i0} are the parameters fitted of the curve and depend on granular characteristics, the breakwater geometry, and incoming wave train characteristics.

This curve was obtained for the breakwater types analyzed and is applicable within the range of adimensional monomials of table 3.3. The results are given for the following types of breakwater:

1. Type A: Porous vertical breakwater (PVB).
2. Type B: Composite breakwater (CB).
3. Type C: Low and high mound breakwater and high mound composite breakwater (LMB, HMB and HMCB).
4. Type D: Rubble mound breakwater with crown wall (RMB-CW).
5. Type E: Rubble mound breakwater (RMB).
6. Type F: S-shaped breakwater (SB).

The following sections give the results obtained for irregular wave action, classified according to breakwater type, and organized as follow (Table A.1):

- **Curves:** Figures with experimental data and parametric fitting of coefficients and phase, depending on the main monomials for each breakwater type.
- **Parameters:** Tables with the values and expressions, as well as the graphs (when relevant) of the parameters defining the corresponding sigmoid curve (γ_i , a_{X_i} , Y_{i1} and Y_{i0}) depending on the principal non-dimensional parameters.
- **Errors:** Error tables of the parametric expressions calculated with equation 4.3 and 4.4.

Type	Functional	Curve	Parameter	Error
Type A	$Y = f\left(\frac{A_{eq}}{L^2}, Dk, \frac{H_L}{L}\right)$	Figure A.1	Table A.2	Table A.3
Type B	$Y = f\left(\frac{A_{eq}}{L^2}, Dk, \frac{h_b}{h}, \frac{H_L}{L}\right)$	Figure A.2	Table A.4	Table A.5
		Figure A.3	Figure A.6	
		Figure A.4		
		Figure A.5		
Type C	$Y = f\left(\frac{A_{eq}}{L^2}, Dk, \frac{h_b}{h}, \frac{F_{MT}}{h}, \frac{B_b}{h}, \frac{H_L}{L}\right)$	Figure A.7	Table A.6	Table A.7
		Figure A.8	Figure A.11	Table A.8
		Figure A.9	Figure A.12	
		Figure A.10		
Type D	$Y = f\left(\frac{A_{eq}}{L^2}, Dk, \frac{h_b}{h}, \frac{F_{MT}}{h}, \frac{B_b}{h}, \frac{H_L}{L}\right)$	Figure A.13	Table A.9	Table A.10
		Figure A.14	Figure A.11	Table A.11
		Figure A.15	Figure A.12	
		Figure A.16		
Type E and F	$Y = f\left(\frac{A_{eq}}{L^2}, Dk, Q_p, Q_t, \frac{H_L}{L}\right)$	Figure A.17	Table A.12	Table A.13
		Figure A.19		

Table A.1.: Summary of the functional, curves, parameters and error of the hydraulic performance curves for the different breakwater types.

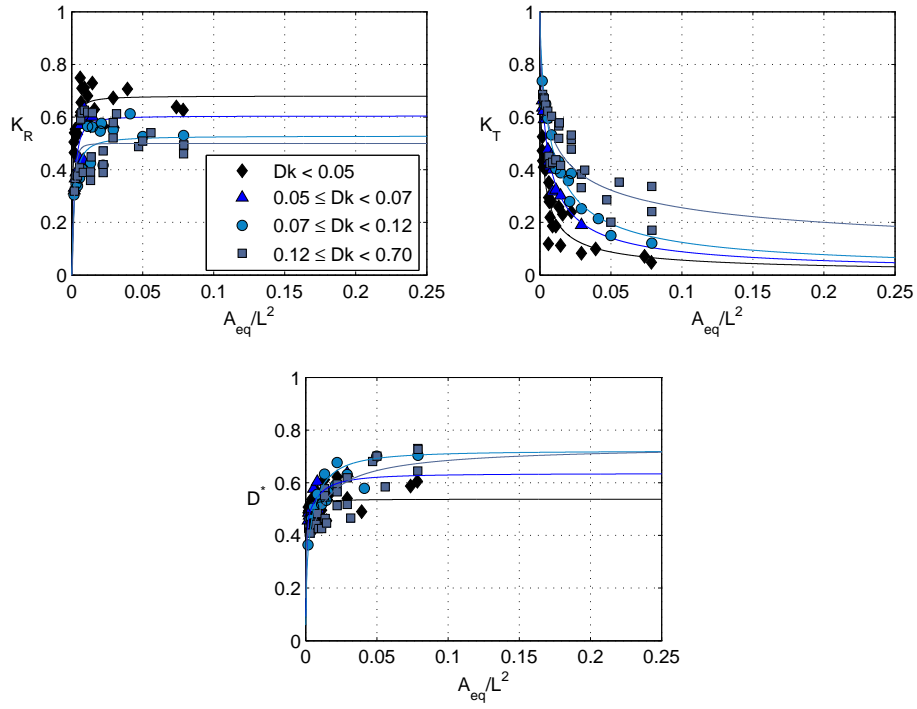


Figure A.1.: Type A (PVB). K_R , K_T and D^* as a function of A_{eq}/L^2 , and various ranges of Dk . Experimental data and best-fitted curves.

Parameter	Coefficients			
	$Dk < 0.05$	$0.05 \leq Dk < 0.07$	$0.07 \leq Dk < 0.12$	$Dk \geq 0.12$
γ_R	1.227	1.497	1.232	2.321
K_R				
a_{XR}	$7.94 \cdot 10^{-4}$	0.0019	0.0018	0.0017
K_{R1}	0	0	0	0
K_{R0}	0.680	0.604	0.528	0.500
γ_T	0.678	0.777	0.791	0.514
K_T				
a_{XT}	0.0016	0.0048	0.0081	0.0096
K_{T1}	1	1	1	1
K_{T0}	0	0.0029	0.0048	0.0319

Table A.2.: Type A (PVB). Sigmoid curve parameters for obtaining K_R and K_T .

Dk	$R^2_{K_R}$	$R^2_{K_T}$	ϵ_R
$Dk < 0.05$	0.50	0.83	0.0074
$0.05 \leq Dk < 0.07$	0.77	0.95	0.0127
$0.07 \leq Dk < 0.12$	0.64	0.97	0.0164
$Dk \geq 0.12$	0.26	0.74	0.0288

Table A.3.: Type A (PVB). Goodness of fit of the sigmoid curves for obtaining K_R and K_T .

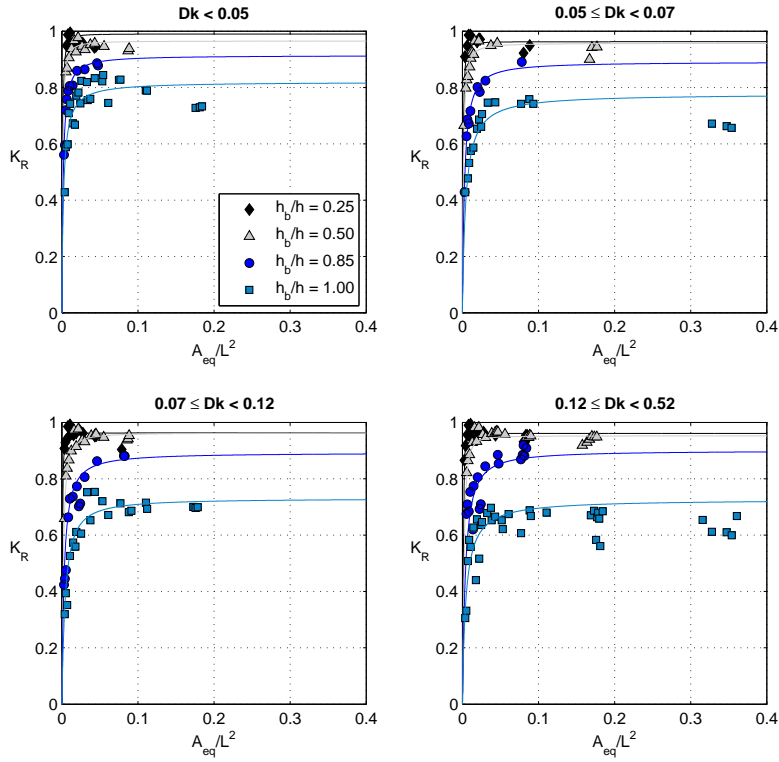


Figure A.2.: Type B (CB). K_R as a function of A_{eq}/L^2 , Dk and h_b/h . Experimental data and best-fitted curves.

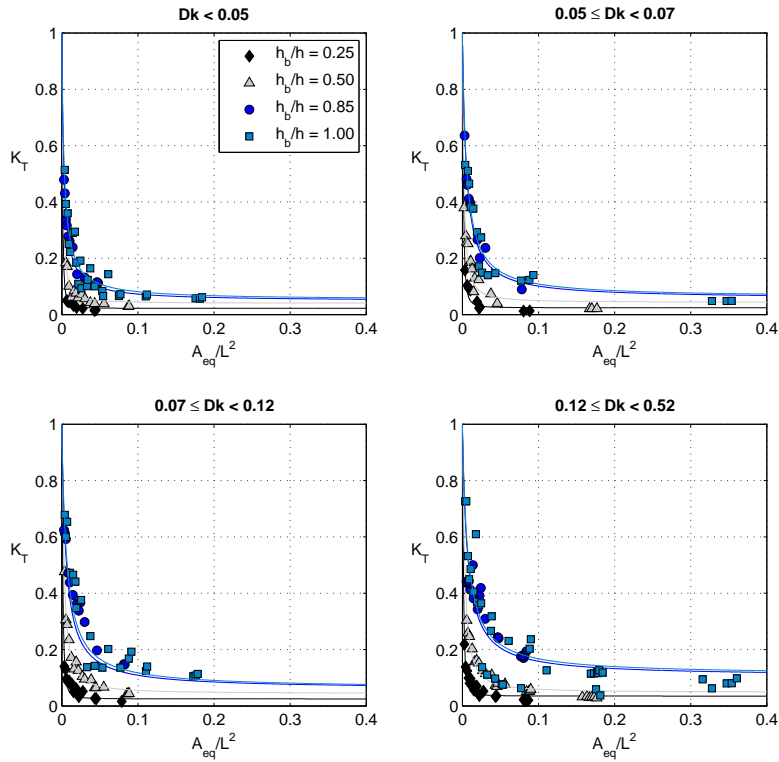


Figure A.3.: Type B (CB). K_T as a function of A_{eq}/L^2 , Dk and h_b/h . Experimental data and best-fitted curves.

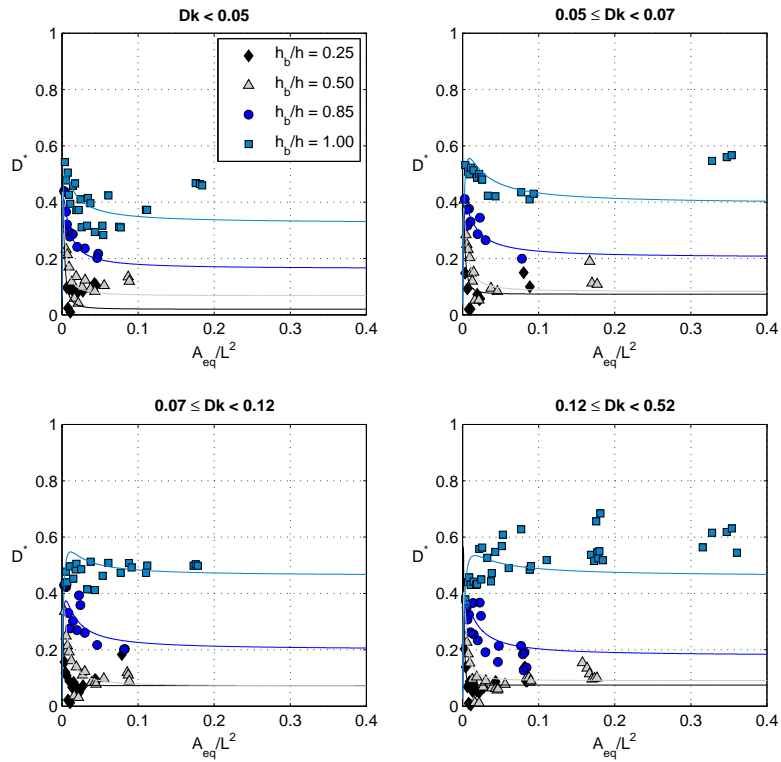


Figure A.4.: Type B (CB). D^* as a function of A_{eq}/L^2 , Dk and h_b/h . Experimental data and best-fitted curves.

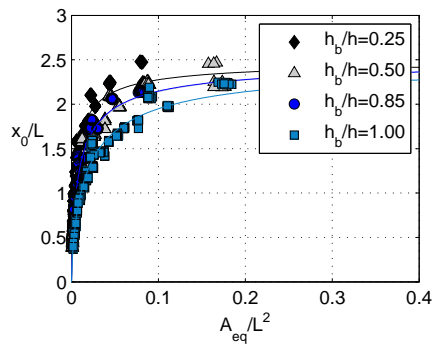


Figure A.5.: Type B (CB). x_0/L ($\phi = 4\pi x_0/L$) as a function of A_{eq}/L^2 and h_b/h for all ranges of Dk . Experimental data and best-fitted curves.

Parameter		Coefficients			
		$Dk < 0.05$	$0.05 \leq Dk < 0.07$	$0.07 \leq Dk < 0.12$	$Dk \geq 0.12$
$\gamma_R = a_{1R}(h_b/h)^{a_{2R}} + a_{3R}$ Figure A.6	a_{1R}	1.049	1.015	1.038	1.012
	a_{2R}	-0.3132	-0.3745	-0.4654	-0.7500
	a_{3R}	0	0	0	0
K_R $a_{XR} = b_{1R}(h_b/h)^{b_{2R}} + b_{3R}$ Figure A.6	b_{1R}	0.0022	0.0036	0.0035	0.0032
	b_{2R}	4.1416	4.5977	4.1665	4.0290
	b_{3R}	0.0006	0.0010	0.0011	0.0017
K_{R1}	-	0	0	0	0
$K_{R0} = c_{1R}(h_b/h)^2 + c_{2R}(h_b/h) + c_{3R}$ Figure A.6	c_{1R}	-0.3643	-0.5598	-0.8011	-0.7837
	c_{2R}	0.2503	0.4741	0.7265	0.7121
	c_{3R}	0.9448	0.8737	0.8222	0.8008
$\gamma_T = a_{1T}(h_b/h)^{a_{2T}} + a_{3T}$ Figure A.6	a_{1T}	0.954	0.954	0.954	0.954
	a_{2T}	-0.432	-0.432	-0.432	-0.432
	a_{3T}	0	0	0	0
K_T $a_{XT} = b_{1T}(h_b/h)^{b_{2T}} + b_{3T}$ Figure A.6	b_{1T}	0.0030	0.0061	0.0068	0.0080
	b_{2T}	1	1	1	1
	b_{3T}	0	0	0	0
K_{T1}	-	1	1	1	1
$K_{T0} = c_{1T}(h_b/h)^{c_{2T}} + c_{3T}$ Figure A.6	c_{1T}	0.0377	0.0468	0.0496	0.1110
	c_{2T}	1	1	1	1
	c_{3T}	0.0160	0.0153	0.0155	0.0023
γ_ϕ	-	0.751	0.751	0.751	0.751
$\frac{x_0}{L}$ $a_{X\phi} = b_{\phi 1}(h_b/h) + b_{\phi 2}$	$b_{\phi 1}$	0.0148	0.0148	0.0148	0.0148
	$b_{\phi 2}$	$7.87 \cdot 10^{-4}$	$7.87 \cdot 10^{-4}$	$7.87 \cdot 10^{-4}$	$7.87 \cdot 10^{-4}$
	$(x_0/L)_1$	-	0	0	0
$(x_0/L)_0$	-	2.50	2.50	2.50	2.50

Table A.4.: Type B (CB). Sigmoid curve parameters for obtaining K_R , K_T and ϕ .

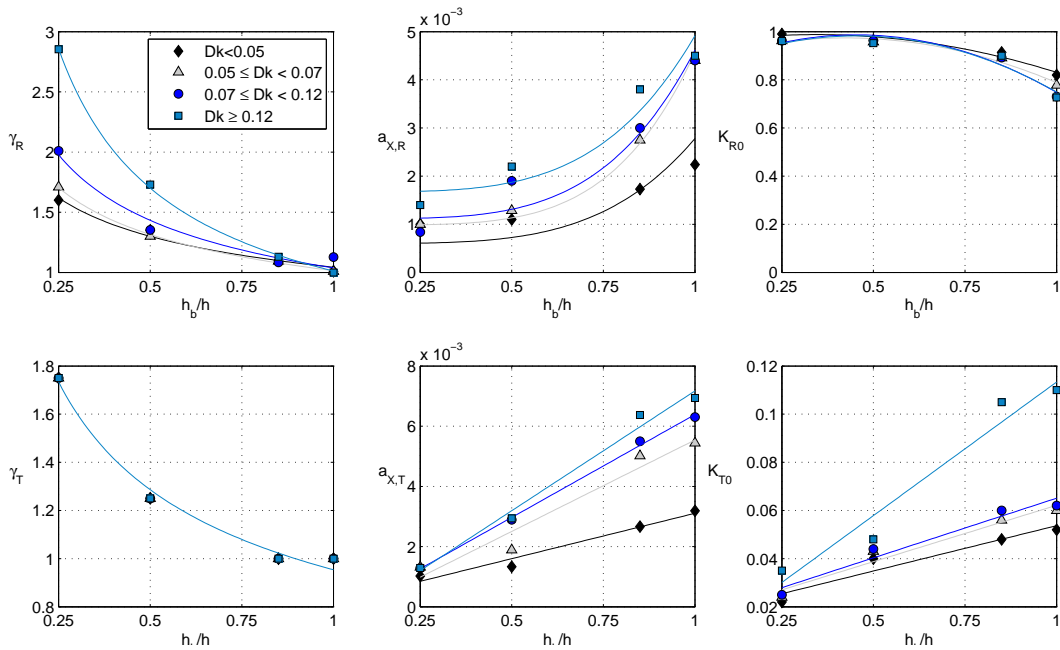


Figure A.6.: Type B (CB). Sigmoid curve parameters for obtaining K_R and K_T . Parameters obtained and best-fitted curves.

h_b/h	Dk	$R_{K_R}^2$	$R_{K_T}^2$	ϵ_R	R_ϕ^2
	$Dk < 0.05$	-	0.68	0.0080	
	$0.05 \leq Dk < 0.07$	-	0.80	0.0010	
0.25	$0.07 \leq Dk < 0.12$	0.81	0.60	0.0005	0.98
	$Dk \geq 0.12$	0.77	0.84	0.0004	
	$Dk < 0.05$	0.65	0.90	0.0004	
	$0.05 \leq Dk < 0.07$	0.90	0.87	0.0006	
0.50	$0.07 \leq Dk < 0.12$	0.90	0.98	0.0005	0.98
	$Dk \geq 0.12$	0.62	0.93	0.0005	
	$Dk < 0.05$	0.93	0.98	0.0014	
	$0.05 \leq Dk < 0.07$	0.97	0.97	0.0010	
0.85	$0.07 \leq Dk < 0.12$	0.90	0.80	0.0097	0.96
	$Dk \geq 0.12$	0.81	0.64	0.0094	
	$Dk < 0.05$	0.66	0.90	0.0058	
	$0.05 \leq Dk < 0.07$	0.79	0.92	0.0069	
1.00	$0.07 \leq Dk < 0.12$	0.91	0.86	0.0067	0.98
	$Dk \geq 0.12$	0.51	0.81	0.0150	

Table A.5.: Type B (CB). Goodness of fit of the sigmoid curves for obtaining K_R , K_T and ϕ .

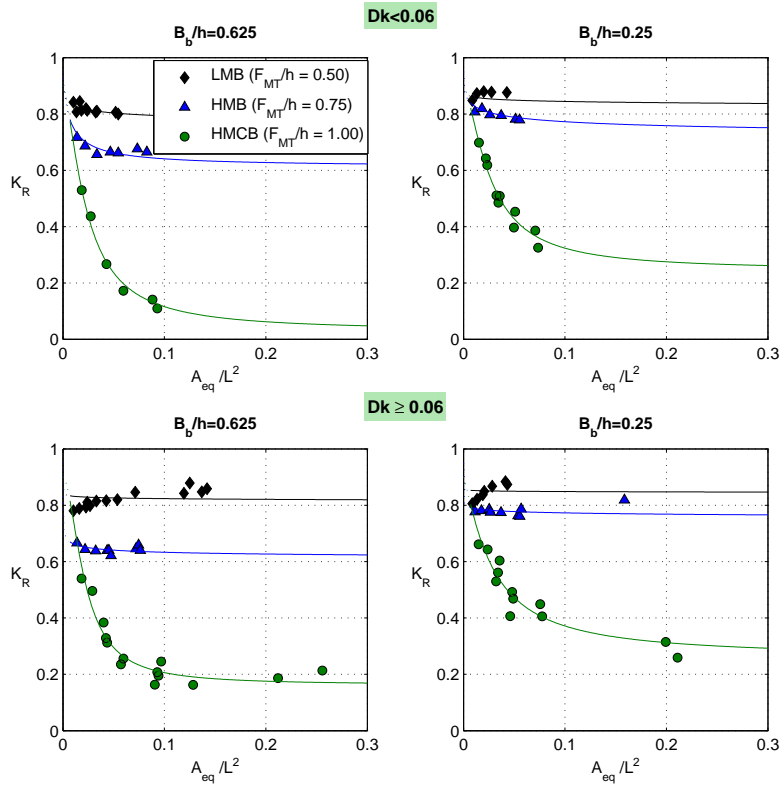


Figure A.7.: Type C (LMB, HMB and HMCB). K_R as a function of A_{eq}/L^2 , Dk , B_b/h and F_{MT}/h ($h_b/h = 0.50$). Experimental data and best-fitted curves.

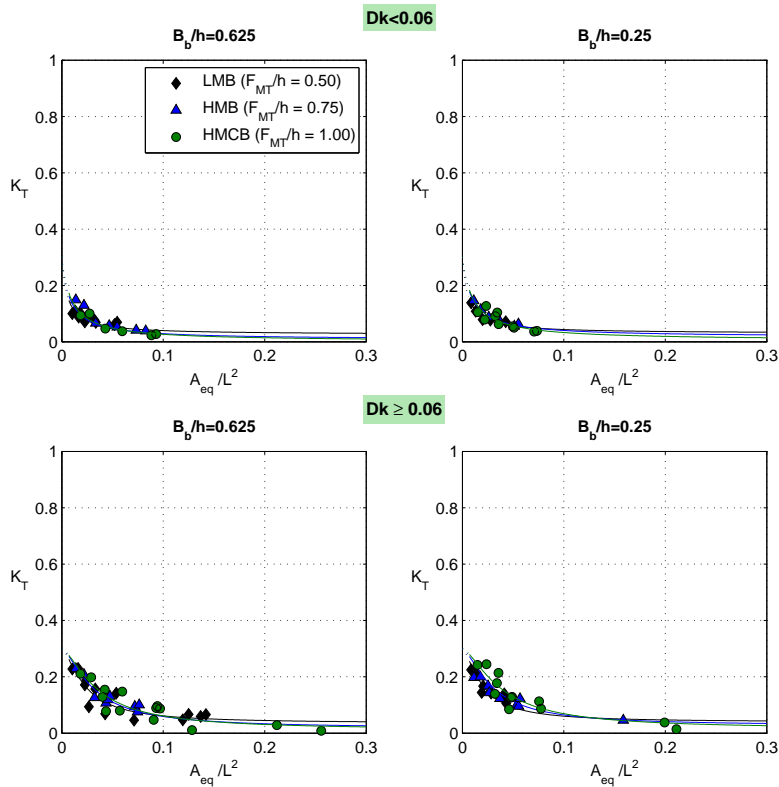


Figure A.8.: Type C (LMB, HMB and HMCB). K_T as a function of A_{eq}/L^2 , Dk , B_b/h and F_{MT}/h ($h_b/h = 0.50$). Experimental data and best-fitted curves.

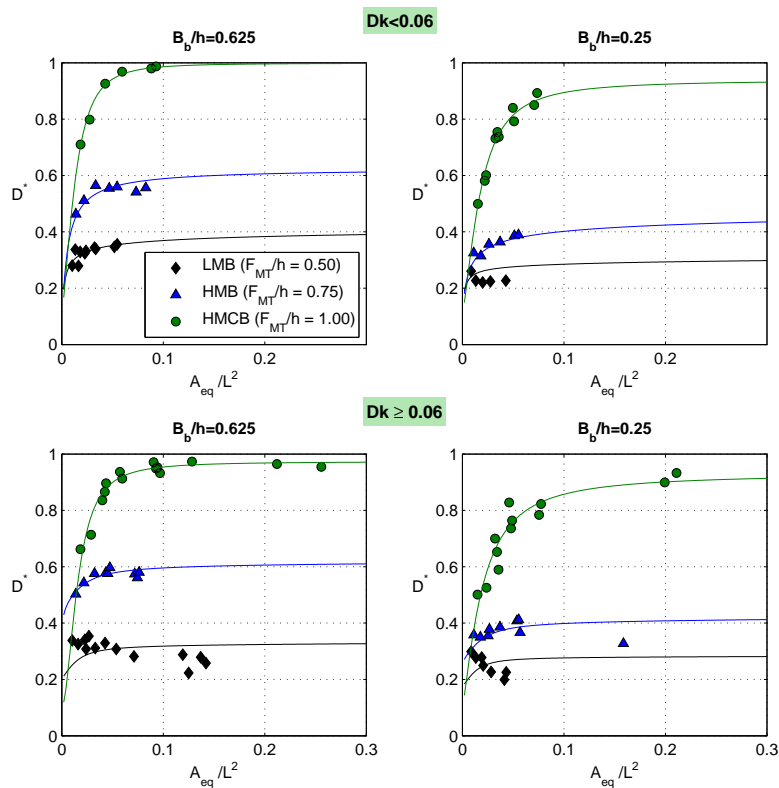


Figure A.9.: Type C (LMB, HMB and HMCB). D^* as a function of A_{eq}/L^2 , Dk , B_b/h and F_{MT}/h ($h_b/h = 0.50$). Experimental data and best-fitted curves.

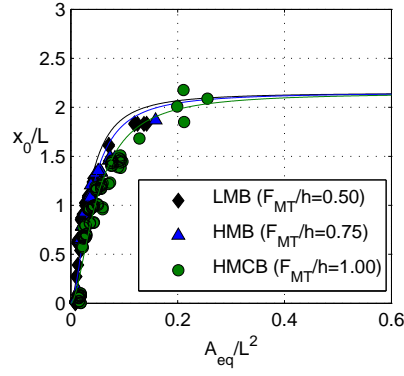


Figure A.10.: Type C (LMB, HMB and HMCB). x_0/L ($\phi = 4\pi x_0/L$) as a function of A_{eq}/L^2 and F_{MT}/h for all ranges of Dk and both two B_b/h . Experimental data and best-fitted curves.

		Coefficients			
		$B_b/h = 0.625$		$B_b/h = 0.250$	
Expression		$Dk < 0.06$	$Dk \geq 0.06$	$Dk < 0.06$	$Dk \geq 0.06$
γ_R Figure A.11	a_{1R}	1.512	1.767	1.495	1.567
	a_{2R}	1.820	5.777	4.150	6.941
	a_{3R}	0	0	0	0
K_R Figure A.11	b_{1R}	0.023	0.021	0.026	0.028
	b_{2R}	3.621	15.484	1.866	14.524
	b_{3R}	0	0	0	0
K_{R1}	-	LMB-HMB=0.95; HMCB=0.90			
K_{R0} Figure A.11	c_{1R}	-0.738	-0.620	-0.530	-0.516
	c_{2R}	5.360	4.247	6.808	6.704
	c_{3R}	0.768	0.783	0.775	0.775
γ_T Figure A.12	-	1	1.5	1	1.5
K_T Figure A.12	b_{1T}	0.0053	0.0233	0.0061	0.0237
	b_{2T}	1	1	1	1
	b_{3T}	0.0038	0.0125	0.0038	0.0118
K_{T1}	-	0.30	0.30	0.30	0.30
K_{T0} Figure A.12	c_{1T}	0.1332	0.1334	0.1116	0.1116
	c_{2T}	-0.1637	-0.1635	-0.2290	-0.2290
	c_{3T}	-0.1281	-0.1182	-0.1036	-0.0936
γ_ϕ	-	1.75	1.75	1.75	1.75
$\frac{x_0}{L}$	$b_{\phi 1}$	0.0412	0.0412	0.0412	0.0412
	$b_{\phi 2}$	0.009	0.009	0.009	0.009
	$(x_0/L)_1$	0	0	0	0
$(x_0/L)_0$	-	2.15	2.15	2.15	2.15

Table A.6.: Type C (LMB, HMB and HMCB). Sigmoid curve parameters for obtaining K_R , K_T and ϕ .

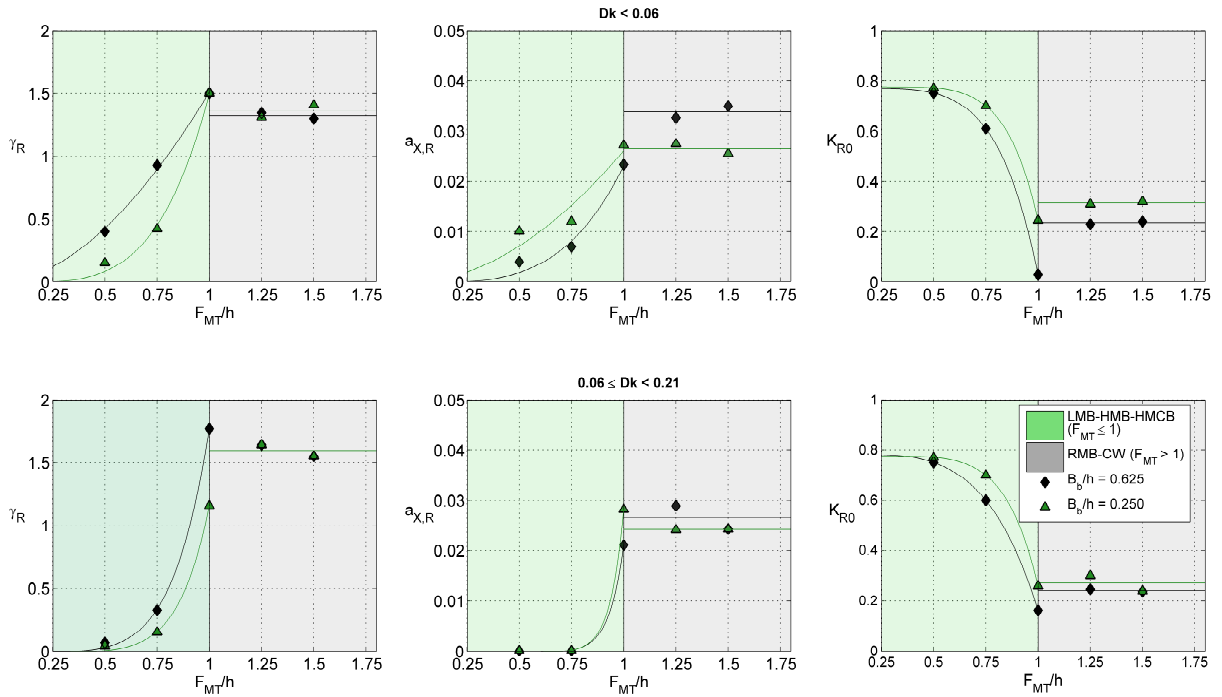


Figure A.11.: Type C (LMB, HMB and HMCB). Sigmoid curve parameters for obtaining K_R . Parameters obtained and best-fitted curves.

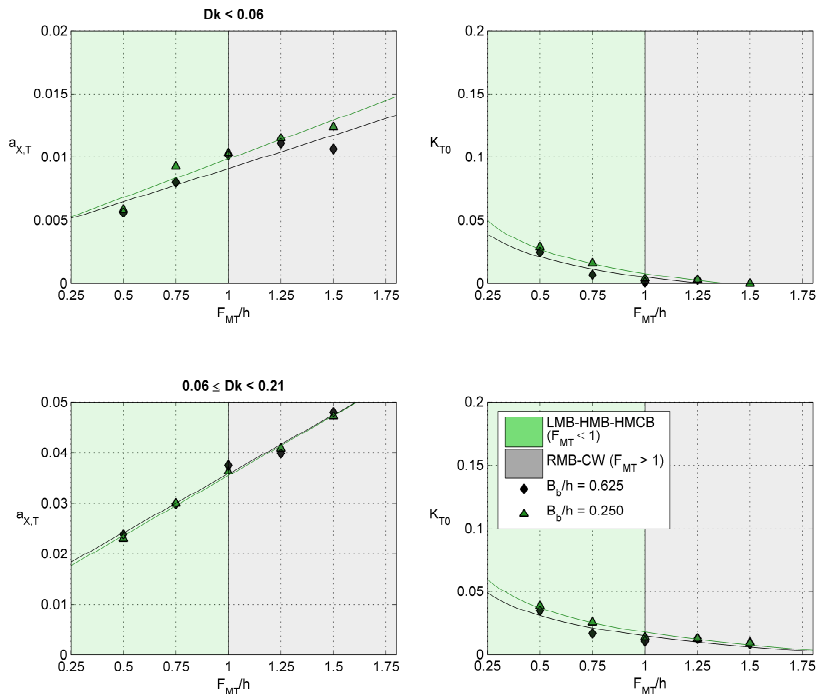


Figure A.12.: Type C (LMB, HMB and HMCB). Sigmoid curve parameters for obtaining K_T . Parameters obtained and best-fitted curves.

B_b/h	F_{MT}/h	Dk	$R^2_{K_R}$	$R^2_{K_T}$	ϵ_R
0.50	0.50	$Dk < 0.06$	-	0.63	0.010
		$Dk \geq 0.06$	-	0.84	0.033
0.625	0.75	$Dk < 0.06$	-	0.71	0.024
		$Dk \geq 0.06$	-	0.71	0.024
1.00	1.00	$Dk < 0.06$	0.95	0.78	0.120
		$Dk \geq 0.06$	0.93	0.92	0.012
0.50	0.50	$Dk < 0.06$	-	0.74	0.020
		$Dk \geq 0.06$	-	0.87	0.030
0.250	0.75	$Dk < 0.06$	-	0.90	0.007
		$Dk \geq 0.06$	-	0.71	0.009
1.00	1.00	$Dk < 0.06$	0.92	0.92	0.060
		$Dk \geq 0.06$	0.90	0.87	0.070

Table A.7.: Type C (LMB, HMB and HMCB). Goodness of fit of the sigmoid curves for obtaining K_R and K_T .

F_{MT}/h	R^2_ϕ
0.50	0.91
0.75	0.90
1.00	0.91

Table A.8.: Type C (LMB, HMB and HMCB). Goodness of fit of the sigmoid curves for obtaining ϕ .

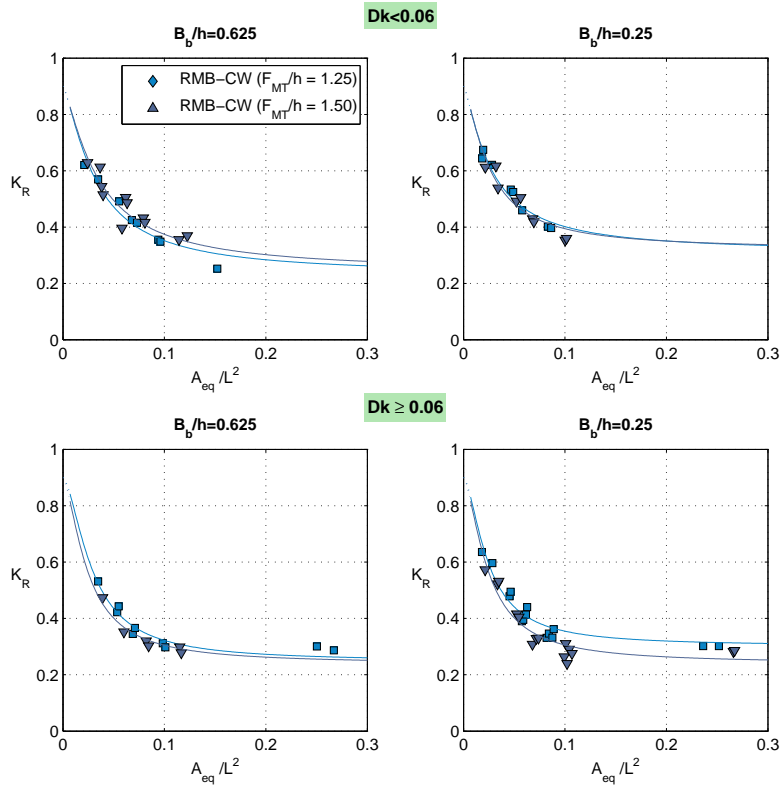


Figure A.13.: Type D (RMB-CW). K_R as a function of A_{eq}/L^2 , Dk , B_b/h and F_{MT}/h ($h_b/h = 0.50$). Experimental data and best-fitted curves.

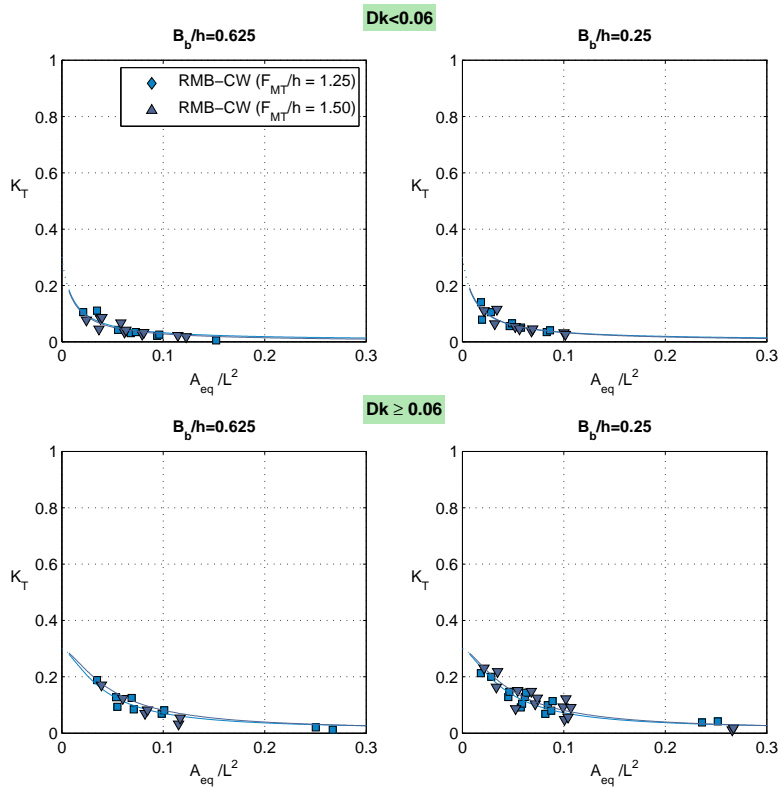


Figure A.14.: Type D (RMB-CW). K_T as a function of A_{eq}/L^2 , Dk , B_b/h and F_{MT}/h ($h_b/h = 0.50$). Experimental data and best-fitted curves.

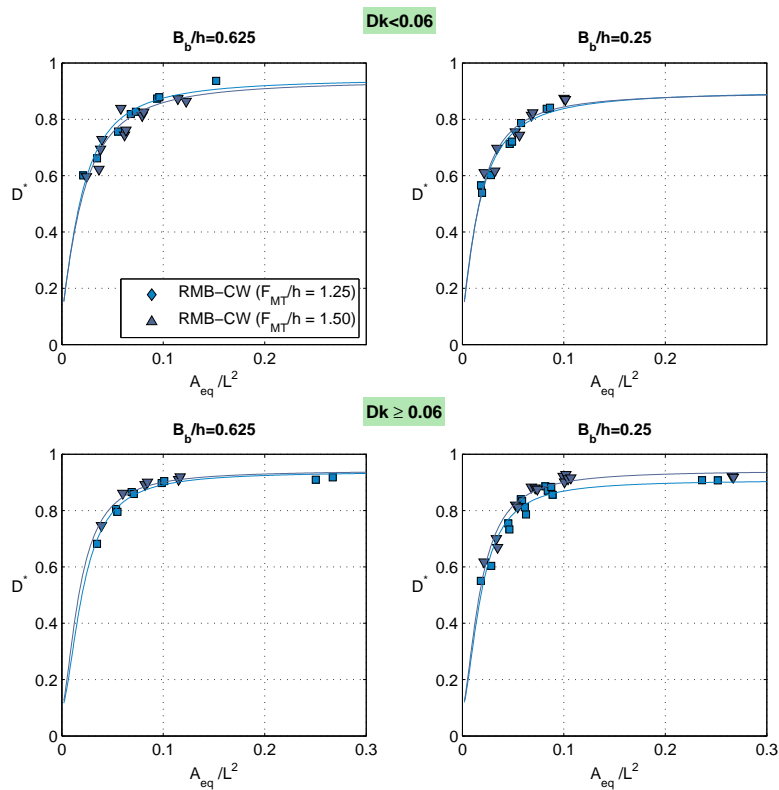


Figure A.15.: Type D (RMB-CW). D^* as a function of A_{eq}/L^2 , Dk , B_b/h and F_{MT}/h ($h_b/h = 0.50$). Experimental data and best-fitted curves.

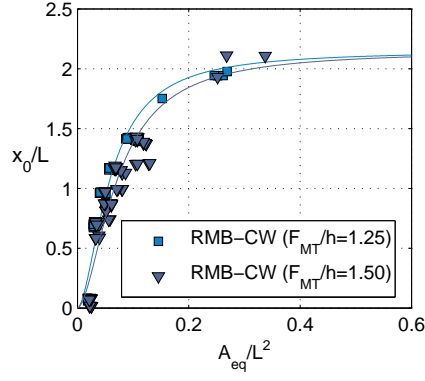


Figure A.16.: Type D (RMB-CW). x_0/L ($\phi = 4\pi x_0/L$) as a function of A_{eq}/L^2 and F_{MT}/h for all ranges of Dk and both two B_b/h . Experimental data and best-fitted curves.

Expression		Coefficients			
		$B_b/h = 0.625$		$B_b/h = 0.250$	
		$Dk < 0.06$	$Dk \geq 0.06$	$Dk < 0.06$	$Dk \geq 0.06$
$\gamma_R = a_{1R}(F_{MT}/h)^{a_{2R}} + a_{3R}$ Figure A.11	a_{1R}	0	0	0	0
	a_{2R}	0	0	0	0
	a_{3R}	1.323	1.595	1.359	1.595
K_R $a_{XR} = b_{1R}(F_{MT}/h)^{b_{2R}} + b_{3R}$ Figure A.11	b_{1R}	0	0	0	0
	b_{2R}	0	0	0	0
	b_{3R}	0.0338	0.0265	0.0265	0.0242
K_{R1}	-	0.90			
$K_{R0} = c_{1R}(F_{MT}/h)^{c_{2R}} + c_{3R}$ Figure A.11	c_{1R}	0	0	0	0
	c_{2R}	0	0	0	0
	c_{3R}	0.235	0.242	0.315	0.271
γ_T Figure A.12	-	1	1.5	1	1.5
K_T $a_{XT} = b_{1T}(F_{MT}/h)^{b_{2T}} + b_{3T}$ Figure A.12	b_{1T}	0.0053	0.0233	0.0061	0.0237
	b_{2T}	1	1	1	1
	b_{3T}	0.0038	0.0125	0.0038	0.0118
K_{T1}	-	0.30	0.30	0.30	0.30
$K_{T0} = c_{1T}(F_{MT}/h)^{c_{2T}} + c_{3T}$ Figure A.12	c_{1T}	0.1332	0.1334	0.1116	0.1116
	c_{2T}	-0.1637	-0.1635	-0.2290	-0.2290
	c_{3T}	-0.1281	-0.1182	-0.1036	-0.0936
γ_ϕ	-	1.75	1.75	1.75	1.75
$\frac{x_0}{L}$ $a_{X\phi} = b_{\phi 1}(F_{MT}/h) + b_{\phi 2}$	$b_{\phi 1}$	0.0412	0.0412	0.0412	0.0412
	$b_{\phi 2}$	0.009	0.009	0.009	0.009
$(x_0/L)_1$	-	0	0	0	0
$(x_0/L)_0$	-	2.15	2.15	2.15	2.15

Table A.9.: Type D (RMB-CW). Sigmoid curve parameters for obtaining K_R , K_T and ϕ .

B_b/h	F_{MT}/h	Dk	$R_{K_R}^2$	$R_{K_T}^2$	ϵ_R
		$Dk < 0.06$	0.93	0.80	0.064
	1.25	$Dk \geq 0.06$	0.93	0.90	0.050
0.625		$Dk < 0.06$	0.84	0.66	0.060
	1.50	$Dk \geq 0.06$	0.63	0.831	0.072
		$Dk < 0.06$	0.95	0.77	0.041
	1.25	$Dk \geq 0.06$	0.92	0.86	0.060
0.250		$Dk < 0.06$	0.88	0.78	0.060
	1.52	$Dk \geq 0.06$	0.90	0.82	0.087

Table A.10.: Type D (RMB-CW). Goodness of fit of the sigmoid curves for obtaining K_R and K_T .

F_{MT}/h	R_ϕ^2
1.25	0.93
1.50	0.90

Table A.11.: Type D (RMB-CW). Goodness of fit of the sigmoid curves for obtaining ϕ .

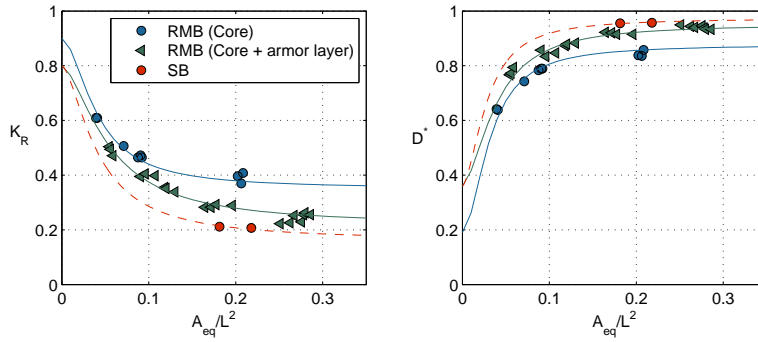


Figure A.17.: Type E and F (RMB and SB). K_R as a function of A_{eq}/L^2 and section type: core (quarry run); core + armor layer (core protected with material of a uniform grain-size distribution). Experimental data and best-fitted curves.

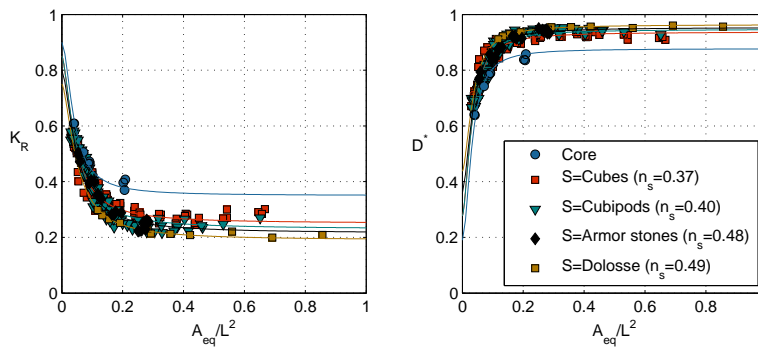


Figure A.18.: Type E and F (RMB and SB). K_R as a function of A_{eq}/L^2 and type of armor unit. Experimental data and best-fitted curves.

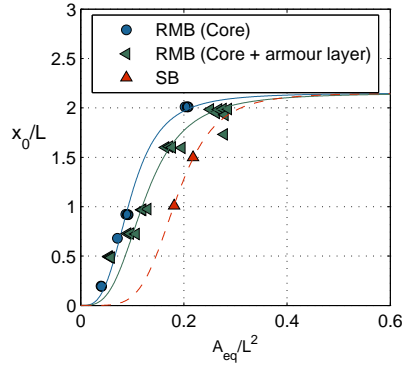


Figure A.19.: Type E and F (RMB and SB). ($\phi = 4\pi x_0/L$) as a function of A_{eq}/L^2 and section type: core (quarry run); core + armor layer (core protected with material of a uniform grain-size distribution). Experimental data and best-fitted curves.

Parameter	Coefficients					
	RMB					SB
	Core	Core + armor layer				
	$Dk \leq 0.06$	$n_s = 0.37$ (Cubes)	$n_s = 0.40$ (Cubipods)	$n_s = 0.48$ (Armorstones)	$n_s = 0.49$ (Dolosse)	$Dk = 0.10$
γ_R	1.80	1.60	1.60	1.60	1.60	1.60
a_{XR}	0.04			$a_{XR} = 0.056n_s + 0.023$		0.0418
K_R	K_{R1}	0.90	0.850	0.85	0.80	0.75
	K_{R0}	0.35		$K_{R0} = -0.40n_s + 0.39$		0.16
	γ_ϕ	3.25	3.25	3.25	3.25	3.25
	$a_{X\phi}$	0.096	0.129	0.129	0.129	0.129
x_0/L	$(x_0/L)_1$	0	0	0	0	0
	$(x_0/L)_0$	2.15	2.15	2.15	2.15	2.15

Table A.12.: Type E and F (RMB and SB). Sigmoid curve parameters for obtaining K_R and ϕ .

Layer	$R^2_{K_R}$	R^2_ϕ
Core	0.96	0.99
Core + armor layer	$n_s = 0.37$	0.90
	$n_s = 0.40$	0.90
	$n_s = 0.48$	0.96
	$n_s = 0.49$	0.93

Table A.13.: Type E (RMB). Goodness of fit of the sigmoid curves for obtaining K_R and ϕ . Note: For SB, there is not sufficient experimental data available to calculate R^2 .

Obtaining the effective depth for waves propagating over a porous structure (Losada et al., 1997b)

When waves impinge over an impermeable step with height from the seabed of $r = F_{MT}$, waves experience a variation in wavelength associated with the change in depth. However, when waves propagate over a porous step, the wave number is complex. The wavelength variation depends on the change in depth, but also on the characteristics of the porous medium (porosity, n , inertial coefficient, s , and friction coefficient, f_r).

For a given wave period, the effective depth, h_{ef} , is the one that provides the same wave number over the horizontal bed as the real part of the complex wave number for the porous step. This effective depth can be determined as follows:

- (a) The complex wave number, $K = k_r - ik_i$ is calculated by means of the dispersion equation of the waves propagating over the porous medium (Losada, 1991) and the total depth:

$$\sigma^2 - gK \tanh(Kh) = F_p [\sigma^2 \tanh(Kh) - gK] \quad (\text{B.1})$$

with

$$F_p = \left(1 - \frac{n}{s - if}\right) \frac{\tanh(Kr)}{1 - \frac{n}{(s-i)\tanh^2(Kr)}} \quad (\text{B.2})$$

The real part of the complex wave number is k_r and the imaginary part is k_i .

The wave number, k , is calculated for an impermeable bed, using an initial effective depth, $h_{ef} = h - r$, and the dispersion equation of the waves propagating over the impermeable horizontal seabed.

$$\sigma^2 = gk \tanh(kh) \quad (\text{B.3})$$

where $h = h_{ef}$.

- (b) It is then necessary to verify whether k_r of equation (a) is equal to k of equation (b). If this is not the case, then a new value of $h_{ef} = h - r + \Delta h$ must be defined where $\Delta h < r$. Step (b) is repeated until the value of h_e is obtained for which $k_r = k$.

Bibliography

- Abramowitz, A. and Stegun, I. A. (1972). *Handbook of Mathematical Functions*. Ed. by Eds. Stegun. New York, Dover (cit. on p. 105).
- Allshop, N. W. H. and Channel, A. R. (1989). “Wave reflections in harbours: Reflection performance of rock armoured slopes in random waves”. In: *Report OD 102. Hydraulics Research Limited* (cit. on pp. 8, 39, 40).
- Altomare, C. and Gironella, X. (2014). “An experimental study on scale effects in wave reflection of low-reflective quay walls with internal rubble mound for regular and random waves”. In: *Coastal Engineering* 90, pp. 51–63 (cit. on p. 8).
- Baquerizo, A. (1995). “Reflexión del oleaje en playas. Métodos de evaluación y de predicción”. PhD thesis. Cantabria (cit. on p. 19).
- Baquerizo, A. and Losada, M. A. (1999). “Wave height to depth ratio in front of coastal structures”. In: *Proc. Coastal Structures* 1, pp. 23–28 (cit. on pp. 68, 73).
- Baquerizo, A., Losada, M. A., Smith, J. M., and Kobayashi, N. (1997). “Cross-shore variation of wave reflection from beaches”. In: *Journal of Waterway, Port, Coastal and Ocean Engineering* 123(5), pp. 274–279 (cit. on pp. 68, 70).
- Battjes, J. A. (1974). “Surf similarity”. In: *Proc. XIV Int. Conf. Coastal Eng. ASCE*, pp. 466–480 (cit. on pp. 8, 12).
- Battjes, J. A. and Groenendijk, H. W. (2000). “Wave height distributions on shallow foreshore”. In: *Coastal Engineering* 40, pp. 161–182 (cit. on p. 68).
- Benedicto, M. I. (2004). “Comportamiento y evolución de la avería de los diques de abrigo frente a la acción del oleaje”. PhD thesis. Granada (cit. on pp. 2, 15, 39, 51).
- Borgman, L.E. (1967). “Random Hydrodynamic Forces on Objects”. In: *Ann. Math Statist.* 38, pp. 37–51 (cit. on p. 89).
- Burcharth, H. F. and Andersen, O. K. (1995). “On the one-dimensional steady and unsteady porous flow equations”. In: *Coastal Engineering* 24.3-4, pp. 233–257 (cit. on pp. 12, 56, 57).
- Burcharth, H. F. and Christensen, C. (1991). *On stationary and non-stationary porous flow in coarse granular materials*. Tech. rep. Alborg University, Department of Civil Engineering Report (cit. on p. 12).
- Cartwright, D. E. and Longuet-Higgins, M. S. (1956). “The statistical distribution of the maxima of random function”. In: *Proc. R. Soc. London, Series A*, (237) 212–232 (cit. on p. 68).
- Castillo, M. C., Castillo, E., Fernández-Canteli, A., Molina, R., and Gómez, R (2012). “Stochastic Model for Damage Accumulation in Rubble-Mound Breakwaters Based on Compatibility Conditions and the Central Limit Theorem”. In: *Journal of Waterway, Port, Coastal & Ocean Engineering* 138.6, pp. 451–463 (cit. on p. 116).
- CEM (2002). *Coastal Engineering Manual (CEM)*. Ed. by U. S. Army Corps of Engineers. (V. 4, Chapter 2. Washington, D.C (cit. on p. 88).
- Churchill, S. W. and Usagi, R. (1972). “A general expression for the correlation of rates of transfer and other phenomena”. In: *AIChE* 18(6), pp. 1122–1128 (cit. on pp. 27, 52).

- CIRIA-CUR-CETMEF (2007). *The Rock Manual: The Use of Rock in Hydraulic Engineering*. CIRIA. London, p. C683 (cit. on p. 16).
- Clavero, M. (2007). "Comportamiento de los diques en talud frente a la acción del oleaje y criterios para el reparto de la probabilidad conjunta de fallo en la vida útil". PhD thesis. Granada (cit. on pp. 2, 15, 46, 115).
- Clavero, M., Vílchez, M., Pérez., D., Benedicto, M. I., and Losada, M. A. (2012). "An unified desing method of maritime works against waves". In: *Coastal Engineering Proceedings, 1(33), structures.76*, pp. 1–9 (cit. on p. 12).
- Cooker, M. J. and Peregrine, D. H. (1990). "A model for breaking wave impact pressures". In: *Proc. 22nd Int. Conference on Coastal Engineering. ASCE, Delf, Holland*, pp. 1473,1486 (cit. on p. 91).
- Correa, M. (2009). *Estudio experimental de la influencia de la anchura del dique en el comportamiento del oleaje*. Tesina Fin de Máster, Universidad de Granada (cit. on pp. 2, 15).
- Dalrymple, R. A., Losada, M. A., and Martín, P. A. (1991). "Reflection and transmission from porous structures under oblique wave attack". In: *Journal of Fluids Mechanics* 224, pp. 625–644 (cit. on pp. 7, 12, 57, 116).
- del Jesus, M., Lara, J. L., and Losada, I. J. (2012). "Three-dimensional interaction of waves and porous coastal structures using OpenFOAM. Part I: Formulation and validation". In: *Coastal Engineering* 64, pp. 57–72 (cit. on pp. 56, 57).
- Dybbs, A. and Edwards, R. V. (1984). *A new look at porous media fluid mechanics - Darcy to turbulent*. Ed. by J. Bear and M. Y. Corapcioglu. 82. Dordrecht: Martinus Nijhoff Publishers, pp. 199–256 (cit. on p. 12).
- Engelund, F. A. (1953). *On the laminar and turbulent flows of ground water through homogeneous sand*. Danish Aca (cit. on pp. 56, 57).
- Ergun, S. (1952). "Fluid flow through packed columns". In: *Chem. Eng. Prog.* 48(2), pp. 89–94 (cit. on p. 56).
- Fand, R. M., Kim, B. Y. K., Lam, A. C. C., and Phan, R. T. (1987). "Resistance to the Flow of Fluids Through Simple and Complex Porous Media Whose Matrices Are Composed of Randomly Packed Spheres". In: *J. Fluids Eng. ASME*, pp. 268–274 (cit. on p. 12).
- Fenton, J. D. (1985). "Wave forces on vertical walls". In: *Journal of Waterway, Port, Coastal and Ocean Division, ASCE* 111.4, pp. 193–717 (cit. on p. 91).
- Garcia, N., Lara, J.L., and Losada, I.J. (2004). "2-D numerical analysis of near-field flow at low-crested permeable breakwaters". In: *Coastal Engineering* 51.10, pp. 991–1020 (cit. on p. 57).
- Garrido, J. M. and Medina, J. R. (2012). "New neural network-derived empirical formulas for estimating wave reflection on Jarlan-type breakwaters". In: *Coastal Engineering* 62, pp. 9–18 (cit. on p. 8).
- Goda, Y. (1985). *Random seas and desing of maritime structures*. University of Tokio Press, pp. 107–162 (cit. on pp. 1, 18, 91, 93).
- Gu, Z. and Wang, H. (1991). "Gravity waves over porous bottoms". In: *Coastal Engineering* 15, pp. 497–524 (cit. on pp. 12, 17).
- Guanche, R., Losada, I. J., and Lara, J. L. (2009). "Numerical analysis of wave loads for coastal structure stability". In: *Coastal Engineering* 56.5-6, pp. 543–558 (cit. on p. 57).
- Günbak, A. R. and Göcke, T. (1984). "Wave screen stability of rubble mound breakwaters". In: *International Symposium of Maritime Structures in the Meditarrean Sea*, pp. 2099–2112 (cit. on p. 91).
- Hannoura, A. A. and Barends, F. B. J. (1981). "Non Darcy flow; A state of art". In: *Proc. UROMECH 143 "Flow and Transport through porous media"*. Balkema, Rotterdam (cit. on p. 56).
- Higuera, P., Lara, J. L., and Losada, I. J. (2014). "Three-dimensional interaction of waves and porous coastal structures using OpenFOAM®. Part I: Formulation and validation". In: *Coastal Engineering* 83, pp. 243–258 (cit. on pp. 25, 56, 57).

- Hsu, T., Sakakiyama, T., and Liu, P. (2002). "A numerical model for wave motions and turbulence flows in front of a composite breakwater". In: *Coastal Engineering* 46.1, pp. 25–50 (cit. on pp. 23, 56).
- Hughes, S. A. and Fowler, J. E. (1995). "Estimating wave-induced kinematics at sloping structures". In: *Journal of Waterway, Port, Coastal and Ocean Engineering* August, pp. 209–215 (cit. on pp. 1, 6, 63).
- Iglesias, G., Rabuñal, J., Losada, M. A., et al. (2008). "A virtual laboratory for stability tests of rubble-mound breakwaters". In: *Ocean Engineering* 35, pp. 1113–1120 (cit. on p. 8).
- Iribarren, R. (1938). *Una fórmula para el cálculo de los diques de escollera*. M. Bermejillo, Pasajes, Guipuzcoa, España (cit. on p. 12).
- (1949). "Protection des ports". In: *XVII International Navigation Congress*. Lisbon (cit. on p. 8).
- Iribarren, R. and Nogales, C. (1950). *Generalización de la fórmula para el cálculo de los diques de escollera y comprobación de sus coeficientes*. Revista de Obras Públicas, pp. 277–289 (cit. on p. 91).
- Jensen, B., Jacobsen, N. G., and Christensen, E. D. (2014). "Investigations on the porous media equations and resistance coefficients for coastal structures". In: *Coastal Engineering* 84, pp. 56–72 (cit. on pp. 25, 56, 57).
- Jensen, O. J. (1984). *A monograph on rubble mound breakwaters*. Horsholm (Denmark): Danish Hydraulic Institute (cit. on p. 91).
- Klopman, G. and van der Meer, J. W. (1999). "Random wave measurements in front of reflective structures". In: *Journal of Waterway, Port, Coastal and Ocean Engineering*, pp. 39–45 (cit. on pp. 1, 51, 69).
- Kortenhaus, A. and Oumeraci, H. (1998). "Classification of wave loading on monolithic coastal structures". In: *Proc. of the 26st International Coastal Engineering Conferece, ASCE*, pp. 867–880 (cit. on pp. 8, 10, 22, 23, 39).
- Kraus, N. C., Smith, J.M., and Sollitt, C. K. (1992). "Supertank laboratory data collection project". In: *Proc. 23th ICCE, ASCE*. Delft, pp. 2191–2204 (cit. on p. 68).
- Lamberti, A. (1994). "Irregular waves reflection and multi-gauge wave measurements near the reflecting structure". In: *Proc. of the 2nd Workshop on Rubble mound Failure Modes (Contract MAS2-CT92-0042)*. Bressanone, p. 5 (cit. on p. 1).
- Lara, J. L., Losada, I. J., and Guanache, R. (2008). "Wave interaction with low-mound breakwaters using a RANS model". In: *Ocean Engineering* 35.13, pp. 1388–1400 (cit. on pp. 23, 56, 57).
- Lara, J. L., Jesus, M. del, and Losada, I. J. (2012). "Three-dimensional interaction of waves and porous coastal structures". In: *Coastal Engineering* 64, pp. 26–46 (cit. on p. 57).
- Lara, Javier L., Losada, Inigo J., Maza, Maria, and Guanache, Raul (2011). "Breaking solitary wave evolution over a porous underwater step". In: *Coastal Engineering* 58.9, pp. 837–850 (cit. on p. 57).
- Lin, P. (1998). "Modelling of Breaking Waves". PhD thesis. Cornell University (cit. on p. 57).
- Liu, P. (1985). "Wave-induced pressure under gravity structures". In: *Journal of Waterway, Ports, Coastal and Ocean Engineering* 111(1), pp. 111–120 (cit. on p. 91).
- Liu, P., Lin, P., Chang, K., and Sakakiyama, T. (1999). "Numerical modeling of wave interaction with porous structures". In: *Journal of Waterway, Ports, Coastal and Ocean Engineering* 125, pp. 322–330 (cit. on pp. 56, 57).
- Liu, Y. and Faraci, C. (2014). "Analysis of orthogonal wave reflection by a caisson with open front chamber filled with sloping rubble mound". In: *Coastal Engineering* 91, pp. 151–163 (cit. on pp. xvii, xviii, 40, 41).
- Longuet-Higgins, M. S. (1952). "On the statistical distributions of heights of sea waves". In: *J. of Mar. Res.* 11, pp. 245–266 (cit. on p. 67).
- Longuet-Higgins, M.S. (1963). "The effect of nonlinearities on statistical distributions in the theory of sea waves." In: *J. Fluid Mech* 17, pp. 459–480 (cit. on p. 68).

- López, C. (1998). *Influencia de la reflexión del oleaje en la estabilidad de diques en talud*. Tesis Doctoral, Universidad de Cantabria (cit. on p. 2).
- Losada, I. J. (1991). “Estudio de la propagación de un tren lineal de ondas por un medio discontinuo”. PhD thesis. Cantabria (cit. on p. 133).
- Losada, I. J., Losada, M. A., and Baquerizo, A. (1993a). “An analytical method to evaluate the efficiency of porous screens as wave dampers”. In: *Applied Ocean Research* 15.4, pp. 207–215 (cit. on p. 1).
- Losada, I. J., Dalrymple, R. A., and Losada, M. A. (1993b). “Water waves on crown Breakwaters”. In: *Journal of Waterway, Port, Coastal and Ocean Engineering* 119.4, pp. 367–380 (cit. on pp. 7, 12, 57, 91, 97).
- Losada, I. J., Losada, M. A., and Martín, F. L. (1995). “Experimental study of wave-induced flow in a porous structure”. In: *Coastal Engineering* 26, pp. 77–98 (cit. on p. 57).
- Losada, I. J., Silva, R., and Losada, M. A. (1997a). “Effects of reflective vertical structures permeability on random wave kinematics”. In: *Journal of Waterway, Port, Coastal and Ocean Engineering* 123.December, pp. 347–353 (cit. on pp. 1, 69, 71).
- Losada, I. J., Patterson, M. D., and Losada, M. A. (1997b). “Harmonic generation past a submerged porous step”. In: *Coastal Engineering* 31, pp. 281–304 (cit. on pp. 1, 7, 46, 133).
- Losada, I. J., Lara, J. L., Guanache, R., and Gonzalez-Ondina, J. M. (2008). “Numerical analysis of wave overtopping of rubble mound breakwaters”. In: *Coastal Engineering* 55.1, pp. 47–62 (cit. on pp. 23, 56, 57).
- Losada, M. A. (1990). *Recent Development in the Design of Mound Breakwater*. Handbook, Herbich, J. Houston, TX: Gulf Publishing Co., pp. 939–1050 (cit. on p. 51).
- Losada, M. A. and Giménez-Curto, L. A. (1979). “The joint effect of the wave height and period on the stability of rubble mound breakwaters using Iribarren’s number”. In: *Coastal Engineering* 3, pp. 77–96 (cit. on pp. 1, 41).
- (1981). “Flow characteristics on rough , permeable slopes under wave action”. In: *Coastal Engineering* 4, pp. 187–206 (cit. on pp. 8, 12, 51).
- Madsen, O. S. and White, S. M. (1976). *Reflection and transmission characteristics of porous rubble mound breakwaters*. Tech. rep. USACE Miscellaneous 76-5 (cit. on p. 57).
- Martín, F. L., Losada, M. A., and Medina, R. (1999). “Wave loads on rubble mound breakwater crown walls”. In: *Coastal Engineering* 37, pp. 149–174 (cit. on p. 91).
- Medina, J. R. and Gómez-Martín, M. E. (2007). “Análisis de la Estabilidad Hidráulica del Manto Principal de Diques en Talud con Cubos y Cubípodos”. In: *Laboratorio de Puertos y Costas de la Universidad de Valencia. Informe N°2. Ensayos LPC-UPV* (cit. on pp. 38, 39).
- Minikin, R. R. (1963). *Winds, Waves and Maritime Structures*. 2nd editio. London, UK: Griffin, Charles (cit. on p. 91).
- Nagai, S. (1973). “Wave forces on structures”. In: *Advances in Hydroscience. Academic Press, New York* 9, pp. 253–324 (cit. on pp. 21, 91).
- Norgaard, J. Q., Andersen, L. V., Andersen, T. L., and A., Burcharth H. (2014). “Displacement of monolithic rubble-mound breakwater crown-walls”. In: *Coastal Engineering Proceedings 1(33)* (cit. on p. 91).
- Oumeraci, H. and Kortenhaus, A. (1997). “Wave impact loading tentative formulae and suggestions for the development of final formulae”. In: *Proceedings 2nd Task 1 Workshop, MAST III, PROVERBS-Proyect: Probabilistics Design Tools for Vertical Breakwaters*. Edinburgh, U.K., p. 13 (cit. on p. 21).
- Oumeraci, H., Klammer, P., and Partenscky, H. W. (1993). “Classification of breaking wave loads on vertical structures”. In: *Journal of Waterway, Port, Coastal Ocean Engineering (ASCE)* 119 (4), pp. 381–397 (cit. on p. 22).
- Pedersen, J. (1996). *Wave forces and overtopping on crown walls of rubble mound breakwaters*. Tech. rep. Aalborg University, Denmark: Series paper 12, Hydraulic and Coastal Engineering Laboratory, Department of Civil Engineering (cit. on p. 91).

- Pérez, D. (2008). *Procesos hidrodinámicos en diques mixtos y efectos de escala*. Tesis Doctoral, Universidad de Granada (cit. on pp. 15, 91, 97, 102, 116).
- Pérez-Romero, D. M., Ortega-Sánchez, M., Moñino, A., and Losada, M. A. (2009). “Characteristic friction coefficient and scale effects in oscillatory porous flow”. In: *Coastal Engineering* 56.9, pp. 931–939 (cit. on pp. 2, 7, 12, 16, 17, 29, 57).
- Polubarinova-Kochina, P. Y. (1962). *Theory of Groundwater Movement*. Princenton University Press, Princenton, N.J. USA (cit. on p. 55).
- Puertos del Estado (2012). *Diques de abrigo en los puertos de interés general del Estado. Años 1986-2011*. Puertos del Estado (cit. on p. 47).
- Requejo, S., Vidal, C., and Losada, I. J. (2002). “Modelling of wave loads and hydraulic performance of vertical permeable structures”. In: *Coastal Engineering* 46.4, pp. 249–276 (cit. on p. 29).
- Rice, S. O. (1944). *Mathematical analysis of random noise* (cit. on pp. 67, 68, 71).
- ROM 0.0 (2001). *ROM 0.0 Procedimiento general con bases de cálculo para el proyecto ROM en las obras portuarias y/o marítimas*. Puertos del Estado (cit. on pp. 87, 89).
- ROM 1.0 (2009). *ROM 1.0. Recomendaciones geotécnicas para obras marítimas y portuarias*. Puertos del Estado (cit. on pp. 5, 8, 45, 87–89, 115).
- Ruíz, J. R., Flores, Z., and Frago, L. (2013). “Reflexión del oleaje en rompeolas superficiales permeables a talud”. In: *Ingeniería Hidráulica y Ambiental* XXXIV.2, pp. 27–40 (cit. on pp. 38, 39).
- Sainflou, M (1928). “Essai sur les digues maritimes verticales”. In: *Annals del Ponts et Chaussées* 98, p. 9 (cit. on p. 91).
- Scarcella, D., Benedicto, M. I., Moñino, A., and Losada, M. A. (2006). “Scale effects in rubble mound breakwaters considering wave energy balance”. In: *Proc. 30th Int. Conf. on Coastal Engineering, ASCE, San Diego*, pp. 4410–4415 (cit. on pp. 16, 57).
- Seelig, W. N. and Ahrens (1981). *Estimation of wave reflection and energy dissipation coefficient for beaches, revetments and breakwater*. Tech. rep. Vicksburg: Fort Belvoir, U.S.A.C.E. MS (cit. on pp. xvii, 8, 41).
- Sivanesapillai, R., Steeb, H., and Hartmaier, A. (2014). “Transition of effective hydraulic properties from low to high Reynolds number flow in porous media”. In: *Geophys. Res. Lett.* 41 (cit. on p. 27).
- Smith, R. W. K. (1990). “Permeability characteristics of rubble material-new formulae”. In: *Proc. Coastal Engineering Conference* (cit. on p. 56).
- Sollitt, C. K. and Cross, R. H. (1972). “Wave transmission through permeable breakwaters”. In: *Proc., 13 International Conference on Coastal Engineering, ASCE*. Vancouver, pp. 1827–1846 (cit. on pp. 46, 56).
- Sutherland, J. and O’Donoghue, T. (1998). “Wave phase shift at coastal structures”. In: *Journal of Waterway, Port, Coastal and Ocean Engineering* April, pp. 90–98 (cit. on pp. 1, 32).
- Takahashi, S. (1996). “Design of vertical breakwaters”. In: *Port and Harbor Research Institute, Reference Document, Japan*. 34 (cit. on pp. 1, 91, 93, 94, 115).
- van der Meer, J. W. (1992). “Conceptual design of rubble mound breakwater”. In: *International Conference on Coastal Engineering*. Venice: Tecnoprint, pp. 47–510 (cit. on p. 1).
- (1998). “Geometrical design of coastal structures”. In: *Seawalls, Dikes and Revetments*. Balkema, Rotterdam: Pilarczyk, K.W. Chap. 9 (cit. on p. 115).
- van der Meer, J. W., Briganti, R., Zanuttigh, B., and Wang, B. (2005). “Wave transmission and reflection at low-crested structures: Design formulae, oblique wave attack and spectral change”. In: *Coastal Engineering* 52.10-11, pp. 915–929 (cit. on p. 52).
- van Gent, M. R. A. (1995). “Wave interaction of permeable coastal structures”. PhD thesis. Delft (The Netherlands, 177) (cit. on pp. 17, 23, 55–57).
- (2014). “Oblique wave attack on rubble mound breakwaters”. In: *Coastal Engineering* 88, pp. 43–54 (cit. on p. 52).

- van Gent, M. R. A. and van der Werf, I. M. (2014). "Rock toe stability of rubble mound breakwaters". In: *Coastal Engineering* 83, pp. 166–176 (cit. on p. 115).
- Vílchez, M., Clavero, M., Pérez, D., et al. (2011a). "Evolución de tipologías de diques de abrigo y comportamiento frente al reparto de flujos de energía". In: *XI Jornadas Españolas de Ingeniería de Costas y Puertos*. Las Palmas (España).
- Vílchez, M., Moyano, J., Clavero, M., Miguel, M. D., and Losada, M. A. (2011b). "Forces and subpressures on non-overtoppable vertical breakwaters". In: *Proceedings of the 6th International Conference of Coastal Structures*, pp. 545–555 (cit. on pp. 2, 102).
- Vílchez, M., Clavero, M., and Losada, M. A. (2015). "Cálculo del comportamiento hidráulico de un dique de abrigo en talud con espaldón (RMB-CW)". In: *XIII Jornadas Españolas de Costas y Puertos*. Avilés (España).
- Vílchez, M., Clavero, M., Lara, J. L., and Losada, M. A. (2016a). "A characteristic friction diagram for the numerical quantification of the hydraulic performance of different breakwater types". In: *Coastal Engineering (Under review)*.
- Vílchez, M., Clavero, M., Baquerizo, A., and Losada, M. A. (2016b). "An approximation to the statistical behavior of wind waves in front and on the face of non-overtopped breakwaters". In: *Coastal Engineering (Under review)*.
- Vílchez, M., Clavero, M., and Losada, M. A. (2016c). "Hydraulic performance of different non-overtopped breakwater types under 2D wave attack". In: *Coastal Engineering* 107, pp. 34–52.
- Vílchez, M., Díaz-Carrasco, P., Clavero, M., and Losada, M. A. (2016d). "Verification of the crown wall stability taking into account the hydraulic performance curves". In: *Coastal Engineering Proceedings (Accepted)*.
- Ward, J.C. (1964). "Turbulent flow in porous media". In: *J. Hydraulic. Div. ASCE* 90 (HY5), pp. 1–12 (cit. on p. 56).
- Yacoub, M. D., Benevides, D., Dias, U. S., and Fraidenraich, G. (2005). "Joint Statistics for Two Correlated Weibull Variates". In: *IEEE Antennas and Wireless Propagation Letters* 4, February, pp. 129–132 (cit. on p. 105).
- Yu, B., Ma, Y., Ma, X., and Dong, G. (2014). "Laboratory Study of the Nonlinear Transformation of Irregular Waves over A Mild Slope". In: *China Ocean Eng.* 28.4, pp. 489–500 (cit. on p. 69).
- Zanuttigh, B. and van der Meer, J. W. (2008). "Wave reflection from coastal structures in design conditions". In: *Coastal Engineering* 55, pp. 771–779 (cit. on pp. xvii, 8, 41).
- Zanuttigh, B., Formentin, S. M., and Briganti, R. (2013). "A neural network for the prediction of wave reflection from coastal and harbor structures". In: *Coastal Engineering* 80, pp. 49–67 (cit. on p. 8).

